LNGS - s.s. 17 bis km 18,910 67010 ASSERGI (AQ) ITALY
tel.+39 0862 4371 fax +39 0862 437559
email: document@lngs.infn.it
http://www.lngs.infn.it

ANNUAL REPORT 2015

LNGS/EXP-02/16
June 2016

INFN

Annual Report 2015

Laboratori Nazionali del Gran Sasso

Cover Image: XENON1T Experiment

ISBN-978-88-940122-1-7

Codice ISBN
978-88-940122-1-7

Annual Report 2015

LNGS Director — Prof. Stefano Ragazzi

Editor — Dr. Roberta Antolini

Technical Assistants — Dr. Alessia Giampaoli
Mr. Marco Galeota

Contents

THE BOREXINO EXPERIMENT

The Borexino collaboration

M. Agostini[t,v], K. Altenmüller[t], S. Appel[t], G. Bellini[l], J. Benziger[p], D. Bick[d], G. Bonfini[k], D. Bravo[r], B. Caccianiga[l], F. Calaprice[o], A. Caminata[c], P. Cavalcante[k], A. Chepurnov[u], D. D'Angelo[l], S. Davini[v], A. Derbin[n], L. Di Noto[c], I. Drachnev[v], A. Etenko[i], K. Fomenko[b], A. Formozov[b,l], D. Franco[a], F. Gabriele[k], C. Galbiati[o] (*), C. Ghiano[c], M. Giammarchi[l], M. Goeger-Neff[t], A. Goretti[o], M. Gromov[u], C. Hagner[d], E. Hungerford[w], Aldo Ianni[k], Andrea Ianni[o], K. Jedrzejczak[f], D. Jeschke[t], M. Kaiser[d], V. Kobychev[g], D. Korablev[b], G. Korga[k], D. Kryn[a], M. Laubenstein[k], B. Lehnert[y], E. Litvinovich[i,j], F. Lombardi[k], P. Lombardi[l], L. Ludhova[l], G. Lukyanchenko[i,j], I. Machulin[i,j], S. Manecki[r], W. Maneschg[e], S. Marcocci[v], E. Meroni[l], M. Meyer[d], L. Miramonti[l], M. Misiaszek[f,k], M. Montuschi[s], P. Mosteiro[o], V. Muratova[n], B. Neumair[t], L. Oberauer[t], M. Obolensky[a], F. Ortica[m], M. Pallavicini[c], L. Papp[t], L. Perasso[c], A. Pocar[q], G. Ranucci[l] (*), A. Razeto[k], A. Re[l], A. Romani[m], R. Roncin[k,a], N. Rossi[k], S. Schönert[t], D. Semenov[n], H. Simgen[e], M. Skorokhvatov[i,j], O. Smirnov[b], A. Sotnikov[b], S. Sukhotin[i], Y. Suvorov[z,i], R. Tartaglia[k], G. Testera[c], J. Thurn[y], M. Toropova[i], E. Unzhakov[n], A. Vishneva[b], R.B. Vogelaar[r], F. von Feilitzsch[t], H. Wang[z], S. Weinz[ii], J. Winter[ii], M. Wojcik[f], M. Wurm[ii], Z. Yokley[r], O. Zaimidoroga[b], S. Zavatarelli[c], K. Zuber[y], G. Zuzel[f]

[a]AstroParticule et Cosmologie, Universitá Paris Diderot, CNRS/IN2P3, CEA/IRFU, Observatoire de Paris, Sorbonne Paris Cité, 75205 Paris Cedex 13, France.
[b]Joint Institute for Nuclear Research, 141980 Dubna, Russia.
[c]Dipartimento di Fisica, Università degli Studi e INFN, Genova 16146, Italy.
[d]Institut für Experimentalphysik, Universität, 22761 Hamburg, Germany.
[e]Max-Planck-Institut für Kernphysik, 69117 Heidelberg, Germany.
[f]M. Smoluchowski Institute of Physics, Jagiellonian University, 30059 Krakow, Poland.
[g]Kiev Institute for Nuclear Research, 06380 Kiev, Ukraine.
[h]Institute for Theoretical and Experimental Physics, 117218 Moscow, Russia.
[i]NRC Kurchatov Institute, 123182 Moscow, Russia.
[j]National Research Nuclear University MEPhI (Moscow Engineering Physics Institute), 115409 Moscow, Russia.
[k] INFN Laboratori Nazionali del Gran Sasso, 67010 Assergi (AQ), Italy.
[l] Dipartimento di Fisica, Università degli Studi e INFN, 20133 Milano, Italy.
[m] Dipartimento di Chimica, Università e INFN, 06123 Perugia, Italy.
[n] St. Petersburg Nuclear Physics Institute NRC Kurchatov Institute, 188350 Gatchina, Russia.
[o] Physics Department, Princeton University, Princeton, NJ 08544, USA.
[p] Chemical Engineering Department, Princeton University, Princeton, NJ 08544, USA.
[q] Amherst Center for Fundamental Interactions and Physics Department, University of Massachusetts, Amherst, MA 01003, USA.
[r] Physics Department, Virginia Polytechnic Institute and State University, Blacksburg, VA 24061, USA.
[s] Dipartimento di Fisica e Scienze della Terra Università degli Studi di Ferrara e INFN, Via Saragat 1-44122, Ferrara, Italy.
[t]Physik-Department and Excellence Cluster Universe, Technische Universität München, 85748 Garching, Germany.
[u] Lomonosov Moscow State University Skobeltsyn Institute of Nuclear Physics, 119234 Moscow, Russia.
[v] Gran Sasso Science Institute (INFN), 67100 Ł'Aquila, Italy.
[w] Department of Physics, University of Houston, Houston, TX 77204, USA.
[y] Department of Physics, Technische Universität Dresden, 01062 Dresden, Germany.
[z] Physics and Astronomy Department, University of California Los Angeles (UCLA), Los Angeles, California 90095, USA.
[ii] Institute of Physics and Excellence Cluster PRISMA, Johannes Gutenberg-Universität Mainz, 55099 Mainz, Germany.
(*) co-spokepersons

Abstract

Borexino is located in the Hall C of the Laboratori Nazionali del Gran Sasso. It features 300 tons of ultra-pure liquid scintillator and 2200 photomultiplier tubes to detect the feeble signal induced by neutrinos which cross it. Borexino started taking data in 2007 with the main goal of studying solar neutrinos in real-time with a low energy threshold. This goal was successfully accomplished: Borexino has performed a complete spectroscopy of solar neutrinos, by detecting most of the components of the solar neutrino flux coming from the so-called proton-proton cycle. In this Report, after summarizing the results achieved by Borexino in the past years, we will focus on two results published in 2015, namely, an updated measurement of the geo-neutrino flux and the world best limit on electron decay into a neutrino and a single monoenergetic gamma. We will also discuss the major on-going effort mainly devoted to improve the precision on ^{7}Be and pep fluxes and our sensitivity to CNO solar neutrino flux.

1 Introduction

The study of solar neutrinos over the years has had a major impact on both solar and particle physics, providing, on one side, a nice confirmation of the Standard Solar Model, and on the other, a convincing proof of the phenomena of neutrino oscillations. In this framework the role of Borexino has been crucial: its exceptional radiopurity has made it possible to work with a very low energy threshold (down to ~ 150 keV), thus allowing the experiment to perform a complete spectroscopy of solar neutrinos.

After shortly summarizing the main features of the detector (Section 2), its major past achievements and the current status of the project (Section 3), we will focus on two recent results published by Borexino in 2015: the updated measurement of the geo-neutrinos flux (Section 4) and a new limit on the electron decay into a neutrino and a photon, a direct test of charge conservation (Section 5). We conclude with an outlook on future perspectives concerning the possibility to detect solar neutrinos from the CNO reaction (Section 6).

2 The Borexino detector

Borexino is located in the Hall C of Laboratori Nazionali del Gran Sasso. The detector design follows the concept of graded-shielding, in which layers of concentric materials of increasing radiopurity shield the innermost ultra-pure core of the experiment. A schematic view of the Borexino design is shown in Figure 1. The core of Borexino is 300 tons of ultra-pure liquid scintillator (pseudocumene + 1.5 g/l of PPO) contained in a 4.25 m-radius, 120 μm-thick nylon vessel. The light emitted by the scintillator is detected by 2214 photomultiplier tubes mounted on a 7 m-radius Stainless Steel Sphere (SSS), concentrical with the nylon vessel. The SSS is filled with ~ 1000 tons of ultra-pure buffer liquid (pseudocumene + DMP, a light quencher) which provide shielding against radioactivity from the photomultipliers and the sphere itself. To further increase shielding, the SSS is surrounded by 2000 tons of ultra-pure water contained in a cylindrical dome. The water in the external part of the detector serves also as an active shield to suppress the residual background due to cosmic muons which are able of penetrating underground. In order to do so, 200 photomultiplier tubes are mounted on the external part of the SSS to detect the Cerenkov light emitted by muons which cross the water. The intrinsic radiopurity of the scintillator has been brought to exceptional levels thanks to the successful purification strategy developed during 15 years of dedicated R&D studies [8]. A detailed description of the Borexino detector can be found in reference [7].

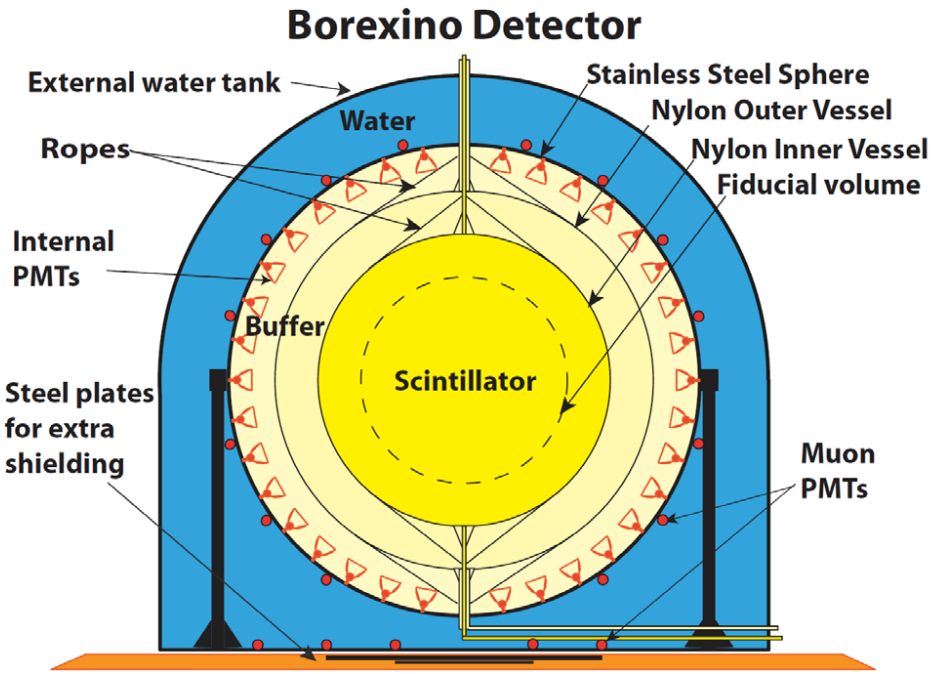

Figure 1: Schematic view of the Borexino detector.

3 Status of the project

Borexino started taking data in 2007. During the so-called Phase 1 (2007-2010), Borexino has reached its original goal of measuring the ^{7}Be flux with high precision (total error below 5%), its day/night asymmetry [1] [2] and its seasonal modulation; it has also performed the first direct observation of neutrinos from the *pep* reaction [4] and has measured the ^{8}B neutrino flux down to the unprecedented threshold of 3 MeV [3]. The results on solar neutrinos of Borexino Phase-I are described in details in [5]. In 2010-2011 the Borexino scintillator has been treated with several cycles of water extraction to further increase its radiopurity. This purification campaign has been successful in reducing the ^{85}Kr content to negligible values ($<$4.7 counts/day at 95% C.L.). It has also significantly reduced the contamination from ^{210}Bi ($\sim$20 counts/day). The current levels of U and Th are two orders of magnitude better than specifications, namely: $^{238}\mathrm{U} < 9.5 \times 10^{-20}$ g/g (95% C.L.); $^{232}\mathrm{Th} < 7.2 \times 10^{-19}$ g/g (95% C.L.). Borexino Phase-II started in 2012 with these improved radiopure conditions and is on-going. The reduced background at low energies of Phase II, together with the complete knowledge of the detector response below 400 keV (obtained exploiting calibration data) has led to the first direct observation of solar neutrinos from the so-called pp reaction ($\mathrm{p} + \mathrm{p} \rightarrow \mathrm{d} + \mathrm{e}^{-} + \nu_e$) [6]. This reaction, which belongs to the proton-proton cycle, is the keystone process for energy production in the Sun and is responsible for 90% of the solar neutrino flux on Earth.

Borexino Phase-II is on-going and the full data-set will be exploited to reduce the uncertainty on the already measured fluxes (^{7}Be, pep, pp) to unprecedented levels and possibly gain sensitivity

to CNO neutrinos. The strategy to reach these goals is based on several pillars: collection of more statistics; upgrade and optimization of the analysis tools; improvement of the stability of the detector temperature (and consequently of the background, see next Section 3.1); reduction of systematic errors with a new calibration campaign at the end of 2016.

Figure 2: Borexino water tank covered with two layers of 10 cm-thick mineral wool.

3.1 Insulation of the Borexino water tank

In order to pursue the goals described above, a major effort has been carried on to stabilize the detector temperature as much as possible. This is needed because there is evidence that sudden changes of the external temperature induce convective motions in the Borexino scintillator which stirs ^{210}Po attached to the nylon Inner Vessel into the fiducial volume. The Borexino Water Tank has been insulated with two 10 cm-thick layers of mineral wool. The work has started in May 2015 and has been completed in November 2015. A picture of the tank covered with the insulation is shown in Fig. 2. Figure 3 shows the temperature evolution as a function of time as detected by sensors located at different heights in the detector. The stabilization of temperatures due to the thermal insulation is evident.

3.2 Preparation of a new trigger system

Borexino has several years of data-taking ahead, both to complete the solar neutrino program and to accomplish the sterile neutrino search with SOX (see dedicated Section in this Annual

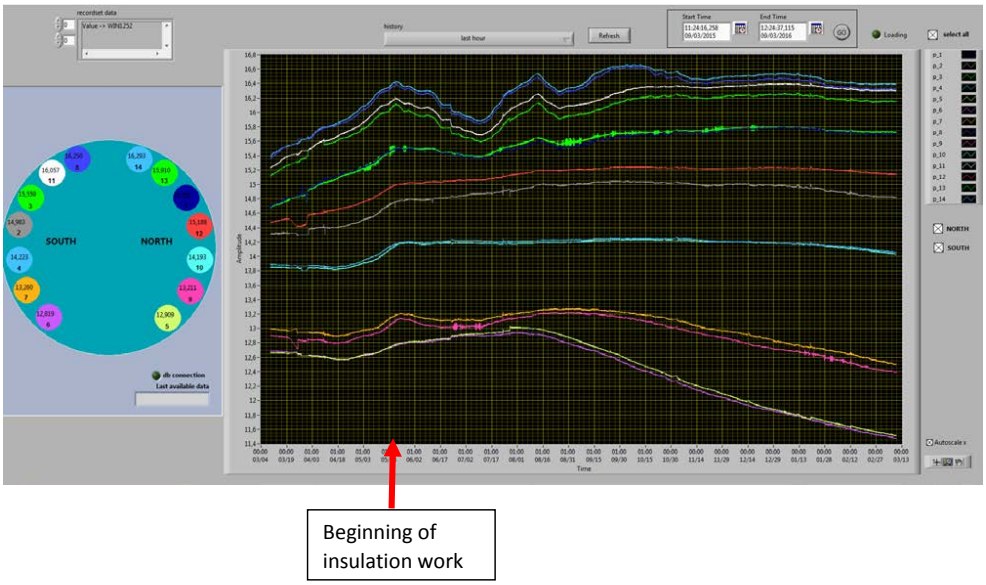

Figure 3: Temperature profiles as a function of time in the Borexino detector (buffer liquid). Each line correspons to a sensor located at a different z-position. The red arrow shows the moment in which the insulation work has started. The stabilization of temperature due to thermal insulation is evident. The decrease of the temperature in the lowest sensors is due to an other operation which was performed on july 15^{th} 2015: in order to increase the temperature gradient, it was decided to stop the water loop which ricirculated water in the water-tank. In this way, the temperature of the lowest part of the detector will slowly tend to the Hall C floor temperature ($\sim$ 8 degrees).

Report). For this reason we have to minimize the risk of hardware failures due to ageing of the detector. In this respect, one of the most critical part is the trigger system which has recently shown some problems which have caused non negligible data loss. For this reason it was decided to start designing a new trigger system which will substitute the current one, whenever ready and thoroughly tested offline. This system, besides being completely based on new hardware and therefore more trustworthy, will also have new features and more flexibility with respect to the old one. Currently, the preliminary test phase at the LNGS electronic laboratory is ongoing. The end of the whole activity is foreseen for the first trimester of 2016.

4 Spectroscopy of geo-neutrinos

Geo-neutrinos are $\bar{\nu}_e$ emitted by radioactive decays of isotopes present in the Earth crust and mantle. They are detected by Borexino via the so-called inverse beta decay reaction, namely, $\bar{\nu}_e + p \rightarrow n + e^+$, which features a very clean signature provided by the delayed coincidence between the positron and the neutron capture. The main contribution to the $\bar{\nu}_e$ signal in Borexino comes from beta decays of isotopes belonging to the ^{238}U and ^{232}Th natural chain. The most relevant background for this analysis is due to anti-neutrinos from reactors. Geo-neutrino

measurements have been previously reported by Borexino and KamLAND (see [9], [10], [11], [12]). This new paper exploits a much higher statistics (data collected between December 15, 2007 and March 8, 2015 for a total of 2055.9 days) and reports the observation of geo-neutrinos with a significance of $5.9\,\sigma$. After applying several selection cuts (mostly intended to exploit the time and space correlation between the prompt and delayed signals) 77 $\bar{\nu}_e$ candidates are found. The expected time correlated and uncorrelated background is estimated to be < 0.65 (at 90 %) C.L.), not including reactor neutrinos. The prompt electron spectrum of the anti-nu candidates is fit to extract the geo and reactor neutrino components (see Fig. 4). If the ratio of U and Th is fixed in the fit following the chondritic model, we obtain the following total number of events for geo and reactor neutrinos:

$$S_{\rm geo}=23.7^{+6.5}_{-5.7}({\rm stat})^{+0.9}_{-0.6}({\rm sys}) \quad (\text{corresponding to } 43.5^{+11.8}_{-10.4}({\rm stat})^{+2.76}_{-2.4}({\rm sys})\,{\rm TNU})$$

$$S_{\rm react}=52.7^{+8.5}_{-7.7}({\rm stat})^{+0.7}_{-0.9}({\rm sys}) \quad (\text{corresponding to } 96.6^{+15.6}_{-14.2}({\rm stat})^{+4.9}_{-5.0}({\rm sys})\,{\rm TNU})$$

where 1 TNU= 1 Terrestrial Neutrino Unit= event/year/10^{32} protons.
From this result, it is possible to extract the contribution of geo-neutrino signal from the Earth mantle (once subtracted the estimated contribution from the Earth crust, both local and global). We find $S_{\rm geo}$(Mantle) $=20.9^{+15.1}_{-10.3}$ (TNU) with the null hypothesis rejected at 98% C.L.
The total radiogenic power corresponding to the measured geo-neutrino rate, in the assuption of chondritic mass ratio and of a potassium-to-uranium mass ratio $\mathrm{m(K)/m(U)} = 10^4$, is $\mathrm{P(U{+}Th{+}K)} = 33^{+28}_{-20}$ TW to be compared with the global terrestrial power output $\mathrm{P_{tot}} = 47 \pm 2$ TW.

Figure 5 shows the probability contours obtained by performing the fit leaving the U and Th spectral contributions as free parameters. The U and Th best-fit contributions are shown in Fig. 4. This measurement shows that a Borexino-like detector, with larger exposure, could separate the contributions from U and Th, and demonstrates the ability of this detection technique to perform real-time spectroscopy of geoneutrinos.

The results discussed in this paragraph are published in [13].

5 New limits on electron decay

Charge conservation is a solid pillar of the Standard Model which is presently undisputed. The non-conservation of the electric charge could in principle be introduced in the Lagrangian of the Standard Model by including additional interactions of leptons with photons or with Z bosons. This would lead to the existence of non-standard processes, such as $e^- \to \nu\gamma$. Setting limits on this charge-violating process is threfore a way to explore the validity of the standard theory and should be pursued with the highest sensitivity. The Borexino collaboration has already published a very stringent limit on the electron decay into a neutrino and a gamma exploiting data coming from the pilot experiment CTF [14]. With respect to CTF, Borexino features a larger mass and a higher radiopurity. Furthermore, the detector response is better known even in the lowest energy range where the electron decay signal should be observed ($\mathrm{E}_\gamma = 256$ keV), thanks to a dedicated calibration campaign in 2009. For these reasons, Borexino has been able to set a limit which is two orders of magnitude more stringent than the CTF one. We find $\tau \geq 6.6 \times 10^{28}$ yr at 90% C.L. In order to obtain this limit a fit to the Borexino energy spectrum below 600 keV has been performed including the contributions of the main radioactive backgrounds (^{14}C and its pile-up, ^{210}Po, ^{210}Bi, ^{85}Kr) and solar neutrinos (pp and ^{7}Be solar neutrinos). The mentioned spectrum and the fit are shown in Fig. 6. All the critical issues of this work (such as the non-linearity of the energy scale due to scintillation quenching and non-uniformity of the detector response) are in common with the analysis performed to extract the pp-solar neutrino signal.

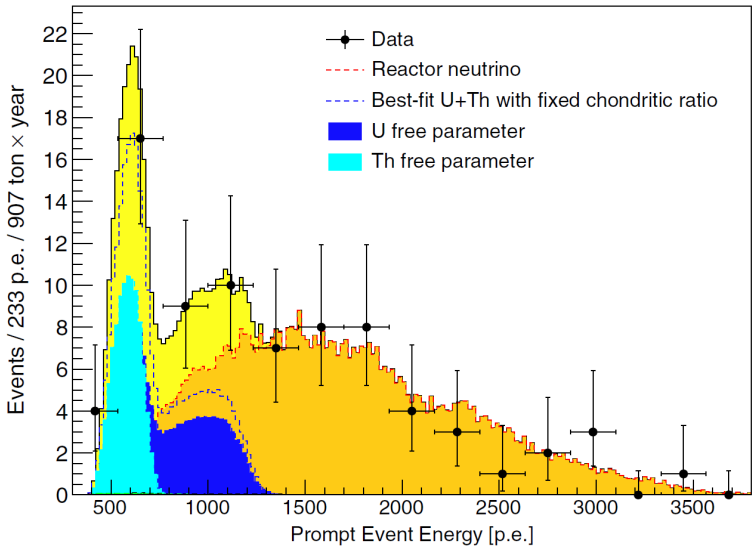

Figure 4: Prompt spectrum, in units of photoelectrons (p.e.), of anti-neutrino candidates and best-fit.

Therefore, this work is mainly based on the experience matured in the pp-analysis context. The results discussed in this paragraph are published in [15].

6 Perspectives

Borexino Phase 2 has started in 2012 and is ongoing. The detector has gained in stability thanks to the thermal insulation of the Water Tank, completed in November 2015. This would allow us to attempt a measurement of the residual ^{210}Bi rate, by tagging through the decay of its daughter, ^{210}Po. In fact, we believe that the ^{210}Bi count rate (of the order of 20 counts per day) is due to ^{210}Pb contamination in the scintillator itself, otherwise it would have decayed away since ^{210}Bi lifetime is short, ~ 5 days. Therefore, the activity of ^{210}Bi, of ^{210}Pb (its parent) and ^{210}Po (its daughter) should be the same. ^{210}Po activity would be relatively easy to measure since it decays α which can be efficiently separated from β via pulse-shape discrimination techniques. Unfortunately, since the beginning of Borexino, the count rate of ^{210}Po has been always largely out of equilibrium with respect to its precursors in the the ^{238}U chain. The origin of this contamination is not yest fully understood. This ^{210}Po is unsupported and therefore decays with its lifetime (of the order of 200 days): after almost 10 years of data-taking, we are now approaching a condition in which the unsupported ^{210}Po is very low and we can therefore measure the ^{210}Po-supported term, and therefore the ^{210}Bi rate. In order to do this we need the detector temperature to be very stable, since we have evidence that variations in the temperature gradient can start convective motions which carry some of the ^{210}Po attached on the nylon vessel into the innermost volume of the scintillator. If we succeed to measure the ^{210}Bi rate in the scintillator with a relatively good accuracy (~ 10 % or better), we might have a chance to say something on

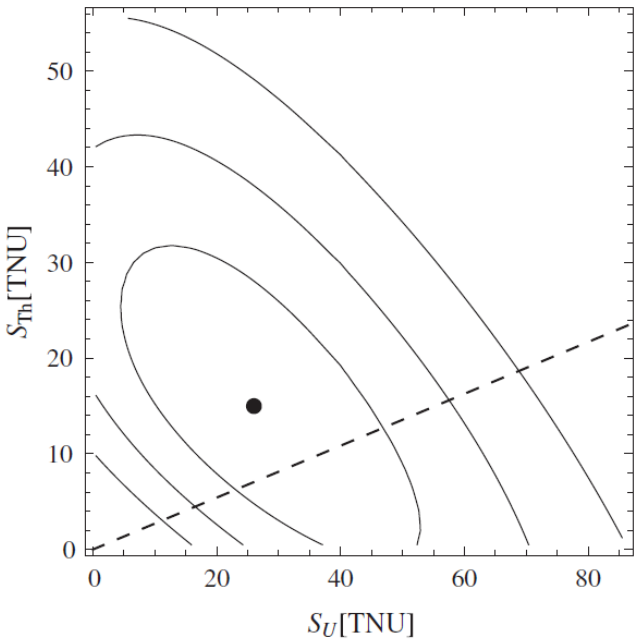

Figure 5: Best-fit contours for 1, 2 and 3σ for a fit with free U and Th contributions. Dashed line corresponds to the chondritic assumption.

CNO neutrinos, for which ^{210}Bi is one of the most annoying background. Knowing the ^{210}Bi rate would be also important to improve the accuracy on other solar neutrino fluxes, like ^{7}Be and pep. We plan in fact to perform a global fit on the entire energy scale to extract simultaneously all the neutrino and background components. The possibility to constraint the ^{210}Bi rate to the one measured independently with the ^{210}Po tag would help reducing the systematic errors due to correlations between different species in the fit. In order to further reduce systematic errors a new calibration campaign is also planned for the end of 2016, before the beginning of SOX.

In parallel, an upgrade of the scintillator purification system has been acquired and is being commissioned for a new phase of scintillator purification to achieve a lower background.

7 Conclusions

The first phase of Borexino started in 2007 and ended in 2010. It produced several results on solar neutrinos from different reactions, namely ^{7}Be (its main goal), pep and ^{8}B.
Phase 2 started in 2012 after a major improvement in the scintillator radiopurity and is still ongoing. This second phase has already produced important results like the first direct detection of solar neutrinos from the pp reaction. Further important results which we expect from the new data of Borexino are the improvement in the precision of the ^{7}Be rate measurement (possibly down to 3%) and of the shape of the electron recoil spectrum. This would be an important achievement "per se" and would also help evidentiating possible effects due to neutrino Non Standard Interactions. In general, in order to probe possible non-standard effects, it would be

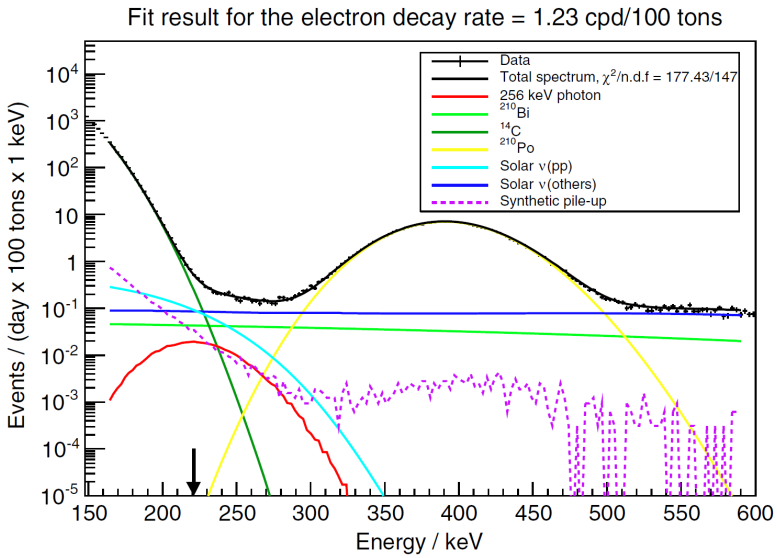

Figure 6: Borexino energy spectrum between 150 and 600 keV and results of the fit. The black arrow shows the expected position of the photon coming from the hypothetical reaction $e^- \rightarrow \gamma\nu$.

important to increase the amount of information in the so-called transition region from vacuum to matter dominated oscillations, by improving the precision on the pep neutrino rate and on the ^{8}B neutrino rate (in the region between 3 and 5 MeV).
The most challenging goal for Borexino Phase 2 is the study of neutrinos from the solar CNO fusion cycle. Observing these neutrinos would be a major breakthrough for stellar evolution theories, since the CNO cycle is believed to be the main mechanism of hydrogen burning in stars more massive than our Sun, but has never been observed directly. Also, the determination of the CNO flux could help disentangling the so-called low and high metallicity hypothesis for the Sun since the reaction strongly depends on the abundances of carbon, oxygen and nitrogen at the solar center [16], [17]. The detection of CNO neutrinos is challenging especially because their spectrum is very similar to that of ^{210}Bi. The increased radiopurity and stability of the detector open the possibility to independently determine the ^{210}Bi rate and, in principle, give us an handle to single out the CNO contribution.

8 List of Publications in 2015

1. M Agostini et al. (BOREXino) "Spectroscopy of geoneutrinos from 2056 days of Borexino data", 2015, *Phys.Rev.* D 031101(R).

   Paper highlighted in the Editor's Suggestion on the PRD website.

2. M. Agostini et al. (BOREXino) "Test of electric charge conservation with Borexino", 2015, *Phys.Rev.Lett.* 115 231802.

   Paper highlighted with a Synopsis on the Physics PRL website.

References

[1] G. Bellini et al. (BOREXino), 2011, *Phys.Rev.Lett.* **107** 141302.

[2] G. Bellini et al. (BOREXino), 2012, *Phys.Lett.* B **707** 22.

[3] G. Bellini et al. (BOREXino), 2010, *Phys.Rev.* D **82**, 033006.

[4] G. Bellini et al. (BOREXino), 2012, *Phys.Rev.Lett.* **108** 051302.

[5] G. Bellini et al. (BOREXino), 2014, *Phys.Rev.* D **89** 112007.

[6] G. Bellini et al. (BOREXino), 2014, *Nature* **512** 383.

[7] G. Alimonti et al. (BOREXino), 2009, *NIM* A **600**, 568.

[8] G. Alimonti et al. (BOREXino), 2009, *NIM* A **609**, 58.

[9] G. Bellini et al. (BOREXino), 2010, *Phys.Lett* B **687**, 299.

[10] G. Bellini et al. (BOREXino), 2013, *Phys.Lett* B **722**, 295.

[11] T. Araki et al. (KamLAND), 2005, *Nature* **436**, 499.

[12] S. Abe et al. (KamLAND), 2008, *Phys.Rev.Lett.* **100**, 221803.

[13] M Agostini et al. (BOREXino), 2015, *Phys.Rev.* D 031101(R).

[14] H. O. Back et al. (BOREXino), 2002, *Phys.Lett.* B **525** 2940.

[15] M. Agostini et al. (BOREXino), 2015, *Phys.Rev.Lett.* **115** 231802.

[16] N. Grevesse and A.J. Sauval, 1998, *Space Sci.Rev.* **85**, 161.

[17] W. Haxton, A. Serenelli and C. Pena-Garay *Ap.J.* **743** 24; arXiv:1104.1639 [astro-ph].

COBRA Annual Report 2015

Kai Zuber[a,*], Daniel Gehre[a], Stefan Zatschler[a], Katja Rohatsch[a], Claus Gößling[b], Kevin Kröninger[b], Reiner Klingenberg[b], Jan Tebrügge[b], Thomas Quante[b], Robert Theinert[b], Robert Temminghoff[b], Christian Nitsch[b], Jan-Hendrik Arling[b], Marcel Gerhardt[b], Caren Hagner[c], Joachim Ebert[c], Björn Wonsak[c], Nadine Heidrich[c], Jan Horst Karl Timm[c], Christian Oldorf[c], Henning Rebber[c], Thilo Michel[d] and Gisela Anton[d]

[a] *Technische Universität Dresden* – Germany,
[b] *Technische Universität Dortmund* – Germany,
[c] *Universität Hamburg* – Germany,
[d] *Universität Erlangen–Nürnberg* – Germany
([*] Spokesperson)

Abstract

The aim of the COBRA experiment (**C**admium Zinc Telluride **0**-Neutrino Double-**B**eta **R**esearch **A**pparatus) is to prove the existence of neutrinoless double beta-decay ($0\nu\beta\beta$-decay) and to measure its half-life. The COBRA demonstrator at LNGS is used to investigate the experimental issues of operating CZT detectors in low background mode while additional studies are proceeding in surface laboratories. The experiment consists of 64 monolithic, calorimetric detectors in a coplanar grid (CPG) design. These detectors are $1{\times}1{\times}1\,\mathrm{cm}^3$ in size and are operated in a $4{\times}4{\times}4$ detector array. As a semiconductor material, Cadmium-Zinc-Telluride (CdZnTe or simply CZT) offers the low radioactivity levels and good energy resolution required for the search for $0\nu\beta\beta$-decay. Furthermore, CZT contains naturally several double beta-decay candidates. The most promising is ^{116}Cd with a Q-value of 2.8 MeV, which lies above the highest prominent γ-line occurring from natural radioactivity.

1 Activities at the LNGS

1.1 The COBRA demonstrator at LNGS

The COBRA collaboration currently operates a demonstrator setup consisting of 4×4×4 detectors at the LNGS. For a recent review article see [1]. The detectors are made of CdZnTe (CZT) – a commercially available room temperature semiconductor. Due to the poor mobility of holes inside CZT a special readout electrode has to be used to compensate for this effect. COBRA uses a so-called coplanar grid (CPG) consisting of two interlocking comb-shaped anodes held at slightly different potentials. The bias in between is referred to as grid bias (GB). This way, only one electrode collects the charge carriers created via a particle interaction in the end. A bias voltage (referred to as BV) at the order of -1 kV forces the electrons to drift towards the CPG anode. The electrode at the lower potential collects these electrons and is called the collecting anode (CA) while the other one acts as a non-collecting anode (NCA). The complete signal reconstruction relies only on the induced electron signal, that is why CZT is referred to as single charge carrier device. Details on this reconstruction can be found in [7].

Each crystal is $1.0\times1.0\times1.0\,\mathrm{cm}^3$ in size and has a mass of about 6 g. Several isotopes which are candidates for double beta-decays are present in CZT according to their natural abundances. An overview can be found in Table 1. The most promising of which are ^{116}Cd due to the high Q-value of 2814 keV and ^{130}Te because of its high natural abundance of about 34% and considerably high Q-value of 2527 keV. In a first step a peak search for five $\beta^-\beta^-$ g.s. to g.s. transitions has been performed. The results of this analysis are summarized in section 2.4.

Table 1: List of $0\nu\beta\beta$-decay candidates contained in CZT with their corresponding decay modes, natural abundances [6] and Q-values [5].

Isotope	**Decay mode**	**Nat. ab.**	**Q-value [keV]**
^{64}Zn	$\beta^+/EC, EC/EC$	49.17%	1095.70
^{70}Zn	$\beta^-\beta^-$	0.61%	998.50
^{106}Cd	$\beta^+\beta^+, \beta^+/EC, EC/EC$	1.25%	2775.01
^{108}Cd	EC/EC	0.89%	272.04
^{114}Cd	$\beta^-\beta^-$	28.73%	542.30
^{116}Cd	$\beta^-\beta^-$	7.49%	2813.50
^{120}Te	$\beta^+/EC, EC/EC$	0.09%	1714.81
^{128}Te	$\beta^-\beta^-$	31.74%	865.87
^{130}Te	$\beta^-\beta^-$	34.08%	2526.97

A detailed description of the COBRA demonstrator operated at the LNGS can be found in a recent publication [2]. This paper reports on hardware aspects like the DAQ electronics as well as the experimental infrastructure to monitor and ensure a stable operation under low background conditions.

Figure 1 shows an overview of the several shielding layers of the demonstrator. The outermost layer consists of 7 cm borated polyethylene acting as a shield against neutrons. Following, there is a frame of welded metal plates to prevent the first part of the readout chain to be affected by electromagnetic interferences (EMI). Inside this EMI box the custom made and actively cooled preamplifier devices are placed. The inner shielding consist of a multi-layered structure of standard lead, ultra low activity lead and copper surrounding the detectors themselves. This inner shielding is embedded into a polycarbonate box which is continuously flushed with evaporated dry nitrogen to prevent radon from diffusing into the setup. In 2015 some problems with the nitrogen flushing system have been encountered which will be discussed in 1.3.

1.2 Maintenance at the LNGS

In Feb.'15 one week of maintenance shift was performed at the LNGS. Several upgrades were installed to ensure a stable performance of the COBRA demonstrator such as the implementation of a second

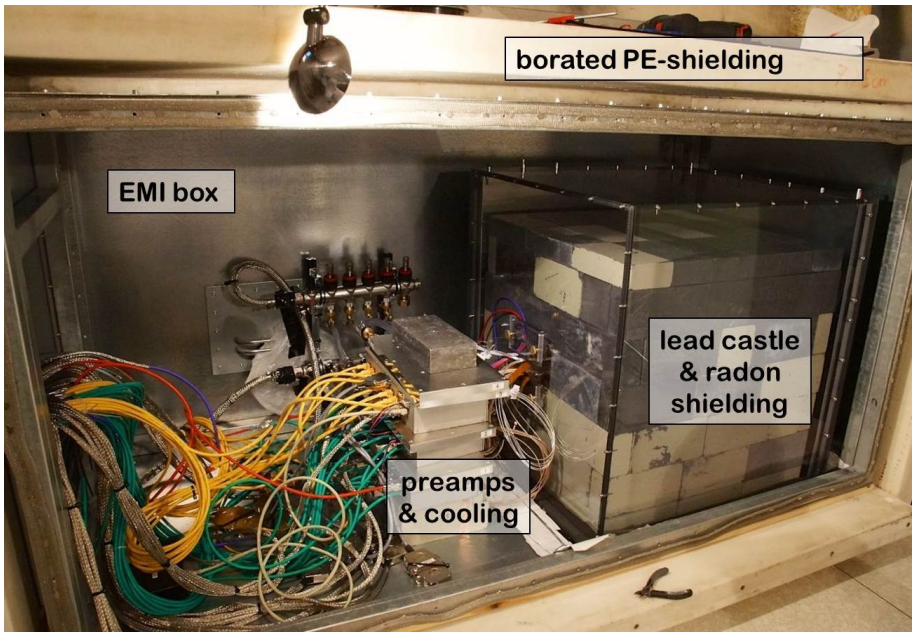

Figure 1: Overview of the experimental setup of the COBRA demonstrator. Highlighted are the different shielding layers and the first stage of the readout chain. The detectors themselves are housed within a copper nest inside the lead castle which can be seen on the right side.

network server. Furthermore, all detector and electronic channels were checked for proper behavior. Two detector channels with known electronic problems could be fixed by exchanging part of the electronics. An additional detector seems to suffer from a broken BV contact acting only as a planar detector. A second detector has to be operated without GB worsen its energy resolution and efficiency drastically. Both of those detectors can still be used as veto for multi-detector events. During the shift it could also be confirmed that only one out of 64 crystals shows no response at all, although the DAQ electronics is fine what has been checked with a pulser system.

In summary, the COBRA demonstrator is running with 61 fully functional CPG detectors, which states that more than 95% of all detectors are active and are operating stable. It is noteworthy that the affected detectors are all related to the first detector layer installed in Sept.'11 and that most of the problems are related to parts of the electronics or contacts and not the detectors themselves. It was decided that opening the inner shielding of the setup to fix the contacting of the detectors is not worth the risk while the demonstrator is performing so stably. The end of the shift was used to check the temperature and source position dependency during calibration measurements to improve the existing Monte Carlo framework of the 4×4×4 detector array.

In Sept.'15 the internal network system has been reconfigured as requested by the LNGS as part of the overall upgrade from 1 Gb/s to 10 Gb/s uplink towards the internet. The data syncing between the on-site storage and several backup servers outside the LNGS greatly benefits from this step. Due to an UPS backup system, none of the short power interruptions caused by maintenance tasks done by the LNGS on the central power lines have affected the demonstrator. In fact, besides the one week of maintenance COBRA can report an up-time which has been only interrupted by several short calibration periods.

1.3 Problem with continuous nitrogen flushing

Beginning of 2015 it was noted that there seemed to be a problem with the continuous dry nitrogen flushing of the inner detector setup. It appeared that the normal biweekly refill rhythm of the dewar was not enough to maintain a continuous flushing, causing the dewar to empty for short periods in between the refilling. During the maintenance shift in Feb.'15 no alteration or damage of the flushing setup could be reported. All slow control values such as temperature, humidity, pressure and fill level of the dewar are logged and stored by the DAQ. It was found that the minimum and maximum values of the dewar fill level have not changed over the years. As a short time solution it was decided to turn off the heater inside the dewar which is used to evaporate the liquid nitrogen more rapidly. This results in a weaker

but longer lasting flushing. In Sept.'15 the situation changed drastically. Even without heating the filling only lasted for about five days compared to the usual duration of about 14 days. To compensate for this, a new weekly refill contract has been set up. As root cause for this sudden change an insufficient vacuum sealing between the inner and outer vessel appeared to be most likeliest. Consequently a new dewar has been purchased by the end of 2015. The exchange of the dewar was done in the beginning of 2016. At the moment no clear evidence for an increased background in the region of interest due to radon and subsequent radioactive decays can be reported. Nevertheless, an increased humidity near the detectors affects the performance and potentially increases the amount of unphysical events caused by more prominent leakage currents. That is why periods without working nitrogen flushing are discarded from the final double beta analysis after all. Furthermore, it has to be studied to what degree the low energy part of the measured LNGS spectrum gets effected by periods without flushing. More details on the low energy part of the spectrum which is dominated by the single β-decay of ^{113}Cd will be discussed in section 2.2.

2 Results of the low background operation

2.1 Data-taking at the LNGS

Figure 2 illustrates the total accumulated and selected exposure for the most recent neutrinoless double beta-decay search. Due to the problems with the gaseous nitrogen flushing by the end of 2015, the thresholds of almost all channels had to be increased to ensure a stable operation.

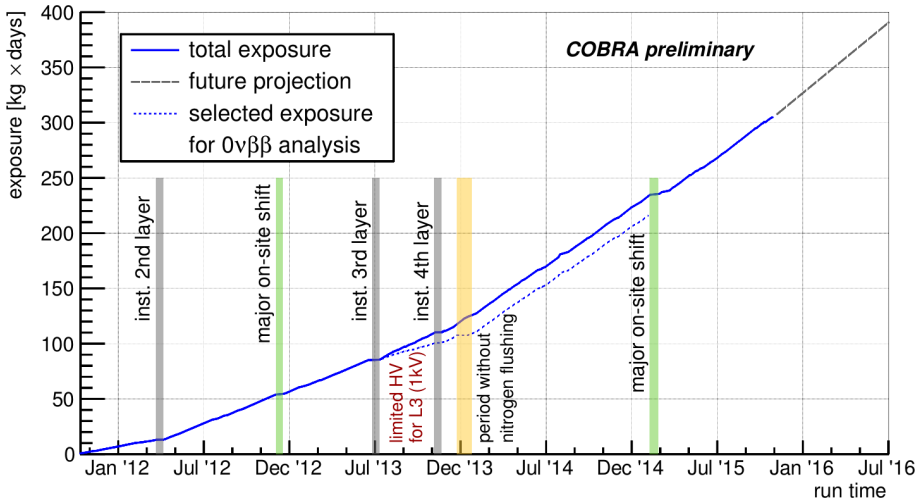

Figure 2: Accumulated low-background exposure of the COBRA demonstrator at LNGS versus run time of the experiment. Between Sept.'11 and Oct.'15 a total exposure of 304.8 kg d has been acquired with complete pulse shape sampling. Additionally indicated are upgrade works on-site like the installation of further detector layers and root causes for periods of lower data quality.

As a consequence the low energy exposure (below about 100 keV) accumulated in this time is not suitable to be included in a planned spectral shape study of ^{113}Cd. This study is highly requested by the nuclear physics community because the spectral shape is sensitive to the axial vector coupling parameter g_A. Nowadays, the so called quenching of g_A is controversially discussed to reproduce experimental results of single and double beta-decay half-life measurements with theoretical calculations. Such predictions from theory are typically strongly dependent on the nuclear model and the value of g_A. Therefore, reliable measurements and experimental data to determine the effective value of g_A are of general interest.

The recent analysis of five $\beta^-\beta^-$ g.s. to g.s. transitions is based on the data accumulated until Feb.'15. Periods without nitrogen flushing have been identified and discarded from this analysis. Additionally, the data of the third detector layer (L3) right after its installation were excluded from the final data set due to an unstable performance. The high voltage had to be held below the optimal settings for most of

the detectors in this layer. The problem has been identified to be caused by a faulty BV contact to the main supply which could be fixed during the installation of the fourth detector layer in Nov.'13. This reduces the available exposure from 234.7 kg d to 216.1 kg d as basis of the recent analysis. The effect of the problems with the flushing system in 2015 mentioned above is currently under investigation.

2.2 Investigation of setup stability based on ^{113}Cd

Since the COBRA detectors are made from natural abundant materials they also contain all naturally occurring isotopes of cadmium, zinc and tellurium. Of special interest is ^{113}Cd with an abundance of 12.2%. This isotope is a radioactive β^--emitter with a half-life of $(8.00 \pm 0.35) \times 10^{15}$ yr and an endpoint of $Q_\beta = 322 \pm 1.2$ keV. The ^{113}Cd content is homogeneously distributed in the detector material, hence, it can be used to monitor the operation stability of the demonstrator setup. The decay rate of ^{113}Cd can be expected to be constant comparing the long half-life of this four-fold forbidden non-unique single β-decay with the experimental lifetime. This means that the stability of the integrated count rate is a direct measure of the detector performance. The results of this investigation can be found in a reviewed publication [4]. Based on the carefully analyzed data set, count rate variations in the lower percent-per-year range have been found ($\Delta_{\text{mean}} = 0.5\% \pm 0.4\%$ per year, see Figure 3). Neither the spectral shape of the ^{113}Cd β-spectrum nor the depth reconstruction of the CPG approach have been found to be affected by this rate variation. This analysis allows for the statement that CZT detectors can be operated stably under ultra low-background conditions over time scales of years, which is a valuable proof of the demonstrator concept.

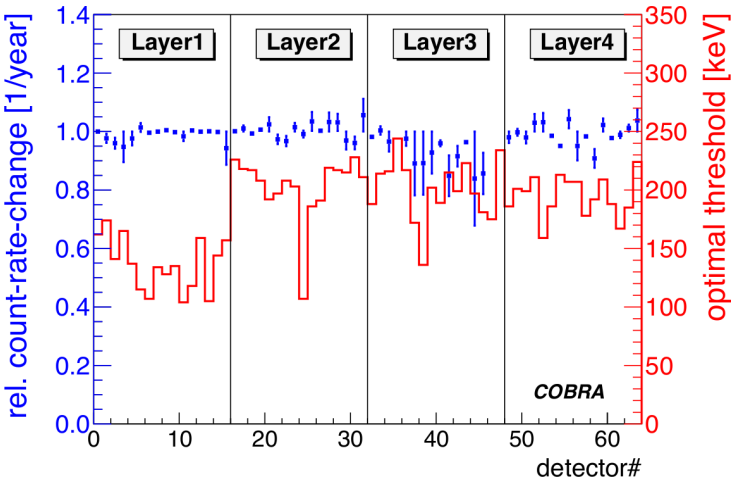

Figure 3: Observed count rate variation per year for the intrinsic four-fold forbidden non-unique single β-decay of ^{113}Cd. The overall count rate depends on the individual detector trigger thresholds, which is evaluated on a run by run time base. Hence, the crucial point for such a stability analysis is to find the optimal trigger threshold as explained in full detail in [4].

2.3 Identification of prominent background features

The crucial point of $0\nu\beta\beta$-decay searches is background identification and reduction. The CPG approach offers additional information for recorded events such as the reconstruction of the interaction depth z as normalized distance between the anode plane ($z = 0$) and cathode side ($z = 1$) [7]. An illustration of identified background features can be seen in Figure 4. The two-dimensional plot shows the reconstructed interaction depth versus the deposited energy. The exposure-weighted count rate is shown in color codes as additional dimension.

The low energy range below 350 keV is dominated by the intrinsic four-fold forbidden non-unique β-decay of ^{113}Cd which corresponds to about 98% of all events. So far no hint for dominant γ-lines from the natural decay chains can be seen in the data. In fact, only two γ-lines are visible related to ^{40}K

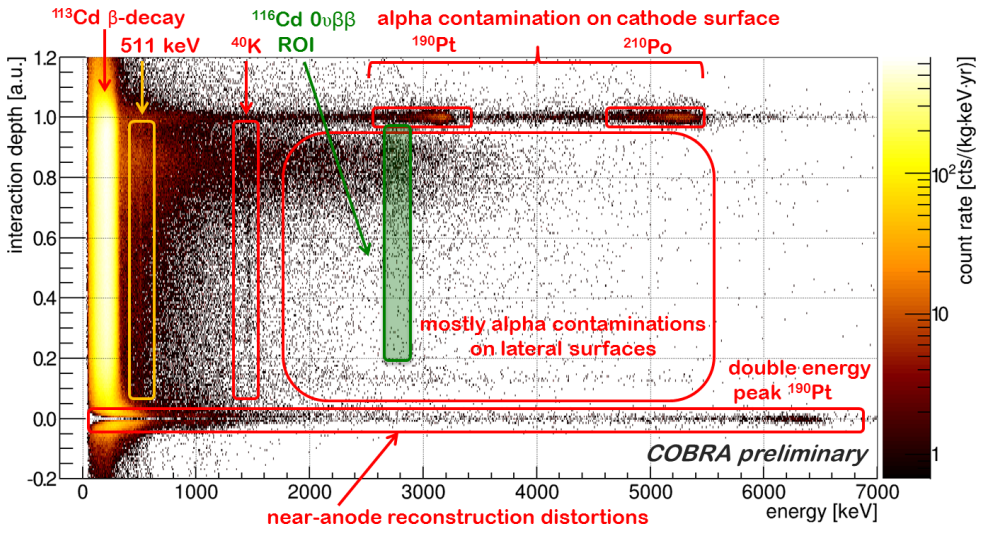

Figure 4: Identified background features using the interaction depth reconstruction of the CPG anode approach. Highlighted are prominent γ-lines visible as straight lines in the two-dimensional plot and features corresponding to near-anode ($z = 0$) or near-cathode ($z = 1$) events. The main region of interest around the Q-value of ^{116}Cd is dominated by alpha-induced events on the lateral detector surfaces.

and the annihilation line at 511 keV. Near the anodes at low depths well-understood distortions of the CPG approach and reconstruction artefacts can be seen. This region is removed as part of the standard data-cleaning cuts, which are used to remove events strongly affected by electromagnetic disturbances and unphysical pulse traces. The indicated region of interest around the Q-value of ^{116}Cd at 2813.5 keV is strongly influenced by contaminations of the cathode with alpha-emitting isotopes. The isotope ^{190}Pt is part of the electrode metallization while the ^{210}Po contribution arises from the radon decay chain. These surface contaminations can be sufficiently removed from the data with a cut on the interaction depth reducing the background index in the ROI by at least a factor of two. The remaining entries in the ROI are likely caused by contaminations on the lateral detector surfaces. One of the key instruments to further reduce background is the so-called pulse shape discrimination (PSD) to identify prominent characteristics in the signal traces induced by certain particle interactions. The COBRA collaboration developed a set of cuts to discriminate between central events and interactions close to the lateral detector surfaces, referred to as lateral surface events (LSE). The techniques are well-described in [8] and have been verified with laboratory data. Using the developed LSE cuts the background index can be reduced further by a factor of five, which leads to about 2.7 cts/(keV kg yr). Additional fiducial cuts to remove the depth region above 0.7 with obvious higher background results in a count rate of less than 0.8 cts/(keV kg yr). Recently another PSD cut has been developed to discriminate between single-site events (SSE) and multi-site events (MSE), which are typically caused by multiply scattered, highly energetic photons. Since the signal for a $0\nu\beta\beta$-decay is expected to be a single crystal event with a point-like energy deposition, all multi-detector events and multiple interactions within the same crystal can be vetoed as background. The effect of the newly developed MSE cut seems to be rather small but supports the fact that the background in the region of interest is only weakly populated by γ-lines from the natural decay chains. Nonetheless, the MSE cut is indispensable for the efficiency estimate of the well-established and excellent working LSE cuts and will be essential for a large-scale experiment.

2.4 Results of neutrinoless double beta-decay search

The analysis results of the recent search for neutrinoless double beta-decay with the COBRA demonstrator have been published in [5]. A Bayesian analysis has been performed to investigate five g.s. to g.s. $\beta^-\beta^-$ transitions of the isotopes ^{114}Cd, ^{128}Te, ^{70}Zn, ^{130}Te and ^{116}Cd. No signal has been observed for any of the investigated transitions and 90% credibility limits could been set subsequently as summarized in Table 2. It is noteworthy that the collaboration was able to set the world leading limit for the $0\nu\beta\beta$-decay

of ^{114}Cd into the ground state of ^{114}Sn.

Table 2: Results of the Bayesian signal estimation after folding in all systematic uncertainties. The second and third column show the exposure and total efficiencies used for the half-life estimation. In the fourth column the background indices for the different ROIs are presented. The last column reports the calculated limit at 90% credibility [5].

Isotope	**Exp. [kg d]**	**Tot. efficiency**	**BI [cts/(keV kg yr)]**	**90% Cred. limit**
^{114}Cd	212.8	0.54±0.70	$213.9^{+1.0}_{-1.7}$	1.8×10^{21} yr
^{128}Te	216.1	0.52±0.70	$65.5^{+0.5}_{-1.6}$	2.0×10^{21} yr
^{70}Zn	216.1	0.51±0.70	$45.1^{+0.6}_{-1.0}$	7.4×10^{18} yr
^{130}Te	216.1	0.38±0.05	$3.6^{+0.1}_{-0.3}$	6.7×10^{21} yr
^{116}Cd	216.1	0.37±0.05	$2.7^{+0.1}_{-0.2}$	1.2×10^{21} yr

In the future the limits could be improved with newly evaluated methods of PSD to reject also multi-site events as stated before. It is a known feature that the techniques used to identify lateral surface events are also sensitive to MSEs. Hence, the efficiency of the LSE cuts is expected to be significantly higher if multi-site events are rejected prior the efficiency calculation. Due to the ongoing efficiency estimation for the developed MSE cut it is not included in the recent double beta analysis. Another way to improve the limits is to reject multi-detector events, which requires an accurate synchronization of all 16 ADC clocks at first. The evaluation of the software tool written for this purpose is still ongoing.

3 Progress in analysis and simulation frameworks

3.1 Time synchronization and coincidence analysis

Another powerful tool to reduce and characterize background is the analysis of coincident events. This, however, makes a synchronization of the 16 FADCs of the COBRA setup necessary. Each FADCs unit has its own clock with slightly different speed resulting in a small drift over time. For this purpose, a pulse generator was installed to create coincident events in all channels with a certain period. Afterwards, a specifically developed offline software is used to synchronize the single FADC clocks with the injected pulser events. This allows to declare events with an energy deposition in more than one crystal in coincidence as background for the $0\nu\beta\beta$-decay analysis. The final evaluation of the synchronization tool is ongoing and will be available for all physics data soon. Additionally, the energy spectrum of multi-detector events can be analyzed with regard to the radioactive contamination of the setup. One commonly used technique is to identify characteristic signatures such as the ^{214}Bi to ^{214}Po coincidence. The detection efficiency for such a coincidence can be determined with detailed MC simulations of the demonstrator setup as are currently under development. This allows for the investigation of the intrinsic detector radiopurity with focus on radioactive elements contained in the natural decay chains. In this way contamination limits can be extracted from the measured LNGS spectra which are essential for the estimate of the total background rate for a large-scale setup and to tune the existing Monte Carlo framework. First results using a synchronized subset of data can be found in [9].

3.2 Improved pulse shape simulation framework

The crucial part of a reliable detector simulation is to describe the charge transport properties to reproduce realistic pulse shapes. Usually, this digitization is not part of Monte Carlo simulations. Nevertheless, an accurate description of the charge transport is a key instrument to cross check the efficiency of PSD techniques. This requires a complete model including the weighting and electric potential inside the detector, the capacitance and resistance of the DAQ, self-interaction and diffusion processes during the drift of the charge clouds towards the anodes and the possibility to add realistic baseline noise. All this has been recently implemented into the COBRA detector simulation and is well documented in [10]. Depending on the position of a particle interaction, the pulse shapes feature characteristics as shown in Figure 5. The comparison of an actual pulse with the simulation is shown in Figure 6.

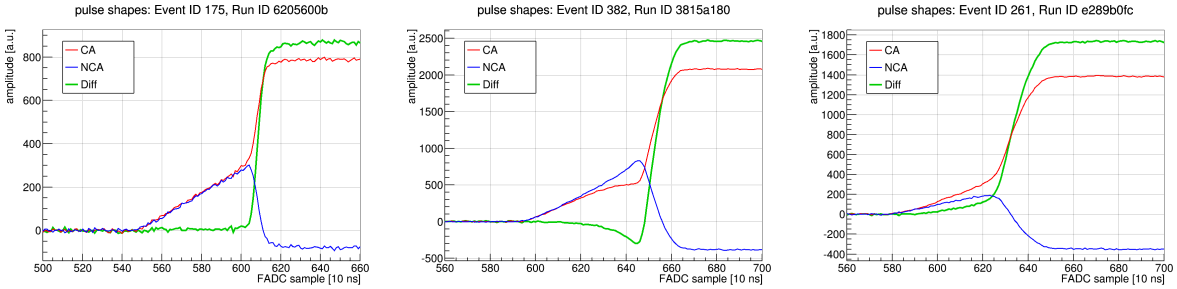

Figure 5: Typical pulse shapes as recorded by the COBRA CPG detectors. The energy equivalent difference pulse (green) is reconstructed from the raw signals of the collecting anode (CA, red) and the non-collecting anode (NCA, blue). Left: central event with single-site energy deposition as expected for a double beta-decay. Middle: near NCA-side events feature a characteristic DIP of the difference pulse. Right: near CA-side events feature an early rise time (ERT) of the difference pulse.

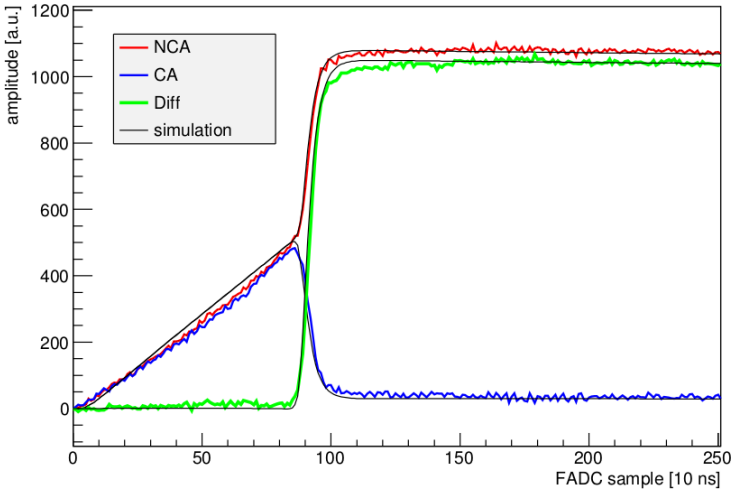

Figure 6: Comparison of simulated and actual pulse shape recorded with a COBRA CPG detector. No signal noise was added to the simulated pulse (black) for clarity reasons.

All features like the common rise of the CA and NCA signal at the beginning and the slowdown during the charge collection after the signal splitting can be reproduced very accurately. Even more impressive is the fact that the characteristics of LSEs, the DIP and ERT of the difference pulse, can be confirmed with the powerful detector simulations as shown in Figure 7. In the future this tool will be of great benefit to test new PSD techniques and to investigate general detector properties such as the impact of the charge carriers mobility. Previous investigations have already shown that there is quite a spread in tabulated values like for instance the electron mobility lifetime product in CZT comparing the individual detectors of the demonstrator. A detailed MC campaign could clarify the effect on the pulse traces to optimize background identification algorithms.

3.3 Discrimination of α/β-interactions via PSD

The interaction of alpha particles and electrons with the detector material generates charge clouds with different expansions in the semiconductor. This difference in size should in principle make it possible to separate these fundamentally different energy depositions, at least statistically. To test this hypothesis, a lab experiment has been performed with one of the usual $1\,\mathrm{cm}^3$ COBRA CPG detectors. In this experiment the cathode side was irradiated with alpha and beta radiation of different energies, up to 2 MeV, to create a pulse shape library of beta and alpha interactions. The cathode side was chosen because it is not lacquered, allowing alpha particles to enter the sensitive volume. Moreover, this offers

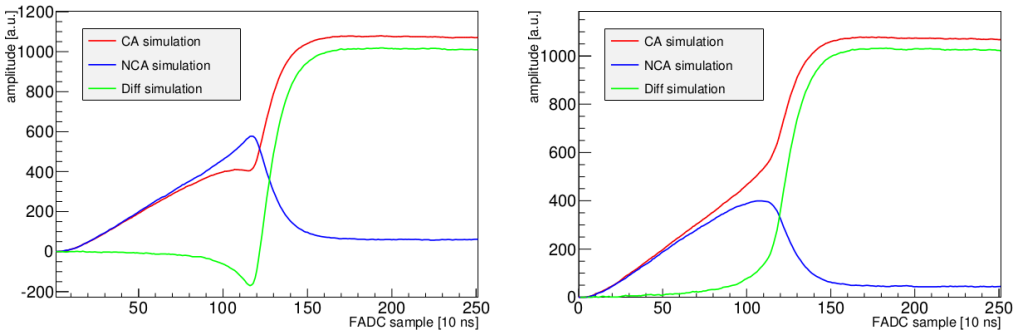

Figure 7: Simulated pulse shapes for events near the lateral detector walls. The characteristic features of LSEs, the DIP and ERT of the difference pulse (green), can be reproduced accurately with the improved detector simulation (compare with Figure 5).

the advantage that the drift time of the charge carriers is maximal and so some aspects of the pulse shapes are particularly easy to analyze. On the other hand, effects such as diffusion and repulsion that would have a negative impact on the discrimination power, are most prominent for this configuration because of the long drift.

The analysis of these data has shown that alpha particles could be reduced to 20% while nearly 60% of the beta induced signals survived the developed cuts for 2 MeV particles. This can be regarded as a measurable success. Furthermore, the behavior of cut efficiency and impurity indicates that all cuts perform even better for higher energies including the ^{116}Cd ROI. This impression was substantiated by the improved detector simulation framework mentioned before. Additionally, the hypothesis that the discrimination of cathode events is complicated by drift effects could been confirmed as well, which also implies that the discrimination criteria will be more efficient near the anodes. Although the results so far are very preliminary, the developed tools already provided a deeper insight into the charge transport and details of the detector behavior of the COBRA CPG detectors. This work will be continued to optimize the efficiency of the methods to discriminate between alpha and beta interactions by means of pulse shapes and to explore additional criteria.

4 Towards a large-scale setup

4.1 Characterization of large quad-CPG CZT crystals

The results of a complete characterization of one of the first large quad-CPG CZT detectors has been published recently [3]. The aim was to investigate the applications of such devices in gamma-ray spectroscopy and low-background operation. This paper focuses on the electric properties as well as the spectroscopic performance of the detector, such as energy response and resolution. In addition, several measurements are conducted to investigate the operational stability.

Figure 8 shows a comparison of the currently investigated detector designs. The small detectors of $1.0\times1.0\times1.0\,\mathrm{cm}^3$ size are used for the COBRA demonstrator at LNGS. Due to improvements in the complex crystal growth process larger detectors with a dimension of $2.0\times2.0\times1.5\,\mathrm{cm}^3$ and a weight of about 36 g are commercially available with a high number of crystals produced per year. The smaller surface-to-volume ratio results in a higher full energy detection efficiency and a reduction of surface contributions. Two different anode designs were proposed for the large detectors. On the one hand a single grid structure like the one on the small detectors and on the other hand a quad grid structure. It has been found that the quad-CPG approach is advantageous compared to the large single CPG in terms of achievable resolution due to the reduced occurrence of leakage currents and capable of additional veto possibilities. The anode design of such a quad detector can be seen in Figure 8. It consists of four independent $1\,\mathrm{cm}^2$ CPGs which are rotated by 90° to each other. This way, the different anode rails are configured in a way that the innermost NCAs are acting as a virtual steering grid separating the CPGs from each other.

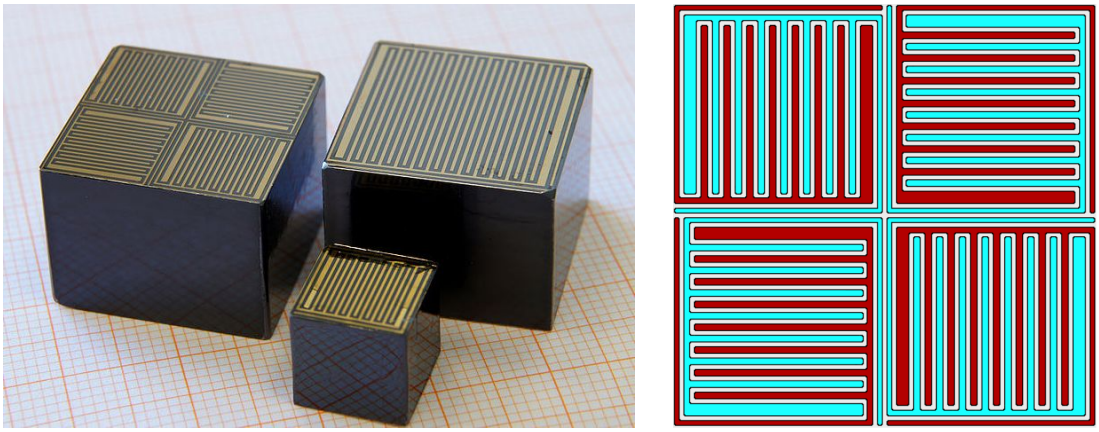

Figure 8: Comparison of currently investigated detector designs. For the new 6 cm^3 detector generation two different anode designs have been tested. Due to the increased veto capabilities and the reduced amount of leakage currents because of the segmented anode the focus is on the so-called quad-CPG approach shown at the right. The CAs are indicated in dark red and the NCAs in light blue [3].

The COBRA collaboration received funding from the German Research Foundation (Deutsche Forschungsgemeinschaft, DFG) to develop and build a basic detector module of the planned large-scale setup. For this purpose several prototype crystals have been purchased from two suppliers (eV Products, Redlen) with the aim to identify the most promising detector approach based on the newly available 6 cm^3 CZT detectors. Additional investigations are needed to compare the prototypes of different suppliers and to understand more details of the quad-CPG approach. In Figure 9 the possibility of sub-grid vetoing shows the capability to suppress γ-induced background on a very impressive level using the underlying Compton kinematics.

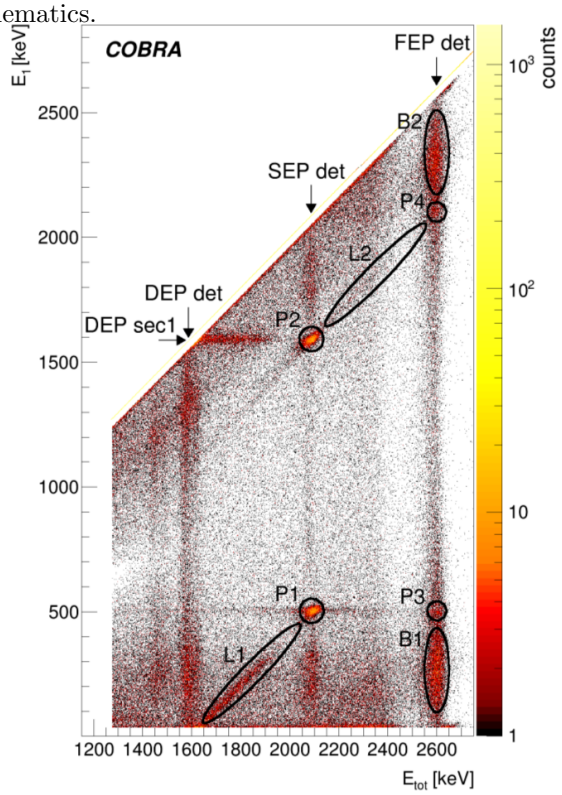

Figure 9: Correlation between the deposited energy in one sub-grid (referred to as sec1) and the energy measured in the whole detector for a calibration measurement with ^{232}Th. Most of the visible features are related to Compton scattered photons and the possible pair production inside the crystal by photons of 2.6 MeV. Such highly energetic photons originate from the deexcitation of ^{208}Tl as part of the thorium decay chain. Clearly visible are the vertical lines corresponding to the full energy peak (FEP), the single escape peak (SEP) and the double escape peak (DEP) for the full detector. The points P1 and P2 are related to the SEP. While the full detector measures a single-escape event, sec1 can see for example a 511 keV photon (P1) or a double-escape (P2). It can be concluded that for the second case the pair production interaction happened below sec1. The points B1 and B2 indicate events where backscattering of 2.6 MeV photons took place [3].

4.2 Prototype layout for new detector layer

The construction of a new detector holder based on the concept for a large-scale setup has been started in the second half of 2015. A first mechanical prototype was build and plans how to implement the new detector module into the existing demonstrator setup were developed. An impression of the mechanical prototype can be seen in Figure 10.

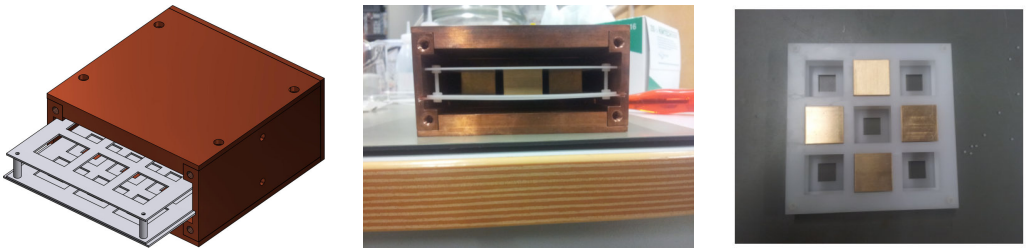

Figure 10: Impression of mechanical prototype detector holder. It is planned to integrate an additional copper nest housing the new detector layer within the lead shielding on top of the existing demonstrator setup at the LNGS [11].

This includes considerations regarding new feedthroughs for calibration sources and the evaporated nitrogen flushing and the cabling needed to operate nine quad-CPG detectors with in total 72 readout channels. Each detector will be supplied with an optimized high voltage and grid bias. At this moment it has not been decided yet if another anode rail acting as a guard ring around the complete anode will be implemented into the quad design and whether it will be read out as well. Recent studies imply that using a guard ring held at the same potential as the CA drastically reduces surface events. This has been observed with the $1\,\mathrm{cm}^3$ detectors and has first to be studied in detail before general conclusion can be drawn. But since the background of the demonstrator is currently dominated by alpha emitters at the surface, this seems to be a very promising approach for the near future.

4.3 ASIC-based electronics readout system

For the large scale setup a readout system based on highly integrated electronics is necessary due to the huge amount of electronic channels. A commercially available ASIC-based readout system which serves COBRA's purposes was identified, purchased and arrived in the first months of 2015. This prototype module was tested at TU Dortmund after the exchange of parts of some redesigned components which was recommended by the Norwegian manufacturer IDEAS. In December 2015 two members of the collaboration followed an invitation to Oslo to learn more about the FPGA readout and signal processing. This meeting was also used to discuss further specifications needed for the COBRA experiment in close contact with the developers.

5 Conclusion

Several papers have been released recently summarizing the main working fields of the collaboration. Using our pulse shape discrimination techniques to identify LSEs a peak search for the expected signal of neutrinoless double beta-decay was performed. No signal has been found and 90% credibility limits based on a Bayesian analysis could be set for all investigated g.s. to g.s. transitions. For one isotope, ^{114}Cd, the world leading half-life limit could been set. In the future the limit calculation will be improved using synchronized data sets to reject multi-detector events and another form of PSD cut to distinguish between signal-like single-site events and background-like multi-site events. For this the improved detector simulation to produce realistic pulse traces will be very useful. The stability of the demonstrator electronics and the detector performance at the LNGS have been investigated by monitoring the intrinsic β-decay of ^{113}Cd. It was found that an excellent detector performance can be reported after several years of operation. The first detector characterizations of larger commercially available CZT detectors have shown that most of the detector understanding gathered with the current $1\,\mathrm{cm}^3$ generation can be

transferred to the new $6\,\mathrm{cm}^3$ approach. This includes not only electrical standard tests but also proves the validity of the energy and interaction depth reconstruction. Furthermore, sub-grid vetoing appears to be a very powerful tool to suppress γ-background in case of quad-CPG detectors. In parallel, the optimization procedure to determine the best operation parameters has been adapted for the quad-CPG approach as well.

The collaboration received funding from the German Research Foundation DFG to build a first prototype detector module consisting of nine $6\,\mathrm{cm}^3$ CZT detectors with ASIC and FPGA based pulse shape readout. As currently major background source alpha-emitting surface contaminations have been identified, which are supposed to be strongly suppressed by continuous clean room handling of all detector components during all production and commissioning steps. The construction of a basic detector module for a large-scale COBRA experiment was started and first signals have been measured with the new readout system. Currently, another set of prototype detectors of different suppliers is under evaluation.

List of publications in 2015

[1] S. Zatschler, *The COBRA experiment – Status and prospects on the search of neutrinoless double beta-decay*, AIP Conference Proceedings 1686 (2015), http://dx.doi.org/10.1063/1.4934916

[2] J. Ebert et al., *The COBRA demonstrator at the LNGS underground laboratory*, NIM A (2016), 10.1016/j.nima.2015.10.079, arXiv:1507.08177

[3] J. Ebert et al., *Characterization of a large CdZnTe coplanar quad-grid semiconductor detector*, NIM A (2016), 10.1016/j.nima.2015.09.116, arXiv:1509.02361

[4] J. Ebert et al., *Long-Term Stability of Underground Operated CZT Detectors Based on the Analysis of Intrinsic Cd-113 β-Decay*, submitted to NIM A (2016), arXiv:1508.03217

[5] J. Ebert et al., *Results of a search for neutrinoless double beta-decay using the COBRA demonstrator*, submitted to Phys. Rev. C (2016), arXiv:1509.04113

References

[6] M. Berglund and M. E. Wiesner, *Isotopic compositions of the elements 2009 (IUPAC Technical Report)*, Pure and Applied Chemistry 83 (2011)

[7] M. Fritts et al., *Analytical model for event reconstruction in coplanar grid CdZnTe detectors*, NIM A 708 (2013), 10.1016/j.nima.2013.01.004, arXiv:1211.6604

[8] M. Fritts et al., *Pulse-shape discrimination of surface events in CdZnTe detectors for the COBRA experiment*, NIM A 749 (2014), 10.1016/j.nima.2014.02.038, arXiv:1401.5844

[9] J. H. K. Timm, *Studien seltener neutroneninduzierter Prozesse und Koinzidenzanalysen zur Bestimmung und Reduktion von Untergrundbeiträgen im COBRA-Experiment*, PhD thesis, Universität Hamburg, 2015

[10] H. Rebber, *Discrimination of Alpha Particles in CdZnTe Detectors with Coplanar Grid*, master thesis, Universität Hamburg, 2015

[11] L. Bodenstein-Dresler, *Entwicklung einer neuen Detektorhalterung inklusive Inbetriebnahme einer ASIC-basierten Auslese für das COBRA-Experiment*, bachelor thesis, TU Dortmund, 2015

The CRESST dark matter search

G. Angloher [a], A. Bento [a,b], C. Bucci [c], L. Canonica [c], X. Defay [d] A. Erb [d,e], F. von Feilitzsch [d], N. Ferreiro [a], P. Gorla [c], A. Gütlein [f,g], D. Hauff [a], J. Jochum [h], M. Kiefer [a], H. Kluck [f,g] H . Kraus [i], J.C. Lanfranchi [d], J. Loebell [h], A. Münster [d], C. Pagliarone [c], F. Petricca [a,+], W. Potzel [d], F. Pröbst [a], F. Reindl[a], K. Schäffner[c], J. Schieck [f,g] S. Schönert [d], W. Seidel [a], L. Stodolsky [a], C. Strandhagen [h], R. Strauss[a], A. Tanzke[a], H.H. Trinh Thi[d] C. Türkoğlu[f] M. Uffinger [h], A. Ulrich [d], I. Usherov[h], S. Wawoczny[d], M. Willers[d], M. Wüstrich [a], A. Zöller[d]

[a] *Max-Planck-Institut für Physik, 80805 Munich, Germany*
[b] *Departamento de Fisica, Universidade de Coimbra, 3004 516 Coimbra, Portugal*
[c] *Laboratori Nazionali del Gran Sasso, 67010 Assergi, Italy*
[d] *Technische Universität München, Physik Department, 85747 Garching, Germany*
[e] *Walther-Meißner-Institut für Tieftemperaturforschung, 85748 Garching, Germany*
[f] *Institut für Hochenergiephysik der Österreichischen Akademie der Wissenschaften 1050 Wien, Austria*
[g] *Atominstitut, Vienna University of Technology, 1020 Wien, Austria*
[h] *Eberhard-Karls-Universität Tübingen, 72076 Tübingen, Germany*
[i] *University of Oxford, Department of Physics, Oxford OX1 3RH, UK*
[+] *Spokesperson e-mail address: petricca@mpp.mpg.de*

Abstract

The CRESST-II experiment is searching for dark matter particles via their elastic scattering off nuclei in a target material. The CRESST target consists of scintillating $CaWO_4$ crystals which are operated as cryogenic calorimeters at millikelvin temperatures and read out by transition edge sensors. Each interaction in the $CaWO_4$ target crystal produces a phonon signal and also a light signal that is measured by a secondary cryogenic calorimeter. The low energy thresholds of these detectors, combined with the presence of light nuclei in the target material, allow to probe the low-mass region of the parameter space for spin-independent dark matter-nucleon scattering with high sensitivity.

1 Introduction

Today we know that dark matter constitutes about 85% of the matter in the Universe [1], nonetheless its nature is still unknown. Unraveling this problem is one of the major challenges of modern physics.
Direct dark matter searches exploit a great variety of different detector technologies, all aiming to observe dark matter particles via their elastic scattering off nuclei in their detectors.
In the last few years, many direct dark matter projects have probed with increasing sensitivity the mass-cross section parameter space for WIMP-nucleus elastic scattering [2]. Most of these experiments are suitable for WIMP masses $\gtrsim 30$ GeV/c^2, where the sensitivity gain is mainly driven by the exposure. Nevertheless, a number of theoretical models favoring lighter dark matter candidates (e.g. [3, 4, 5, 6, 7]) have recently moved the interest of the community to the mass region below 10 GeV/c^2. As such light dark matter particles produce only very low-energy nuclear recoils (below keV), the challenge for their detection is to achieve a sufficiently low threshold in terms of recoil energy, with enough background discrimination at these low energies.
Cryogenic experiments currently provide the best sensitivity for light dark matter particles, with the CRESST-II experiment advancing to the sub-GeV/c^2 dark matter particle mass regime.

2 Detector principle

Cryogenic detectors are low-temperature (mK) calorimeters that measure the energy deposited in the absorber by a particle interaction as an increase of temperature in an appropriate temperature sensor. Experiments based on this type of detectors developed strategies to distinguish background from a possible dark matter signal on an event-by-event base.
The CRESST target consists of scintillating $CaWO_4$ crystals (*phonon detectors*). Each interaction in $CaWO_4$ produces a phonon signal in the target crystal, yielding a precise energy measurement (approximately independent of the type of interacting particle), and a light signal that is measured by a secondary independent cryogenic calorimeter (*light detector*) allowing for particle identification [8, 9]. A phonon detector and the corresponding light detector form a so-called *detector module*.
Both, phonon and light detectors are read out via tungsten transition edge sensors (TES) and are equipped with a heater to stabilize the temperature in their operating point in the transition between normal and superconducting state. The heater is also used to inject pulses which are needed for the energy calibration and for the determination of the energy threshold.

3 The CRESST Setup at LNGS

The main part of the facility at LNGS is a cryostat, whose design had to combine the requirements of low temperature with those of low background. As can be seen in Fig. 1, the dilution unit of the cryostat and the dewars containing cryogenic liquids do not extend into the experimental area.

The low temperatures are provided by a ^{3}He-^{4}He dilution refrigerator and transferred to the detectors via a 1.3 m long copper cold finger. The detectors are arranged in a common support structure, the so-called *carousel*, and mounted inside the *cold box* which consists of five concentric radiation shields surrounding the experimental volume and the cold finger. Two internal cold shields, consisting of lead with low intrinsic radioactivity, are attached to the

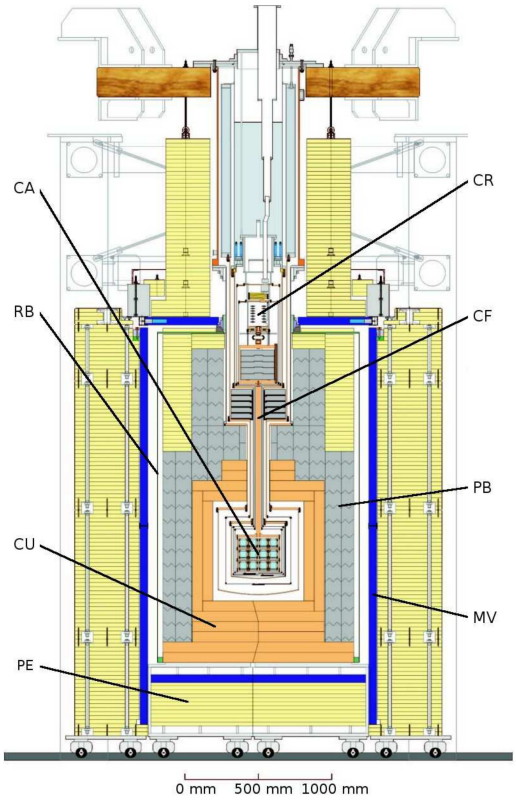

Figure 1: Schematic drawing of the CRESST setup. A cold finger (CF) links the cryostat (CR) to the experimental volume, where the detectors are arranged in a common support structure, the so called carousel (CA). This volume is surrounded by layers of shielding from copper (CU), lead (PB), and polyethylene (PE). The copper and lead shieldings are additionally enclosed in a radon box (RB). An active muon veto (MV) tags events which are induced by cosmic radiation.

mixing chamber and to a thermal radiation shield at liquid N_2 temperature, respectively, in order to block any line-of-sight from the non-radio-pure parts of the dilution refrigerator to the detectors inside the cold box. The cold box is surrounded by several layers of shielding against the main types of background radiation: layers of highly pure copper and lead shield against γ-rays, while polyethylene serves as a moderator for neutrons. The inner layers of shielding are contained in a gas tight box to prevent radon from penetrating them. In addition, an active muon veto using plastic scintillator panels is installed to tag muons. The veto surrounds the lead and copper shielding and covers 98.7 % of the solid angle around the detectors, a small hole on top is necessary to leave space for the cryostat.

4 Current status of the experiment

The second long data-taking period of the CRESST-II experiment, referred to as phase 2, extended from July 2013 to August 2015. In this period 18 detector modules of four different designs were operated, corresponding to a total mass of 5 kg. The dark matter data acquired in the two years of measurement time is accompanied by calibrations with 122 keV γ-rays (^{57}Co-source), high-energy γ-rays (^{232}Th-source) and neutrons (AmBe-source).

In 2014 we reported on first results from phase 2, analyzing the detector module with the best overall performance in terms of background level, trigger threshold and background rejection [10]. This non-blind analysis proved that CRESST-II detectors provide reliable data for recoil energies down to the threshold of 0.6 keV [10]. As a consequence of this observation, we lowered the trigger thresholds of several detectors, achieving the lowest value of 0.3 keV with the module Lise. The results obtained from 52.2 kg days of data taken with the module Lise with its threshold set at 0.3 keV are reported in [11] and will be briefly outlined in the following.

5 Results

Differently from the module used for the 2014 result [10] which is equipped with the upgraded crystal holding scheme employing $CaWO_4$-sticks [12] and a self-grown crystal, the detector module Lise used for the result presented in [11] has a conventional design where metal clamps hold a commercially available crystal. It has to be stressed that the lower threshold of Lise is neither connected to the holding concept, nor to the intrinsic background level of the crystal, but arises from a superior performance of the phonon sensor.
The threshold of the detector is determined directly by injecting low-energy heater pulses with a shape similar to pulses induced by particle interactions and measuring the fraction causing a trigger. The result of this dedicated measurement is illustrated in figure 2.

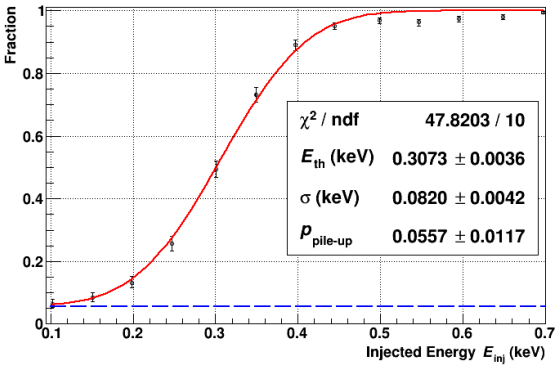

Figure 2: Fraction of heater pulses triggering, injected with discrete energies E_{inj}. The error bars indicate the statistical (binomial) uncertainty at the respective energy. The solid red curve is a fit with the sum of a scaled error function and a constant pile-up probability $p_{\text{pile-up}}$ (blue dashed line). The fit yields an energy threshold of $E_{\mathrm{th}} = (307.3 \pm 3.6)\,\mathrm{eV}$ and a width of $\sigma = (82.0 \pm 4.2)\,\mathrm{eV}$.

The methods used for the analysis of the data are thoroughly described and discussed in [10, 11] and references therein. A blind analysis was carried out by first defining a statistically insignificant part of the data set as a training set, on which all methods of data preparation and selection are developed, that are then applied blindly without any change to the final data set. The validity of this approach is exhaustively discussed in [11]. The survival probability of the signal in the data selection is determined by performing the cuts on a set of artificial pulses with discrete energies. The fraction of signals with a certain simulated energy passing each cut yields the respective survival probability. Figure 3 illustrates the cumulative survival probability after each selection criterion.

All events surviving the selection criteria, corresponding to the 52.2 kg days of exposure of the detector Lise, are presented in figure 4 in the light yield - energy plane. The light yield

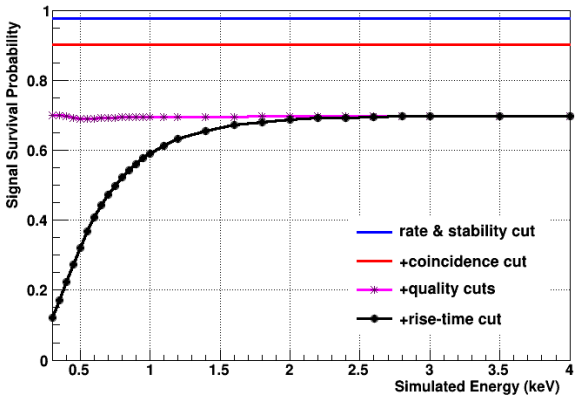

Figure 3: The solid lines represent the signal survival probability after successive application of the selection criteria. The simulated pulses correspond to nuclear recoil events at discrete energies starting from the threshold of 0.3 keV (data points).

is defined for every event as the ratio of light to phonon signal. Electron recoils have a light yield set to one by calibration (at 122 keV). Nuclear recoils produce less light than electron recoils. The reduction is quantified by the quenching factors for the respective target nuclei, which are precisely known from dedicated independent measurements [13]. In figure 4 the solid blue lines mark the 90 % upper and lower boundaries of the e^-/γ-band, with 80 % of electron recoil events expected in between. From this band, with the knowledge of the quenching factors for the different nuclei present in the target material, the nuclear recoil bands for scatterings off tungsten, calcium and oxygen (respectively solid green, not shown and solid red in figure 4) can be analytically calculated.

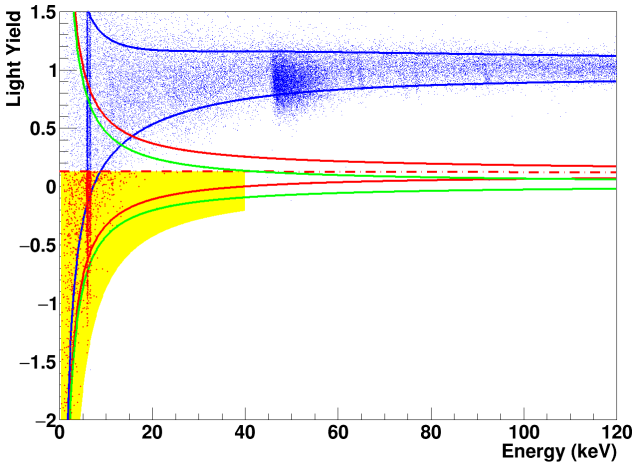

Figure 4: Data taken with the detector module Lise depicted in the light yield - energy plane. The solid lines mark the 90 % upper and lower boundaries of the e^-/γ-band (blue), the band for recoils off oxygen (red) and off tungsten (green). The upper boundary of the acceptance region (yellow area) is set to the middle of the oxygen band (dashed dotted red), the lower one to the 99.5 % lower boundary of the tungsten band. Events therein are additionally highlighted in red.

The e^-/γ-band exhibits two prominent features, a double-peak at ~ 6 keV originating from an external ^{55}Fe-source and a β-decay spectrum from an intrinsic contamination of the crystal with ^{210}Pb starting at 46.5 keV.

The acceptance region for the dark matter analysis (yellow region in figure 4) extends in energy from the threshold of 307 eV to 40 keV and in light yield the from the 99.5 % lower boundary of the tungsten band to the center of the oxygen band (dashed-dotted red line in figure 4).
For the calculation of the exclusion limit all events inside the acceptance region (highlighted in red) are considered as potential signal events. This assumption is extremely conservative due to the clear large leakage of e^-/γ-events into the acceptance region, which is caused by the limited resolution of the light detector in use in this detector module.
Using the Yellin optimum interval method [14, 15] to calculate an upper limit with 90 % confidence level on the elastic spin-independent interaction cross-section of dark matter particles with nucleons, the exclusion limit resulting from the blind analysis reported in [11] is drawn in solid red in figure 5. For dark matter particle masses higher than $\sim 5\,\mathrm{GeV}/c^2$ this module does not have a competitive sensitivity due to the large number of background events present in the acceptance region. However, for dark matter particles lighter than $\sim 2\,\mathrm{GeV}/c^2$ we explore new regions of the parameter space.

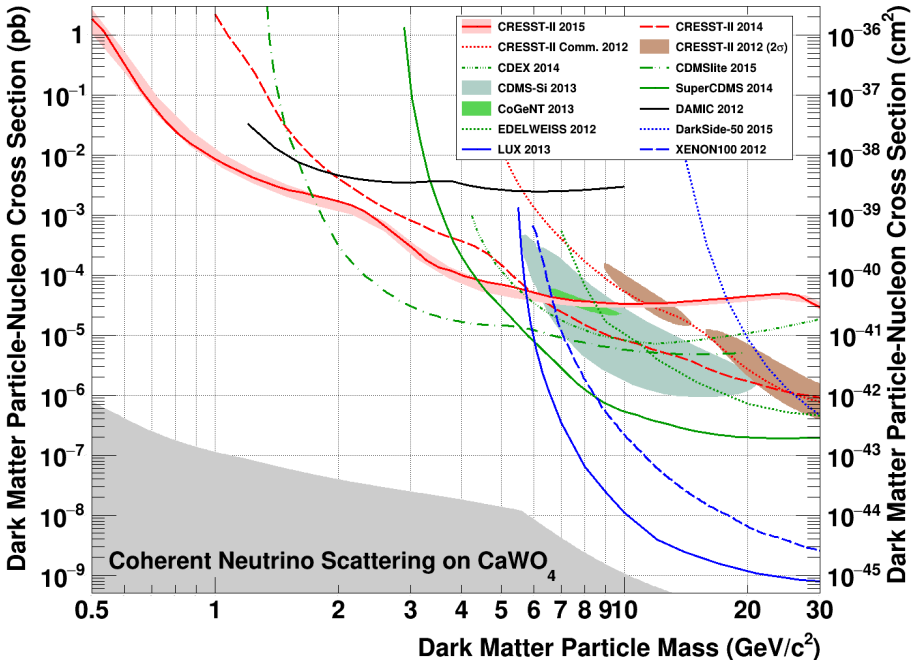

Figure 5: Parameter space for elastic spin-independent dark matter-nucleon scattering. The result from the analysis presented in [11] is drawn in solid red together with the expected sensitivity (1σ confidence level (C.L.)) from a data-driven background-only model (light red band). The remaining red lines correspond to previous CRESST-II limits [10, 16]. The favored parameter space reported by CRESST-II phase 1 [17], CDMS-Si [18] and CoGeNT [19] are drawn as shaded regions. For comparison, exclusion limits (90 % C.L.) of the liquid noble gas experiments [20, 21, 22] are depicted in blue, from germanium and silicon based experiments in green [23, 24, 25, 26, 27]. In the gray area coherent neutrino nucleus scattering, dominantly from solar neutrinos, will be an irreducible background for a $CaWO_4$-based dark matter search experiment [28].

The improvement with respect to the 2014 result [10] (red dashed line) is due to the significantly lower threshold of the detector Lise and to the almost constant background level down to the threshold. The result for the first time extends the reach of direct dark matter searches

to dark matter particle masses down to $0.5\,\mathrm{GeV}/c^2$.

6 Conclusions and Outlook

With an exposure of 52 kg live days and a threshold of 307eV for nuclear recoils we obtain in [11] an unprecedented sensitivity for light dark matter, probing a new region of parameter space for dark matter particles of masses below $2\mathrm{GeV/c}^2$, previously not covered in direct detection searches. With the results obtained we extend the reach of direct dark matter searches to the sub-GeV/c^2 region and we prove that a low energy threshold is the key requirement to achieve sensitivity to dark matter particles of $1\,\mathrm{GeV/c}^2$ and below.
We expect significant progress exploring the low mass regime with the upcoming CRESST-III experiment, featuring next-generation detectors optimized towards the detection of recoil energies as small as 100 eV.

7 List of Publications

1. G. Angloher et al., (CRESST Collaboration): Results on light dark matter particles with a low-threshold CRESST-II detector
   Eur. Phys. J. C. 76 (2016) 25, arXiv:1509.01515[astro-ph.CO]

2. R. Strauss et al., (CRESST Collaboration): A detector module with highly efficient surface-alpha event rejection operated in CRESST-II Phase 2
   Eur. Phys. J. C 75 (2015) 352, arXiv:1410.1753[physics.ins-det]

3. R. Strauss et al., (CRESST Collaboration): Beta/gamma and alpha backgrounds in CRESST-II Phase 2
   JCAP 06 (2015) 030, arXiv:1410.4188 [physics.ins-det]

4. M. Kiefer et al., (CRESST Collaboration): In-Situ Performance Characterization of CRESST Detector Modules
   arXiv:1503.07806 [astro-ph.IM]

5. A. Gütlein et al., (CRESST Collaboration): Impact of Coherent Neutrino Nucleus Scattering on Direct Dark Matter Searches based on CaWO4 Crystals
   Astropart. Phys. 69 (2015) 44-49, arXiv:1408.2357[hep-ph]

6. G. Angloher et al., (CRESST Collaboration): Probing low WIMP masses with the next generation of CRESST detector
   arXiv:1503.08065 [astro-ph.IM]

7. F. Reindl et al., (CRESST Collaboration): The CRESST Dark Matter Search - Status and Perspectives
   arXiv:1509.09124 [physics.ins-det]

8. J. Schieck et al., (CRESST Collaboration): Direct Dark Matter Search with the CRESST-II Experiment
   arXiv:1505.03289 [astro-ph.CO]

9. A. Münster et al., (CRESST Collaboration): Status of the CRESST-II Experiment for Direct Dark Matter Search
   proceedings of the 11th Patras Workshop on Axions, WIMPs and WISPs PATRAS2015, Zaragoza, pp. 111 - 115, http://www-library.desy.de/preparch/desy/proc/proc15-02.pdf

Acknowledgements

We are grateful to LNGS for the generous support of CRESST, in particular to Marco Guetti for his constant assistance.

References

[1] P.A.R.Ade et al. (Planck Collaboration): 2014 A&A 571 A16, arXiv:1303.5076 [astro-ph.CO].

[2] P. Cushman et al.: arXiv:1310.8327 [hep-ex].

[3] T. Cohen et al.: Phys. Rev. D82 (2010) 056001, arXiv:1005.1655 [hep-ph].

[4] D. E. Kaplan et al.: Phys. Rev. D79 (2009) 115016, arXiv:0901.4117 [hep-ph].

[5] K. Sigurdson et al.: Phys. Rev. D70 (2004) 083501, arXiv:astro-ph/0406355.

[6] J. Fortin et al.: Phys. Rev. D85 (2012) 063506, arXiv:1103.3289 [hep-ph].

[7] J. Feng et al.: Phys. Lett. B 704 (2011) 534, arXiv:1102.4331 [hep-ph].

[8] G. Angloher et al., (CRESST Collaboration): Astropart.Phys. 23 (2005) 325-339, arXiv:astro-ph/0408006.

[9] G. Angloher et al., (CRESST Collaboration): Astropart.Phys. 31 (2009) 270-276, arXiv:0809.1829[astro-ph].

[10] G. Angloher et al., (CRESST Collaboration): Eur. Phys. J. C 74 (2014) 3184, arXiv:1407.3146[astro-ph.CO].

[11] G. Angloher et al., (CRESST Collaboration): Eur. Phys. J. C 76 (2016) 25, arXiv:1509.01515[astro-ph.CO].

[12] R. Strauss et al., (CRESST Collaboration): Eur. Phys. J. C 75 (2015) 352, arXiv:1410.1753[physics.ins-det].

[13] R. Strauss et al., (CRESST Collaboration): Eur. Phys. J. C 74 (2014) 2957, arXiv:1401.3332[astro-ph.IM].

[14] S. Yellin: Phys. Rev. D 66, 032005 (2002), arXiv:physics/0203002[physics.data-an].

[15] S. Yellin: Software for computing an upper limit given unknown background (02/2011) http://cdms.stanford.edu/Upperlimit/

[16] A. Brown et al.: Phys. Rev. D 85, 021301 (2012), arXiv:1109.2589[astro-ph.CO].

[17] G. Angloher et al., (CRESST Collaboration): 2012 Eur. Phys. J. C 72 (2012) 1971, arXiv:1109.0702[astro-ph.CO].

[18] R. Agnese et al., (CDMS Collaboration): Phys. Rev. Lett. 111, 251301 (2013), arXiv:1304.4279[hep-ex].

[19] C.E. Aalseth et al., (CoGeNT Collaboration): Phys. Rev. D 88, 012002 (2013), arXiv:1208.5737[astro-ph.CO].

[20] P. Agnes et al., (DarkSide Collaboration): Phys. Lett. B 743 (2015) 456-466, arXiv:1410.0653[astro-ph.CO].

[21] D.S. Akerib et al., (LUX Collaboration): 2014 Phys. Rev. Lett. 112, 091303 (2014), arXiv:1310.8214[astro-ph.CO].

[22] E. Aprile et al., (XENON100 Collaboration): Phys. Rev. Lett. 109, 181301 (2012), arXiv:1207.5988[astro-ph.CO].

[23] Q. Yue et al., (CDEX Collaboration): Phys. Rev. D 90 (2014) 091701, arXiv:1404.4946[hep-ex].

[24] R. Agnese et al., (SuperCDMS Collaboration): accepted for publication in Phys. Rev. Lett. (2015), arXiv: 1509.02448[astro-ph.CO].

[25] R. Agnese et al., (SuperCDMS Collaboration): Phys. Rev. Lett. 112, 241302 (2014), arXiv:1402.7137 [hep-ex].

[26] J. Barreto et al.: Physics Letters B 711 (2012) 264-269, arXiv:1105.5191 [astro-ph.IM].

[27] E. Armengaud et al., (EDELWEISS Collaboration): Phys. Rev. D 86 (2012) 051701, arXiv:1207.1815[astro-ph.CO].

[28] A. Gütlein et al., (CRESST Collaboration): Astropart. Phys. 69 (2015) 44-49, arXiv:1408.2357[hep-ph].

CUORE — 2015 LNGS Report

C. Alduino,[1] K. Alfonso,[2] D. R. Artusa,[1,3] F. T. Avignone III,[1] O. Azzolini,[4] M. Balata,[3] T. I. Banks,[5,6] S. Banfi,[7] G. Bari,[8] A. Battistello,[4] A. Bau,[7] J.W. Beeman,[9] F. Bellini,[10,11] A. Bersani,[12] A. Bianco,[13] D. Biare,[6] M. Biassoni,[14,7] F. Bragazzi,[12] C. Brofferio,[14,7] A. Buccheri,[11] C. Bucci,[3] C. Bulfon,[11] A. Camacho,[4] A. Caminata,[12] L. Canonica,[3] X. G. Cao,[15] S. Capelli,[14,7] M. Capodiferro,[11] L. Cappelli,[12,3,16] L. Carbone,[7] L. Cardani,[10,11] M. Cariello,[12] P. Carniti,[14,7] N. Casali,[10,11] L. Cassina,[14,7] R. Cereseto,[12] G. Ceruti,[7] A. Chiarini,[8] D. Chiesa,[14,7] N. Chott,[1] M. Clemenza,[14,7] D. Conventi,[4] S. Copello,[17,12] C. Cosmelli,[10,11] O. Cremonesi ⋆,[7] C. Crescentini,[8] R. J. Creswick,[1] J. S. Cushman,[18] I. Dafinei,[11] C. J. Davis,[18] F. Del Corso,[8] S. Dell'Oro,[3,19] M. M. Deninno,[8] S. Di Domizio,[17,12] M. L. Di Vacri,[3,20] L. DiPaolo,[6] A. Drobizhev,[5,6] G. Erme,[3,16] D. Q. Fang,[15] M. Faverzani,[14,7] J. Feintzeig,[6] G. Fernandes,[17,12] E. Ferri,[14,7] F. Ferroni,[10,11] S. Finelli,[8] E. Fiorini,[7,14] M. A. Franceschi,[21] S. J. Freedman †,[6,5] B. K. Fujikawa,[6] R. Gaigher,[7] A. Giachero,[7] L. Gironi,[14,7] A. Giuliani,[22] L. Gladstone,[23] P. Gorla,[3] C. Gotti,[14,7] C. Guendalini,[8] M. Guerzoni,[8] M. Guetti,[3] T. D. Gutierrez,[13] E. E. Haller,[9,24] K. Han,[25,18] E. Hansen,[23,2] K. M. Heeger,[18] R. Hennings-Yeomans,[5,6] K. P. Hickerson,[2] H. Z. Huang,[2] M. Iannone,[11] L. Ioannucci,[3] E. Johnston,[13] R. Kadel,[26] G. Keppel,[4] Yu. G. Kolomensky,[5,26,6] A. Leder,[23] C. Ligi,[21] K. E. Lim,[18] X. Liu,[2] Y. G. Ma,[15] M. Maino,[14,7] L. Marini,[17,12] V. Martelli,[27,28] M. Martinez,[10,11,29] R. H. Maruyama,[18] M. F. Marzioni,[10,11] R. Mazza,[7] Y. Mei,[6] R. Michinelli,[8] A. Miller,[5] N. Moggi,[30,8] S. Morganti,[11] P. J. Mosteiro,[11] T. Napolitano,[21] M. Nastasi,[14,7] S. Nisi,[3] C. Nones,[31] E. B. Norman,[32,33] A. Nucciotti,[14,7] T. O'Donnell,[5,6] F. Orio,[11] D. Orlandi,[3] J. L. Ouellet,[23,5,6] C. E. Pagliarone,[3,16] M. Pallavicini,[17,12] V. Palmieri,[4] G. Pancaldi,[8] A. Passerini,[7] G. Panone,[3] L. Pattavina,[3] M. Pavan,[14,7] R. Pedrotta,[34] A. Pelosi,[11] M. Perego,[7] G. Pessina,[7] V. Pettinacci,[11] G. Piperno,[10,11] C. Pira,[4] S. Pirro,[3] S. Pozzi,[14,7] E. Previtali,[7] D. Reggio,[5] D. Rose,[13] C. Rosenfeld,[1] C. Rusconi,[7] E. Sala,[14,7] S. Sangiorgio,[32] D. Santone,[3,20] N. D. Scielzo,[32] B. Scott,[13] J. Sekerak,[13] B. Sheff,[5] V. Singh,[5] M. Sisti,[14,7] A. R. Smith,[6] F. Stivanello,[4] L. Taffarello,[34] L. Tatananni,[3] M. Tenconi,[22] F. Terranova,[14,7] M. Tessaro,[34] C. Tomei,[11] S. Trentalange,[2] G. Ventura,[27,28] M. Vignati,[11] S. L. Wagaarachchi,[5,6] J. Wallig,[35] B. S. Wang,[32,33] H. W. Wang,[15] J. Wilson,[1] L. A. Winslow,[23] T. Wise,[18,36] A. Woodcraft,[37] L. Zanotti,[14,7] C. Zarra,[3] G. Q. Zhang,[15] B. X. Zhu,[2] S. Zimmermann,[35] and S. Zucchelli[38,8]

[1] *Department of Physics and Astronomy, University of South Carolina, Columbia, SC 29208 - USA*
[2] *Department of Physics and Astronomy, University of California, Los Angeles, CA 90095 - USA*
[3] *INFN - Laboratori Nazionali del Gran Sasso, Assergi (L'Aquila) I-67010 - Italy*
[4] *INFN - Laboratori Nazionali di Legnaro, Legnaro (Padova) I-35020 - Italy*
[5] *Department of Physics, University of California, Berkeley, CA 94720 - USA*
[6] *Nuclear Science Division, Lawrence Berkeley National Laboratory, Berkeley, CA 94720 - USA*
[7] *INFN - Sezione di Milano Bicocca, Milano I-20126 - Italy*
[8] *INFN - Sezione di Bologna, Bologna I-40127 - Italy*
[9] *Materials Science Division, Lawrence Berkeley National Laboratory, Berkeley, CA 94720 - USA*
[10] *Dipartimento di Fisica, Sapienza Università di Roma, Roma I-00185 - Italy*
[11] *INFN - Sezione di Roma, Roma I-00185 - Italy*

⋆ Spokesperson: O. Cremonesi, cuore-spokesperson@lngs.infn.it
† Deceased

[12]*INFN - Sezione di Genova, Genova I-16146 - Italy*
[13]*Physics Department, California Polytechnic State University, San Luis Obispo, CA 93407 - USA*
[14]*Dipartimento di Fisica, Università di Milano-Bicocca, Milano I-20126 - Italy*
[15]*Shanghai Institute of Applied Physics, Chinese Academy of Sciences, Shanghai 201800 - China*
[16]*Dipartimento di Ingegneria Civile e Meccanica, Università degli Studi di Cassino e del Lazio Meridionale, Cassino I-03043 - Italy*
[17]*Dipartimento di Fisica, Università di Genova, Genova I-16146 - Italy*
[18]*Department of Physics, Yale University, New Haven, CT 06520 - USA*
[19]*INFN - Gran Sasso Science Institute, L'Aquila I-67100 - Italy*
[20]*Dipartimento di Scienze Fisiche e Chimiche, Università dell'Aquila, L'Aquila I-67100 - Italy*
[21]*INFN - Laboratori Nazionali di Frascati, Frascati (Roma) I-00044 - Italy*
[22]*CSNSM, Univ. Paris-Sud, CNRS/IN2P3, Université Paris-Saclay, 91405 Orsay, France*
[23]*Massachusetts Institute of Technology, Cambridge, MA 02139 - USA*
[24]*Department of Materials Science and Engineering, University of California, Berkeley, CA 94720 - USA*
[25]*Department of Physics and Astronomy, Shanghai Jiao Tong University, Shanghai 200240 - China*
[26]*Physics Division, Lawrence Berkeley National Laboratory, Berkeley, CA 94720 - USA*
[27]*Dipartimento di Fisica, Università di Firenze, Firenze I-50125 - Italy*
[28]*INFN - Sezione di Firenze, Firenze I-50125 - Italy*
[29]*Laboratorio de Fisica Nuclear y Astroparticulas, Universidad de Zaragoza, Zaragoza 50009 - Spain*
[30]*Dipartimento di Scienze per la Qualità della Vita, Alma Mater Studiorum - Università di Bologna, Bologna I-47921 - Italy*
[31]*Service de Physique des Particules, CEA / Saclay, 91191 Gif-sur-Yvette - France*
[32]*Lawrence Livermore National Laboratory, Livermore, CA 94550 - USA*
[33]*Department of Nuclear Engineering, University of California, Berkeley, CA 94720 - USA*
[34]*INFN - Sezione di Padova, Padova I-35131 - Italy*
[35]*Engineering Division, Lawrence Berkeley National Laboratory, Berkeley, CA 94720 - USA*
[36]*Department of Physics, University of Wisconsin, Madison, WI 53706 - USA*
[37]*SUPA, Institute for Astronomy, University of Edinburgh, Blackford Hill, Edinburgh EH9 3HJ - UK*
[38]*Dipartimento di Fisica e Astronomia, Alma Mater Studiorum - Universit`a di Bologna, Bologna I-40127 - Italy*

CUORE is a challenging experiment which aims to exploit the cryogenic bolometer technique at an unprecedented scale to achieve a half-life sensitivity of 10^{26} years for $\beta\beta(0\nu)$ decay of ^{130}Te. With this sensitivity we may begin to explore the inverted hierarchy region of neutrino masses. The detector consists of a close-packed array of TeO_2 crystals containing $\sim$ 206 kg of ^{130}Te in total which will be cooled to an operating temperature of $\sim$ 10 mK inside a large, dedicated cryostat.

In the enclosed report we summarize the activities of the collaboration in the past year at LNGS. It has been a critical period for CUORE in which we have continued the science program of CUORE-0, successfully completed the final stages of the phased commissioning plan of the CUORE cryostat, and further developed the subsystems that will support operation of the experiment. Our recently concluded cryostat run in which the fully integrated cryogenic system maintained stable operating temperatures well below the target specification of 10 mK marks a crucial milestone and leaves us well placed to embark on the next steps — namely installation of the detector array and commissioning to stable operations.

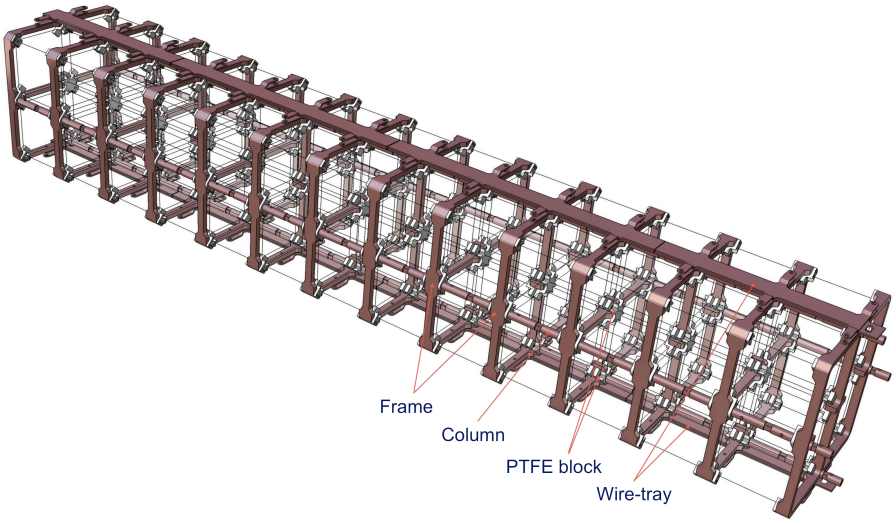

FIG. 1. Detailed view of the components of a single CUORE tower.

I. DETECTOR OVERVIEW

While no doubt familiar from previous reports, we briefly summarize here some of the key features of CUORE. The detector consists of 988 ultra-radiopure TeO_2 crystals arranged into 19 identical towers. Each tower contains 52 crystals held inside a copper structure by PTFE brackets in an arrangement of 13 four-crystal floors (Fig. 1)

A temperature sensor (neutron-transmutation doped (NTD) Germanium thermistor) and a Joule heater are glued to one face of each crystal. These sensors are wire bonded directly to readout ribbons held by copper trays fixed to the tower structure. All copper components directly facing the crystals were cleaned using an aggressive and intricate cleaning procedure developed and executed at LNL. To minimize recontamination of components during subsequent handling all the towers were constructed in a dedicated underground assembly line at LNGS which featured a class-1000 clean room and purpose-specific nitrogen-fluxed gloveboxes for each assembly step. Data from the CUORE-0 tower demonstrate that materials selection, cleaning, and subsequent handling and assembly protocols resulted in an almost 7 fold reduction of backgrounds from surface contamination. Assembly of all 19 towers is complete and they are stored underground at LNGS awaiting installation in the CUORE cryostat.

II. CRYOGENICS

The CUORE cryostat commissioning has followed a phased program in which we have progressively added complexity to the system, testing each evolution in a full cold run. We have followed this approach in order to identify and remedy problems before they become deeply intergrated into the final complex system.

In Phase 1 we tested the cryostat sections down to 4 K and separately benchmarked the performance of the Dilution Unit (DU) in a standalone Test Cryostat. In Phase 2 we tested the performance of the various sections of the cryogenic system in a sequence of ultra-low temperature cold runs, in which new elements were added at each cooldown. In September 2014, the first cold run of Phase 2 (Run 1 or "no load") was successfully concluded with the

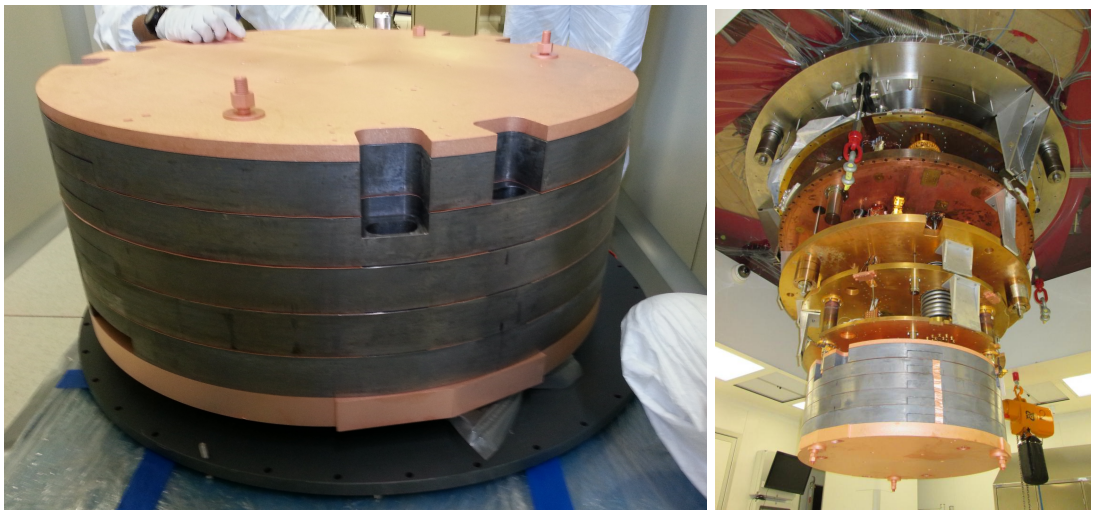

FIG. 2. Top lead shield assembly at LNGS (left) and after installation, suspended inside the CUORE cryostat (right).

cryostat reaching a stable base temperature of ∼6 mK.

After Run 1 we installed the full readout chain from room temperature to the coldest temperature stage ($\lesssim$10 mK) and performed a second cold run (Run 2). Reaching a stable temperature well below 10 mK we demonstrated that the heat load from the full CUORE wiring was within the design budget. As part of Run 2 we also installed a mini bolometric array (MiniTower) made out of 8 CUORE TeO_2 bolometers.

Unfortunately a super leak (a leak that appears only when He is in the superfluid phase) appeared on the DU. This problem consumed significant effort to correct and required us to extract the DU from the main cryostat and install it in our much-smaller Test Cryostat for more efficient trouble-shooting. The cold leak was fixed by redoing all the indium joints of the DU.

The subsequent run (Run 3) was envisioned to test the impact of the cold lead shields. As delivery of the roman lead parts (Sec. II C) was delayed, only the "top lead" section was installed for this run. With a mass of about 2.5 tons, this disk (which is thermalized at 50 mK) represents a significant heat load inside the cryostat.

The top lead was first installed and aligned (Fig. 2 left) with the other elements of the cryostat. The Tower Support Plate (TSP) was then installed just below the lead disk (Fig. 2 right). This plate, is thermalized at the 10 mK stage and is the element from which the 19 CUORE towers will be suspended. With the TSP installed, we paused preparations for Run 3 and took the opportunity to test detector installation tools and procedures (Sec. V) by installing a mockup tower onto the TSP with the custom-built installation tools.

Following this, the final sections of the Detector Calibration (DCS) and of the Fast Cooling (FCS) systems closest to the detector were installed before closing the cryostat vessels. The cooldown started in July 2015.

For this cooldown the CUORE FCS was used for the first time and overall performed well (Section II A). The cooldown time (∼ 16 days) with the FCS was consistent with our expectations (Fig. II top). Unfortunately the temperature by the coldest stage (nominally 10 mK) was larger than desired and was not stable, in fact it exhibited significant oscillations characterized by a period of about 4 hours.

Similar behavior (with an almost identical frequency) was also observed during Run 1. In that instance we observed that the cryostat was actually oscillating (the cryostat is a pendulum

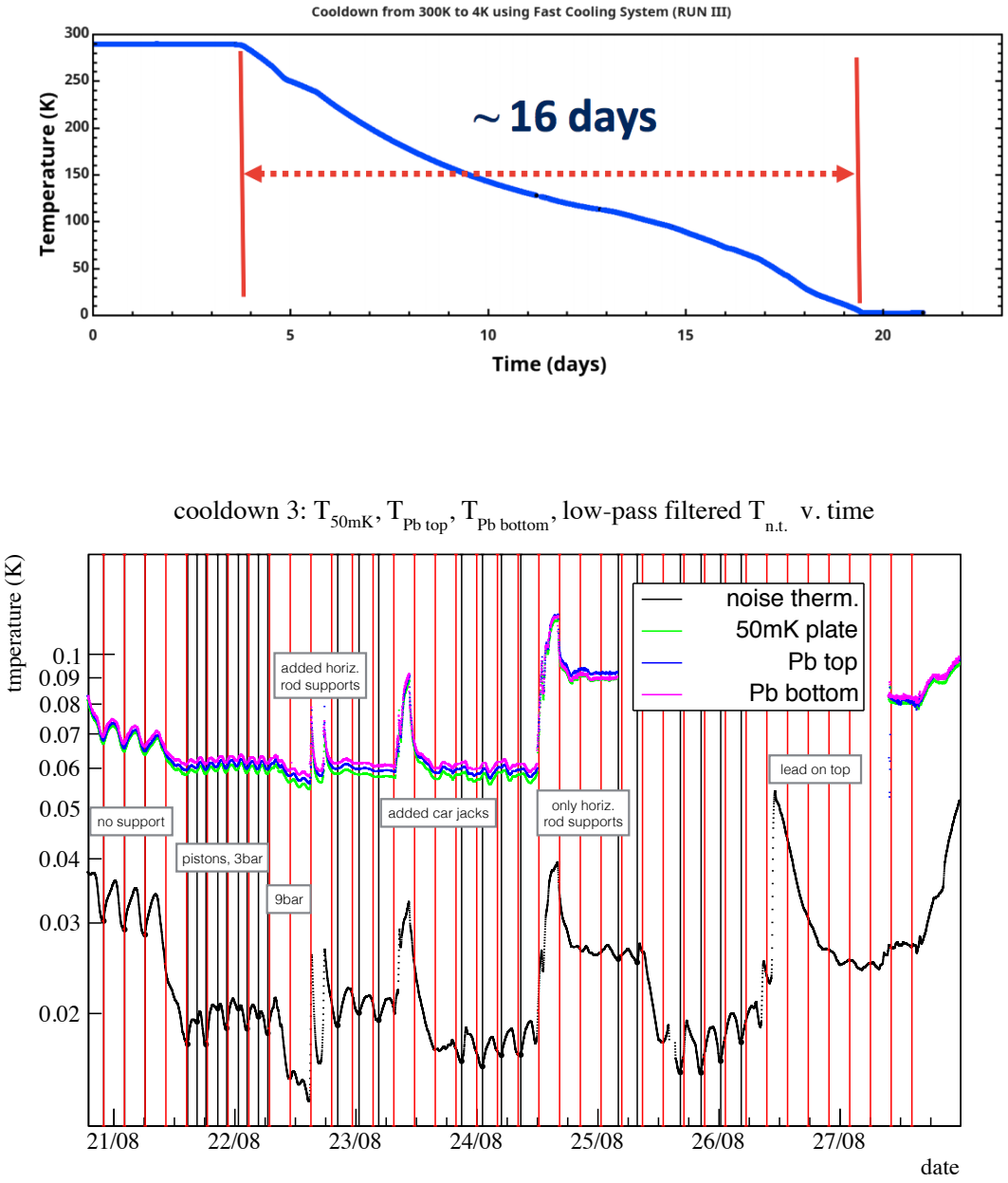

FIG. 3. Temperature profiles during Run 3 cooldown (top) and around base temperature (bottom).

suspended by three stainless steel ropes) and the "problem" was solved by blocking this movement with a simple mechanical system; subsequently the temperature dropped and stabilized below 6 mK, as mentioned above.

Motivated by this experience we applied similiar techniques during Run 3. While some improvement was seen (Fig. II bottom) the oscillations persisted — though with reduced amplitude. Unfortunatey the lowest temperature obtained was $\sim$ 12 mK. After exhaustive diagnostic tests

we decided to abort the run and warmed up the cryostat.

Our interpretation of this problem is that: 1. the oscillations of the cryostat are induced by the action of the pulse tubes, 2. some inner part of the cryostat (on which the external actions are irrelevant) was still oscillating during Run 3.

We then proceeded to install newly conceived hardware to block the cryostat mechanical movements — both internally and externally — and we installed the lateral Roman-lead shield which had been prepared in the interim. When preparations were complete in late November we started a fourth cooldown (Run 4) in which the cryogenic system was essentially fully integrated (i.e., full complement of cold lead shielding, all twelve DCS strings installed, readout wiring etc. installed).

We are pleased to report that by mid December 2015 the cryostat reached a stable base temperature of ~ 6.3 mK. In the subsequent weeks we have performed several crucial test measurements including: operating the frontend electronics and DAQ to readout signals from the MiniTower; tests of the detector calibration system in which the source strings were deployed from room temperature to the coldest stage several times; tests of a PID-based temperature control system to maintain the TSP at user-defined temperatures; tests of the external lead shielding (ELS) in which the MiniTower data was acquired with and without the ELS raised. Additionally we performed a series of test measurements where we operated on the enviroment external to the cryostat — optimizing vibration isolatation of the pulse-tubes, routing of electronics cables — in order to continuously improve the energy resolution observed in the bolometers of the MiniTower. At the time of writing we have achieved a positive result and are satisfied that bolometers can be successfully operated in the CUORE cryostat. Run 4 has now concluded and we are preparing the cryostat for installation of the detector array.

A. CUORE Fast Cooling System

The five CUORE Pulse Tubes (PTs) alone are not able to cool down the whole CUORE Cryostat, lead shields and bolometric crystals to 4 K in an acceptable time. For this reason, in addition to PTs, a Fast Cooling System (FCS) has been designed and constucted for a quick precooling of CUORE Inner Vacuum Chamber (IVC), from room temperature to less than 20-30 K in about 10 days. Despite of other CUORE cooling systems (Pulse Tubes and Dilution Unit), that are Cryogen-Fluid-Free Refrigerators, the FCS uses Helium to reach such a performance in terms of mass, volume and time. CUORE FCS can be schematically described as an external vessel (Fast Cooling Unit, FCU) with two main heat exchangers (a third one is outside the FCU), three CRYOMECH AL600 Single Stage Gifford-McMahon Cryo-coolers (each with a cooling power of about 600 W at 77 K), a helium blower, double-walled pipes, a gas handling system and finally an automated FC Control System (see Fig. 4(a)). The FCU Cryostat consists of two nested vessels where in the inner one (Inner Fast Cooling, IFC) there is a copper heat exchanger, the coldest part of the FCU and in the external one (Outer Fast Cooling, OFC) there is a counter-flow heat exchanger, corresponding to HEX2 and HEX1 respectively of Fig.4(a). The Helium gas, moved by a blower, is progressively cooled down. It enters first the HEX0, then the FCU cryostat through HEX1 and finally it passes to the third cooling stage, where it reaches the desired temperature by means of the three GM cryocoolers thermally linked to HEX2. Thus, it exits the FCU to enter the CUORE cryostat IVC and cool down the entire IVC volume (copper, lead shields and crystal towers). The gas is extracted from CUORE and recirculated by means of the external blower. The Fast Cooling Unit (FCU), shown in Fig. 4(b), is a cryostat, cooled down by three GM cryocoolers. A big effort has been put to clean

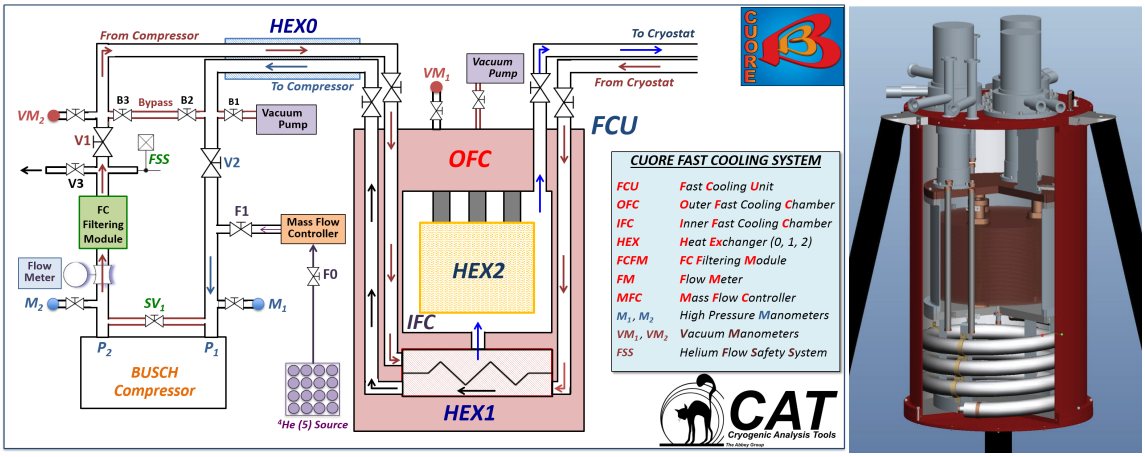

(a) (b)

FIG. 4. Fast Cooling System Layout (a); Fast Cooling Unit 3D Cross Section (b).

all the involved parts with different methods. Since the Fast Cooling System injects Helium into the IVC, the gas needs to match restrictive purity requirements. Although all the FCS parts, in contact with the Helium gas, have been conveniently cleaned, a He filtering module is fundamental in order to avoid unexpected particles to enter the cryostat. The Filtering Module consists of four different filters (blower - aerosol fine - aerosol superfine - HEPA filters). The temperature of the FCS is acquired placing numerous thermometers all over the entire FCU as well as into CUORE cryostat. Three different kind of thermometers are used: Platinum PT-100, PT-1000 and Silicon Diode Thermometers DT-470.

The thermometer position has been studied in order to have a perfect reconstruction of the temperature gradient inside the entire FCS especially along the copper exchanger, the coldest part of the system. Moreover, for redundancy, more than one thermometer has been located in the same position; in this way, it is possible to have a crosscheck of the temperature as well as to have a more reliable monitoring system. Since different kind of thermometers have been used, different acquisition electronics needs to be used too. In fact, while for both PT-100 and PT-1000 a resistance measurement is used, for DT-470 a voltage measurement is required. Platinum thermometers are read by means of two Picowatt AVS47B, that is a resistance bridge for very low temperature. A developed dedicated software, using single calibration for each thermometer, makes the conversion from R to T. In the case of DT-470, thermometers are read by a Lakeshore 218 Temperature Monitor, which is an eight input temperature monitor that can be used with diode or resistive temperature sensors. The FCS injects helium only inside CUORE IVC, thus it is important to supervise the associated thermometry, mainly related to the He path from the entrance of the cryostat (at 300K plate level) down to the bottom of the 10mK plate, where the helium is released. In order to do that, several sensors have been carefully located along the He injection line inside CUORE cryostat. Furthermore, the pressure of CUORE IVC during the cool down is strictly dependent on the frequency and pressure of the Fast Cooling System. The IVC pressure is one of the crucial requirements to be satisfied, and its value needs to be within a specific range for two main reasons: the pressure needs to be always higher than atmospheric pressure in order to prevent air to enter the FCS and, consequently, the CUORE cryostat; however the pressure in the FCS circuit cannot exceed a threshold set by the IVC o-ring seal to avoid damages. This threshold has been evaluated equal to 1360 mbar. The He flowing temperature gradient is constantly kept below 40 K and the He pressure gradient

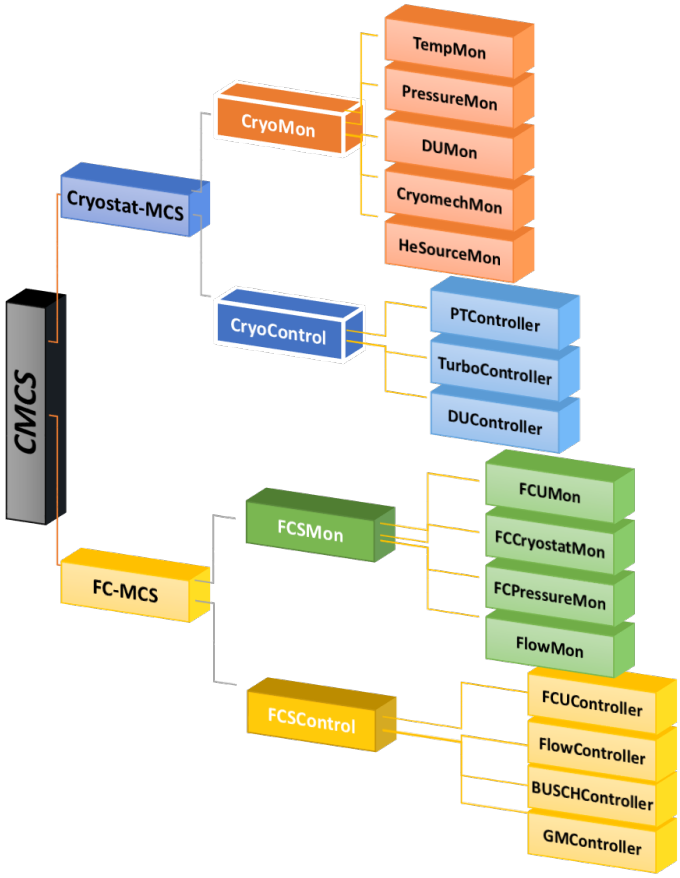

FIG. 5. CUORE Cryogeny Monitor and Control System and its sub-branches.

below 300 mbar. FCS is equipped with several pressure gauges in order to monitor the system behaviour and to have a feedback signal to use for the automatic refill of helium during the cool down process as well as releasing gas in case of dangerous overpressure.

During CUORE Commissioning Run 4, that started November 2015, we have been able to go from 300 K to 4 K in about 16 days.

The FCS development and commissioning is one of the responsibilities of the UNICLAM-LNGS Group (the LNGS Group from University of Cassino and Southern Lazio).

B. External Shield

The external shield is designed to screen the cryostat from environmental neutrons and γ's. Neutron thermalization and absorption is achieved by a borated polyethylene terephthalate (PET) floor and by lateral walls of PET followed by boric-acid powders, which are poured in plastic frames. The B-PET shield is followed by lead blocks. To ease its installation on the ground floor of the hut, the steel structure holding the shield was divided into three horizontal rings. The rings were produced by Comasud (Teramo, Italy) and delivered to LNGS. The installation of the shield was interleaved with commissioning activities at the ground floor of the CUORE building. The shield is presently completely installed and performed well during tests in Run4.

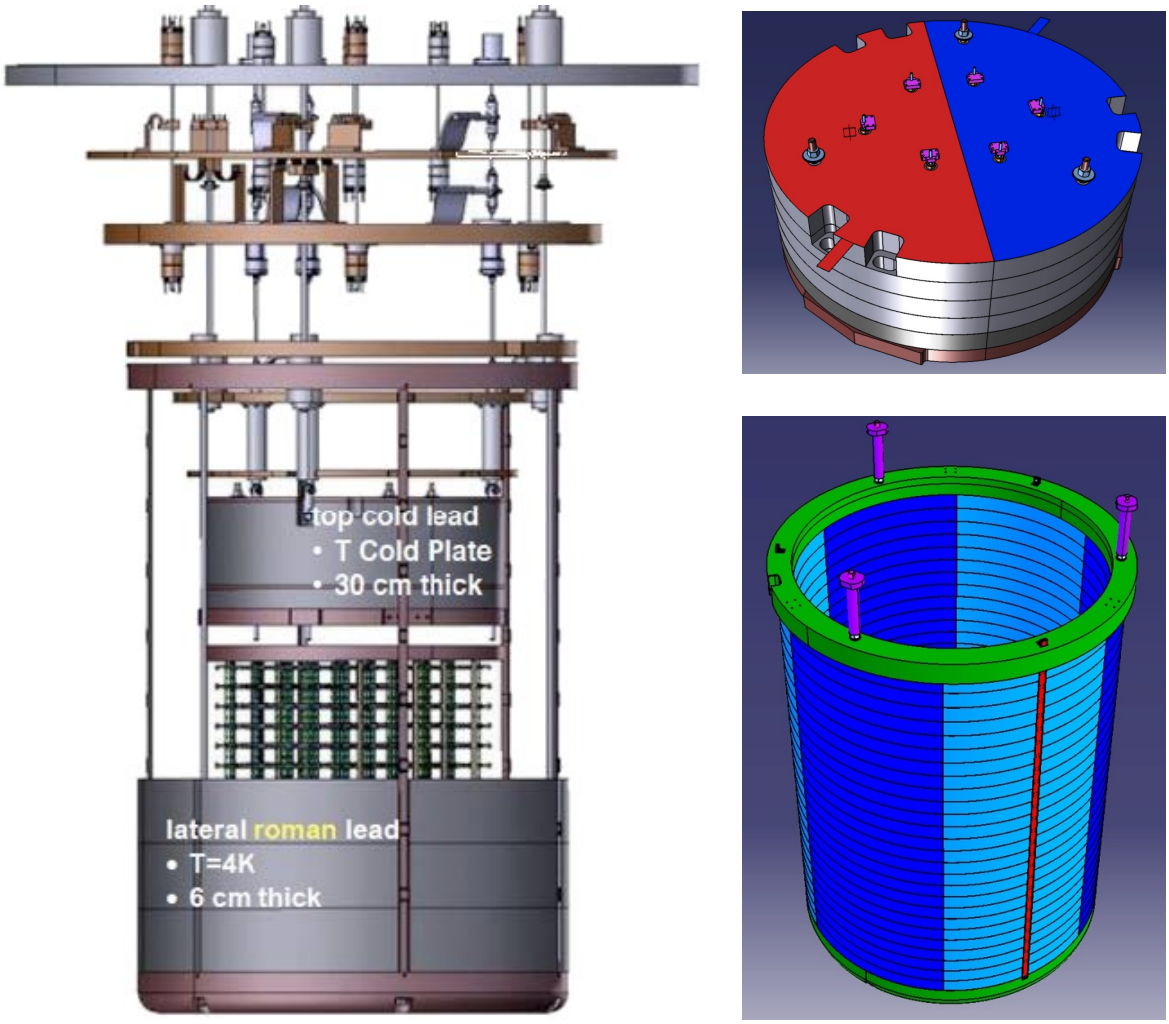

FIG. 6. General view of the CUORE cold lead shields (left) and schemes of the top and lateral sections (right).

C. Cold Lead shield

The cold lead shield of CUORE consists of two sections: A top disc (30 cm lead + 5 cm copper) and a lateral bottom-closed cylindrical structure (6 cm lead + copper structure). See Fig. 6. The top disc is built with modern lead and is maintained at ∼50 mK, while the lateral shield is built from ancient lead and is thermalized at 4 K.

1. Top lead disc

The ∼2 tons of modern lead for the top lead shield were melted at COMETA (Ardea, Italy) in 2014. The five layers (and the copper structure) were then assembled in a clean room at LNGS (above ground laboratory) in April 2015 and installed inside the CUORE cryostat in May 2015. (Fig. 2).

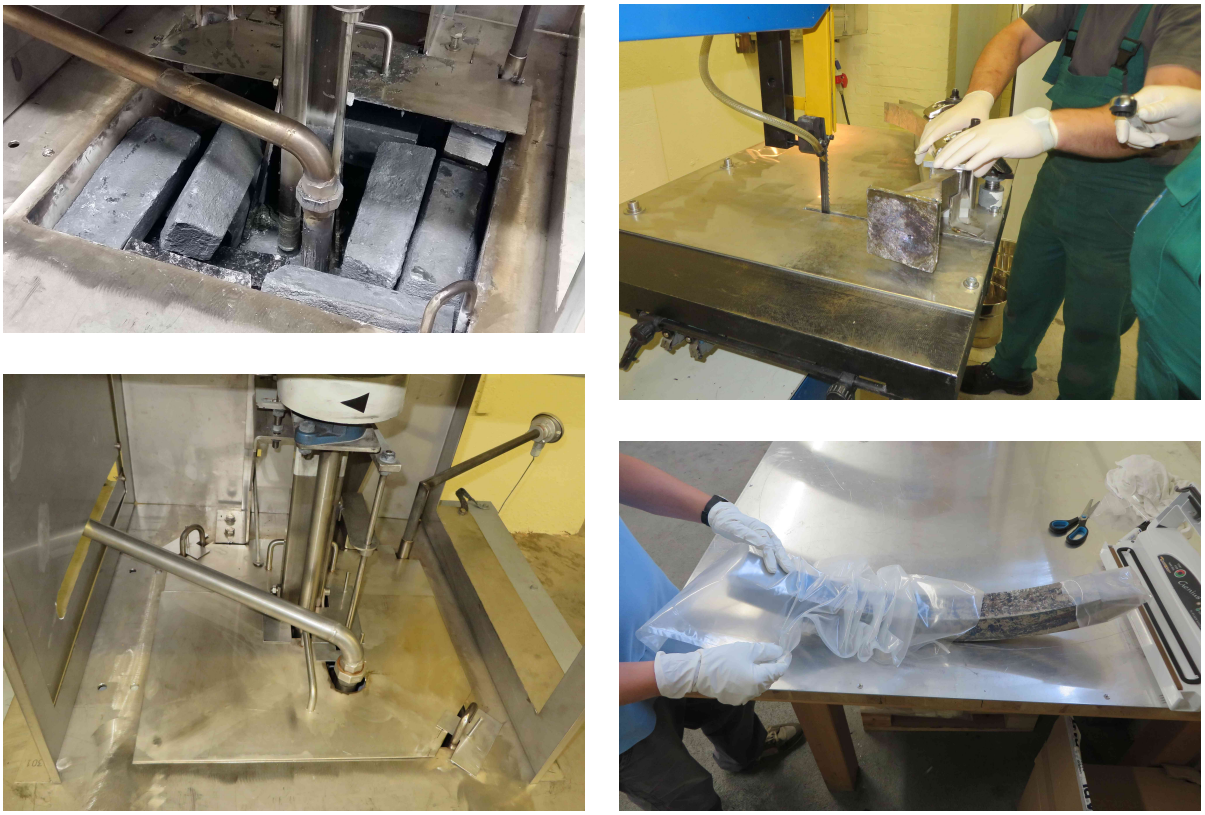

FIG. 7. Particular attention during the lateral shield production phase is paid to the cleanliness of the material. (Left) The kettle is completely closed and flushed with nitrogen gas when the lead is the molten phase. (Right) After the casting, the final pieces are handled only with powder-free nitrile gloves during the various operations.

2. Lateral shield production

Cleaning of the ancient lead with a cryo-blasting technique was completed close to LNGS in Spring 2015.

The casting of the parts from the ancient roman ingots took place between August and September 2015 at Metall-Technik Halsbrücke GmbH & Co. KG (MTH, Halsbrücke, Saxony, Germany).

Preliminary inspections were performed in July 2015 at the company by INFN personnel to select the materials and to define the procedures to be used during the casting in order to achieve adequate cleanliness. In particular, only stainless steel or aluminum tools and no other materiala (including any release agent for the detachment of the pieces from the mould) were allowed. This also applied to the kettle and the mould, which were new and made of stainless and aluminum, respectively. Furthermore, in order to prevent contamination from Rn, we continuously flushed nitrogen gas when the lead was in the molten phase. The O_2 level in the nitrogen atmosphere was required to be $\lesssim 2\%$. The casting was constantly monitored by two shifters from INFN.

The first two weeks of production were devoted to solve a number of problems with the mould design and to optimize the whole process. In its final version, in a fully productive day, 10 or more pieces could be casted. A total amount of 194 pieces were casted, enough for the lateral shield and some spare parts. These were sealed under vacuum and shiped to LNGS. The freshly casted roman lead parts for the lateral shield were delivered at LNGS and installed cryostat in

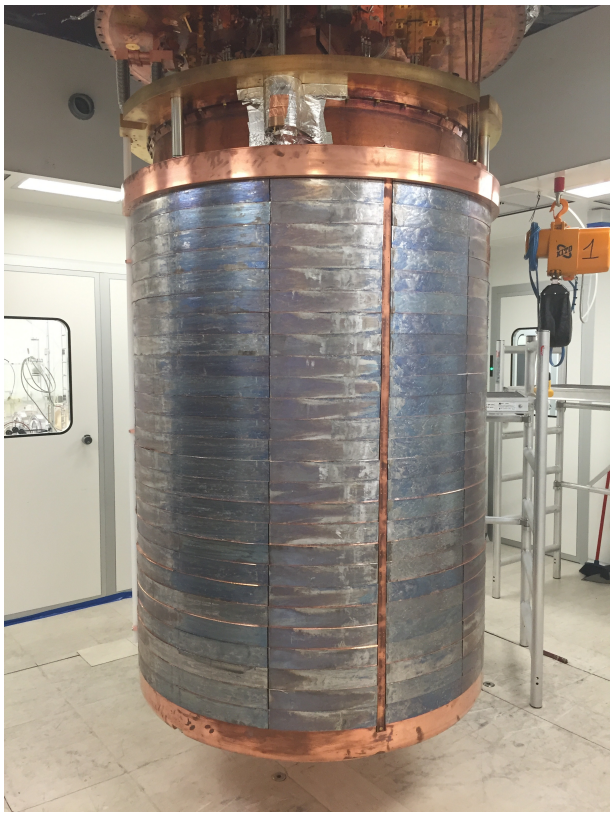

FIG. 8. The roman lead, cold lateral shield of CUORE suspended under the 600 mK plate of the cryostat.

October 2015

III. ELECTRONICS AND DATA ACQUISITION

The goal of the CUORE electronics is to provide an effective low-noise system for reading and monitoring CUORE detectors. It is interfaced to the CUORE data acquisition system (DAQ) which records the data and provides a link with the slow-control and data analysis tools.

A. Front-end electronics

During 2015 the Front-end electronics system was largely completed apart from a small number of components that await their final testing. The system was designed at INFN of Milano-Bicocca, the production was done at the University of South Carolina, testing and calibration were done both at the University of California at Los Angeles, and at INFN Milano-Bicocca. The system consists of several sections, namely:

- the connecting links between the detectors and the mixing chamber
- the connecting links between the mixing chamber and the room temperature connectors on the top of the cryostat
- the connections between the fridge connectors and the very front-end inputs

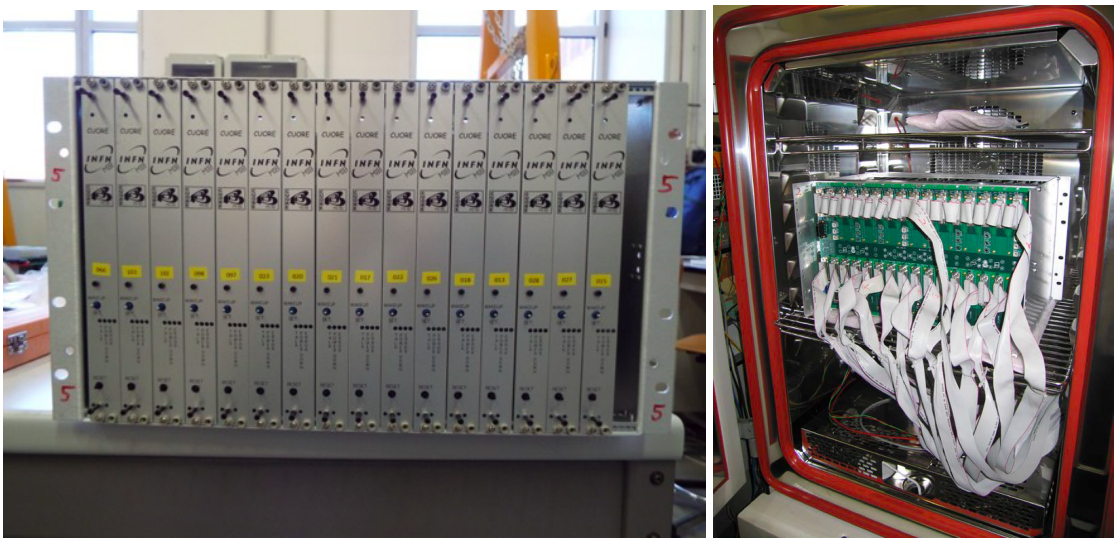

FIG. 9. One of the crates with the bessel filters (left) and the climatic chamber used for the front-end pre-installation tests (right).

- the preamplifiers
- the very front-end, located on the mainboards, on top of the fridge
- the antialising filters, close to the DAQ system

In addition to the components for extracting data from the detectors, a pulser/DC generator is used to correct gain instabilities. This device is a voltage source capable of generating pulses and DC signals with a very high stability, at the level of a ppm/ °C. The power supply to all these boards consists of a 3 stage system: AC/DC, DC/DC and the linear power regulator, several units are provided. All the listed parts are fully programmable and can also be monitored thanks to a series of 32-bit CISC ARM micro-controllers located on the boards themselves. Communication between the micro-controllers and the DAQ is through a CAN-bus interface on optical fibers. A series of additional secondary boards, such as backplanes and similar, have also been developed.

All the Front-end main boards, the Bessel filter boards, the Pulser boards and the power supply DCDC and linear regulators have been fabricated and tested. The full set of Bessel and Front-end boards boards have been pre-installed in racks in Milan and delivered to LNGS (Fig. 9). Presently, only a small number of the pulser boards are still undergoing the pre-installation tests.

B. Faraday cage

The Faraday Cage is needed to shield the high-impedance signal links between the detectors and the front-end electronics from disturbances coming from the main power line (50 Hz), cryogenic pumps and all other EMI interferences which may be injected from the outside. Located on the second floor of the CUORE building, the cage will exploit the existing vertical beams (building steel work) as mechanical support. The current design consists of a room 6x6 m^2 wide, 2.5 m tall, made of panels chosen for their shielding properties and supported by aluminum and

steel profiles. The interfaces between panels were optimized with simulations. The shielding panels (Skudal S3022 by Selite) and the profiles were purchased. At the time of writing all the hardware needed to mount the Faraday cage is ready and stored at LNGS and installation has started.

C. Data acquisition system

We have completed procurement of all the hardware for the CUORE data acquisition system. It is composed of 64 NI-PXI-6284 digitizer boards, for a total of 1024 analog input channels. The digitizer boards are hosted in six PXI chassis that are mounted in two rack cabinets (3 chassis each). These two cabinets also contain the DAQ-Bessel interface boards. A third rack cabinet hosts the six computers dedicated to the data readout (one per chassis) and the event builder computer. The three DAQ rack cabinets were pre-installed in Genova, and were delivered to LNGS in summer 2015. They are currently hosted in the LNGS computing room, and will be placed on the second floor of the CUORE hut once the CUORE faraday room installation is complete.

D. Readout system for the commissioning of the CUORE cryostat

A complete readout system for the commissioning of the CUORE cryostat was installed in the second floor of the CUORE hut in December 2014. This was a very good occasion to test the Electronics and the DAQ systems, as we installed a full readout system, although a version with a reduced number of channels. We have achieved several milestones: system layout, pre-installation, installation, working condition, detector characterization and signal acquisition. The readout system, featuring a total of 78 readout channels, consists of:

- A set of 6 cryostat to very front-end cables: the bolometers and the NTD thermometers can be connected on several output ports.
- One complete very front-end chassis hosting 13 complete boards (78 channels) and its linear power supplies.
- One chassis hosting 7 CUORE Bessel filter boards, 84 channels.
- Three calibration CUORE pulser board, with 4 pulser channels.
- A complete USB to CANBUS communication system between the DAQ and every board for slow control. A set of, specially developed, glue boards were fabricated to convert the electrical digital signals to optical signals for fiber transmission.
- A supply chain consisting of an ACDC followed by DCDC and a filter to supply the linear power supply.
- A commercial power supply with +/-30 V output range, used as voltage reference for the bolometers bias. This device makes it possible to measure the characteristic I-V curve of the NTD sensors over a wide range of bias currents.
- One chassis with 5 digitizer boards, 80 channels total.
- One chassis hosting 4 DAQ-Bessel interface boards, 96 channels total.

The DAQ, Bessel, and DAQ-Bessel interface chassis were hosted in a rack cabinet, that also hosted a power distribution unit. The front end and pulser boards were placed on top of the CUORE cryostat support structure, as close as possible to the 300 K flange. The signal connection between the front end and the Bessel boards, and between the Bessel boards and the DAQ-Bessel interface boards, was made of commercial DB-25 shielded cables. The signal connection between the DAQ-Bessel interface boards and the DAQ boards was made with commercial NI-SHC68 shielded cables. The CUORE data acquisition and electronics control software was hosted on a dedicated computer. The data transmission between the DAQ chassis and computer was provided by a commercial optical link (NI-PCI-PXI-8336).

The installed readout system was successfully used during the commissioning tests of the CUORE cryostat (Run2, Run3, and Run4). The oppportunity to test the CUORE electronics for the readout of real bolometric detectors in the MiniTower was very valuable. A lot of useful information was obtained, the basic functionality of all the components were successfully verified, and the few minor bugs in software and firmware that were identified have been solved.

IV. SLOW CONTROL AND SLOW MONITOR SYSTEM

This system features a low-level data-acquisition and control interface, a high-level system for organizing and displaying the data in a web-accessible interface and a Nagios system for monitoring.

A. CUORE-Cryogeny Monitor and Control System (CMCS)

The CUORE-Cryogeny Monitor and Control System (CMCS)is a LabVIEW-based software package developed by the UNICLAM-LNGS Group (the LNGS Group from University of Cassino and Southern Lazio). It provides slow control of the whole CUORE Cryogenic System, including monitor and control of the apparatus related to CUORE Cryostat interfacing with all the instrumentation with their different protocols; it performs online analysis of relevant variables and generates time-ordered data files for offline analysis and input to the high-level web interfaces. The tool consists of several monitor/control interfaces, each of them focused either on a particular physical variable (i.e. pressure, temperature) or on a cooling system (i.e. PT, FCS), divided as shown in Fig.5. An example of the interface we developed is shown in Fig.10(a)

B. Fast Cooling Monitor and Control System

The Fast Cooling Monitor and Control System (FC-MCS) is the branch of the CUORE Cryogeny Monitor and Control System (CMCS) dedicated to the Fast Cooling System. It is in charge to supervise the FCS activities during the entire cool down process, controlling the cooling performances in order to match temperature and pressure requirements. It is divided in two sub-branches: Fast Cooling System Monitor (FCSMon); Fast Cooling System Control (FCSControl);

The temperature of the FCU parts, as well as the FCS injection into the CUORE IVC, need to be continuously monitored and kept in a specific range. Because of this, a CUORE Fast Cooling Unit Monitor Panel and the CUORE Fast Cooling System and Cryostat Temperature Monitor have been developed; they allow monitoring the temperature values of all the thermometers related to the FCU, the high side and low side pressure in the He circuit, their time

evolution plots and a global view of the temperature of both FCS injection parts and the involved CUORE cryostat parts. One of the main developed features gives the cooling speed plot for each monitored thermometer. Once the status and value of all the needed variables of the FCS has been acquired by the monitoring branch of the FC-MCS, it is crucial to have a control branch that acts on the system in order to match the cooling requirements. This is the target of the Fast Cooling System Control (FCSControl). The main control interface, called the Fast Cooling System Control Panel, is depicted in Fig.10(b). It contains all the crucial information to make the FCS work properly. On top-left corner, the Fast Cooling Global Alarm System interface can be seen. An automatic algorithm, acting on a mass flow meter and a solenoid valve, has been developed and tested to keep the pressure within a well defined range.

C. Slow Monitor Database and Interface

The MIT group is developing the high level interfaces for convenient monitoring of the slow control data (Slow Monitoring). This year the Slow Monitoring data pipeline and interface website have been significantly upgraded with improved data collection, organization, and display interfaces. We collect data from the CMCS onto a single server, where it is organized in a MongoDB database. We installed the new server this year and configured the network so that it can securely communicate with the system acquiring sensor data and share this data through a password protected publicly-accessible website.

We developed new software for the Slow Monitoring interface webpage. On this page, each of several diagnostic plots updates every 10 seconds. The plots are a curated selection of the most relevant variables to show the state of cryostat state.

We developed an interactive plotting interface through which users can plot any parameter in the Slow Monitoring database in their browser. The parameters are displayed in two ways, both as a list separated into sub-systems and as a series of images with dots at the location of the devices. The page grants access to view all cryostat thermometry data except the NTDs. It includes position and temperature data from the calibration system, state parameters of the pulse tubes, the radon abatement system, and the dilution unit. These website has been tested and revised with user feedback during cryostat cooldowns and test runs this year.

Furthermore we begun developing an active alarm system that alerts users when parameters go outside a specified range. This year, we developed the software for interfacing with the database and displaying triggered alarms on the website. In early 2016, we completed a user

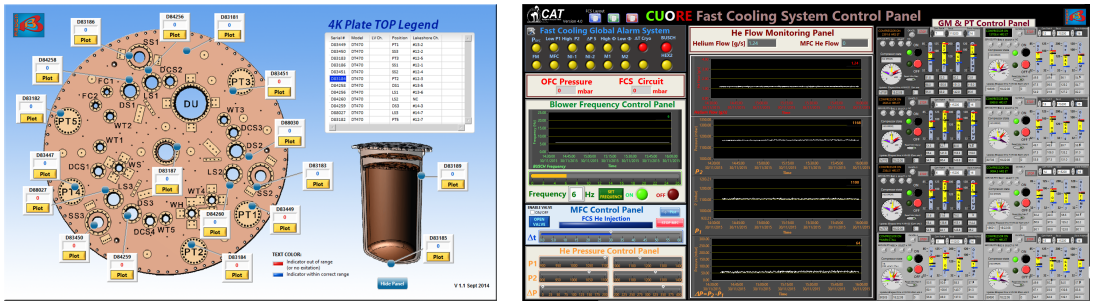

(a) (b)

FIG. 10. CUORE Cryogeny Monitor and Control System: Temperature Monitor Interface (a); Fast Cooling System Control Panel (b).

interface that allows website users to set alarms through the website (instead of logging onto the server directly), and the system for emailing users when alarms trigger.

D. Nagios Monitor

The Bologna group has setup a Nagios monitoring system onsite to ensure that the whole system runs smoothly. Nagios is an open-source tool that enables remote monitoring of services (ssh, http, tcp/udp ports, ping...), resources (CPU load, disk space, memory, swap, single processes...) and network devices (host, switch, routers...). It is used within the slow-control system to monitor all vital processes are running and that the vital network connections are active. Nagios runs inside the CUORE internal network and pushes the information collected there to an external instance that can be reached from the internet. The status of monitored systems is shown on a web page.

V. DETECTOR INSTALLATION

Installation of the 19 towers in the cryogenic system is a very challenging and high-risk operation. One must avoid damaging the delicate components and avoid contaminating the ultra-radiopure detector materials. During this year we have invested significant effort in developing and testing the procedures for detector installation in the cryostat. In September 2015 we conducted a very positive external review of the installation plan.

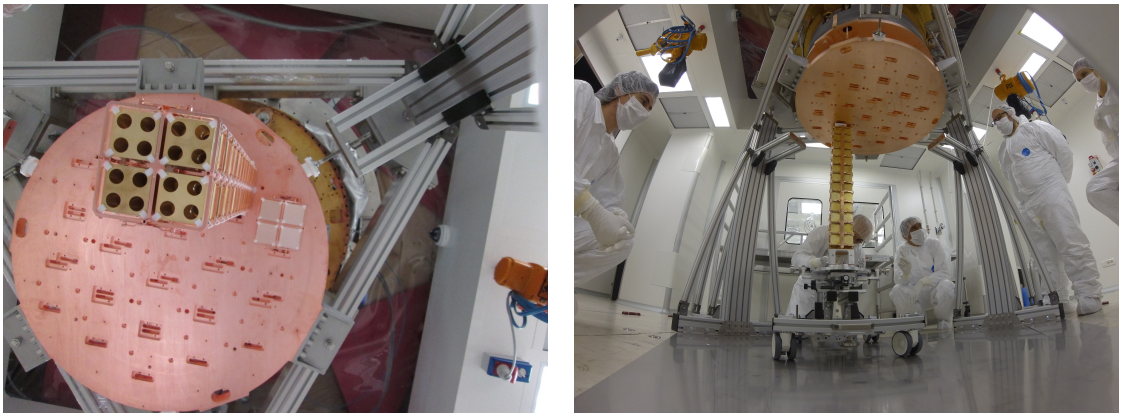

(a) (b)

FIG. 11. (a) TSP fixed with the DIT, with mockup tower installed. (b) A moment during the mock-up tower installation, with the DIT installed and the DIC to position the tower.

The installation will take place in a dedicated environment, called Clean Room 6 (CR6), installed inside the CUORE Clean Room. The CR6 volume will contain the lower part of the CUORE cryostat, and the Tower Support Plate (TSP) to which the towers will be mechanically attached. CR6 is an acrylic-walled room whose atmosphere will be provided by a radon-free ventilation system. The radon level in the CR6 exhaust is constantly monitored by the Gerda experiment radon monitor, as well as many other critical parameters like oxygen and humidity levels and temperature. Monitoring systems have been developed in 2015. The installation operations will be performed by three people (one physicist and two engineers/technicians) from the so called "Installation Team" working inside the CR6. Except for the time required to install

a tower, the previously installed towers and the whole TSP will be enveloped in an acrylic bag flushed with nitrogen.

Two particularly complex tools have been developed for the installation: the Detector Installation Tool (DIT, Fig. 11(a)) and the Detector Installation Cart (DIC). The DIT is a tripod-like structure that holds the TSP in a fixed position. The DIC is a specially designed cart that will be used to safely and cleanly move the tower from the storage area and put it precisely in the installation position under the TSP in CR6. The DIC cart also hosts a number of accessories that will be used during the installation, for example a support for the long wire strips that will be connected to the cryostat readout cabling when the tower is installed.

All the tools and procedures have been extensively and successfully tested with a mock-up tower, i.e. an array of dummy crystals identical to a real tower both from the mechanical and electrical point of view, including bonding wires(Fig. 11(b)).

The same mock-up will be used for a final testing session before the real installation campaign once CR6 and the ancillary systems have been installed.

VI. CUORE-0

CUORE-0 was the first tower produced using the CUORE assembly line. We operated it as a standalone detector from March 2013 to March 2015 in Hall A of LNGS, using the same cryostat that previously hosted Cuoricino. In March this year we concluded data-taking once the sensitivity of Cuoricino had been surpassed. Afterwards, we performed a number of technical measurements in view of CUORE (i.e. special calibrations, new trigger algorithms, studied bolometric performance). We decommissioned the detector in November 2015.

A. Data taking and detector performance

The *physics data* for the search of $\beta\beta(0\nu)$ were collected in two campaigns which ran from March 2013 to August 2013 and from November 2013 to March 2015, for a total TeO_2 exposure of 35.2 kg·yr or 9.8 kg·yr of ^{130}Te considering the isotopic abundance, 34.167%. The duty cycle of the CUORE-0 detector was 78.6% overall, with a total *physics data* livetime of 64.1%.

We evaluated energy resolution using calibration data collected while the detector was exposed to a thoriated tungsten wire source. In this way we calibrated each bolometer using the known gamma lines from ^{232}Th chain. We used the high-statistics 2615 keV ^{208}Tl line to establish the detector response to a monoenergetic deposit near the ROI. Figure 12 shows the unbinned extended Maximum Likelihood (UEML) fit to the calibration data. In addition to a double-gaussian lineshape for each bolometer-dataset, the fit function includes terms to model a multiscatter Compton continuum, a ∼30 keV Te X-ray escape peak, and a continuum background. The FWHM of the projected fit is 4.8 keV. This demonstrates that the CUORE goal of 5 keV can be reached.

We also evaluated the continuum event rate between 2700 keV and 3900 keV, to estimate the surface-alpha background reduction. We measured this to be 0.016 ±0.001 c/keV/kg/yr, a ∼ 7 fold reduction relative to Cuoricino. Based on Monte Carlo simulations, considering the reduced surface-background and the radiopurity of materials selected for the new CUORE cryostat, we conclude that the target ROI background level for CUORE, 0.01 c/keV/kg/yr, can be achieved.

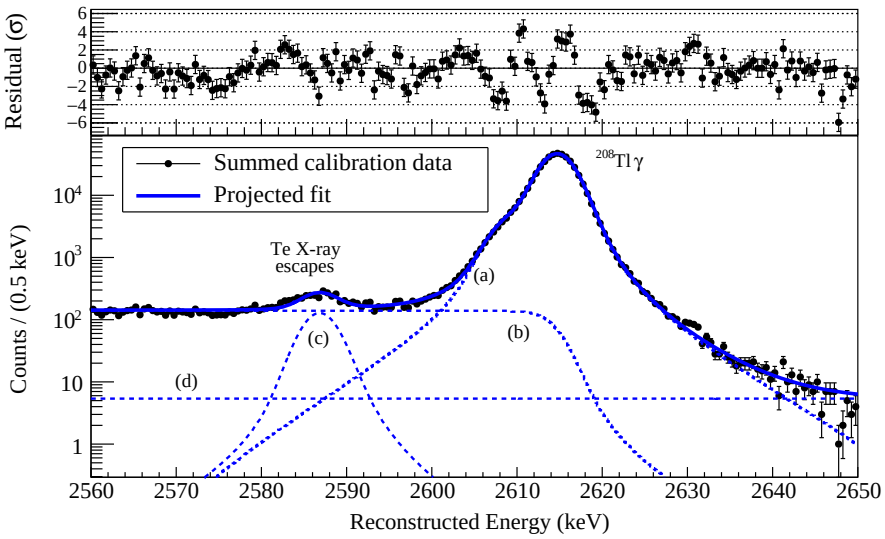

FIG. 12. Bottom: Calibration data in the region around the 2615 keV 208Tl γ-ray line, integrated over all bolometer in the entire statistic. The blue line is the projection of the UEML fit to data. Top: Normalized residuals of the data and the best-fit model.

B. Result on the search for ^{130}Te $\beta\beta(0\nu)$

Throughout the data analysis, we blinded the ROI (between 2470 keV and 2570 keV) using a form of data salting (we randomly exchanged a blinded fraction of events within $\pm$10 keV of the 2615 keV γ line with events within $\pm$10 keV of the Q-value). This blinding algorithm produced an artificially large fake peak around the Q-value. After fixing all the selection cuts and analysis procedures we unblinded the data in the ROI at the end of February 2015.

In the final dataset the ROI contains 233 candidate events from a total ^{130}Te exposure of 9.8 kg·y. We determined the yield of $\beta\beta(0\nu)$ decay events from a simultaneous UEML fit in the energy region 2470–2570 keV (Fig. 13). The fit has three components: a posited signal peak at $Q_{\beta\beta}$, a peak at $\sim$2507 keV from ^{60}Co double-gammas, and a smooth continuum background attributed to multiscatter Compton events from ^{208}Tl and surface decays. We model both peaks using the lineshape established with the study of the 2615 keV ^{208}Tl in calibration runs. The $\beta\beta(0\nu)$ decay rate is treated as a global free parameter.

The result of the UEML fit is shown in Fig. 13. The best-fit value for the $\beta\beta(0\nu)$ decay rate is $\Gamma_{0\nu} = 0.01 \pm 0.12\,(\text{stat.}) \pm 0.01\,(\text{syst.}) \times 10^{-24}\text{yr}^{-1}$, the background index in the ROI is $0.058 \pm 0.004\,(\text{stat.}) \pm 0.002\,(\text{syst.})$ c/keV/kg/yr.

We find no evidence for $0\nu\beta\beta$ of ^{130}Te and set a 90% C.L. Bayesian upper limit on the decay rate using a uniform prior distribution ($\pi(\Gamma_{0\nu}) = 1$ for $\Gamma_{0\nu} >= 0$) at $\Gamma_{0\nu} < 0.25 \times 10^{-24}\,\text{yr}^{-1}$ or $T_{0\nu}^{1/2} > 2.7{\times}10^{24}$ yr (statistical uncertainties only). Including the systematic uncertainties (due to modelling of the lineshape, the calibration uncertainties, the parametrization of the background in the ROI and the UEML fit) the 90% C.L. limits are $\Gamma_{0\nu} < 0.26 \times 10^{-24}\,\text{yr}^{-1}$ or $T_{0\nu}^{1/2} > 2.7 \times 10^{24}$ yr.

We combine our data with Cuoricino (19.75 kg·yr exposure of ^{130}Te). The combined 90% C.L. limit is $T_{1/2}^{0\nu} > 4.0 \times 10^{24}$ yr which is the most stringent limit to date on this quantity. Using different NME models, we interpret our combined Bayesian half-life result as a limit on the effective Majorana neutrino mass: $m_{\beta\beta} < 270 - 650$ meV.

The results of this analysis were published in PRL in September 2015. A more detailed paper

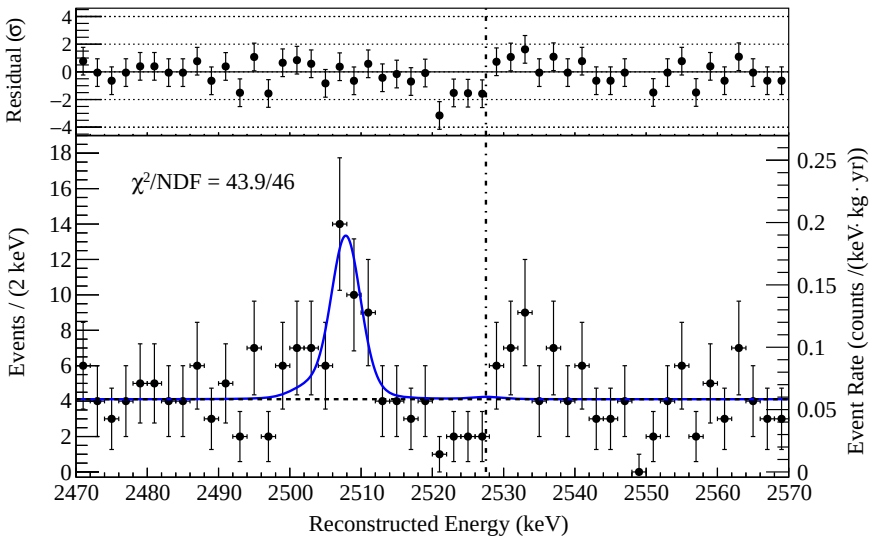

FIG. 13. Bottom: The best-fit model from the UEML fit (solid blue line) overlaid on the spectrum of $0\nu\beta\beta$ decay candidates in CUORE-0 (data points); The peak at ∼2507 keV is attributed to ^{60}Co; the dotted black line shows the continuum background component of the best-fit model. Top: The normalized residuals of the best-fit model and the binned data. The vertical dot-dashed black line indicates the position of $Q_{\beta\beta}$.

describing the analysis techniques used in CUORE-0 has recently been accepted by PRC. An instrumentation paper describing the design, operation and performance of CUORE-0 and a paper detailing a measurement of the $2\nu\beta\beta$ decay half-life of ^{130}Te are in preparation.

VII. PUBLICATIONS IN 2015

1. K. Alfonso *et al.*, "Search for Neutrinoless Double-Beta Decay of ^{130}Te with CUORE-0", Phys. Rev. Lett **115** 102502 (2015)

2. K. Alfonso *et al.*, "Analysis Techniques for the Evaluation of the Neutrinoless Double-Beta Decay Lifetime in ^{130}Te with CUORE-0", http://arxiv.org/abs/1601.01334, accepted to Phys. Rev. C

DAMA

Collaboration:

P. Belli[a], R. Bernabei[a,@], A. Bussolotti[a,*], A. Di Marco[a], F. Montecchia[a], A. d'Angelo[b], A. Incicchitti[b], A. Mattei[b,*], V.M. Mokina[b,c], O.G. Polischuk[b,c], F. Cappella[d], R. Cerulli[d], V. Caracciolo[d], C.J. Dai[e], H.L. He[e], H.H. Kuang[e], X.H. Ma[e], X.D. Sheng[e], R.G. Wang[e], Z.P. Ye[e,f]

in some detector developments, by-product results and small scale experiments:

A. Addazi[g,d], A.S. Barabash[h], Z. Berezhiani[g,d], R.S. Boiko[c], V.B. Brudanin[i], D.M. Chernyak[c], F.A. Danevich[c], V.Yu. Denisov[c], O.V. Hladkovska[c], D.V. Kasperovych[c], V.V. Kobychev[c], S.I. Konovalov[h], G.P. Kovtun[j], N.G. Kovtun[j], B.N. Kropivyansky[c], M. Laubenstein[d], S. Nisi[d], D.V. Poda[c], A.P. Shcherban[j], V.N. Shlegel[k], V.I. Tretyak[c], I.A. Tupitsyna[l], V.I. Umatov[h], Ya.V. Vasiliev[k], I.M. Vyshnevskyi[c],

in some studies on $\beta^+\beta^+$, EC/β^+, EC/EC decay modes (under the joint Indo-Italian DST-MAE project and inter-universities agreement):

P.K. Raina[m], A.K. Singh[n], P.K. Rath[o], S. Ghorui[m], Soumik Das[m,n]

[a]Dep. Phys., Univ. Roma "Tor Vergata" and INFN Tor Vergata, 00133 Roma, Italy.
[b]Dep. Phys., Univ. Roma "La Sapienza" and INFN-Roma, 00185 Roma, Italy.
[c]Institute for Nuclear Research, MSP 03680, Kiev, Ukraine.
[d]Laboratorio Nazionale del Gran Sasso, INFN, 67010 Assergi (Aq), Italy.
[e]IHEP, Chinese Academy of Sciences, P.O. Box 918/3, Beijing 100049, China.
[f]Dep. Phys., Jinggangshan University 343009, Jiangxi, China.
[g]Dep. Phys., Univ. L'Aquila, 67100 Coppito, AQ, Italy
[h]Institute of Theoretical and Experimental Physics, 117259 Moscow, Russia
[i]Joint Institute for Nuclear Research, 141980 Dubna, Russia.
[j]Nat. Science Center Kharkiv Institute of Physics and Technology, Kharkiv, Ukraine.
[k]Nikolaev Institute of Inorganic Chemistry, 630090 Novosibirsk, Russia.
[l]Institute for Scintillation Materials, 61001 Kharkiv, Ukraine.
[m]Indian Institute of Technology Ropar, Ropar, India.
[n]Indian Institute of Technology, Kharagpur, India.
[o]University of Lucknow, Lucknow IN-220628, India
[@] Spokesperson; [*] technical staff

Abstract

DAMA is as an observatory for rare processes located deep underground at the Gran Sasso National Laboratory of the I.N.F.N. (LNGS); it develops and exploits low background scintillators. In 2015 the main experimental activities have been performed with: i) the second

generation DAMA/LIBRA set-up (sensitive mass: $\simeq$ 250 kg highly radiopure NaI(Tl)), upgraded so far in 2008, 2010 and at the end of 2012; ii) the DAMA/LXe set-up (sensitive mass: $\simeq$ 6.5 kg liquid Kr-free Xenon enriched either in ^{129}Xe or in ^{136}Xe); iii) the DAMA/R&D set-up (a facility dedicated to perform relatively small scale experiments, mainly investigating double beta decay modes in various isotopes); iv) the DAMA/Ge set-up (mainly dedicated to sample measurements and to specific measurements on rare processes); some activities are also performed with the detectors Ge-Multi, GeCris and the recently-installed Broad Energy Germanium detector of the STELLA facility; v) a small set-up (named DAMA/CRYS) for prototype tests and detectors' qualification. The main DAMA activities during 2015 are summarized in the following.

1 DAMA/LIBRA

DAMA/LIBRA (Large sodium Iodide Bulk for Rare processes) is a unique apparatus for its sensitive mass, target material, intrinsic radio-purity, methodological approach and all the controls performed on the experimental parameters (see Ref. [1, 2, 3, 4, 5, 6, 7, 8, 9, 10, 11, 12, 13] an the 2015 publication list). It is the successor of DAMA/NaI [14, 15, 16, 17, 18, 19, 20, 21, 22, 23, 24, 25, 26], with a higher exposed mass, higher duty cycle and increased sensitivity. The main goal of DAMA/LIBRA is the investigation of the Dark Matter (DM) particles in the galactic halo by exploiting the DM model independent annual modulation signature [27, 28].

The granularity of the apparatus (25 detectors in a matrix 5×5) is an important feature to study Dark Matter and for background identification since Dark Matter particles can just contribute to events where only one of the 25 detectors fires (*single-hit* events) and not to whose where more than one detector fire in coincidence (*multiple-hit* events). The apparatus has also the unique feature (as well as DAMA/NaI) that gamma calibrations are regularly performed down to the software energy threshold in the same conditions as the production runs, without any contact with the environment and without switching-off the electronics. The high light yield and other response features have allowed working in a safe and reliable way down to 2 keV (DAMA/LIBRA- phase1). At the end of 2010 new photomultipliers (PMTs) with higher quantum efficiency [6] have been installed, some other optimizations have been done and the data taking of DAMA/LIBRA-phase2 then started. Among the scientific goals of this set-up we also recall here: i) investigation with high sensitivity of the DM particle component in the galactic halo by the model independent approach known as DM annual modulation signature, with highly precise determination of the modulation parameters (which carry crucial information); ii) corollary investigations on the nature of the candidate and on the many possible astrophysical, nuclear and particle physics scenarios; iii) investigations on other possible model dependent and/or model independent approaches to study Dark Matter particles, second order effects and some exotic scenarios; iv) improved search for processes of Pauli exclusion principle violation in ^{23}Na and ^{127}I; v) search for possible electric charge non-conservation (CNC) processes, as the electron decay into invisible channels and in the $e^- \to \nu_e + \gamma$ channel, and excitations of nuclear levels of ^{23}Na and ^{127}I after CNC electronic capture, ... ; vi) search for possible nucleon, di-nucleon and tri-nucleon decay into invisible channels in ^{23}Na and ^{127}I; vii) search for solar axions by Primakoff effect in NaI(Tl); viii) search for nuclear rare decays in ^{23}Na, ^{127}I and Tl isotopes (as e.g. superdense states, cluster decay, ...); ix) search for neutral particles (QED new phase) in ^{241}Am decays, etc.

Most of these investigations require further dedicated data taking and high exposure to reach more competitive sensitivities. As regards the DM features, which can be suitably exploited further collecting very large exposure, see e.g. the Sect 6 of Ref. [19] and the Appendix of Ref. [2]. In particular, the latter shows how the decreasing of the software energy threshold as in

the present DAMA/LIBRA-phase2 offers the unique possibility to investigate the modulation amplitude at the lowest energy, where a discrimination power can disentangle among many of the possible DM scenarios.

1.1 Final model-independent result of DAMA/LIBRA-phase1 on DM annual modulation

The results obtained with the total exposure of 1.04 ton × yr collected by DAMA/LIBRA-phase1 during 7 annual cycles have been presented at international conferences and the paper on the final model independent result of DAMA/LIBRA-phase1 was published [4].

Fig. 1 shows the time behaviour of the experimental residual rates of the *single-hit* scintillation events in the (2–6) keV energy interval for the complete DAMA/LIBRA–phase1. The residuals of the DAMA/NaI data (0.29 ton × yr) are given in Refs. [2, 18, 19].

In general it is worth noting that rejection strategies cannot safely be applied to the data when a model-independent signature based on the correlation of the measured experimental rate with the Earth galactic motion is pursued; in fact, the effect searched for (which is typically at level of some %) would be largely affected by the uncertainties associated to the applied procedure. On the other hand, the signature itself acts as an effective background rejection [28].

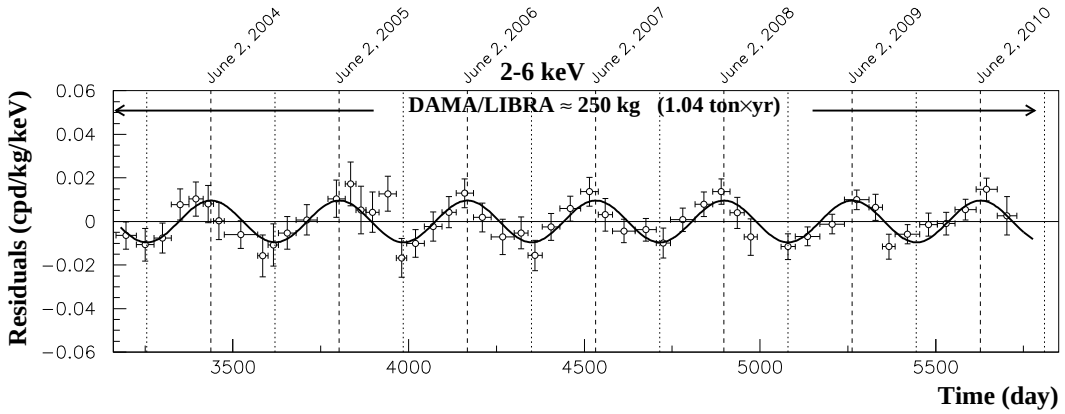

Figure 1: Experimental residual rate of the *single-hit* scintillation events measured by DAMA/LIBRA–phase1 in the (2–6) keV energy interval as a function of the time. The time scale is maintained the same of the previous DAMA papers for coherence. The data points present the experimental errors as vertical bars and the associated time bin width as horizontal bars. The superimposed curve is the cosinusoidal function behaviour $A\cos\omega(t-t_0)$ with a period $T=\frac{2\pi}{\omega}=1$ yr, a phase $t_0=152.5$ day (June 2^{nd}) and modulation amplitude, A, equal to the central value obtained by best fit on the data points of the entire DAMA/LIBRA–phase1. The dashed vertical lines correspond to the maximum expected for the DM signal (June 2^{nd}), while the dotted vertical lines correspond to the minimum.

The DAMA/LIBRA-phase1 data give evidence for the presence of DM particles in the galactic halo, on the basis of the exploited model independent DM annual modulation signature by using highly radio-pure NaI(Tl) target, at 7.5 σ C.L.. Including also the first generation DAMA/NaI experiment (cumulative exposure 1.33 ton × yr, corresponding to 14 annual cycles), the C.L. is 9.3 σ. At present status of technology the DM annual modulation is the only model independent signature available in direct dark matter investigation that can be effectively exploited. All the many specific requirements of the signature are fulfilled by the data and no systematic or side reaction able to mimic the exploited DM signature is available (see

e.g. Refs.[2, 3, 4, 17, 18, 19, 29, 30, 31, 32, 33, 34, 7, 8, 13] and the 2015 publication list). In particular, only systematic effects or side reactions simultaneously able to fulfil all the specific requirements of the DM annual modulation signature and to account for the whole observed modulation amplitude could mimic this signature; thus, no other effect investigated so far in the field of rare processes offers a so stringent and unambiguous signature.

Studies on other DM features, second order effects, and several other rare processes are in progress with the aim to reach very high sensitivity. Studies for measurements with data taking dedicated to other rare processes are continuing.

The DAMA obtained model independent evidence is compatible with a wide set of scenarios regarding the nature of the DM candidate and related astrophysical, nuclear and particle Physics. For example, some of the scenarios available in literature and the different parameters are discussed in Refs. [18, 19, 15, 20, 21, 22, 23, 24, 25, 5, 35, 36], in Appendix A of Ref. [2], and in the 2015 publication list. A further large literature is available on the topics; many possibilities are open.

No other experiment exists, whose result – at least in principle – can directly be compared in a model independent way with those by DAMA/NaI and DAMA/LIBRA. In particular, all the results presented so far in the field are not in conflict with the model independent DM annual modulation result of DAMA in many scenarios, also considering the large uncertainties in theoretical and experimental aspects, the same holds for indirect approaches; see e.g. some arguments in 2015 publication list and quoted references.

1.2 Activities of DAMA/LIBRA during 2015

- During 2015 DAMA/LIBRA has continued to take data in the new phase2 configuration with the PMTs of higher quantum efficiency [6] and new preamplifiers.

- In Summer 2015 DAMA/LIBRA-phase2 has concluded the data taking of the 4th full annual cycle, and started the data taking of the 5th cycle.

- Designs for the developments of some other new electronic modules were realized for further implementation of the apparatus for low energy studies.

- A paper has been published (see Sect. 1.2.1), which examines the model-independent annual modulation result obtained by DAMA/NaI and DAMA/LIBRA–phase1 in terms of asymmetric mirror DM, assuming that dark atoms interact with target nuclei in the detector via kinetic mixing between mirror and ordinary photons, both being massless. The relevant ranges for the kinetic mixing parameter are obtained taking into account various existing uncertainties in nuclear and particle physics quantities as well as characteristic density and velocity distributions of dark matter in different halo models.

- A paper has been published (see Sect. 1.2.2) about the analysis of the model-independent annual modulation result in terms of an effect expected in case of DM candidates inducing nuclear recoils and having high cross-section with ordinary matter, which implies low DM local density in order to fulfill the DAMA/LIBRA DM annual modulation results. This effect is due to the different Earth depths crossed by those DM candidates during the sidereal day.

- Studies for feasibility towards the DAMA/LIBRA-phase3 with the aim to further enhance the sensitivity of the experiment by improving the light collection of the detectors are in progress.

- Other studies on other DM features, second order effects, and several other rare processes are in progress with the aim to reach very high sensitivity thanks to the progressive increasing of the exposure.

- Studies for further measurements with dedicated data taking to investigate other rare processes are continuing.

1.2.1 DAMA annual modulation effect and asymmetric mirror matter

The model independent annual modulation effect observed by the DAMA experiments has also been investigated in terms of a mirror-type dark matter candidates in some given scenarios (see the 2015 publication list).

In the framework of asymmetric mirror matter, the DM originates from hidden (or shadow) gauge sectors which have particles and interaction content similar to that of ordinary particles. In the asymmetric mirror matter considered scheme, it is assumed that the mirror parity is spontaneously broken and the electroweak symmetry breaking scale v' in the mirror sector is much larger than that in the Standard Model, $v = 174$ GeV. In this case, the mirror world becomes a heavier and deformed copy of our world, with mirror particle masses scaled in different ways with respect to the masses of the ordinary particles. Taking the mirror weak scale e.g. of the order of 10 TeV, the mirror electron would become two orders of magnitude heavier than the ordinary electron while the mirror nucleons p' and n' only about 5 times heavier than the ordinary nucleons. Then dark matter would exist in the form of mirror hydrogen composed of mirror proton and electron, with mass of about 5 GeV which is a rather interesting mass range for dark matter particles. Owing to the large mass of mirror electron, mirror atoms should be more compact and tightly bound with respect to ordinary atoms. Asymmetric mirror model can be considered as a natural benchmark for more generic types of atomic dark matter with *ad hoc* chosen parameters. The annual modulation observed by DAMA in the framework of asymmetric mirror matter has been analysed in the light of the very interesting interaction portal which is kinetic mixing $\frac{\epsilon}{2}F^{\mu\nu}F'_{\mu\nu}$ of two massless states, ordinary photon and mirror photon. This mixing mediates the mirror atom (that are very compact objects) scattering off the ordinary target nuclei in the NaI(Tl) detectors of the DAMA/LIBRA set-up with the Rutherford-like cross sections.

The data analysis in the Mirror DM model framework allows the determination of the $\sqrt{f}\epsilon$ parameter (where f is the fraction of DM in the Galaxy in form of mirror atoms and ϵ is the coupling constant). In the analysis several uncertainties on the astrophysical, particle physics and nuclear physics models have been taken into account in the calculation. For detailed discussion see the 2015 publication list. To estimate the free parameter of the analysis (e.g. $\sqrt{f}\epsilon$ in the DM model) a comparison of the expectations of the mirror DM with the experimental results has been performed considering a χ^2 analysis. The obtained values of the $\sqrt{f}\epsilon$ parameter in the case of mirror hydrogen atom, $Z' = 1$, ranges between 7.7×10^{-10} to 1.1×10^{-7}; they are well compatible with cosmological bounds.

In addition, releasing the assumption $M_{A'} \simeq 5m_p$, the allowed regions for the $\sqrt{f}\epsilon$ parameter as function of $M_{A'}$, mirror hydrogen mass, obtained by marginalizing all the models for each considered scenario, are shown in Fig. 2 where the $M_{A'}$ interval from few GeV up to 50 GeV is explored. Different scenarios are reported with different hatching of the allowed regions; the black line is the overall boundary.

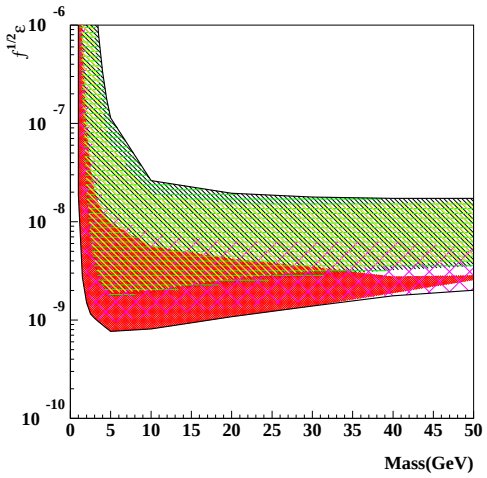

Figure 2: Allowed regions for the $\sqrt{f}\epsilon$ parameter as function of $M_{A'}$, mirror hydrogen mass, obtained by marginalizing all the models for each considered scenario. The $M_{A'}$ interval from few GeV up to 50 GeV is explored. These allowed intervals identify the $\sqrt{f}\epsilon$ values corresponding to C.L. larger than 5σ from the *null hypothesis*, that is $\sqrt{f}\epsilon = 0$. The allowed regions corresponding to five different scenarios are depicted in different hatching; the black line is the overall boundary. See the 2015 publication list.

1.2.2 Investigating Earth shadowing effect with DAMA/LIBRA-phase1

The results obtained in the investigation of possible diurnal effects for low-energy *single-hit* scintillation events of DAMA/LIBRA–phase1 (1.04 ton × year exposure) have been analysed in terms of Earth Shadow Effect, a model-dependent effect that could be expected in case of DM candidates inducing just nuclear recoils and having high cross-section with ordinary matter, which implies low DM local density in order to fulfil the DAMA/LIBRA DM annual modulation results (see the 2015 publication list).

In fact a diurnal variation of the low energy rate could be expected [37, 38] for these specific candidates, because during the sidereal day the Earth shields a given detector with a variable thickness, eclipsing the wind of DM particles. The induced effect should be a daily variation of their velocity distribution, therefore of their flux and, of course, of the signal rate measured deep underground. However, this effect is very small and would be appreciable only in case of high cross-section spin independent coupled candidates that could constitute a little fraction (ξ) in the Galactic dark halo.

The Earth's velocity in the galactic frame, $\vec{v}_e(t)$[1], defines an angle, θ, with the vector joining the center of the Earth to the position of the laboratory. Because of the Earth's rotational motion, the θ angle varies with the diurnal sidereal time and ranges between a minimum and a maximum which depend on the laboratory position on the Earth. In particular the larger is the allowed range of θ the larger is the effect resulting. The time dependence of θ can be expressed as a function of the laboratory latitude, λ, and the sidereal time.

By the fact, the diurnal variation of the velocity distribution and of the counting rate is undetectable for cross-sections on nucleon $\leq 10^{-3}$ pb (being the latter dependent on the DM particle mass m_{DM}), since the Earth is practically transparent to similar particles, while high

[1]The Earth's orbital speed around the Sun, which is the most relevant component for the annual modulation signature among the terms contributing to $\vec{v}_e(t)$, can be neglected in the present case because the data, taken in different periods during the year, contribute approximately to the same diurnal time intervals.

cross-section values give velocity distributions (and counting rates) significantly dependent on the considered time interval, producing a well detectable diurnal effect.

A study on diurnal variation in the rate with suitable exposure and stability can allow to investigate in given model scenarios high cross sections (σ_n) DM particle component (with small ξ) in the dark halo and decouple ξ from σ_n.

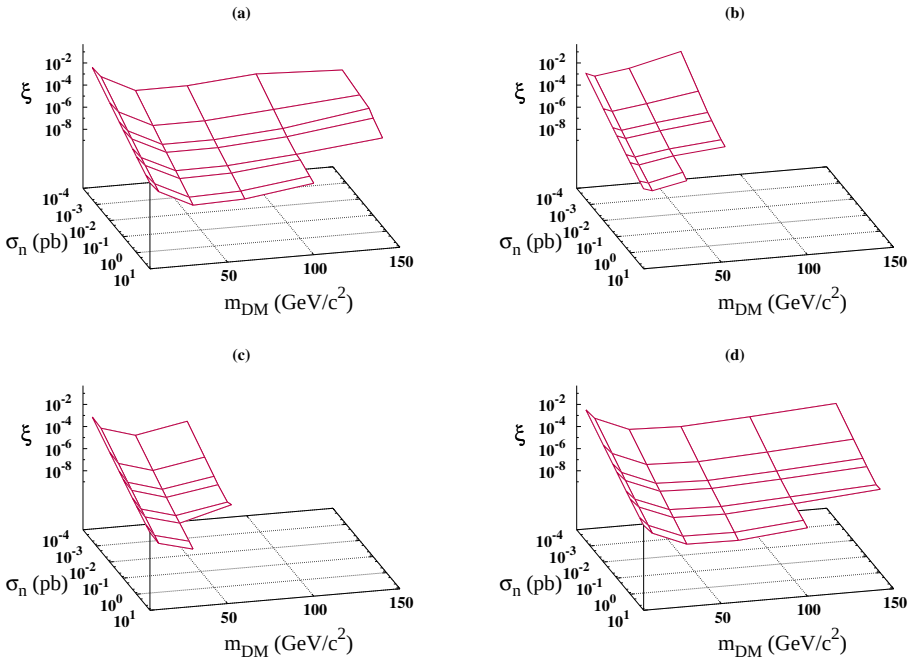

Figure 3: Examples of the mean values of the allowed region of ξ as function of σ_n and m_{DM}, represented as an allowed surface. The plots have been obtained for $v_0 = 220$ km/s by considering different scenarios regarding quenching factors value and other uncertainties (see publication list for details). We note that the "thickness" of the allowed regions around the surfaces is $\leq \pm 30\%$; therefore, for simplicity it is not represented in these figures. Finally, we recall that other uncertainties not considered here are present and can extend the result. See the 2015 publication list.

In particular, the obtained results constrain at 2σ C.L., in the considered scenario, the ξ, σ_n and m_{DM} parameters (see for example Fig. 3) when including the positive results from the DM annual modulation analysis of the DAMA/LIBRA–phase1 data [4]. For example, in the considered scenario for quenching factors Q_I with *channeling* effect (see publication list 2015), B parameters set, $v_0 = 220$ km/s and $m_{DM} = 60$ GeV, the obtained upper limits on ξ do exclude $\sigma_n > 0.05$ pb and $\xi > 10^{-3}$. When also including other uncertainties as other halo models, etc. the results would be extended. See the 2015 publication list for details.

2 DAMA/1ton

A multi-purpose 1 ton (full sensitive mass) set-up made of highly radio-pure NaI(Tl) was proposed in 1996 to INFN-CSN2, and the funded R&D-II, DAMA/LIBRA and R&D-III were considered as intermediate steps. We have already cited some items in the report to CSLNGS on March 2011. It is worth noting that the whole 1 ton will be fully sensitive to the processes

of interest. As mentioned there, the final design is based on the fulfillment of three additional replica of the present DAMA/LIBRA set-up, solution that offers many technical and scientific advantages; thus, the technical design is completely known, since DAMA/LIBRA is operative. As already mentioned, some activities were/are/will-be carried out in the light of overcoming the present problems regarding the supplying and purifications of high quality NaI and, mainly, TlI powders and the creation of suitable protocols.

3 DAMA/LXe

We pointed out since 1990 [39] the possible interest in using the liquid Xenon as target-detector material for particle DM investigations. Since the end of 80's (former Xelidon experiment of the INFN) we have built several liquid Xenon (LXe) prototype detectors. Since 1996 we pointed out to the INFN-CSN2 the intrinsic problems of this detector medium for large scale experiments dedicated to DM investigation (poor collection of the far UV light, response disuniformity on large detectors, self-absorption, rebuilding of the sensitive part for each liquefaction with no proof of the same condition, no possibility of routine calibration in keV region, degassing of materials, operating parameters stability, etc.) and agreed to pursue the activity by exploiting Kr-free enriched Xenon gases in limited volume (see the 2015 publication list).

The presently running set-up (with a Cu inner vessel filled by $\simeq$ 6.5 kg, that is $\simeq$2 l, of liquid Xenon) can work either with Kr-free Xenon enriched in ^{129}Xe at 99.5% or Kr-free Xenon enriched in ^{136}Xe at 68.8% [40, 41, 42]. Many competing results were achieved on several rare processes [40, 41, 42, 43, 44, 45]. It is worth noting that e.g. the mass exposed when using the Xenon enriched in ^{129}Xe corresponds for spin-dependent coupled particles to expose 24.5 kg (full sensitive mass) of natural Xenon, while the exposed mass when using the Xenon enriched in ^{136}Xe corresponds for spin-independent coupled particles to an exposed mass of 50.4 kg (full sensitive mass) of natural Xenon.

In the period of interest, the annual maintenance of the cryogenic system has been carried out. The vacuum and purification procedures have been performed and the set-up has then been in data taking filled with Xenon enriched in ^{136}Xe, still mainly focusing the high energy region. Some preliminary analyses are continuing.

4 DAMA/R&D

The DAMA/R&D installation is a general-purpose low background set-up used for measurements on low background prototypes and for relatively small-scale experiments [46, 47, 48, 49, 50, 51, 52, 53]

The measurements mainly investigate 2β decay modes in various isotopes; both the active and the passive source techniques have been exploited as well as the coincidence technique. Particular attention is dedicated to the isotopes allowing the investigation of the $2\beta^+$ processes and, in particular, to resonant 2ϵ or $\epsilon\beta^+$ decay channels. The investigation of neutrino-less $2\beta^+$, 2ϵ and $\epsilon\beta^+$ processes can refine the understanding of the contribution of right-handed currents to neutrino-less 2β decay; therefore developments of experimental technique to search for 2ϵ, $\epsilon\beta^+$, and $2\beta^+$ processes are strongly required considering also that in the $2\beta^+$ investigations a gap of several orders of magnitude between theoretical expectations and experimental results is the usual situation and the better achieved sensitivities do not exceed the level of $T_{1/2} \simeq 10^{21}$ yr. Even more important motivation to search for double electron capture appears from a possibility of a resonant process thanks to energy degeneracy between initial and final state of

the parent and daughter nuclei. Such a resonant process could occur if the energy of transition ($Q_{2\beta}$) minus the energies of two bounded electrons on K or/and L atomic shells of daughter nucleus is near to the energy of an excited level (E_{exc}) of the daughter isotope.

Therefore, investigations on various kinds of new scintillators and preliminary works for the future measurements are also in progress within the DAMA activities.

Some of the main results during 2015 are listed in the following.

- The Aurora measurements to investigate double beta decay of ^{116}Cd with the help of 1.162 kg cadmium tungstate crystal scintillators enriched in ^{116}Cd to 82% is continuously in data taking. The half-life of ^{116}Cd relatively to the two neutrino double beta decay is measured with the highest up-to-date accuracy $T_{1/2} = (2.62 \pm 0.14) \times 10^{19}$ yr. The sensitivity of the experiment to the neutrinoless double beta decay of ^{116}Cd to the ground state of ^{116}Sn is estimated as $T_{1/2} \geq 1.9 \times 10^{23}$ yr at 90% CL, which corresponds to the effective Majorana neutrino mass limit $\langle m_\nu \rangle \leq (1.2 - 1.8)$ eV. New limits are obtained for the double beta decay of ^{116}Cd to the excited levels of ^{116}Sn, and for the neutrinoless double beta decay with emission of majorons. Partial exposures have been already released in several Conferences (see Sect. 4.1). The experiment is continuously running.

- Search for long-lived superheavy eka-tungsten with radiopure $ZnWO_4$ crystal scintillator has been performed and a dedicated paper has been published (see Sect. 4.2)

- The work for the future (some years from now) installation of the $^{116}CdWO_4$ detectors in the low-background GeMulti set-up has further been progressed and other future measurements (among them: developments on new SrI_2(Eu) crystals, on new enriched $CdWO_4$ depleted in ^{113}Cd, on highly radio-pure $ZnWO_4$, further pursuing the goals of our project for achieving highly radio-pure scintillators for the search of rare processes) have been prepared.

This DAMA/R&D set-up is as a general-purpose set-up and will assure us also in future the possibility to produce many kinds of low background measurements in an efficient way at well reduced cost. In particular the present measurements with the $^{116}CdWO_4$ crystals are planned with further improvements to continue for the next years as needed to reach the proposed goal; then, the other measurements will start in the DAMA/R&D setup after preliminary measurements in DAMA/CRYS (see e.g. later).

4.1 Search for 2β decay of ^{116}Cd with enriched $^{116}CdWO_4$ crystal scintillators

The Aurora measurements in DAMA/R&D is in progress to investigate 2β processes in ^{116}Cd by using enriched $^{116}CdWO_4$ scintillation detectors. In details, two $^{116}CdWO_4$ crystal scintillators with a total mass 1.162 kg (1.584×10^{24} of ^{116}Cd nuclei) are installed in the DAMA/R&D set-up. The low background set-up with the $^{116}CdWO_4$ detectors has been modified several times to improve the energy resolution and to decrease background. In the last configuration of the set-up the $^{116}CdWO_4$ crystal scintillators are fixed in polytetrafluoroethylene containers filled with ultrapure liquid scintillator. The liquid scintillator improves the light collection from the $^{116}CdWO_4$ crystal scintillators and serves as an anti-coincidence veto counter. The scintillators are viewed through high purity quartz light-guides ($\oslash 7 \times 40$ cm) by low background high quantum efficiency PMTs.

The energy spectrum of β and γ events accumulated over 12015 h by the $^{116}CdWO_4$ detectors is presented in Fig. 4. The β and γ events were selected with the help of two pulse-shape

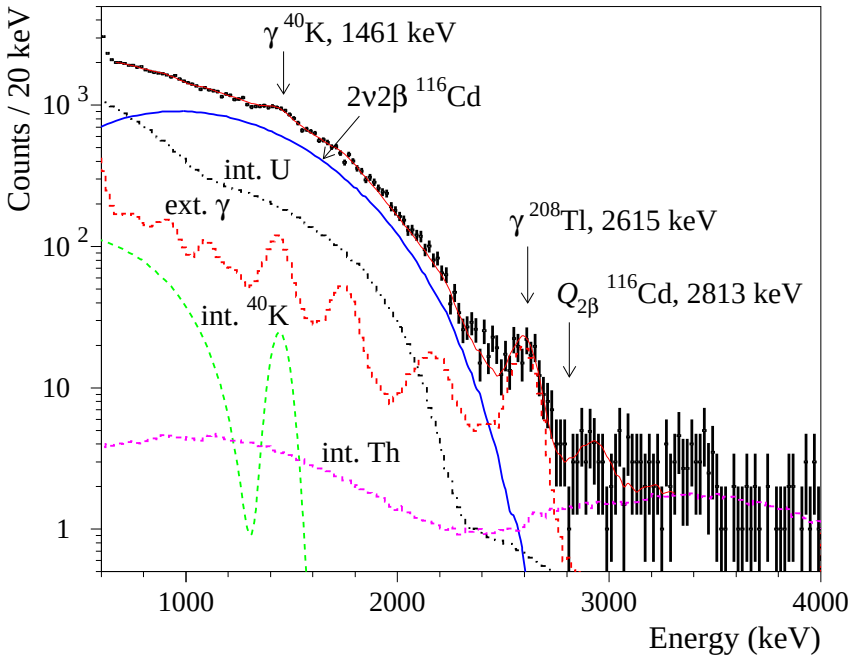

Figure 4: The energy spectrum of β and γ events accumulated over 12015 h together with the main components of the background model: $2\nu2\beta$ decay of ^{116}Cd ("$2\nu2\beta$ ^{116}Cd"), the distributions of the internal contamination of the $^{116}CdWO_4$ crystals by potassium ("int. ^{40}K"), thorium ("int. Th") and uranium ("int. U"), and the contribution from external γ quanta ("ext. γ"). See the 2015 publication list.

discrimination methods: the optimal filter method to select α particles, and the front edge analysis to select Bi–Po events (fast sub-chains ^{212}Bi–^{212}Po and ^{214}Bi–^{214}Po from ^{232}Th and ^{238}U chains, respectively) from internal contamination of the crystals by U and Th. The experimental spectrum was fitted in the energy interval $(660 - 3300)$ keV by the model constructed from the two neutrino double beta ($2\nu2\beta$) spectrum of ^{116}Cd, the distributions of the $^{116}CdWO_4$ crystal scintillators internal contamination by potassium, thorium and uranium (taking into account possible disequilibrium of the ^{232}Th and ^{238}U chains), and the contribution from external γ quanta (from radioactive contamination of the PMTs, quartz light-guides and copper of the passive shield). The response of the $^{116}CdWO_4$ detector to the 2β processes in ^{116}Cd as well as to the radioactive contamination of the set-up were simulated with EGS4 package [54]. The initial kinematics of the particles emitted in the decay of the nuclei was given by an event generator DECAY0 [55]. The fit gives the following half-life of ^{116}Cd relatively to the $2\nu2\beta$ decay to the ground state of ^{116}Sn (see the 2015 publication list):

$$T_{1/2}^{2\nu2\beta} = [2.62 \pm 0.02(stat.) \pm 0.14(syst.)] \times 10^{19} \text{ yr}.$$

The signal to background ratio is 2.6:1 in the energy interval (1.1−2.8) MeV. The comparison of the ^{116}Cd $2\nu2\beta$ half-life obtained in the Aurora experiment with other experiments is given in Fig. 5. The result is in agreement with the previous experiments [56, 57, 58, 59, 60, 61], however the half-life of ^{116}Cd is determined in the present study with the highest accuracy.

There are no other peculiarities in the experimental data which could be interpreted as 2β processes in ^{116}Cd. To estimate limit on $0\nu2\beta$ decay of ^{116}Cd to the ground state of ^{116}Sn we have used data of two runs with the lowest background in the region of interest: the current one and

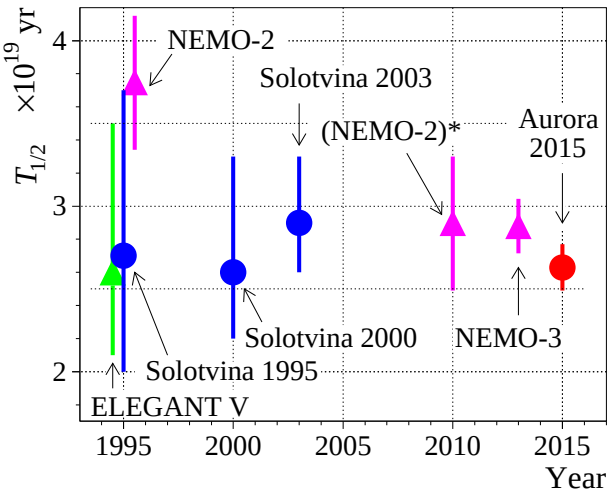

Figure 5: Comparison of the ^{116}Cd $2\nu2\beta$ half-life obtained in the Aurora experiment with other experiments: ELEGANT V [56], Solotvina [59, 60, 61], NEMO-2 [57] and NEMO-3 [58]. A reevaluated NEMO-2 value [62] is labeled as (NEMO-2)*.

that accumulated over 8696 h in the set-up described in [63]. The background counting rate of the detector in the energy interval (2.7−2.9) MeV (which contains 80% of the $0\nu2\beta$ distribution) is ≈ 0.1 counts/(yr×kg×keV). A fit of the spectrum in the energy interval (2560 − 3200) keV by the background model constructed from the distributions of the $0\nu2\beta$ decay of ^{116}Cd (effect searched for), the $2\nu2\beta$ decay of ^{116}Cd with the half-life 2.62×10^{19} yr, the internal contamination of the crystals by ^{110m}Ag and ^{228}Th, and the contribution from external γ quanta gives an area of the expected peak $S = -3.7\pm10.2$, which gives no evidence of the effect, obtaining the following limit for the $0\nu2\beta$ decay of ^{116}Cd to the ground state of ^{116}Sn (see the 2015 publication list):

$$T_{1/2}^{0\nu2\beta} \geq 1.9 \times 10^{23} \text{ yr at 90\% CL.}$$

The half-life limit corresponds to the effective neutrino mass limit $\langle m_\nu \rangle \leq (1.2 - 1.8)$ eV, obtained by using the recent nuclear matrix elements reported in [64, 65, 66, 67], the phase space factor from [68] and the value of the axial vector coupling constant $g_A = 1.27$.

New limits on the 2β decay to excited levels of ^{116}Sn and the $0\nu2\beta$ decay with emission of one, two and bulk majorons were set at the level of $T_{1/2} \geq (10^{20} - 10^{22})$ yr. Using the limit $T_{1/2} \geq 1.1 \times 10^{22}$ yr on the $0\nu2\beta$ decay with one majoron emission we have obtained one of the strongest limits on the effective majoron neutrino coupling constant $g_{\nu\chi} \leq (5.3 - 8.5) \times 10^{-5}$.

It is worth noting that we have observed a segregation of thorium, radium and potassium in the crystal growing process, which provides a possibility to substantially improve the radiopurity of the $^{116}CdWO_4$ crystal scintillators by re-crystallization, which is in progress now.

4.2 Search for long-lived superheavy eka-tungsten with radiopure $ZnWO_4$ crystal scintillator

The data collected over 2130 h, with a 699 g radioactively pure $ZnWO_4$ crystal scintillator measured in the low background DAMA/R&D set-up, were used to search for possible concentration of superheavy eka-W (seaborgium Sg, $Z = 106$) in the crystal. Chemical properties of seaborgium, in fact, are similar to those of tungsten (see the 2015 publication list), and it is

expected that Sg in some amount follows W in processes of chemical purification and growth of a $ZnWO_4$ crystal.

We recall that the possible existence of superheavy elements (SHE) with atomic masses $A \gtrsim 250$ and atomic numbers $Z \gtrsim 104$ was already discussed in 1950's [69]. In 1960's, the development of new methods of calculation of the shell model corrections to the liquid drop model [70, 71, 72, 73, 74] predicted a neutron-rich "island of stability" around the double magic $Z = 114$, $N = 184$, with half-life of the nucleus $^{294}_{184}110$ calculated as 10^8 yr [73] and 2.5×10^9 yr [74]. Various recent calculations [75, 76, 77, 78, 79, 80, 81, 82] related to different macro-micro and microscopic models predict $N = 184$ as the magic number of neutrons and $Z = 114, 120$ or 126 as the proton magic number for spherical nuclei.

In experiments on the artificial synthesis of the SHE in fusion of ions with accelerators, more than one hundred different unstable isotopes with $Z = 104 - 118$ were created [83, 84, 85, 86], with half-lives from microseconds to hours (for ^{268}Db $T_{1/2} = 29^{+9}_{-6}$ h [84]). New isotopes with $Z = 107 - 118$ predominantly undergo a chain of α decays followed by spontaneous fission (SF) [85]. Note that the SHE formed in fusion reaction [83, 84] are proton-rich (or neutron-deficient), and the half-lives of SHE with number of neutrons near the magic number 184 are expected to be longer.

While maybe only the edge of the "island of stability" is reached to-date in the laboratory conditions, long-lived SHE probably were produced in explosive stellar events by a sequence of rapid neutron captures and β^- decays [87]. Past and update results are summarized in the paper (see the 2015 publication list).

In our experiment the $ZnWO_4$ crystal scintillator was fixed inside a cavity of $\oslash 47 \times 59$ mm in the central part of a polystyrene light-guide 66 mm in diameter and 312 mm in length. The cavity was filled up with high purity silicone oil. The light-guide was optically connected on opposite sides by optical coupling to two low radioactivity EMI9265–B53/FL 3" photomultipliers (PMT). The light-guide was wrapped by PTFE tape.

The used approach was based on the search for high energy α particles ($Q_\alpha > 8$ MeV) possibly emitted in a chain of decays of eka-W (seaborgium Sg, $Z = 106$). Chemical properties of seaborgium are similar to those of tungsten (see the 2015 publication list), and it is expected that Sg in some amount follows W in processes of chemical purification and growth of a $ZnWO_4$ crystal.

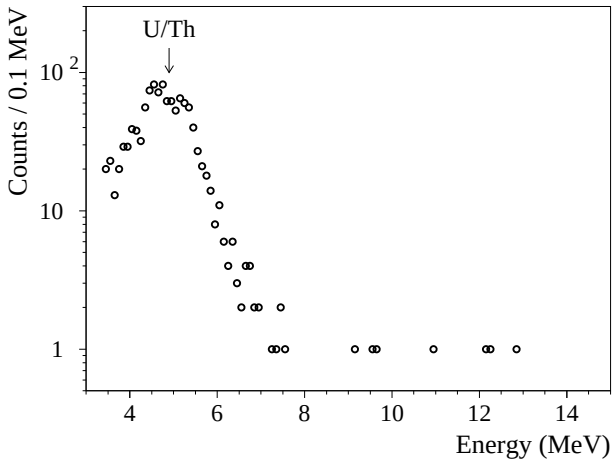

Figure 6: One-dimensional energy spectrum of α particles registered by the 699 g $ZnWO_4$ detector during 2130 h.

In Fig. 6 the measured energy spectrum of α particles registered by the 699 g $ZnWO_4$ detector during 2130 h is depicted.

The superheavy isotopes can decay through emission of β^- particle or by electron capture EC (or β^+ decay), α decay or spontaneous fission; cluster decay also starts to be important at higher Z values (see the 2015 publication list). In general, energy release Q_α in α decay is increasing with the increase of the atomic number Z; in accordance with [88], experimental Q_α values for superheavy elements with $Z = 102 - 107$ lay in the interval 7.8 – 10.6 MeV.

No evidence of the decays searched for have been observed. Assuming that one of the daughters in a chain of decays of the initial Sg nucleus decays with emission of high energy α particles ($Q_\alpha > 8$ MeV) and that half-life of the long-lived Sg is 10^9 yr, we obtained the limit on Sg concentration as: $N(\mathrm{Sg})/N(\mathrm{W}) < 5.5 \times 10^{-14}$ atoms/atoms at 90% C.L. This is comparable with the limit $\simeq 10^{-14}$ atoms/atoms obtained for concentration of eka-Os in Os in the recent SHIN experiment [89]. One should note that the detection of spontaneous fission, as in SHIN, and the detection of high energy α particles, as here, are complementary approaches in the searches for SHE in nature.

5 DAMA/CRYS

DAMA/CRYS is a small test set-up mainly dedicated to tests on new scintillation detectors' performances and small scale experiments. The activities in the period of interest are reported in the following.

- The assumption of a concentration of radioactive contamination in a thin ($\sim 0.1 - 1$ mm) surface layer of $ZnWO_4$ crystals (an effect already observed in $CdWO_4$ [59]) was checked, aimed to the development of highly radiopure $ZnWO_4$ detectors for dark matter and double beta decay experiments. For this purpose a thin surface layer (≈ 0.4 mm) of the $ZnWO_4$ crystal with mass 141 g was removed by diamond needle files. The crystal was obtained by recrystallization of the large volume $ZnWO_4$ sample (mass 699 g). The radioactive contamination of the both crystals was measured earlier in the DAMA/R&D set-up [49]. The radioactive contamination of crystal after the surface layer removing was tested in the DAMA/CRYS set-up over 1683 h. The alpha activity of uranium and thorium with their daughters was estimated by using pulse-shape discrimination, while the ^{228}Th activity was determined by the time-amplitude analysis of the fast sub-chain $^{220}\mathrm{Rn} \rightarrow {}^{216}\mathrm{Po} \rightarrow {}^{212}\mathrm{Pb}$. The total alpha activity of the sample before (after) the surface layer removing is determined as 0.47 ± 0.07 (0.44 ± 0.05) mBq/kg, while the ^{228}Th activity in the both samples is 0.002 ± 0.002 mBq/kg. To conclude, no effect of radioactive contamination concentration in surface layer of the crystal was observed.

- The $^{106}CdWO_4$ crystal scintillator contains ^{113m}Cd on the level of $\simeq$100 Bq/kg [90]. The ^{113m}Cd half-life is known with a rather modest accuracy as $T_{1/2} = 14.1(5)$ yr [91], while the beta spectral shape was never studied systematically. The ^{113m}Cd beta spectrum was measured in November 2011 and in April 2015 in the framework of the experiments to search for double beta decay of ^{106}Cd. The data allow to study the shape of beta spectrum and the half-life of ^{113m}Cd with a higher accuracy (the half-life can be determined precisely after a third measurement of the ^{113m}Cd beta distribution foreseen in 2017 – 2018 after the double beta decay experiment with the $^{106}CdWO_4$ crystal in coincidence with two $CdWO_4$ crystal scintillators). The data analysis is in progress.

- The $^{106}CdWO_4$ crystal scintillator – used in the experiment reported in Sect. 6.1 – was measured a few month in the DAMA/CRYS set-up to check the radioactive contamination of the set-up (mainly of the copper shield), which is important for background reconstruction for the next stage experiment to search for double beta processes in ^{106}Cd by using the $^{106}CdWO_4$ crystal scintillator in coincidence with two large volume $CdWO_4$ scintillation detectors in close geometry.

- A strong segregation of thorium, radium and potassium in the $^{116}CdWO_4$ crystal growing process was observed (see the 2015 publication list), which provides a possibility to improve substantially the radiopurity of the $^{116}CdWO_4$ crystal scintillators [52] by recrystallization. One of the $^{116}CdWO_4$ crystals (No. 3 with mass 325.6 g [52]) was measured in the DAMA/CRYS set-up in 2014. Recently the sample was recrystallized by the low-thermal-gradient Czochralski technique (see [92] and references therein). The recrystallized crystal sample with mass 195 g was installed in the DAMA/CRYS set-up to test the recrystallization effect on the radioactive contamination of the $^{116}CdWO_4$ crystal. Preliminary we observe substantial reduction of the total U/Th alpha activity in the sample by a factor of ≈ 16. The measurements are in progress to estimate the thorium and radium contaminations variation.

- A cryogenic system to be installed in DAMA/CRYS (to allow also measurements of the responses of various new/improved scintillators as a function of the temperature) is under test at LNGS.

6 DAMA/Ge and LNGS STELLA facility

The measurements on samples and on various R&D developments are performed by means of the DAMA low background Ge detector, specially built with a low Z window; it is operative deep underground in the STELLA facility of the LNGS. In addition other Ge detectors (in particular, GeMulti, GeCris and the recently-installed Broad Energy Germanium detector) are also used for some peculiar measurements. Published results can be found in Ref. [93, 94] and in the 2015 Publication list.

The main data takings/results during year 2015 with DAMA/Ge and LNGS STELLA facility are summarized in the following.

- The data taking of the experiment to search for double beta processes in ^{106}Cd by using cadmium tungstate crystal scintillator enriched in ^{106}Cd ($^{106}CdWO_4$, mass of 216 g [47]) in coincidence with the four crystals HPGe detector GeMulti (the volume of each germanium crystal is 225 cm^3) has completed in 2015 at the STELLA facility after 13085 h of data taking (see Sect. 6.1).

- An experiment to search for 2β decay of ^{150}Nd to excited levels of ^{150}Sm is in progress by using the GeMulti detector. Deeply purified (and pressed to improve the detection efficiency) neodymium oxide samples with a total mass of about 2.38 kg are utilized as source of ^{150}Nd (the samples contents 4.8×10^{23} nuclei of ^{150}Nd). The experiment is in progress. With the current background rate of ~ 2 counts/keV/d in the region of the expected γ peaks of 334.0 keV and 406.5 keV, the sensitivity is $T_{1/2} = 1.3 \times 10^{20}$ yr at 90% C.L. after 500 days of measurements.

- The second stage of the experiment to search for double beta decay of ^{184}Os, ^{192}Os (^{184}Os is of especial interest thanks to possibility of resonant neutrinoless double electron capture) and alpha decay of ^{184}Os to excited levels of ^{180}W was started in 2015 by using the ultra-pure osmium samples cut in $0.8 - 1.0$ mm plates to improve the detection efficiency. The experiment is in progress at the STELLA facility with an ultra-low background Broad Energy Germanium detector especially designed for low energy gamma-ray spectrometry. The measurement of the isotopic concentration of ^{184}Os (the representative isotopic composition of ^{184}Os is known with a rather rough accuracy as 0.02(1)% [95]) in the sample is in progress at the John De Laeter Centre of mass-spectrometry of the Curtin University of Technology (Perth, Australia).

- The first experiment to search for double beta decay of cerium isotopes by using low background HPGe has demonstrated a rather high contamination of the high purity cerium oxide by thorium at the level of 0.6 Bq/kg [94]. The cerium oxide sample was additionally purified by the liquid extraction method to remove traces of thorium contamination. New search for double beta decay of ^{136}Ce and ^{138}Ce is in progress at the STELLA facility.

- The R&D of low background GSO(Ce) crystal scintillators to investigate double beta processes in ^{152}Gd and ^{160}Gd has been progressed.

- The R&D of low background barium containing crystal scintillators to investigate double beta processes in ^{130}Ba and ^{132}Ba has been progressed.

- The R&D of methods to purify samarium, ytterbium and erbium has been progressed to search for neutrinoless resonant double electron capture processes in ^{144}Sm, ^{162}Er, ^{164}Er and ^{168}Yb. Deep purification of the samples is under investigation in order to improve the sensitivity reachable in the measurements in preparation.

- The results of a preliminary study on feasibility of an experiment looking for excited state double beta transitions in tin have been published (see Sect. 6.2).

- Preparations of other future measurements are in progress.

6.1 Search for 2β decay of ^{106}Cd with enriched $^{106}CdWO_4$ crystal scintillator in coincidence with four HPGe detectors

A second stage of the experiment to search for double beta decay processes in ^{106}Cd with the help of enriched in ^{106}Cd (to 66%) low background $^{106}CdWO_4$ scintillation detector was completed in 2015 at the STELLA facility. The $^{106}CdWO_4$ scintillator, viewed by a low background PMT through the lead tungstate crystal light-guide produced from deeply purified archaeological lead, was operated in coincidence with the four ultra-low background high purity germanium detectors in a single cryostat GeMulti. New improved limits on the double beta processes in ^{106}Cd have been set on the level of $10^{20} - 10^{21}$ yr after 13085 h of data taking. In particular, the coincidence energy spectrum of the $^{106}CdWO_4$ detector is presented in Fig. 7. The half-life limit on the two neutrino electron capture with positron emission derived from the data, $T_{1/2}^{2\nu\varepsilon\beta^+} \geq 1.1 \times 10^{21}$ yr, has reached the region of theoretical predictions. With this half-life limit the effective nuclear matrix element for the $2\nu\varepsilon\beta^+$ decay is bounded as $M_{eff}^{2\nu\varepsilon\beta^+} \leq 1.1$. The resonant neutrinoless double electron captures to the 2718 keV, 2741 keV and 2748 keV excited states of ^{106}Pd are restricted at the level of $T_{1/2} \geq (8.5 \times 10^{20} - 1.4 \times 10^{21})$ yr. Results have been presented at

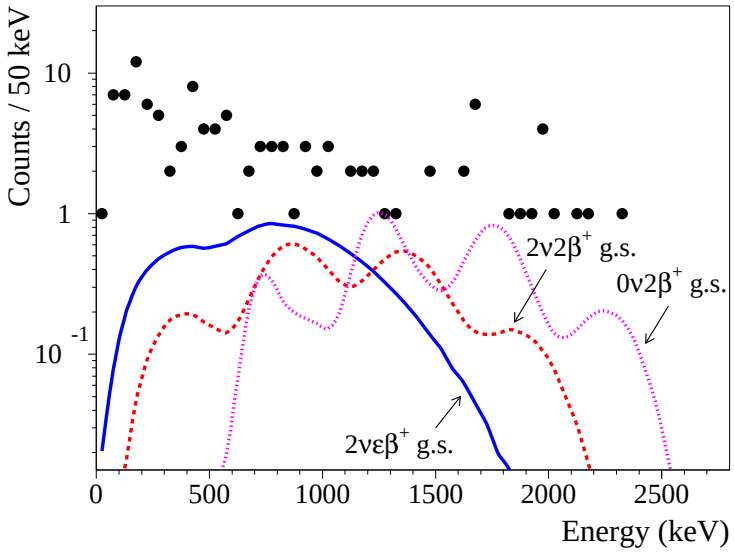

Figure 7: Energy spectrum of the $^{106}CdWO_4$ detector in coincidence with 511 keV annihilation γ quanta in at least one of the HPGe detectors (filled circles) acquired over 13085 h. The excluded distributions of different 2β processes in ^{106}Cd are shown by different lines.

Conferences and the paper describing the final results of the 2nd stage experiment is submitted for publication (see the 2015 Publication list).

Advancement of the experiment is in progress using the $^{106}CdWO_4$ detector in coincidence with two large volume $CdWO_4$ scintillation detectors in close geometry in the DAMA/CRYS set-up to improve the detection efficiency to gamma quanta emitted in the double beta processes in ^{106}Cd.

6.2 Preliminary study of feasibility of an experiment looking for excited state double beta transitions in Tin

With the aim to study the feasibility of a new experiment to search for double beta decay in ^{124}Sn and ^{112}Sn in the upcoming India-based Neutrino Observatory site, we study with indian colleagues the radioactive contamination of a Sn sample by using ultra-low background HPGe detector (244 cm^3). A natural tin sample of 13.3 g mass (purity 99.997%) was measured over 2367.5 h while the background of the detector was measured over 6109.4 h. The energy spectra of sample and background, normalized to the time of measurement of sample, are shown in Fig. 8.

The radioactive contaminations of the tin sample measured by HPGe have been calculated by means of the full-energy-peak efficiency estimated by using Monte-Carlo based on GEANT4 and on EGS4 (see the 2015 publication list).

The collected data have also been considered to calculate the present sensitivity for the double beta decay processes in ^{112}Sn and ^{124}Sn nuclei. In fact, the gamma rays produced by the de-excitations of the excited levels of either ^{112}Cd or ^{124}Te (produced after the double beta decay in ^{112}Sn and ^{124}Sn respectively) can be detected by the HPGe detector. In this way it was possible to investigate the decay processes to the ground state as well as to the excited states in ^{112}Sn and to the excited states in ^{124}Sn using γ -ray spectrometry. Half-life limits of order of $10^{17} - 10^{18}$ yr for β^+EC and EC-EC processes in ^{112}Sn and 10^{18} yr for $\beta^-\beta^-$ transition in ^{124}Sn have been obtained. For the 0νEC-EC decay of ^{112}Sn to the ground state of its daughter

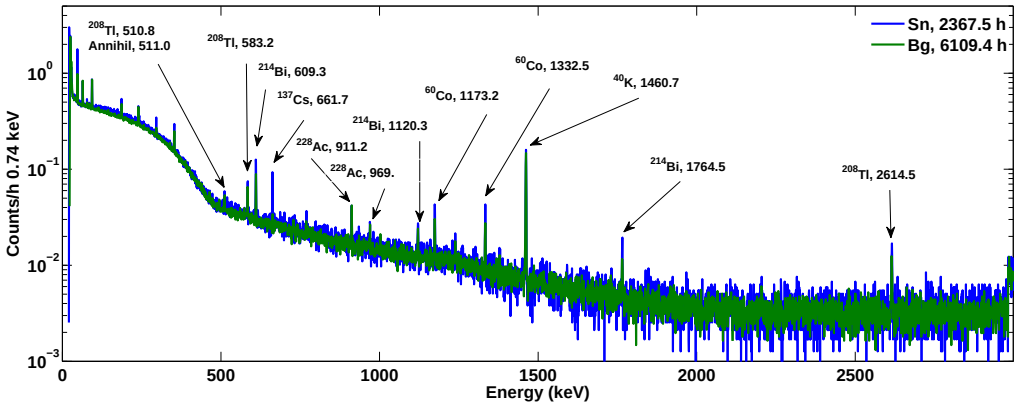

Figure 8: Energy spectrum with 13.3 g of natural tin sample (Sn) for 2367.5 h of measurement in comparison with background spectrum (Bg) of ultra low-background HPGe detector measured for 6109.4 h. The energy of the γ lines are in keV.

nuclide we obtained a half-life limit of 1.27×10^{18} yr. For a complete list of the experimental limits obtained for the processes searched for, see the corresponding paper reported in the 2015 publication list. Finally, in the paper, we showed also that an experiment with larger mass, and material enriched to high levels of either ^{112}Sn or ^{124}Sn, could reach with the same HPGe detector half-life limits for both tin isotopes on the order of 10^{22} yr for the decays to the excited levels.

7 Other activities

In 2015 the activity studying the feasibility of a directionality experiment for dark matter is continued. In the particular case of DM candidates inducing nuclear recoils, the directionality studies the correlation of the nuclear recoils with the Earth galactic motion.

In recent years we have made extensive efforts and measurements with $ZnWO_4$ crystal scintillators, already interesting to investigate double beta decay of Zn and W isotopes [48, 49]. These scintillators [96] have the particular feature to be anisotropic in the light output and in the pulse shape for heavy particles (p, α, nuclear recoils) depending on the direction with respect to the crystal axes. The response to γ/β radiation is isotropic instead. Among the anisotropic scintillators, the $ZnWO_4$ has unique features, which make it an excellent candidate for this type of research, and there is still plenty of room for the improvement of its performances. The possibility of a low background pioneer experiment (named ADAMO, Anisotropic detectors for DArk Matter Observation) to exploit deep underground the directionality approach by using anisotropic $ZnWO_4$ scintillators has been explored [96]. Finally, we have also discussed as first in written project and Conferences the potentiality to build detectors with anisotropic features by using Carbon Nanotubes (CNT) [97].

8 Conclusions

During 2015 DAMA/LIBRA has continued to take data in the phase2 configuration.

Studies on other DM features, second order effects, and several other rare processes are in progress with the aim to reach very high sensitivity also thanks to the progressive increasing of the exposure. In particular, a paper which examines the model-independent DM annual modulation result in terms of asymmetric mirror DM has been released. In addition, an investigation on the Earth shadowing effect, expected in case of DM candidates inducing nuclear recoils and having high cross-section, has been published.

Studies are under way towards possible DAMA/LIBRA–phase3 (whose R&D has been funded) and/or DAMA/1ton (proposed since 1996).

Moreover, results on several 2β decay processes of ^{116}Cd and ^{106}Cd, searches on long-lived superheavy eka-tungsten, feasibility of an experiment using tin isotopes have been published; preparations for future experiments (among them: developments on new SrI_2(Eu) crystals, on new enriched $CdWO_4$ depleted in ^{113}Cd, on highly radio-pure $ZnWO_4$, further developing the goals of our project to develop highly radio-pure scintillators for the search of rare processes, etc.) are also in progress.

In addition the work for the future (some years from now) installation of the ^{116}Cd detectors in the low-background GeMulti set-up has been progressed.

Finally, in 2015 all the DAMA set-ups have regularly been in data taking and various kinds of measurements are in progress and planned for the future.

During 2015, more than 25 presentations at Conferences and Workshops (many of them by invitation) have been done. Moreover, R. Bernabei was in the International Advisory Committee of the NDM 2015 Conference, R. Bernabei and P. Belli were in the Local Organizing Committee of the 14th Marcel Grossmann Meeting (MG14) and P. Belli was the chairperson of the DM2 session of MG14.

9 List of Publications during 2015

1. P. Belli, Direct detection of Dark Matter, to appear in the Proc. of the RICAP 2014 Conference.

2. R. Bernabei, P. Belli, F. Cappella, V. Caracciolo, R. Cerulli, C.J. Dai, A. d'Angelo, S. d'Angelo, A. Di Marco, H.L. He, A. Incicchitti, H.H. Kuang, X.H. Ma, F. Montecchia, X.D. Sheng, R.G. Wang, Z.P. Ye, DAMA/LIBRA-phase1 results and perspectives of the phase2, to appear in the Proc. of the RICAP 2014 Conference.

3. R. Bernabei, P. Belli, F. Cappella, V. Caracciolo, S. Castellano, R. Cerulli, C.J. Dai, A. d'Angelo, S. d'Angelo, A. Di Marco, H.L. He, A. Incicchitti, H.H. Kuang, X.H. Ma, F. Montecchia, D. Prosperi, X.D. Sheng, R.G. Wang, Z.P. Ye, Final model independent results of DAMA/LIBRA-phase1 and perspectives of phase2, Physics of Particles and Nuclei 46 (2015) 138-146.

4. O.G. Polischuk, P. Belli, R. Bernabei, V.D. Brudanin, F. Cappella, V. Caracciolo, R. Cerulli, D. M. Chernyak, F. A. Danevich, S. d'Angelo, A. Incicchitti, M. Laubenstein, V. M. Mokina, D.V. Poda, V.I. Tretyak, I.A. Tupitsyna, Search for 2β processes in ^{106}Cd with $^{106}CdWO_4$ crystal scintillator, Functional Materials 22 n. 1 (2015) 135-139.

5. P. Belli, R. Bernabei, F. Cappella, R. Cerulli, F. Danevich, V. Yu. Denisov, A. d'Angelo, A. Incicchitti, V.V. Kobychev, D.V. Poda, O.G. Polischuk, V.I. Tretyak, Search for long-lived superheavy eka-tungsten with radiopure $ZnWO_4$ crystal scintillator, Physica Scripta 90 (2015) 085301.

6. R. Bernabei, P. Belli, S. d'Angelo, A. Di Marco, F. Montecchia, A. d'Angelo, A. Incicchitti, F. Cappella, V. Caracciolo, R. Cerulli, Investigating Earth Shadowing effect with DAMA/LIBRA-phase1, Eur. Phys. J. C 75 (2015) 239.

7. Soumik Das, S.K. Ghorui, P.K. Raina, A.K. Singh, P.K. Rath, F. Cappella, R. Cerulli, M. Laubenstein, P. Belli, R. Bernabei, Preliminary study of feasibility of an experiment looking for excited double beta transitions in tin, Nucl. Instrum. and Meth. A 797 (2015) 130.

8. O.G. Polischuk, A.S. Barabash, P. Belli, R. Bernabei, F. Cappella, V. Caracciolo, R. Cerulli, D.M. Chernyak, F.A. Danevich, S. d'Angelo, A. Incicchitti, V.V. Kobychev, S.I. Konovalov, M. Laubenstein, V.M. Mokina, D.V. Poda, V.N. Shlegel, V.I. Tretyak, V.I. Umatov, Ya.V. Vasiliev, Investigation of double beta decay of ^{116}Cd with the help of enriched $^{116}CdWO_4$ crystal scintillators, AIP Conf. Proc. 1686 (2015) 020017.

9. F.A. Danevich, P. Belli, R. Bernabei, V.B. Brudanin, F. Cappella, V. Caracciolo, R. Cerulli, D.M. Chernyak, S. d'Angelo, A. Incicchitti, M. Laubenstein, V.M. Mokina, D.V. Poda, O.G. Polischuk, V.I. Tretyak, I.A. Tupitsyna, Search for double beta processes in ^{106}Cd with enriched $^{106}CdWO_4$ crystal scintillator in coincidence with four crystals HPGe detector, to appear in the Proc. of the MEDEX 2015 Conference.

10. A. Addazi, Z. Berezhiani, R. Bernabei, P. Belli, F. Cappella, R. Cerulli, A. Incicchitti, DAMA annual modulation effect and asymmetric mirror matter, Eur. Phys. J. C 75 (2015) 400.

11. R. Bernabei, P. Belli, A. Incicchitti, F. Cappella, R. Cerulli, Liquid noble gases for dark matter searches: an updated survey, Int. J. of Mod. Phys. A 30 (2015) 1530053-1 (76 pages).

12. R. Bernabei, P. Belli, S. d'Angelo, A. Di Marco, F. Montecchia, A. d'Angelo, A. Incicchitti, F. Cappella, V. Caracciolo, R. Cerulli, C.J. Dai, H.L. He, H.H. Kuang, X.H. Ma, F. Montecchia, X.D. Sheng, R.G. Wang, Z.P. Ye, Particle Dark Matter in the galactic halo, Int. J. of Mod. Phys. A 30 (2015) 1545006.

13. R. Bernabei, P. Belli, S. d'Angelo, A. Di Marco, F. Montecchia, A. d'Angelo, A. Incicchitti, F. Cappella, V. Caracciolo, R. Cerulli, C.J. Dai, H.L. He, H.H. Kuang, X.H. Ma, X.D. Sheng, R.G. Wang, Z.P. Ye, Recent results from DAMA/LIBRA-phase1 and perspectives, to appear in Nuclear and Particle Physics Proceedings (2015).

14. R. Bernabei, P. Belli, A. d'Angelo, S. d'Angelo, A. Di Marco, F. Montecchia, A. Incicchitti, F. Cappella, V. Caracciolo, R. Cerulli, C.J. Dai, H.L. He, H.H. Kuang, X.H. Ma, X.D. Sheng, R.G. Wang, Z.P. Ye, Highlights of DAMA/LIBRA, in the volume Proceed. of Physics, ICNFP Conference, 24-30 Agosto 2015, Creta, Grecia.

15. R. Bernabei, P. Belli, A. Di Marco, F. Montecchia, A. d'Angelo, A. Incicchitti, F. Cappella, V. Caracciolo, R. Cerulli, C.J. Dai, H.L. He, H.H. Kuang, X.H. Ma, X.D. Sheng, R.G. Wang, Z.P. Ye, Results on DAMA/LIBRA-phase1 and perspectives of the phase2, in the volume Bled Workshop in Physics, Vol. 16, n. 2 (2015) 13.

16. R. Bernabei, P. Belli, S. d'Angelo, A. Di Marco, F. Montecchia, A. d'Angelo, A. Incicchitti, F. Cappella, V. Caracciolo, R. Cerulli, C.J. Dai, H.L. He, H.H. Kuang, X.H. Ma, X.D. Sheng, R.G. Wang, Z.P. Ye, Recent results from DAMA/LIBRA-phase1 and perspectives,

to appear in the Proceed. of the 5-th Gamow International Conference Astrophysics and Cosmology after Gamow: progress and perspectives, 16-23 August, 2015, Odessa, Ukraine.

17. P. Belli, R. Bernabei, V.B. Brudanin, F. Cappella, V. Caracciolo, R. Cerulli, D.M. Chernyak, F.A. Danevich, S. d'Angelo, A. Di Marco, A. Incicchitti, M. Laubenstein, V.M. Mokina, D.V. Poda, O.G. Polischuk, V.I. Tretyak, I.A. Tupitsyna, Search for 2β decay of ^{106}Cd with enriched $^{106}CdWO_4$ crystal scintillator in coincidence with four HPGe detector, submitted for publication.

18. P. Belli, Results and strategies in dark matter detection, in publication in Int. J. of Mod. Phys. D.

19. R. Bernabei, P. Belli, F. Cappella, V. Caracciolo, R. Cerulli, C.J. Dai, A. d'Angelo, S. d'Angelo, A. Di Marco, H.L. He, A. Incicchitti, H.H. Kuang, X.H. Ma, F. Montecchia, X.D. Sheng, R.G. Wang, Z.P. Ye, DAMA results at Gran Sasso underground lab, Nuclear and Particle Physics Proceedings 263-264 (2015) 87.

20. R. Bernabei, P. Belli, F. Cappella, V. Caracciolo, R. Cerulli, C.J. Dai, A. d'Angelo, S. d'Angelo, A. Di Marco, H.L. He, A. Incicchitti, H.H. Kuang, X.H. Ma, F. Montecchia, X.D. Sheng, R.G. Wang, Z.P. Ye, DAMA/LIBRA–phase1 results and perspectives of the phase2, EPJ web of Conf. 95 (2015) 03001.

21. P. Belli, Results and strategies in dark matter detection, to appear in the Proceed. della Conferenza MG14.

22. R. Bernabei, P. Belli, F. Cappella, V. Caracciolo, R. Cerulli, C.J. Dai, A. d'Angelo, S. d'Angelo, A. Di Marco, H.L. He, A. Incicchitti, H.H. Kuang, X.H. Ma, F. Montecchia, X.D. Sheng, R.G. Wang, Z.P. Ye, DAMA/LIBRA-phase1 results and perspectives of the phase2, to appear in the Proceed. della Conferenza MG14.

23. V.I. Tretyak, P. Belli, R. Bernabei, V.B. Brudanin, F. Cappella, V. Caracciolo, R. Cerulli, D.M. Chernyak, F.A. Danevich, S. d'Angelo, A. Di Marco, A. Incicchitti, M. Laubenstein, V.M. Mokina, D.V. Poda, O.G. Polischuk, I.A. Tupitsyna, New limits on 2β processes in ^{106}Cd, to appear in the Proceed. of the TAUP 2015 Conference.

24. P. Belli, Dark Matter direct detection: crystals, to appear in the Proceed. of the TAUP 2015 Conference.

25. F. A. Danevich, A. S. Barabash, P. Belli, R. Bernabei, F. Cappella, V. Caracciolo, R. Cerulli, D. M. Chernyak, S. d'Angelo, A. Incicchitti, V. V. Kobychev, S. I. Konovalov, M. Laubenstein, V. M. Mokina, D. V. Poda, O. G. Polischuk, V. N. Shlegel, V. I. Tretyak, V. I. Umatov, Search for double beta decay of ^{116}Cd with enriched $^{116}CdWO_4$ crystal scintillators (Aurora experiment), to appear in the Proceed. of the TAUP 2015 Conference.

26. V. Caracciolo, R. Bernabei, P. Belli, F. Cappella, R. Cerulli, F.A. Danevich, A. d'Angelo, A. Di Marco, A. Incicchitti, D.V. Poda, V.I. Tretyak, The ADAMO Project and Developments, to appear in the Proceed. of the TAUP 2015 Conference.

27. R. Bernabei, P. Belli, A. Di Marco, F. Montecchia, A. d'Angelo, A. Incicchitti, F. Cappella, V. Caracciolo, R. Cerulli, C.J. Dai, H.L. He, H.H. Kuang, X.H. Ma, X.D. Sheng, R.G. Wang, Z.P. Ye, Recent results on DAMA/LIBRA-phase1 data, to appear in the Proceed. of the TAUP 2015 Conference.

28. R. Bernabei, P. Belli, S. d'Angelo, A. Di Marco, F. Montecchia, A. d'Angelo, A. Incicchitti, D. Prosperi, F. Cappella, V. Caracciolo, R. Cerulli, C.J. Dai, H.L. He, H.H. Kuang, X.H. Ma, X.D. Sheng, R.G. Wang, Z.P. Ye, Recent results from DAMA/LIBRA and perspectives, to appear in the Proceed. of the 17th Lomonosov Conference on Elementary Particle Physics.

References

[1] R. Bernabei et al., Nucl. Instr. and Meth. A 592 (2008) 297.

[2] R. Bernabei et al., Eur. Phys. J. C 56 (2008) 333.

[3] R. Bernabei et al., Eur. Phys. J. C 67 (2010) 39.

[4] R. Bernabei et al., Eur. Phys. J. C 73 (2013) 2648.

[5] P. Belli et al., Phys. Rev. D 84 (2011) 055014.

[6] R. Bernabei et al., J. of Instr. 7 (2012) P03009.

[7] R. Bernabei et al., Eur. Phys. J. C 72 (2012) 2064.

[8] R. Bernabei et al., Int. J. of Mod. Phys. A 28 (2013) 1330022 (73 pages).

[9] R. Bernabei et al., Eur. Phys. J. C 62 (2009) 327.

[10] R. Bernabei et al., Eur. Phys. J. C 72 (2012) 1920.

[11] R. Bernabei et al., Eur. Phys. J. A 49 (2013) 64.

[12] R. Bernabei et al., Eur. Phys. J. C 74 (2014) 2827.

[13] R. Bernabei et al., Eur. Phys. J. C 74 (2014) 3196.

[14] P. Belli, R. Bernabei, C. Bacci, A. Incicchitti, R. Marcovaldi, D. Prosperi, DAMA proposal to INFN Scientific Committee II, April 24^{th} 1990.

[15] R. Bernabei et al., Phys. Lett. B 389 (1996) 757; R. Bernabei et al., Phys. Lett. B 424 (1998) 195; R. Bernabei et al., Phys. Lett. B 450 (1999) 448; P. Belli et al., Phys. Rev. D 61 (2000) 023512; R. Bernabei et al., Phys. Lett. B 480 (2000) 23; R. Bernabei et al., Phys. Lett. B 509 (2001) 197; R. Bernabei et al., Eur. Phys. J. C 23 (2002) 61; P. Belli et al., Phys. Rev. D 66 (2002) 043503.

[16] R. Bernabei et al., Il Nuovo Cim. A 112 (1999) 545.

[17] R. Bernabei et al., Eur. Phys. J. C18 (2000) 283.

[18] R. Bernabei el al., La Rivista del Nuovo Cimento 26 n.1 (2003) 1-73.

[19] R. Bernabei et al., Int. J. Mod. Phys. D 13 (2004) 2127.

[20] R. Bernabei et al., Int. J. Mod. Phys. A 21 (2006) 1445.

[21] R. Bernabei et al., Eur. Phys. J. C 47 (2006) 263.

[22] R. Bernabei et al., Int. J. Mod. Phys. A 22 (2007) 3155.

[23] R. Bernabei et al., Eur. Phys. J. C 53 (2008) 205.

[24] R. Bernabei et al., Phys. Rev. D 77 (2008) 023506.

[25] R. Bernabei et al., Mod. Phys. Lett. A 23 (2008) 2125.

[26] R. Bernabei et al., Phys. Lett. B408 (1997) 439; P. Belli et al., Phys. Lett. B460 (1999) 236; R. Bernabei et al., Phys. Rev. Lett. 83 (1999) 4918; P. Belli et al., Phys. Rev. C60 (1999) 065501; R. Bernabei et al., Il Nuovo Cimento A112 (1999) 1541; R. Bernabei et al., Phys. Lett. B 515 (2001) 6; F. Cappella et al., Eur. Phys. J.-direct C14 (2002) 1; R. Bernabei et al., Eur. Phys. J. A 23 (2005) 7; R. Bernabei et al., Eur. Phys. J. A 24 (2005) 51; R. Bernabei et al., Astrop. Phys. 4 (1995) 45.

[27] K.A. Drukier et al., Phys. Rev. D 33 (1986) 3495.

[28] K. Freese et al., Phys. Rev. D 37 (1988) 3388.

[29] R. Bernabei et al., AIP Conf. Proceed. 1223 (2010) 50 (arXiv:0912.0660).

[30] R. Bernabei et al., J. Phys.: Conf. Ser. 203 (2010) 012040 (arXiv:0912.4200); http://taup2009.lngs.infn.it/slides/jul3/nozzoli.pdf, talk given by F. Nozzoli.

[31] R. Bernabei et al., in the volume Frontier Objects in Astrophysics and Particle Physics (Vulcano 2010), S.I.F. Ed. (2011) 157 (arXiv:1007.0595).

[32] R. Bernabei et al., Can. J. Phys. 89 (2011) 11.

[33] R. Bernabei et al., Physics Procedia 37 (2012) 1095.

[34] R. Bernabei et al., arXiv:1210.6199; arXiv:1211.6346.

[35] A. Bottino et al., Phys. Rev. D 85 (2012) 095013.

[36] A. Bottino et al., arXiv:1112.5666.

[37] J.I. Collar et al., Phys. Lett. B 275 (1992) 181.

[38] J.I. Collar and F.T. Avignone III, Phys. Rev. D 47 (1993) 5238.

[39] P. Belli et al., Il Nuovo Cim. 103A (1990) 767.

[40] P. Belli et al., Phys. Lett. B 387 (1996) 222 and Phys. Lett. B 389 (1996) 783 (erratum); R. Bernabei et al., New J. Phys. 2 (2000) 15.1; Eur. Phys. J.-direct C11 (2001) 1; Phys. Lett. B 436 (1998) 379; R. Bernabei et al., in the volume "Beyond the Desert 2003", Springer (2003) 365.

[41] R. Bernabei et al., Nucl. Instrum. and Meth. A 482 (2002) 728.

[42] R. Bernabei et al., Phys. Lett. B 546 (2002) 23; F. Cappella, PhD Thesis, Università di Roma "Tor Vergata", 2005.

[43] P. Belli et al., Il Nuovo Cim. C 19 (1996) 537; Astrop. Phys. 5 (1996) 217.

[44] R. Bernabei et al., Phys. Lett. B 527 (2002) 182.

[45] P. Belli et al., Phys. Rev. D 61 (2000) 117301; Phys. Lett. B 465 (1999) 315; R. Bernabei et al., Phys. Lett. B 493 (2000) 12; Eur. Phys. J. A 27 s01 (2006) 35.

[46] R. Bernabei et al., Astropart. Phys. 7 (1997) 73; R. Bernabei et al., Il Nuovo Cim. A 110 (1997) 189; P. Belli et al., Astropart. Phys. 10 (1999) 115; P. Belli et al., Nucl. Phys. B 563 (1999) 97; R. Bernabei et al., Nucl. Phys. A 705 (2002) 29; P. Belli et al., Nucl. Instrum. and Meth. A 498 (2003) 352; R. Cerulli et al., Nucl. Instrum. and Meth. A 525 (2004) 535; R. Bernabei et al., Nucl. Instrum. and Meth. A 555 (2005) 270; R. Bernabei et al., Ukr. J. Phys. 51 (2006) 1037; P. Belli et al., Nucl. Phys. A 789 (2007) 15; P. Belli et al., Phys. Rev. C 76 (2007) 064603; P. Belli et al., Eur. Phys. J. A 36 (2008) 167; P. Belli et al., J. Phys. G 38 (2011) 015103; D. Poda et al., Radiation Measurements 56 (2013) 66.

[47] P. Belli et al., Nucl. Instrum. and Meth. A 615 (2010) 301.

[48] P. Belli et al., Nucl. Phys. A 826 (2009) 256; P. Belli et al., Phys. Lett. B 658 (2008) 193.

[49] P. Belli et al., Nucl. Instrum. and Meth. A 626-627 (2011) 31.

[50] P. Belli et al., Phys. Rev. C 85 (2012) 044610.

[51] P. Belli et al., J. Phys. G: Nucl. Part. Phys. 38 (2011) 115107.

[52] A.S. Barabash et al., JINST. 6 (2011) P08011.

[53] P. Belli et al., Eur. Phys. J. A 50 (2014) 134.

[54] W.R. Nelson et al. The EGS4 code system, SLAC-Report-265 (Stanford, 1985).

[55] O.A. Ponkratenko et al., Phys. Atom. Nuclei 63 (2000) 1282.

[56] H. Ejiri et al., J. Phys. Soc. Japan 64 (1995) 339.
[57] R. Arnold et al., Z. Phys. C 72 (1996) 239.
[58] V.I. Tretyak et al., AIP Conf. Proc. 1572 (2013) 110.
[59] F.A. Danevich et al., Phys. Lett. B 344 (1995) 72.
[60] F.A. Danevich et al., Phys. Rev. C 62 (2000) 045501.
[61] F.A. Danevich et al., Phys. Rev. C 68 (2003) 035501.
[62] A.S. Barabash, Phys. Rev. C 81 (2010) 035501.
[63] D.V. Poda et al., EPJ Web of Conferences 65 (2014) 01005.
[64] T.R. Rodriguez, G. Martinez-Pinedo, Phys. Rev. Lett. 105 (2010) 252503.
[65] F. Šimkovic et al., Phys. Rev. C 87 (2013) 045501.
[66] J. Hyvärinen, J. Suhonen, Phys. Rev. C 91 (2015) 024613.
[67] J. Barea et al., Phys. Rev. C 91 (2015) 034304.
[68] J. Kotila, F. Iachello, Phys. Rev. C 85 (2012) 034316.
[69] G. Schaff-Goldhaber, Nucleonics 15 (1957) 122.
[70] W.D. Myers, W.J. Swiatecki, Nucl. Phys. 81 (1966) 1.
[71] V.M. Strutinsky, Nucl. Phys. A 95 (1967) 420; 122 (1968) 1.
[72] S.G. Nilsson et al., Nucl. Phys. A 115 (1968) 545.
[73] S.G. Nilsson et al., Nucl. Phys. A 131 (1969) 1.
[74] E.O. Fiset, J.R. Nix, Nucl. Phys. A 193 (1972) 647.
[75] R. Smolanczuk, Phys. Rev. C 56 (1997) 812.
[76] P. Moller, J.R. Nix, K.-L. Kratz, At. Data Nucl. Data Tables 66 (1997) 131.
[77] T. Bürvenich et al., Eur. Phys. J. A 3 (1998) 139.
[78] A.T. Kruppa et al., Phys. Rev. C 61 (2000) 034313.
[79] J.F. Berger et al., Nucl. Phys. A 685 (2001) 1c; Int. J. Mod. Phys. E 13 (2004) 79.
[80] M. Bender, W. Nazarewicz, P.-G. Reinhard, Phys. Lett. B 515 (2001) 42.
[81] A. Sobiczewski, K. Pomorski, Prog. Part. Nucl. Phys. 58 (2007) 292.
[82] V.Yu. Denisov, Phys. At. Nucl. 70 (2007) 244.
[83] S. Hofmann, G. Münzenberg, Rev. Mod. Phys. 72 (2000) 733.
[84] Yu. Oganessian, J. Phys. G 34 (2007) R165.
[85] J.H. Hamilton, S. Hofmann, Y.T. Oganessian, Annu. Rev. Nucl. Part. Sci. 63 (2013) 383.
[86] M. Thoennessen, At. Data Nucl. Data Tables 99 (2013) 312.
[87] D.N. Schramm, W.A. Fowler, Nature 231 (1971) 103.
[88] I. Silisteanu, A.I. Budaca, At. Data Nucl. Data Tables 98 (2012) 1096.
[89] A. Svirikhin et al., AIP Conf. Proc. 1175 (2009) 297.
[90] F.A. Danevich et al., AIP Conf. Proc. 1549 (2013) 201.
[91] J. Blachot, Nuclear Data Sheets for A = 113, Nuclear Data Sheets 111 (2010) 1471.
[92] D.N. Grigoriev et al., JINST 9 (2014) C09004.
[93] P. Belli et al., Nucl. Instr. and Meth. A 572 (2007); P. Belli et al., Nucl. Phys. A 806 (2008) 388; P. Belli et al., Nucl. Phys. A 824 (2009) 101; O. P. Barinova et al., Nucl. Instrum. and Meth. A 607 (2009) 573; P. Belli et al., Eur. Phys. J. A 42 (2009) 171; P. Belli et al., Nucl. Phys. A 846 (2010) 143; P. Belli et al., Nucl. Phys. At. Energy 11 (2010) 362; P. Belli et

al., Nucl. Phys. A 859 (2011) 126; P. Belli et al., Phys. Rev. C 83 (2011) 034603; P. Belli et al., Eur. Phys. J. A 47 (2011) 91; P. Belli et al., Nucl. Instrum. and Meth. A 670 (2012) 10; P. Belli et al., Phys. Lett. B 711 (2012) 41; P. Belli et al., Nucl. Instrum. and Meth. A 704 (2013) 40; P. Belli et al., Eur. Phys. J. A 49 (2013) 24; P. Belli et al., Phys. Rev. C 87 (2013) 034607.

[94] P. Belli et al., Nucl. Phys. A 930 (2014) 195.

[95] M. Berglund, and M.E. Wieser, Pure Appl. Chem. 83 (2011) 397.

[96] F. Cappella et al., Eur. Phys. J. C 73 (2013) 2276.

[97] FIRB 2013: "Sviluppo di rivelatori a risposta anisotropa", PI: Cappella Fabio, Reference number: RBFR13THVM; Talk by R. Cerulli at Int. Conf. Dark matter, Dark Energy and their detection, Novosibirsk, Russia, July 2013, http://people.roma2.infn.it/∼dama/pdf/cerulli_novosibirsk2013.pdf; Talk by P. Belli at What Next workshop, Tor Vergata University, Rome, Italy, March 2014, http://people.roma2.infn.it/∼belli/belli_TorVergata_mar14.pdf.

DarkSide Annual Report to LNGS

C. E. Aalseth,[1] G. Acconcia,[2,3] F. Acerbi,[4,5] P. Agnes,[6] L. Agostino,[7] I. F. M. Albuquerque,[8,9] T. Alexander,[10,11] A. K. Alton,[12] P. Ampudia,[13,14] R. Ardito,[15,3] K. Arisaka,[16] I. J. Arnquist,[1] D. M. Asner,[1] H. O. Back,[1] B. Baldin,[11] G. Batignani,[17,18] K. Biery,[11] M. G. Bisogni,[17,18] V. Bocci,[19] A. Bondar,[20,21] G. Bonfini,[22] W. Bonivento,[14] M. Bossa,[23,22] B. Bottino,[24,25] A. Brigatti,[3] J. Brodsky,[8] F. Budano,[26,27] R. Bunker,[1] S. Bussino,[26,27] M. Buttafava,[2,3] A. Buzulutskov,[20,21] M. Cadeddu,[28,14] L. Cadonati,[10] M. Cadoni,[28,14] N. Calandri,[2,3] F. Calaprice,[8] L. Campajola,[29,30] N. Canci,[31,22] A. Candela,[22] H. Cao,[8] M. Caravati,[28,14] M. Cariello,[25] M. Carlini,[22] M. Carpinelli,[32,14] A. Castellani,[15,3] S. Catalanotti,[29,30] P. Cavalcante,[22] A. Chepurnov,[33] C. Cicalò,[14] M. Citterio,[3] A. G. Cocco,[30] S. Corgiolu,[13,14] G. Covone,[29,30] L. Crippa,[34,3] D. D'Angelo,[34,3] M. D'Incecco,[22] M. Daniel,[35] S. Davini,[23,22] S. De Cecco,[7] M. De Deo,[22] G. De Guido,[36,3] M. De Vincenzi,[26,27] P. Demontis,[32,14,37] A. Derbin,[38] A. Devoto,[28,14] F. Di Eusanio,[8] G. Di Pietro,[22,3] C. Dionisi,[19,39] A. Dolgov,[21] I. Dormia,[36,3] S. Dussoni,[18,17] E. Edkins,[40] A. Empl,[31] A. Fan,[16] A. Ferri,[4,5] C. O. Filip,[41] G. Fiorillo,[29,30] K. Fomenko,[42] G. Forster,[10,11] D. Franco,[6] G. E. Froudakis,[43] F. Gabriele,[22] A. Gabrieli,[32,14] C. Galbiati,[8,22] M. Ghioni,[2,3] A. Ghisi,[15,3] S. Giagu,[19,39] G. Gibertoni,[36,3] C. Giganti,[7] M. Giorgi,[18,17] G. K. Giovanetti,[22,8] M. L. Gligan,[41] A. Gola,[4,5] A. M. Goretti,[22] F. Granato,[44] M. Grassi,[17] J. W. Grate,[1] M. Gromov,[33] M. Guan,[45] Y. Guardincerri,[11] A. Gulinatti,[2,3] R. K. Haaland,[46] B. R. Hackett,[40] B. Harrop,[8] K. Herner,[11] E. W. Hoppe,[1] E. V. Hungerford,[31] Al. Ianni,[47,22] An. Ianni,[8,22] O. Ivashchuk,[48] I. James,[26,27] T. N. Johnson,[49] C. Jollet,[50] K. Keeter,[51] C. L. Kendziora,[11] V. Kobychev,[52] G. Koh,[8] D. Korablev,[42] G. Korga,[31,22] A. Kubankin,[48] M. Kuss,[17] M. Lissia,[14] X. Li,[8] G. U. Lodi,[36,3] P. Lombardi,[3] G. Longo,[29,30] P. Loverre,[19,39] S. Luitz,[53] R. Lussana,[2,3] L. Luzzi,[54,3] A. A. Machado,[55,22] I. N. Machulin,[56,57] L. Mais,[13,14] A. Mandarano,[23,22] L. Mapelli,[8] M. Marcante,[4,5] M. Mariani,[54,3] J. Maricic,[40] M. Marinelli,[24,25] L. Marini,[24,25] S. M. Mari,[26,27] C. J. Martoff,[44] M. Mascia,[13,14] Y. Ma,[45] A. Meregaglia,[50] P. D. Meyers,[8] T. Miletic,[44] R. Milincic,[40] J. D. Miller,[31] S. Moioli,[36,3] S. Monasterio,[13,14] D. Montanari,[11] A. Monte,[10] M. Montuschi,[22] M. Monzani,[53] M. Morrocchi,[18,17] P. Mosteiro,[8] B. J. Mount,[51] V. N. Muratova,[38] P. Musico,[25] J. Napolitano,[44] A. Nelson,[8] V. Nosov,[20,21] N. N. Nurakhov,[56] S. Odrowski,[22] A. Oleinik,[48] M. Orsini,[22] F. Ortica,[58,59] L. Pagani,[24,25] M. Pallavicini,[24,25] S. Palmas,[13,14] E. Pantic,[49] E. Paoloni,[17,18] S. Parmeggiano,[3] G. Paternoster,[4,5] F. Pazzona,[32,14] K. Pelczar,[60] L. A. Pellegrini,[36,3] N. Pelliccia,[58,59] S. Perasso,[6] P. Peronio,[2,3] F. Perotti,[15,3] R. Perruzza,[22] C. Piemonte,[4,5] F. Pilo,[17] A. Pocar,[10,8] S. Pordes,[11] D. A. Pugachev,[56,57] H. Qian,[8] K. Randle,[8] G. Ranucci,[3] M. Razeti,[14] A. Razeto,[22,8] I. Rech,[2,3] V. Regazzoni,[5] B. Reinhold,[40] A. L. Renshaw,[31,16] M. Rescigno,[19] M. Ricotti,[54,3] Q. Riffard,[6] S. Rizzardini,[13,14] A. Romani,[58,59] L. Romero,[35] B. Rossi,[30,8] N. Rossi,[22] D. Rountree,[61] A. Ruggeri,[2,3] D. Sablone,[22] P. Saggese,[3] P. Salatino,[62,30] L. Salemme,[62,30] W. Sands,[8] S. Sangiorgio,[63] M. Sant,[32,14] R. Santorelli,[35] M. Sanzaro,[2,3] C. Savarese,[23,22] E. Sechi,[13,14] E. Segreto,[55] D. A. Semenov,[38] A. Shchagin,[48] L. Shekhtman,[20,21] E. Shemyakina,[20,21] E. Shields,[8] M. Simeone,[62,30] P. N. Singh,[31] M. D. Skorokhvatov,[56,57] M. Smallcomb,[12] O. Smirnov,[42] A. Sokolov,[20,21] A. Sotnikov,[42] C. Stanford,[8] G. B. Suffritti,[32,14,37] Y. Suvorov,[16,22,56] D. Tamborini,[2,3] R. Tartaglia,[22] J. Tatarowicz,[44] G. Testera,[25] A. Tonazzo,[6] A. Tosi,[2,3] P. Trinchese,[29] E. V. Unzhakov,[38] A. Vacca,[13,14] M. Verducci,[19,39] F. Villa,[2,3] A. Vishneva,[42] B. Vogelaar,[61] M. Wada,[8] S. Walker,[29,30] H. Wang,[16] Y. Wang,[45,16] A. W. Watson,[44] S. Westerdale,[8] J. Wilhelmi,[44] M. M. Wojcik,[60] X. Xiang,[8] J. Xu,[8] C. Yang,[45] J. Yoo,[11] F. Zappa,[2,3] G. Zappalà,[4,5]

S. Zavatarelli,[25] A. Zec,[10] W. Zhong,[45] C. Zhu,[8] A. Zullo,[19] M. Zullo,[19] and G. Zuzel[60]

[1] *Pacific Northwest National Laboratory, Richland, WA 99354, USA*
[2] *Electronics, Information and Bioengineering Department, Politecnico di Milano and INFN, Milano 20133, Italy*
[3] *Istituto Nazionale di Fisica Nucleare, Sezione di Milano, Milano 20133, Italy*
[4] *Fondazione Bruno Kessler, Trento 38122, Italy*
[5] *TIFPA, Trento Institute for Fundamental Physics and Applications INFN, Trento 38123, Italy*
[6] *APC, Université Paris Diderot, CNRS/IN2P3, CEA/Irfu, Obs. de Paris, Sorbonne Paris Cité, Paris 75205, France*
[7] *LPNHE Paris, Université Pierre et Marie Curie, Université Paris Diderot, CNRS/IN2P3, Paris 75252, France*
[8] *Department of Physics, Princeton University, Princeton, NJ 08544, USA*
[9] *Instituto de Física, Universidade de São Paulo, São Paulo 05508-090, Brazil*
[10] *Amherst Center for Fundamental Interactions and Dept. of Physics, University of Massachusetts, Amherst, MA 01003, USA*
[11] *Fermi National Accelerator Laboratory, Batavia, IL 60510, USA*
[12] *Department of Physics and Astronomy, Augustana University, Sioux Falls, SD 57197, USA*
[13] *Department of Chemistry, Università degli Studi, Cagliari 09042, Italy*
[14] *Istituto Nazionale di Fisica Nucleare, Sezione di Cagliari, Cagliari 09042, Italy*
[15] *Civil and Environmental Engineering Department, Politecnico di Milano and INFN, Milano 20133, Italy*
[16] *Department of Physics and Astronomy, University of California, Los Angeles, CA 90095, USA*
[17] *INFN Sezione di Pisa, I-56127 Pisa, Italy*
[18] *Dipartimento di Fisica, Università di Pisa, I-56127 Pisa, Italy*
[19] *Istituto Nazionale di Fisica Nucleare, Sezione di Roma Uno, Roma 00185, Italy*
[20] *Budker Institute of Nuclear Physics SB RAS, Novosibirsk 630090, Russia*
[21] *Novosibirsk State University, Novosibirsk 630090, Russia*
[22] *Laboratori Nazionali del Gran Sasso, Assergi AQ 67010, Italy*
[23] *Gran Sasso Science Institute, L'Aquila AQ 67100, Italy*
[24] *Department of Physics, Università degli Studi, Genova 16146, Italy*
[25] *Istituto Nazionale di Fisica Nucleare, Sezione di Genova, Genova 16146, Italy*
[26] *Istituto Nazionale di Fisica Nucleare, Sezione di Roma Tre, Roma 00146, Italy*
[27] *Department of Physics and Mathematics, Università degli Studi Roma Tre, Roma 00146, Italy*
[28] *Department of Physics, Università degli Studi, Cagliari 09042, Italy*
[29] *Department of Physics, Università degli Studi Federico II, Napoli 80126, Italy*
[30] *Istituto Nazionale di Fisica Nucleare, Sezione di Napoli, Napoli 80126, Italy*
[31] *Department of Physics, University of Houston, Houston, TX 77204, USA*
[32] *Department of Chemistry and Pharmacy, Università degli Studi Sassari, Sassari 07100, Italy*
[33] *Skobeltsyn Institute of Nuclear Physics, Lomonosov Moscow State University, Moscow 119991, Russia*
[34] *Department of Physics, Università degli Studi, Milano 20133, Italy*
[35] *Centro de Investigaciones Energéticas, Medioambientales y Tecnológicas (CIEMAT), 28040 Madrid, Spain*
[36] *Chemistry, Material and Chemical Engineering Department, Politecnico di Milano and INFN, Milano 20133, Italy*
[37] *Consorzio Interuniversitario Nazionale per la Scienza e Tecnologia dei Materiali (INSTM), Università degli Studi Sassari, Sassari 07100, Italy*
[38] *St. Petersburg Nuclear Physics Institute NRC Kurchatov Institute, Gatchina 188350, Russia*
[39] *Università di Roma (Roma Uno), Roma 00185, Italy*
[40] *Department of Physics and Astronomy, University of Hawai'i, Honolulu, HI 96822, USA*
[41] *I(NCD)TIM, Cluj-Napoca 400293, Romania*
[42] *Joint Institute for Nuclear Research, Dubna 141980, Russia*
[43] *University of Crete, Rethymno 74100, Greece*
[44] *Department of Physics, Temple University, Philadelphia, PA 19122, USA*
[45] *Institute of High Energy Physics, Beijing 100049, China*
[46] *Fort Lewis College, Durango, CO 81301, USA*
[47] *Laboratorio Subterráneo de Canfranc, Canfranc Estación 22880, Spain*
[48] *Radiation Physics Laboratory, Belgorod National Research University, Belgorod 308007, Russia*

[49] *Department of Physics, University of California, Davis, CA 95616, USA*
[50] *IPHC, Université de Strasbourg, CNRS/IN2P3, Strasbourg 67037, France*
[51] *School of Natural Sciences, Black Hills State University, Spearfish, SD 57799, USA*
[52] *Institute for Nuclear Research, National Academy of Sciences of Ukraine, Kiev 03680, Ukraine*
[53] *SLAC National Accelerator Laboratory, Menlo Park, CA 94025, USA*
[54] *Energy Department, Politecnico di Milano and INFN, Milano 20133, Italy*
[55] *Institute of Physics Gleb Wataghin, Universidade Estadual de Campinas, São Paulo 13083-859, Brazil*
[56] *National Research Centre Kurchatov Institute, Moscow 123182, Russia*
[57] *National Research Nuclear University MEPhI, Moscow 115409, Russia*
[58] *Department of Chemistry, Biology and Biotechnology, Università degli Studi, Perugia 06123, Italy*
[59] *Istituto Nazionale di Fisica Nucleare, Sezione di Perugia, Perugia 06123, Italy*
[60] *Smoluchowski Institute of Physics, Jagiellonian University, Krakow 30348, Poland*
[61] *Department of Physics, Virginia Tech, Blacksburg, VA 24061, USA*
[62] *Department of Chemistry, Università degli Studi Federico II, Napoli 80126, Italy*
[63] *Lawrence Livermore National Laboratory, Livermore, CA 94550, USA*

The DarkSide Collaboration is currently running DarkSide-50, an experiment which searches for dark matter in the form of weakly interacting massive particles (WIMPs) colliding with argon nuclei and producing recoil atoms with tens of keV energy. The experiment uses a two-phase liquid argon time projection chamber as a detector, now filled with a total of 155 kg of low radioactivity argon. The TPC produces two light signals for each event; a direct scintillation signal (S1), and a delayed signal from proportional scintillation of ionization charge extracted into a high-field region of argon vapor above the liquid (S2). Powerful nuclear recoil discrimination is provided by pulse shape analysis of S1. The probability of misidentifying an electron recoil event as a nuclear recoil has been shown to be below one in 1.5×10^7, while maintaining the nuclear recoil acceptance at 90% for Ar recoil kinetic energies above 42 keV. The TPC is surrounded by a 4.0 m diameter Liquid Scintillator Veto (LSV), consisting of a stainless steel sphere instrumented with 110 PMTs and filled with 30 tonnes of low-^{14}C, boron-loaded liquid scintillator. The LSV is in turn surrounded by the 1 kt Water Cerenkov Detector (WCD; formerly the Borexino CTF) instrumented with 80 PMTs to veto the $1.1/(\mathrm{m}^2{\cdot}\mathrm{hr})$ cosmic-ray muons present at LNGS depth (3800 m.w.e.) [1, 2]. Signals from the LSV and WCD are used to reject events in the LAr TPC caused by cosmogenic (muon-induced) neutrons [3, 4] or by neutrons and γ-rays from radioactive contamination in the detector components.

During the past year, the collaboration passed a number of important milestones, culminating in the publication of the first dark matter search results obtained using a target of low-radioactivity argon extracted from underground sources. With a background-free exposure of (2616 ± 43) kg d we derived 90 % C.L. exclusion limits for the spin-independent WIMP-nucleon cross section of 3.1×10^{-44} cm^2 (1.4×10^{-43} cm^2, 1.3×10^{-42} cm^2) for WIMP masses of 100 GeV/c^2 (1 TeV/c^2, 10 TeV/c^2). When combined with the null result of our previous (1422 ± 67) kg d exposure with AAr, we obtain an exclusion limit of 2.0×10^{-44} cm^2 (8.6×10^{-44} cm^2, 8.0×10^{-43} cm^2) for WIMP masses of 100 GeV/c^2 (1 TeV/c^2, 10 TeV/c^2).

Considerable progress has also been made on R&D and funding proposals for the next scale-up phase of the DarkSide program, DarkSide-20k.

PACS numbers: 29.40.Gx, 95.35.+d, 95.30.Cq, 95.55.Vj

I. INTRODUCTION

Results from Previous Work: At the time of the previous Annual Report we were in the midst of recommissioning the detector after filling with 155 kg of low radioactivity argon from underground sources ("UAr"). This material had been extracted from underground gas wells in Colorado, purified at FNAL, and transported by sea to LNGS. After a final hot-Zr getter purification underground, the UAr was condensed into DarkSide-50 during the first week of April, 2015. Light yield and ionization charge lifetime of the UAr were measured in the detector and found to be essentially identical to those of the previous fill with purified commercial high purity argon.

The Annual Report presented in 2015 also detailed the reconstitution of the LSV after the discovery of excess ^{14}C radioactivity, traced to the inadvertent use of tetramethyl borane (TMB) synthesized from organic carbon sources. A technical paper descrbing the performance of the veto system has been published [5]. *In situ* calibration with gamma and neutron sources was carried out using the CALIS insertion system. Agreement with Geant4-based Monte Carlo results was achieved, indicating that the detector response to electron recoil events ("ER") as well as nuclear recoils ("NR") was well understood. The reconstituted veto was shown to detect all relevant neutron capture signals from the borated scintillator, giving a lower limit for the veto efficiency sufficient to insure zero neutron background for the full anticipated 3 yr run time.

This Year's Accomplishments: Principal results obtained by the collaboration this year include:

- Residual radioactivity in UAr was thoroughly studied. It contains ^{39}Ar activity a factor $(1.4 \pm 0.2) \times 10^3$ less than atmospheric argon. UAr was also found to contain (2.05 ± 0.13) mBq/kg of ^{85}Kr and <2 mBq/kg of radon-daughter alpha emitters.

- All detector systems have operated with excellent stability and noise performance in practically continuous running since last April.

- Algorithms for transverse localization of events ("(xy) localization") have been improved and are being validated using optical effects intrinsic to the detector.

- A new *in-situ* neutron calibration has been carried out with a ^{241}Am^{13}C source. When combined with further development of the "g4ds" Monte Carlo, this should lead to a significant improvement in the lower limit on the veto efficiency.

- The first dark matter search results with underground argon have been posted to the ArXiv [6] and accepted for publication as a Rapid Communication to Physical Review D.

- Preparations for a much larger experiment (DarkSide-20k) have begun, with significant R&D results on SiPM photodetectors and development of a baseline design.

II. RESIDUAL RADIOACTIVITY IN UAR

Fig. 1 (left) compares the measured zero-field spectra for the UAr and AAr targets, normalized to exposure. The background γ-ray lines originate from identified levels of ^{238}U, ^{232}Th, ^{40}K, and ^{60}Co in the detector construction materials, and are consistent with the expectations from our materials screening. The repeatability in the positions of the peaks between the AAr and UAr data shows the stability of the detector system as a whole. However, one unanticipated feature was found.

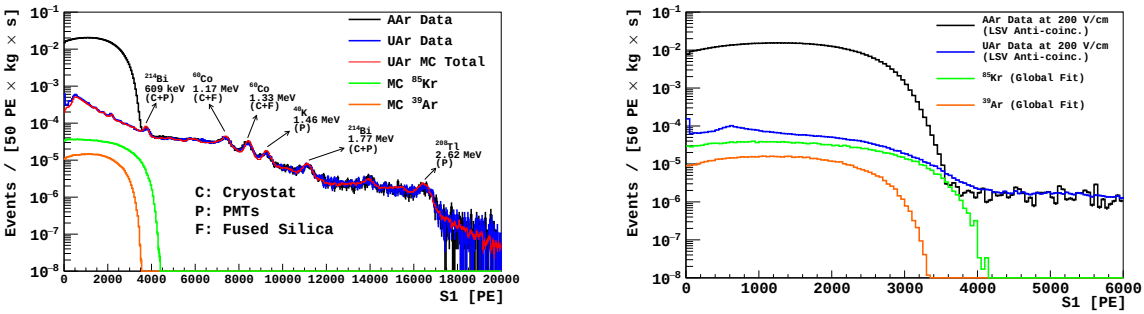

FIG. 1: **Left:** Live-time-normalized S1 pulse integral spectra (see text) obtained at zero drift field, with an AAr fill (black) and a UAr fill (blue). Also shown are the GEANT4 MC fit to the UAr data (red) and individual components of ^{85}Kr (green) and ^{39}Ar (orange) extracted from the fit. **Right:** Live-time normalized S1 pulse integral spectra from single-scatter events in AAr (black) and UAr (blue) taken with 200 V/cm drift field. Also shown are the ^{85}Kr (green) and ^{39}Ar (orange) levels as inferred from a MC fit. Note the peak in the lowest bin of the UAr spectrum, which is due to ^{37}Ar from cosmic-ray activation. The peak at ∼600 PE is due to γ-ray Compton backscatters.

During the fitting process it became apparent that a ^{85}Kr component is also present. This is particularly evident in Fig. 1 (right), which compares the UAr and AAr spectra taken with a 200 V/cm drift field. A z-cut (residual mass of ∼34 kg) has been applied to remove γ-ray events from the anode and cathode windows. Events identified as multiple scatters or coincident with a prompt signal in the LSV have also been removed. The ^{39}Ar activity of (0.73 ± 0.11) mBq/kg and ^{85}Kr activity of (2.05 ± 0.13) mBq/kg in UAr are determined by a combined MC fit to the spectra of S1 with field off (Fig. 1, left), S1 with field on (Fig. 1, right) and the z-position distribution. The uncertainties in the fitted activities are dominated by systematic uncertainties from varying fit conditions. The ^{39}Ar activity of the UAr corresponds to a depletion by a factor of $(1.4 \pm 0.2) \times 10^3$ relative to AAr.

An independent estimate of the ^{85}Kr decay rate is obtained by measuring its 0.43 % decay branch to metastable ^{85m}Rb, which gives a γ-ray with mean lifetime 1.46 µs following the β [7]. These decays give delayed coincidences, which appear as events with two (S1, S2) pulse pairs in a single event record. Such events are identifiable with ∼66 % efficiency, estimated using MC. We obtain a decay rate of ^{85}Kr via ^{85m}Rb of (33.1 ± 0.9) events/d. This is in agreement with the value (35.3 ± 2.2) events/d obtained from the known branching ratio and the spectral fit result. The presence of ^{85}Kr in UAr was unexpected, and we had not attempted to remove it by cryogenic distillation. The ^{85}Kr in UAr could come from atmospheric leaks or from deep underground natural fission decays. Fission-produced ^{85}Kr has been observed in deep underground water reservoirs, with specific activities the same order of magnitude as those of ^{39}Ar [8].

The wide dynamic range afforded by the dual-digitizer DAQ in DarkSide-50 allows full-energy alpha particle pulses to be collected during normal dark matter running. Clean peaks due to ^{222}Rn and its daughter ^{218}Po are seen within a fraction of a per cent of the expected pulse heights. The spatial distribution of these events is consistent with uniformity throughout the active volume, at rates corresponding to < 2 mBq/kg in the bulk argon.

III. CRYOSYSTEM PERFORMANCE AND STABILITY

Very low radon contamination is observed despite the presence of unavoidable radon emanation from cables, electronics, etc. This is achievable due to continuous fast gas-phase recirculation (30 slpm) through the DarkSide-50 purification loop, which includes an LN-cooled charcoal radon trap as well as a heated Zr getter. A correspondingly high level of chemical purification is achieved by

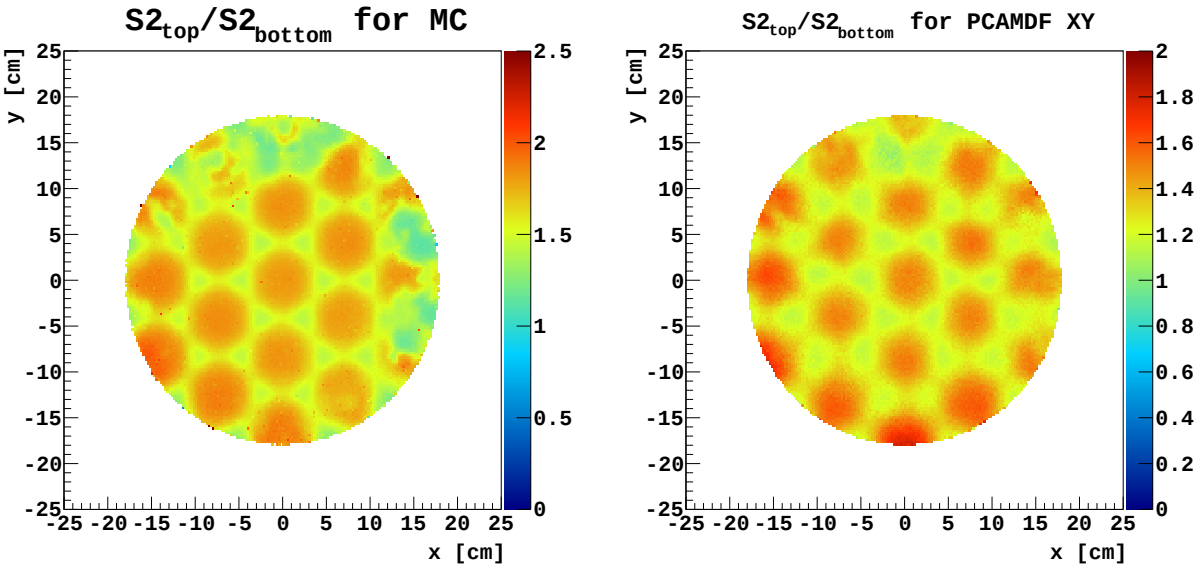

FIG. 2: Two-dimensional histogram showing the average ratio of S2 light detected on the top PMT array to that detected on the bottom array in each transverse position bin. Left: Monte Carlo AAr events. These events are uniformly distributed through the TPC volume. The Monte Carlo model includes reduced-efficiency regions of the TPB coating (e.g. upper right quadrant periphery) mapped from exeperimental data. Right: events from experimental data with AAr, with transverse position reconstructed usint one of the algorithms that have been developed (based on Principal Component Analysis [9, 10]. In both panels the red areas (top/bottom ratio approaching 2:1) occur under the known positions of the top PMT's, while the blue-green areas (top/bottom ratio only 1.5:1 or below) occur under the top PTFE reflector between PMTs. The general fidelity of the reconstructed pattern is evident. Quantitative comparison with the Monte Carlo distributons to determine the resolution is in progress.

this system, as indicated by the absence of a discernible decrease in S2 pulse height with event depth in the TPC. The corresponding lower limit on the drift lifetime exceeds 5 msec, compared to a maximum drift time in the detector of 0.37 msec. The system achieves this while maintaining long-term pressure stabillitiy in the TPC target within 0.6 mbar, and temperature stability within .02 K during months of steady operation.

IV. TRANSVERSE EVENT LOCALIZATION

Several independent algorithms have been developed which determine the transverse location of events using the distribution of S2 light over the 19 top PMT's. Validation of these methods was initially impeded by the generally smooth transverse distribution of events, lacking any localized features within the detector. Recently an optical effect within the detector has been found which provides transverse features for validation of the algorithms.

Each of the closely packed arrays of 19 circular PMTs in DarkSide-50 (one at the top and one at the bottom), are mounted and supported by a PTFE reflector with holes through which the PMTs view the scintillation light. The high reflectivity of this PTFE gives rise to a difference in the fraction of S2 light detected on the top vs. the bottom array ("top to bottom ratio"), for events occurring directly beneath a top PMT vs. events occurring between PMT's and therefore beneath the PTFE reflector. This difference is observed in the data and confirmed by the g4ds Monte Carlo, which includes a full simulation of the TPC optics.

The shape of the reflector is precisely known, so a plot of the top to bottom ratio vs. reconstructed transverse position can be compared to the known shape and the g4ds result, to determine the accuracy of the transverse position reconstruction. Fig. 2 shows an example of such a plot, com-

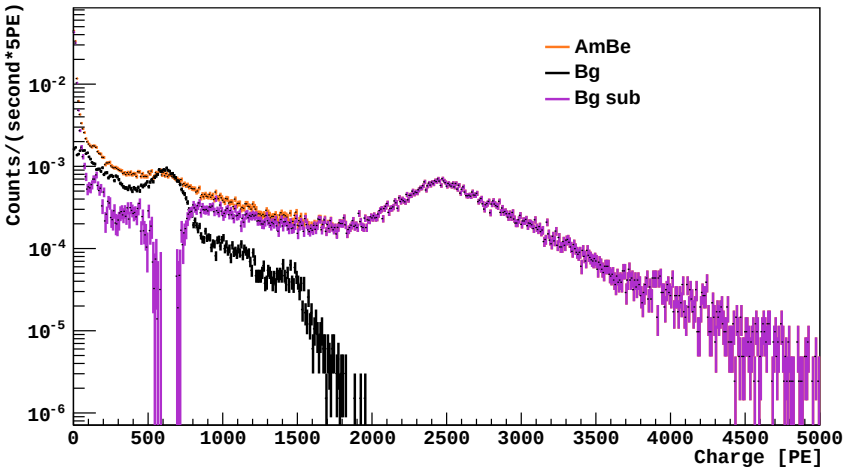

FIG. 3: Cluster charge spectra from self-triggered LSV, showing ^{241}Am^{13}C, background, and the difference, normalized to the ^{60}Co peak from the cryostat steel. The excess of events below 300 PE is believed to be from neutron elastic scattering during thermalization in the scintillator. Similar events (not shown) are also observed in prompt coincidence with identified neutron events in the TPC, as neutrons scatter out of the LAr and back into the scintillator.

paring Monte Carlo events on the left with AAr data reconstructed using one of the xy algorithms on the right. Events in this plot were subject to a data quality cut requiring that they reconstruct within the active radius of the detector with all three of the xy reconstruction algorithms that have been developed. The general fidelity of the reconstruction over the area is apparent, as are known and iteratively mapped areas of varying sensitivity in the transverse plane that are included in the Monte Carlo. Analysis is underway to quantify the relationship between the reconstructed data and the MC predictions.

While this method gives an average measure of the accuracy of the transverse reconstruction, it has not so far enabled a sensitive study of possible rare outliers or absolute accuracy of the algorithm. Work continues on this subject.

V. ^{241}AM^{13}C NEUTRON CALIBRATION

In situ neutron source calibrations with AmBe were described in our previous Annual Report. Signals from neutron capture on ^{10}B in the TMB were observed well above the LSV analysis threshold for both allowed channels [11]:

$$\begin{aligned} ^{10}\mathrm{B} + n &\rightarrow \alpha\,(1775\,\mathrm{keV}) + {}^{7}\mathrm{Li} \qquad (\mathrm{BR}: 6.4\,\%) \\ ^{10}\mathrm{B} + n &\rightarrow \alpha\,(1471\,\mathrm{keV}) + {}^{7}\mathrm{Li}^{*} \qquad (\mathrm{BR}: 93.6\,\%) \\ {}^{7}\mathrm{Li}^{*} &\rightarrow {}^{7}\mathrm{Li} + \gamma\,(478\,\mathrm{keV}) \end{aligned}$$

The neutron capture lifetime τ_c was determined to be 22.1 ± 0.2 μsec, consistent with expectations for the present 5% TMB concentration in the scintillator.

From AmBe data and MC simulations, we estimated a detection efficiency of $\sim$99.2 % for radiogenic neutrons coming from detector components when using these neutron capture signals in a $5\tau_c$ veto gate after a TPC event. About 15% of the detector live time was lost due to accidental coincidences with the long capture gate. This efficiency is sufficient to completely suppress the expected radiogenic neutron background in DarkSide-50. Further improvement in the veto efficiency with a possible reduction of the accidental coincidence losses would be expected

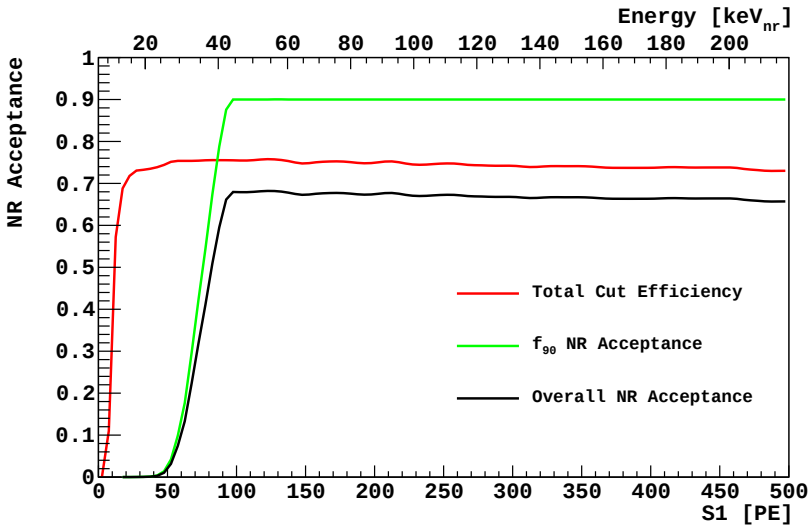

FIG. 4: Combined acceptance of the physics cuts (red), acceptance of the f_{90} NR cut (green) and the final cumulative NR acceptance in UAr data (black).

from detecting the prompt signals generated by neutron elastic scattering prior to thermalization in the scintillator. However, the prompt γ-rays present with the AmBe neutrons interfered with the investigation of detection efficiency for the thermalization signal.

To access the thermalization signal, a neutron source based on ^{241}Am^{13}C was used. The neutron production mechanism in this case is $\alpha + {}^{13}\mathrm{C} \rightarrow {}^{16}\mathrm{O}(\mathrm{g.s.}) + \mathrm{n}$. The produced neutrons are quasi-monoenergetic at 4 MeV. To eliminate decay γ-rays or other radiation in prompt coincidence with the neutrons, the energy of the alpha particles is degraded well below the 5.05 MeV threshold for production of ^{16}O*, before the alphas encounter the ^{13}C. The 59 keV gamma rays from the ^{241}Am decay are suppressed by five orders of magnitude with a 2 mm thick Pb shield around the source, and higher energy decay gamma rays occur only at a few parts in 10^5 per alpha decay. This leaves the prompt region after a TPC event clear of background, allowing the thermalization signals to be studied.

A calibration exposure of several weeks was undertaken using a ~0.1 n/sec AmC source. Figure 3 shows cluster charge spectra with the ^{241}Am^{13}C source in the LSV when it is self-triggered (no TPC hit requirement). The resulting data is still being analyzed, but there are strong indications that the pulses below 300 PE in Figure 3 are thermalization signals, and that these are being observed with high efficiency as expected. This may allow the criteria for vetoing an event as neutron-associated based on LSV signals to be changed, reducing the accidental coincidence live time losses without affecting the veto efficiency.

VI. UAR DARK MATTER SEARCH RESULT

A non-blind physics analysis has been performed on data from an initial running period with the UAr fill, consisting of 70.9 live-days after data quality cuts. The LAr TPC event selection and data analysis procedures were intentionally kept as similar as possible to those of the previous AAr exposure described in Ref. [12]. Details of the analysis are given in a paper posted to the ArXiv [6] and accepted for publication as a Rapid Communication to Physical Review D.

The combined acceptance of all the physics cuts (including the veto cuts) to retain single-scatter NR events is shown as a function of S1 in Fig. 4. The acceptance is >70 % and approximately independent of S1 above 20 PE, with the major loss being due to the accidental rate of the delayed veto cut. The distribution of events in the f_{90} vs. S1 plane, after all quality and physics cuts, is

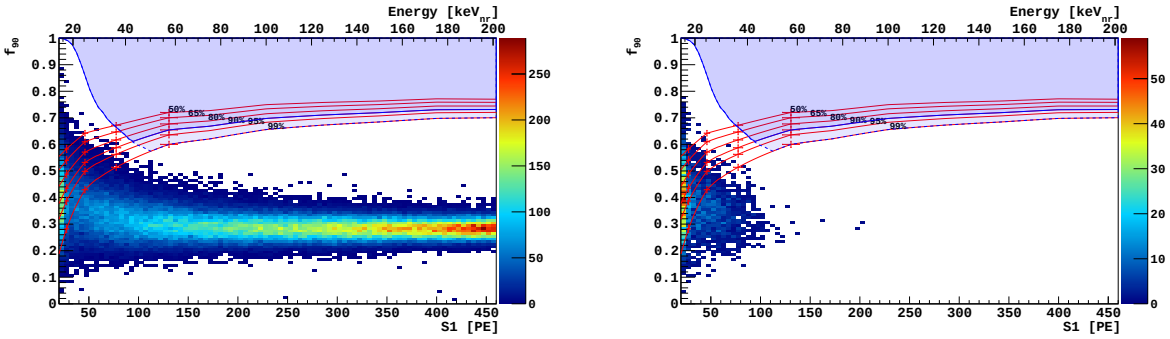

FIG. 5: **Left:** Distribution of events in the f_{90} vs S1 plane which survive all quality and physics cuts (including veto cuts). Shaded blue with solid blue outline: WIMP search region. Percentages label the f_{90} acceptance contours for NRs, drawn by connecting points (shown with uncertainties) at which the acceptance was determined from the corresponding SCENE measurements. Lighter shaded blue with dashed blue line show that extending the WIMP search region to 99 % f_{90} NR acceptance is still far away from ER backgrounds. **Right:** Distribution of events in the f_{90} vs S1 plane which survive all quality and physics cuts, and which in addition survive a radial cut and a S2/S1 cut (see text).

shown in the left panel of Fig. 5.

The WIMP search region is defined as a region in the f_{90} vs. S1 plane with known high acceptance for nuclear recoils and low leakage of single-scatter ER events. NR acceptance curves are established using the median f_{90} values for NR measured in the SCENE experiment [13, 14], inserted into a statistical model for the f_{90} distribution, as described in Refs. [12, 15, 16].

The initial period of UAr data contains 1.26×10^5 events in the energy region of interest, defined as 20 PE to 460 PE (13 $\mathrm{keV_{nr}}$ to 201 $\mathrm{keV_{nr}}$), with none falling in the WIMP search box.

Dark matter limits from the present exposure are determined from our WIMP search region using the standard isothermal galactic WIMP halo parameters (v_{escape}=544 km/s, v_0=220 km/s, v_{Earth}=232 km/s, ρ_{dm}=0.3 GeV/(c^2 cm^3), see [12] and references cited therein). Given the background-free result shown above, we derive a 90 % C.L. exclusion curve corresponding to the observation of 2.3 events for spin-independent interactions. When combined with the null result of our previous AAr exposure, we obtain a 90 % C.L. upper limit on the WIMP-nucleon spin-independent cross section of 2.0×10^{-44} cm^2 (8.6×10^{-44} cm^2, 8.0×10^{-43} cm^2) for a WIMP mass of 100 GeV/c^2 (1 TeV/c^2, 10 TeV/c^2). Fig. 6 compares these limits to those obtained by other experiments.

At present we are in the midst of changing to a blind analysis for the whole DarkSide-50 UAr exposure not included in the above initial study. Software has been developed and is being put in place which hides from analyzers those events within an expanded region encompassing the WIMP search box used for the non-blind analysis. As improved background models are developed they will be tested by opening restricted regions on the borders of the blinded region (but still outside the eventual anticipated WIMP search region), and comparing the model predictions to the test-region data. This process is to converge to an understanding of all backgrounds at the level necessary to predict the remaining background in a suitable WIMP search region (or as anticipated, the absence thereof) at the level of 0.1 event in the full DarkSide-50 exposure.

The DarkSide-50 detector is currently operating and accumulating exposure in a stable, low-background configuration. Data taking is interrupted only for scheduled calibrations. Currently over 225 live-days of UAr data has been accumulated, with the progression indicated in Figure 7.

We plan to conduct a 3 yr dark matter search. Further planned improvements include increased calibration statistics, improvements in data analysis including the inception of blind analysis, and improved understanding of non-^{39}Ar backgrounds. Fig. 5 (right) demonstrates available improvements in background rejection, which we did not utilize in this analysis. For this figure, xy fiducialization was added, requiring the reconstructed radius to be less than 10 cm. An S2/S1 cut

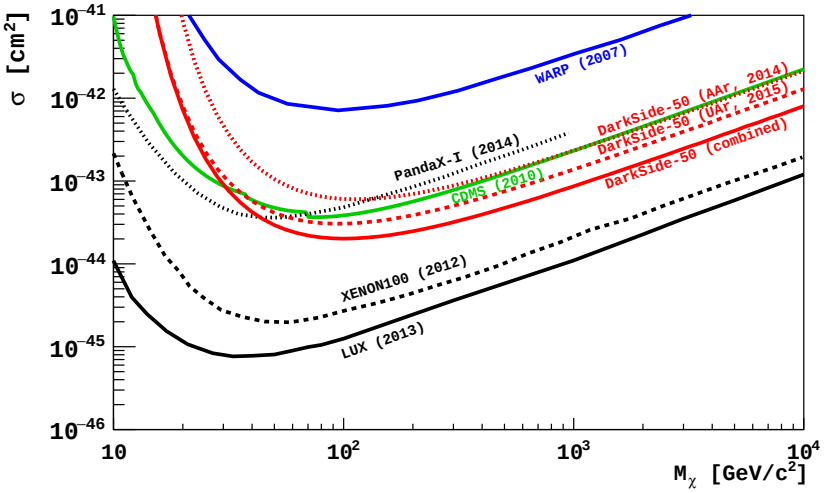

FIG. 6: Comparison of spin-independent WIMP-nucleon cross section 90 % C.L. exclusion plot for the DarkSide-50 AAr (dotted red) and UAr campaign (dashed red), and combination of the UAr and AAr [12] campaigns (solid red). Also shown are results from LUX [17] (solid black), XENON100 [18] (dashed black), CDMS [19] (solid green), PandaX-I [20] (dotted black), and WARP [21] (magenta).

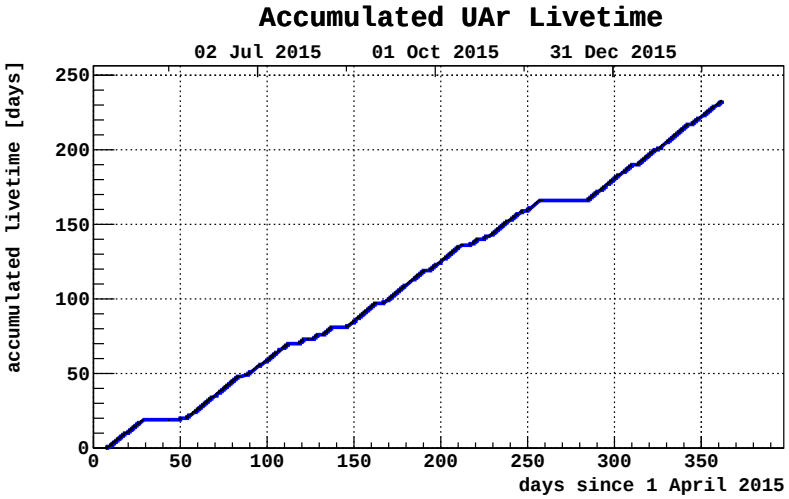

FIG. 7: DarkSide-50 WIMP search livetime history since UAr fill on April 1, 2015.

requiring that S2/S1 be lower than the median value for NRs was also applied. As the figure shows, this gives an even greater separation between the events surviving the selection and the previously defined WIMP search region. Should a signal appear in region of interest, the S2/S1 parameter would provide a powerful additional handle in understanding its origin.

VII. PROGRESS TOWARD THE NEXT GENERATION DARKSIDE DETECTOR

Based on the overall success of DarkSide-50 and the UAr running particularly, members of the collaboration have been working intensively on a wide-ranging program of R&D (supported by INFN) to enable the next generation LAr detector, currently referred to as DarkSide-20k. This is envisioned as a 30 t (20 t fiducial) detector, filled with low radioactivity argon. DarkSide-20k is designed to achieve a background-free exposure of 100 t yr, reaching WIMP-nucleon cross section exclusion/detection limits of $10^{-47}(10^{-46})$ cm^2 for a WIMP mass of 1(10) TeV/c^2. The design

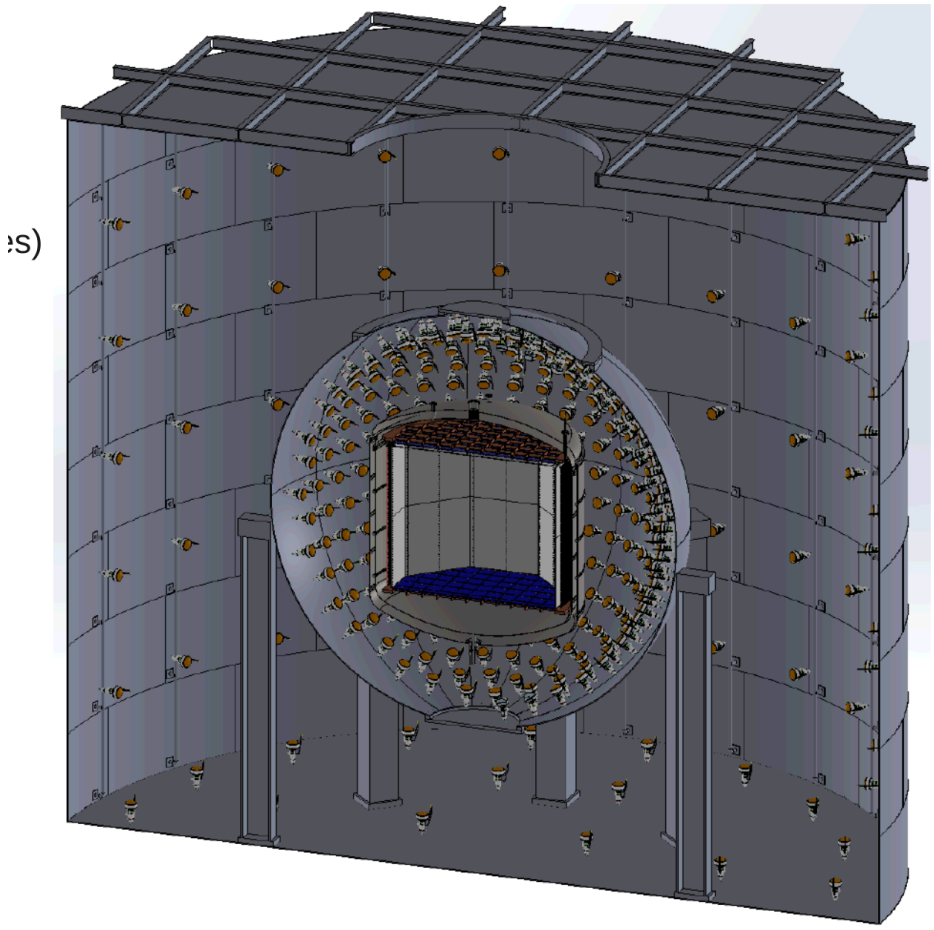

FIG. 8: Conceptual overview of DarkSide-20k within its new veto/shield system. The TPC active volume is 241 cm tall and 356 mm in diameter. A new LSV 7 meters in diameter, and a new WCD 14 meters in diameter and 14 meters tall are required for the design.

incorporates a number of technology advances, perhaps most notably the use of SiPM light sensors instead of PMTs. R&D in collaboration with SiPM producer FBK has already yielded impressive results (Figure 9), achieving dark count rates per unit area at LAr temperature comparable to those of PMT's.

Timely production of sufficient low radioactivity argon to fill DarkSide-20k is a major challenge. Two new facilities are envisioned to meet this challenge. Urania is the name given to a new, greatly improved and expanded extraction plant to be constructed at the same Doe Canyon, Colorado underground gas well from which the existing UAr supply was extracted. Urania is projected to extract and purify UAr at ∼100 kg/day. Meanwhile a very large cryogenic distillation facility for active isotopic purification of argon has begun construction at the Carbosulcis Seruci mine in Sardinia, with support from INFN and La Regione Sarda. This facility, referred to as "Aria", will accept UAr as feedstock and deliver DAr- argon further depleted in ^{39}Ar by a factor of ∼10 per pass, and with ^{85}Kr reduced by a factor of about 1000 per pass. The Aria throughput is anticipated to be initially 10 kg/d, increasing to 150 kg/d in a second phase.

The collaboration eagerly anticipates further membership growth and additional support for DarkSide-20k from agencies in the USA and other countries, enabling a planned 2020 completion of the detector and start of data taking.

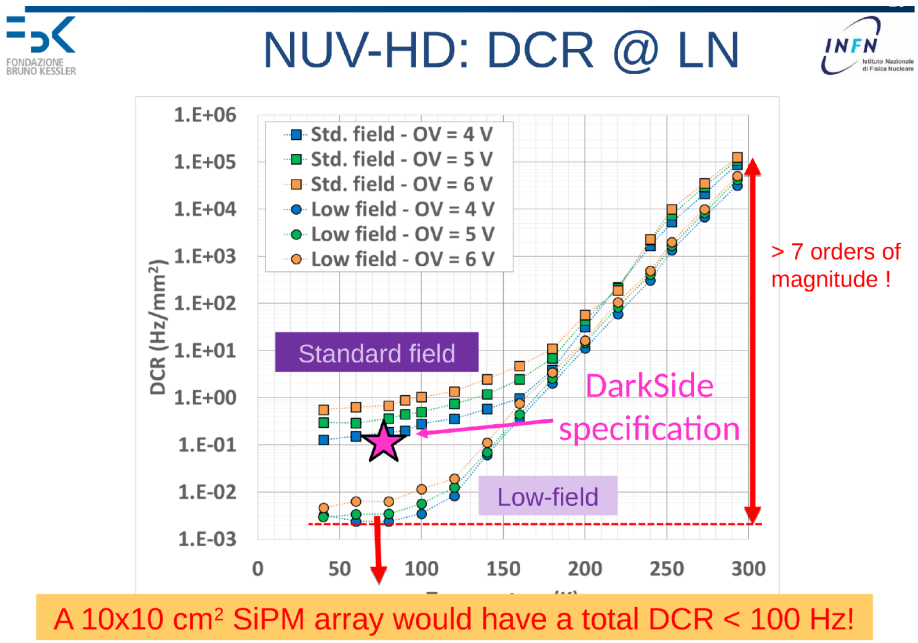

FIG. 9: Temperature dependence of the dark count rate (DCR) per unit area for R&D SiPM's produced at FBK for DarkSide. At the boiling temperature of LAr, the new "Low Field" variant has a rate corresponding to <100 Hz in a 10 x 10 cm^2 collecting area.

VIII. ACKNOWLEDGMENTS

ACKNOWLEDGMENTS

The DarkSide-50 Collaboration would like to thank LNGS laboratory and its staff for invaluable technical and logistical support. This report is based upon work supported by the US NSF (Grants PHY-0919363, PHY-1004072, PHY-1004054, PHY-1242585, PHY-1314483, PHY-1314507 and associated collaborative grants; Grants PHY-1211308 and PHY-1455351), the Italian Istituto Nazionale di Fisica Nucleare, the US DOE (Contract Nos. DE-FG02-91ER40671 and DE-AC02-07CH11359), and the Polish NCN (Grant UMO-2012/05/E/ST2/02333). We thank the staff of the Fermilab Particle Physics, Scientific and Core Computing Divisions for their support. We acknowledge the financial support from the UnivEarthS Labex program of Sorbonne Paris Cité (ANR-10-LABX-0023 and ANR-11-IDEX-0005-02) and from the São Paulo Research Foundation (FAPESP).

[1] G. Bellini et al. (The Borexino Collaboration), JINST, **6**, P05005 (2011).
[2] G. Bellini et al. (The Borexino Collaboration), JCAP, **2012**, 015 (2012).
[3] G. Bellini et al. (The Borexino Collaboration), JCAP, **2013**, 049 (2013).
[4] A. Empl, E. V. Hungerford, R. Jasim, and P. Mosteiro, JCAP, **2014**, 064 (2014).
[5] P. Agnes et al., Journal of Instrumentation, **11**, P03016 (2016).
[6] P. Agnes et al., ArXiv:1510.00702 (2015), accepted by Phys. Rev. D. Rapid Comm.
[7] R. B. Firestone, C. M. Baglin, and S. Y. F. Chu, *Table of isotopes*, Wiley-Interscience (1999).
[8] B. E. Lehmann, S. N. Davis, and J. T. Fabryka-Martin, Water Resour. Res., **29**, 2027 (2010).
[9] *TPrincipal class reference*, `https://root.cern.ch/doc/v606/classTPrincipal.html`, accessed: 2016-03-29.
[10] *TMultiDimFit class reference*, `https://root.cern.ch/doc/master/classTMultiDimFit.html`, accessed: 2016-03-29.

[11] A. Wright, P. Mosteiro, B. Loer, and F. P. Calaprice, Nucl. Inst. Meth. A, **644**, 18 (2011).
[12] P. Agnes et al. (The DarkSide Collaboration), Phys. Lett. B, **743**, 456 (2015).
[13] T. Alexander et al. (The SCENE Collaboration), Phys. Rev. D, **88**, 092006 (2013).
[14] H. Cao et al. (The SCENE Collaboration), Phys. Rev. D, **91**, 092007 (2015).
[15] D. V. Hinkley, Biometrika, **56**, 635 (1969).
[16] M. G. Boulay and A. Hime, Astropart. Phys., **25**, 179 (2006).
[17] D. S. Akerib et al. (The LUX Collaboration), Phys. Rev. Lett., **112**, 091303 (2014).
[18] E. Aprile et al. (The XENON100 Collaboration), Phys. Rev. Lett., **109**, 181301 (2012).
[19] D. S. Akerib et al. (The CDMS Collaboration), Science, **327**, 1619 (2010).
[20] M. Xiao et al. (The PandaX Collaboration), Sci. China Phys. Mech. Astron., **57**, 2024 (2014).
[21] P. Benetti et al. (The WArP Collaboration), Astropart. Phys., **28**, 495 (2008).

GERDA – the search for neutrino less double beta decay of ^{76}Ge

M. Agostini [a], M. Allardt [d], A.M. Bakalyarov [m], M. Balata [a], I. Barabanov [k], L. Baudis [s], C. Bauer [g], E. Bellotti [h,i], S. Belogurov [l,k], S.T. Belyaev [m], A. Bettini [p,q], L. Bezrukov [k], T. Bode [o], D. Borowicz [c,e], V. Brudanin [e], R. Brugnera [p,q], A. Caldwell [n], C. Cattadori [i], A. Chernogorov [l], V. D'Andrea [a], E.V. Demidova [l], N. Di Marco [a], A. Domula [d], E. Doroshkevich [k], V. Egorov [e], R. Falkenstein [r], N. Frodyma [c], A. Gangapshev [k,g], A. Garfagnini [p,q], C. Gooch [n], P. Grabmayr [r], V. Gurentsov [k], K. Gusev [m,e,o], C. Hahne [d], J. Hakenmüller [g], A. Hegai [r], M. Heisel [g], S. Hemmer [p,q], W. Hofmann [g], M. Hult [f], L.V. Inzhechik [k], L. Ioannucci [a], J. Janicskó Csáthy [o], J. Jochum [r], M. Junker [a], V. Kazalov [k], T. Kihm [g], I.V. Kirpichnikov [l], A. Kirsch [g], A. Kish [s], A. Klimenko [g,e], R. Kneißl [n], J. Knies [r], K.T. Knöpfle [g], O. Kochetov [e], V.N. Kornoukhov [l,k], V.V. Kuzminov [k], M. Laubenstein [a], A. Lazzaro [o], V.I. Lebedev [m], B. Lehnert [d], H.Y. Liao [n], M. Lindner [g], I. Lippi [q], A. Lubashevskiy [g,e], B. Lubsandorzhiev [k], G. Lutter [f], B. Majorovits [n], W. Maneschg [g], G. Marissens [f], E. Medinaceli [p,q], M. Miloradovic [s], R. Mingazheva [s], M. Misiaszek [c], P. Moseev [k], I. Nemchenok [e], S. Nisi [a], K. Panas [c], L. Pandola [b], K. Pelczar [c], A. Pullia [j], M. Reissfelder [g], S. Riboldi [j], N. Rumyantseva [e], C. Sada [p,q], F. Salamida [i], M. Salathe [g], C. Schmitt [r], B. Schneider [d], J. Schreiner [g], O. Schulz [n], B. Schwingenheuer [g], S. Schönert [o], A-K. Schütz [r], H. Seitz [n], O. Selivanenko [k], E. Shevchik [e], M. Shirchenko [m,e], H. Simgen [g], A. Smolnikov [g], L. Stanco [q], L. Vanhoefer [n], A.A. Vasenko [l], A. Veresnikova [k], K. von Sturm [p,q], V. Wagner [g], A. Wegmann [g], T. Wester [d], C. Wiesinger [o], M. Wojcik [c], E. Yanovich [k], I. Zhitnikov [e], S.V. Zhukov [m], D. Zinatulina [e], K. Zuber [d], and, G. Zuzel [c].

[a]) INFN Laboratori Nazionali del Gran Sasso and Gran Sasso Science Institute, Assergi, Italy

[b]) INFN Laboratori Nazionali del Sud, Catania, Italy

[c]) Institute of Physics, Jagiellonian University, Cracow, Poland

[d]) Institut für Kern- und Teilchenphysik, Technische Universität Dresden, Dresden, Germany

[e]) Joint Institute for Nuclear Research, Dubna, Russia

[f]) Institute for Reference Materials and Measurements, Geel, Belgium

[g]) Max-Planck-Institut für Kernphysik, Heidelberg, Germany

[h]) Dipartimento di Fisica, Università Milano Bicocca, Milan, Italy

[i]) INFN Milano Bicocca, Milan, Italy

[j]) Dipartimento di Fisica, Università degli Studi di Milano e INFN Milano, Milan, Italy

[k]) Institute for Nuclear Research of the Russian Academy of Sciences, Moscow, Russia

[l]) Institute for Theoretical and Experimental Physics, Moscow, Russia

[m]) National Research Centre "Kurchatov Institute", Moscow, Russia
[n]) Max-Planck-Institut für Physik, Munich, Germany
[o]) Physik Department and Excellence Cluster Universe, Technische Universität München, Germany
[p]) Dipartimento di Fisica e Astronomia dell'Università di Padova, Padua, Italy
[q]) INFN Padova, Padua, Italy
[r]) Physikalisches Institut, Eberhard Karls Universität Tübingen, Tübingen, Germany
[s]) Physik Institut der Universität Zürich, Zurich, Switzerland

1 Introduction

The GERmanium Detector Array (GERDA) experiment searches for neutrinoless double beta decay of the isotope ^{76}Ge. In a first phase Ge detectors made from material with an enriched ^{76}Ge fraction of about 86% were operated in a liquid argon cryostat [12]. Data taking stopped in October 2013. With an exposure of 21.6 kg·yr and a background index at the Q value of the decay ($Q_{\beta\beta} = 2039\,\text{keV}$) of 0.01 cts/(keV·kg·yr) a lower limit for the half life of $T^{0\nu}_{1/2} > 2.1 \cdot 10^{25}$ yr (90% C.L.) was measured. After about two years of hardware modifications and commissioning data taking for the second phase started in December 2015.

This report discusses results published in 2015 from Phase I data and the hardware activities before the start of Phase II.

2 Published results

Out of the papers and proceedings published during the year 2015 (see sec. 6) we would like to highlight some of the results in this section. Two figures from our publications have been selected as cover pages of the journals (IOP Image of the week and Eur. J. Phys. C 57); in addition the paper on the excited states was high lighted by the IOP lab talk selection.

2.1 Improved half life for $2\nu\beta\beta$ emission

A previous publication with an exposure of about 5 kg·yr had provided a value for the half life for $2\nu\beta\beta$ emission [13]. Using the full data set of Phase I as well as the validated background model an improved result was obtained [14]. The inclusion of more components into the reference background model results in a slight increase of the best estimate for $T^{2\nu}_{1/2}$. In this analysis the emphasis was given to determine the systematic uncertainties in particular. The half live from the Phase I was determined to $T^{2\nu}_{1/2} = (1.926 \pm 0.094) \cdot 10^{21}$ yr [11] with an unprecedented precision (<5 %) with respect to previous experiments using ^{76}Ge.

2.2 $2\nu\beta\beta$ decay of ^{76}Ge into excited states

Double beta emission might proceed via an excited states of the daughter nucleus, albeit with smaller phase space due to the reduced available energy. The population of an excited state is recognized by the respective decay gamma. Thus the data set was searched for coincidences between two germanium detectors. The background model was used to predict single and coincident spectra; it served also to optimize the selection and cut criteria. In Fig. 1, left the simulation clearly show the Compton scattering of the 1542 keV photon from ^{42}K. On the right the selected

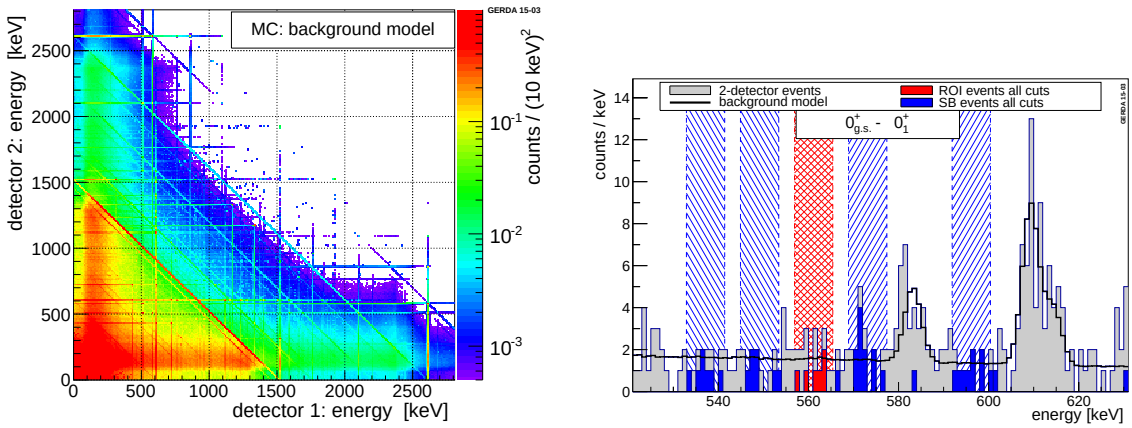

Figure 1: Left: Events simulated for the background model showing the coincident energy deposition in two detectors. *(IOP image of the week.)*
Right: Single-energy spectra around the ROI for the decay mode $0^+_{\rm gs} \rightarrow 0^+_1$. Shown are all two-detector events after the optimized individual detector threshold and sum energy limit cuts (light gray) and the corresponding background curves (black). The optimized cuts result in different two-detector spectra for each decay mode. Also shown are the ROI (shaded red) and SB region (shaded blue). Highlighted are events that are tagged as ROI (red) and SB (blue) after all cuts and that are used for the limit setting. Note that the histograms contain two entries per event and that one entry may lie outside the tagging region.

data for the $0^+_{\rm gs} \rightarrow 0^+_1$ are shown together with background simulations and the region of interest (ROI, red) and the "side band" (SB, blue) for background estimation. No signal was found and the best previous limit could be improved by a factor of 50 to $T^{2\nu}_{1/2}(0^+_{gs} \rightarrow 0^+_1) > 3.7 \cdot 10^{23}$ yr (90%C.L.) [1].

2.3 New limit on Majoron emission

The double beta decay may be accompanied by the emission of one or more new particles like Majorons. Their number and masses determine the phase space and thus the shape of the spectrum. The GERDA Phase I energy distributions have been searched for possible contributions with the corresponding spectral shapes. Since the background is lower than in previous Ge experiments, GERDA could set half live limits in the range of 10^{23} yr for the different decay modes - about a factor of 5 better than before. For the standard mode (one Majoron, spectral index $n = 1$), see Fig. 2, the lower limit is determined as $T^{0\nu\chi}_{1/2} > 4.2 \cdot 10^{23}$ yr (90% C.L.). From the lower limit on $T^{0\nu\chi}_{1/2}$ an upper limit on the effective neutrino-Majoron coupling constant $\langle g \rangle < (3.4 - 8.7) \cdot 10^{-5}$ can be inferred [11].

2.4 Improved energy resolution via the ZAC filter

The presence of low-frequency noise in the signals of GERDA Phase I mostly induced by microphonic disturbance leads to a degraded energy resolution for some of the deployed detectors. Spectroscopic performance can be improved by the use of the Zero Area Cusp (ZAC) shaping filter. This novel filter is obtained by subtracting two parabolas from the sides of the cusp filter keeping the area under the parabolas equal to that underlying the cusp (Fig. 3 left). A selection

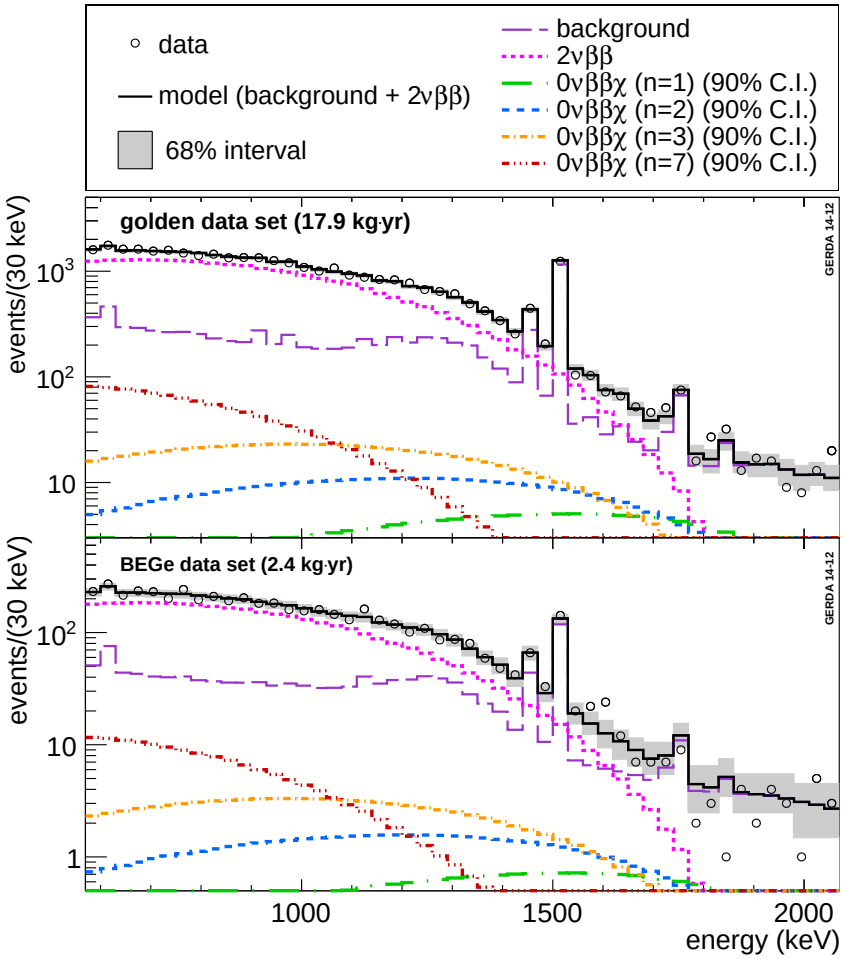

Figure 2: Best-fit model and data energy spectrum for the coaxial and the BEGe data sets for the case of Majoron emission (spectral index $n = 1$). The contributions from $2\nu\beta\beta$ decay and the background contributions are shown separately. The best-fit model does not contain the contributions from $0\nu\beta\beta\chi$. The smallest interval of 68 % probability for the model expectation is indicated in grey. Also shown is the upper limit for $0\nu\beta\beta\chi$ decay with $n = 1$ as determined from the 90 % quantile of the marginalized posterior probability for $1/T_{1/2}^{0\nu\chi}$. For illustrative purpose, also the upper limits at 90 % C.I. of the other three spectral indices $n = 2, 3, 7$ are reported.

of calibration runs has been exploited for the optimization of the ZAC filter. All calibration data sets have then been reprocessed using the optimal filter parameters. An average improvement of 0.30 keV in FWHM for the 2.6 MeV ^{208}Tl peak has been obtained for both coaxial and BEGe detectors. In one case (Fig. 3 right) the energy resolution improved by 0.86 keV with the excellent low-frequency rejection provided by the ZAC filter [5].

The stability of the filter parameters over time for the same detector configuration in GERDA along with its outstanding low-frequency noise rejection capabilities provides a FWHM improvement of 0.40 (0.30) keV at the ^{42}K line in the Phase I physics data for the coaxial (BEGe) detectors. Any improvement in the energy resolution will increase the sensitivity of the experiment and allow a better understanding of the experimental background.

In a future analysis of the $0\nu\beta\beta$ decay, the existing Phase I data will be reprocessed with the

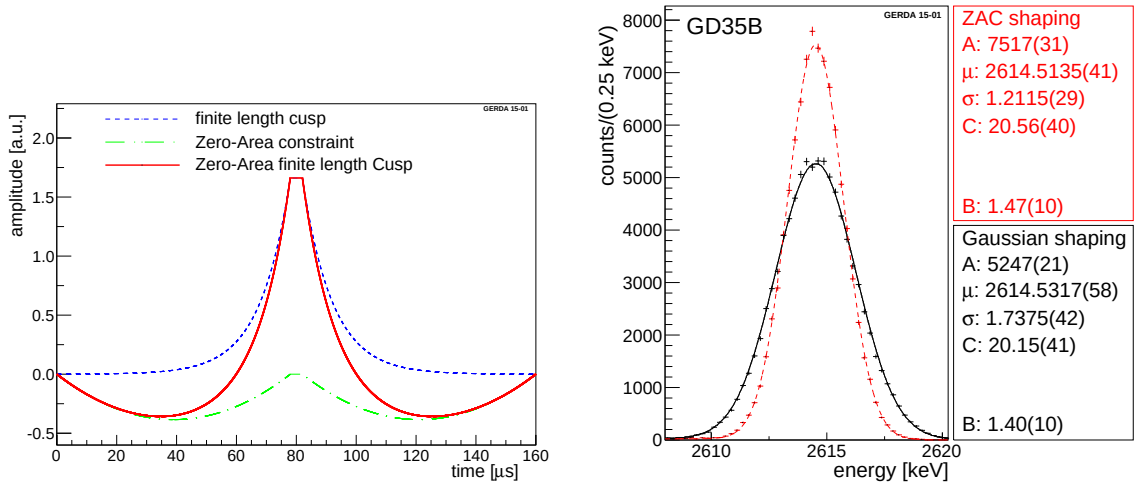

Figure 3: Left: Amplitude versus time for the ZAC filter (red full line). It is composed of the finite-length cusp (blue dashed) from which two parabolas are subtracted on the cusp sides (green dash-dotted).
Right: ^{208}Tl FEP data for GD35B at 2614.5 keV. The curves and parameter values corresponding to the best fit for the ZAC and the pseudo-Gaussian shaping are shown.

ZAC filter and combined with Phase II data.

3 Hardware modifications

The hardware modifications for Phase II include the installation of a new veto based on the readout of the argon scintillation light and new holders and electronics for the Ge detectors. Due to the larger number of electronic channels inside the argon, the complete cabling including the energy chain and feedthroughs were exchanged as well as some hardware for the calibration system. The latter includes new ^{228}Th sources and new safety features to avoid damages to the mechanics such as the one experienced in Phase I.

In 2015, six commissioning tests runs with one to five detector strings were performed. In the following the hardware and some commissioning results will be discussed.

3.1 LAr veto

To optimize the detection of argon scintillation light and to increase the reliability a hybrid system was chosen comprising of PMTs and wavelength-shifting fibers (WLS) with Silicon Photo-Multipliers (SiPM) readout. The light instrumentation is enclosing a cylindrical volume around the germanium detector array (Fig. 4), with the fibers forming its mantle in the central part and the PMTs are located at the end surfaces. The whole setup including the germanium detectors is assembled in a glove box in nitrogen atmosphere, then enclosed in a lock, pumped and eventually submersed in the GERDA cryostat.

The top (bottom) end surface of the cylindrical volume is equipped with 9 (7) 3" size PMTs of type Hamamatsu R11065-20 MOD with 40 % quantum efficiency at its maximum at 380 nm wavelength. The photocathodes are coated with the wavelength shifter Tetra-Phenyl-Butadiene (TPB) that has a fluorescence maximum at 420 nm wavelength which coincides well with the

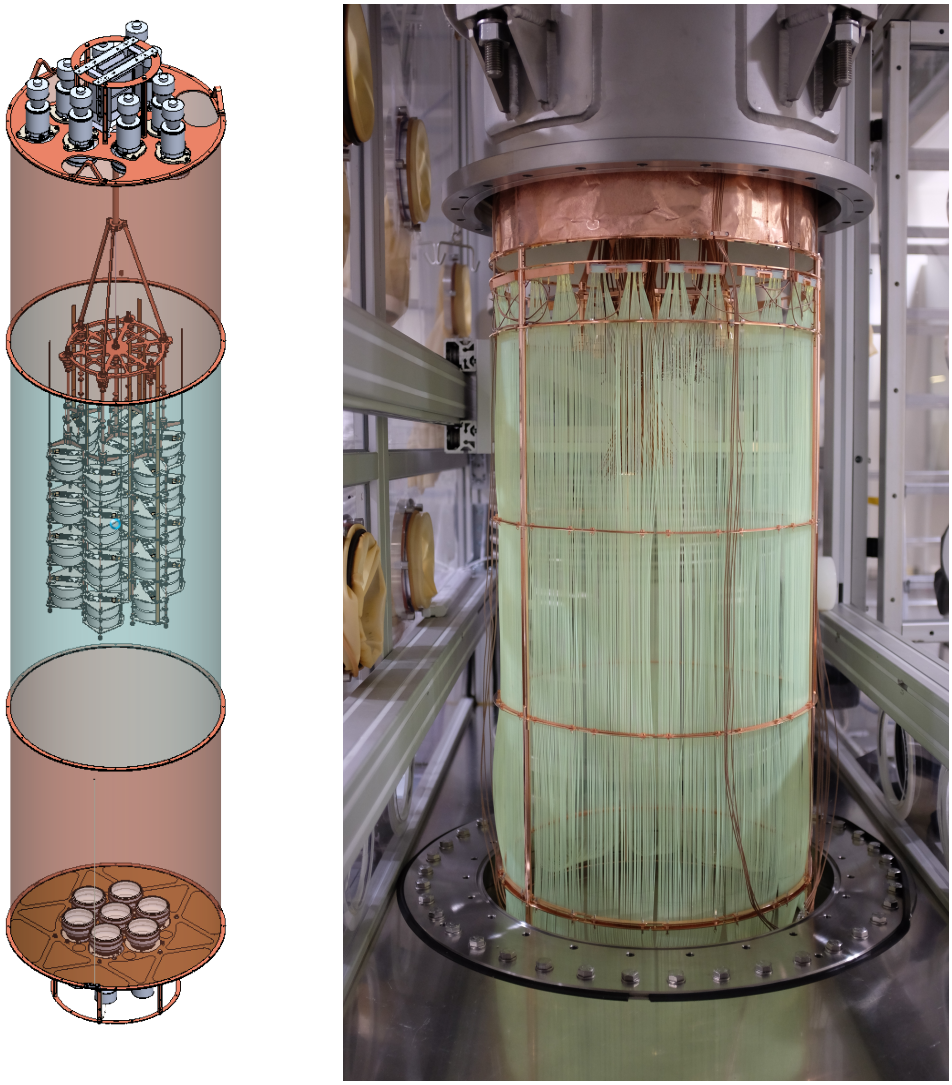

Figure 4: Left: Sketch of the design of the argon veto with the Ge detector array. Right: LAr veto fiber shroud.

quantum efficiency curve of the PMTs. Between the end plates and the fibers are cylinders made of copper foils lined with Tetratex foils soaked with TPB. These serve as light guide and wavelength shifter and allow for a larger distance between the Ge detectors and the PMTs to reduce the influence of their relatively large radioactivity. The PMTs are equipped with custom made voltage dividers. Special care was taken to minimize the heat load and radioactivity. Both, PMTs and dividers contain less than about 2 mBq of relevant radiation from ^{226}Ra and ^{228}Th a piece. The PMT instrumentation is estimated by Monte Carlo (MC) to be well below a total background contribution of 10^{-4} cts/(keV·kg·yr). The PMT signals are amplified, shaped and then - like the SiPM signals for the fiber readout - digitized by FADCs when a Ge detector triggers. The veto is applied offline. Copies of the PMT signals are also fed to custom made scaler modules which determine the individual rates. The scalers are connection to the GERDA slow control which allows for real-time online monitoring of the system and switch off of the high voltage in case the rates are too high.

The central part of the of the LAr veto consists of an array of 810 wavelength shifting (WLS) fibers mounted on a copper frame with 47 cm diameter and 1 m height. The fibers are of multiclad type and have a square cross section.

For easier handling the fiber cylinder is built from modules of 54 fibers. The number of the fibers is given by the fact that nine, 1×1 mm^2 square fiber can be coupled to a 3×3 mm^2 SiPM and six SiPMs are connected in parallel to one amplifier input. Thus one fiber module corresponds to one electronic channel.

The fiber modules were coated with TPB by vacuum deposition. The TPB shifted scintillation light can be detected with the green WLS fiber (BCF-91A). A special vacuum chamber was built to ensure the uniform deposition of TPB along the full length of the fiber module. The TPB thickness of the final modules was varying around 300 nm.

The SiPMs used have an active area of 3×3 mm^2 with 100 μm pixel size (model PM33100) from Ketek GmbH. To satisfy the radio-purity requirements the SiPMs were purchased in 'die' and packaged at TUM. In total there are 90 SiPMs distributed over 15 read-out channels with a total sensitive area of 8.1 cm^2 which is probably the largest SiPM array operated at cryogenic temperature in the moment of writing.

The construction and the installation of the LAr veto was finished in 2014 and it was used during the commissioning runs in 2015. Although some SiPMs and PMTs were replaced it proved to be reliable and fully functional since March 2015.

Fig. 5 demonstrates that the single photo-electron peak is visible in both PMT and SiPM spectra. Therefore a background event can be rejected with only one photon detected.

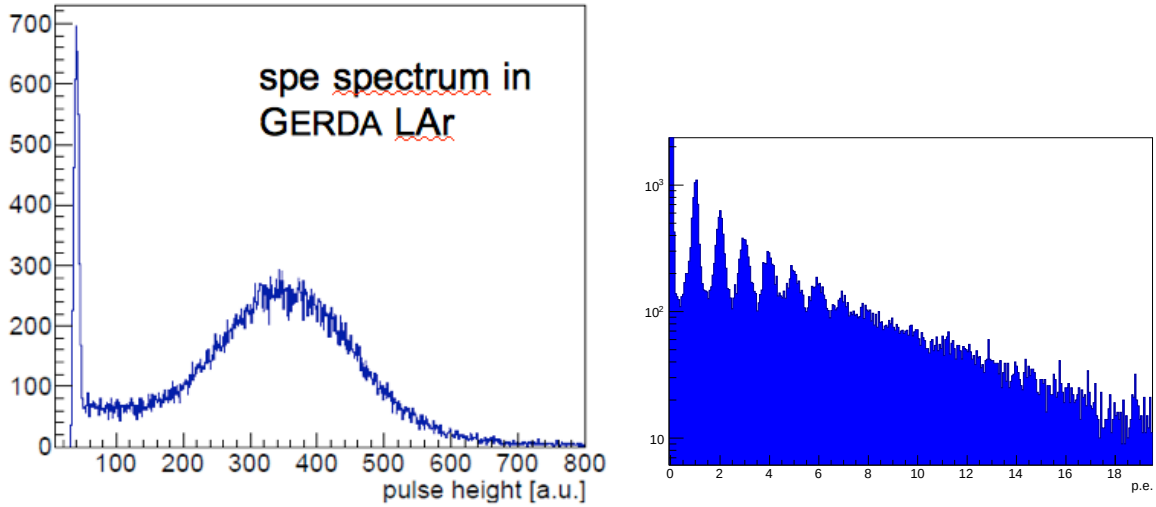

Figure 5: Single photo-electron spectra from PMTs (left) and SiPMs (right).

During the commissioning runs ^{226}Ra and ^{228}Th sources were used to assess the background reduction capability of the LAr veto. The spectra taken are shown in Fig. 6 for ^{226}Ra (right) and ^{228}Th (left). The background reduction factors after detector anti-coincidence, liquid argon veto and pulse shape discrimination at $Q_{\beta\beta}$ have been measured to be 25±2.2 for ^{226}Ra and 390±28 for ^{228}Th. The LAr veto alone reduces the backgrounds by factors of 5.1±0.2 and of 85±3.2, respectively.

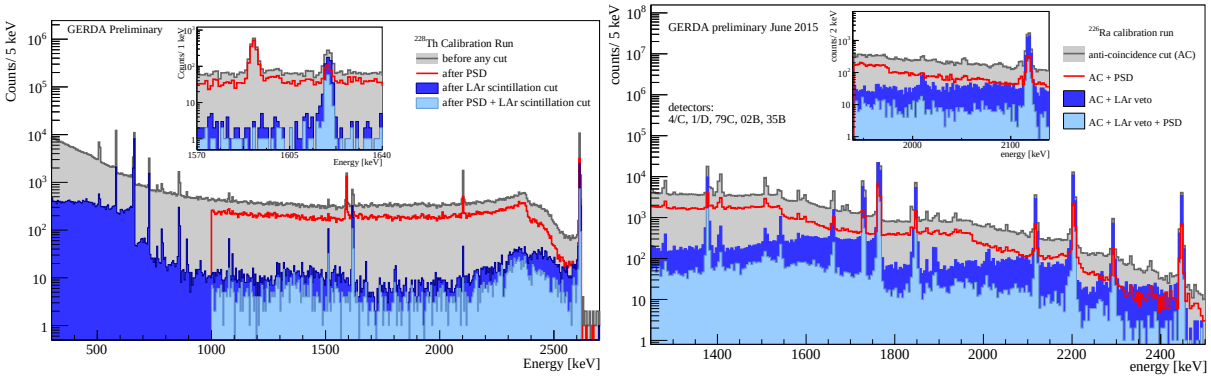

Figure 6: Calibration spectrum for ^{228}Th (left) and ^{226}Ra (right) suppressed by detector anti-coincidence, pulse-shape discrimination and LAr veto.

4 Ge detector integration

In Phase II, 40 detectors are mounted in 7 strings: 3 semi-coaxial detectors from natural Ge (7 kg total mass), 7 semi-coaxial detectors from enriched Ge (15 kg) and 30 BEGe detectors from enriched Ge (20 kg). The latter detector type has a small p^+ contact for readout and the rest of the surface is the high voltage n^+ contact (see Fig. 7). In Phase II the amount of copper and PTFE used for the detector holders was reduced compared to Phase I and monocrystaline silicon was used instead when possible. The electrical contact is done by wire bonding which requires the evaporation of aluminum bond pads on the detectors.

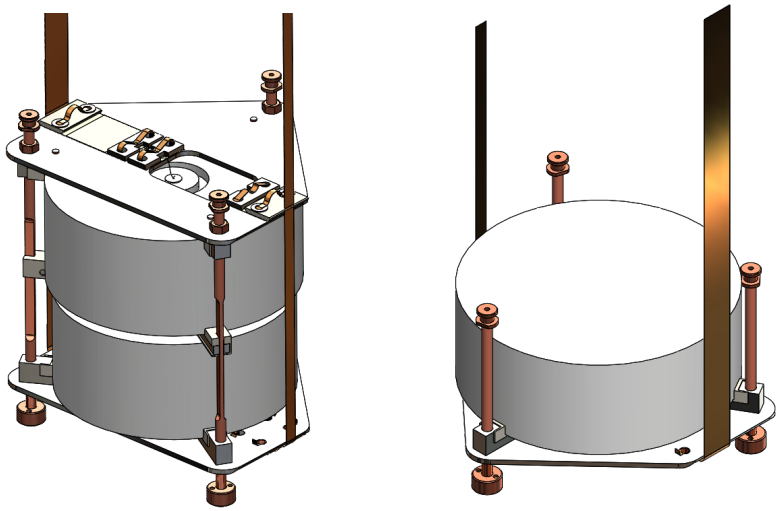

Figure 7: GERDA Phase II pair (left) and single (right) BEGe holders. The top detectors of a pair have the groove between the inner p^+ and outer n^+ contacts facing upwards - as visible on the picture. Also visible are the bond wire from the p^+ contact to the flexible (signal) cable and the two cables for signal and high voltage.

To profit from the small capacitance of BEGe detectors, the JFET plus the feedback capacitor and resistor of the charge sensitive amplifier were planned to be placed directly at the detector,

mounted on a flexible cable made from Cuflon or Kapton fixed to the Si plate of the holder (Fig. 7). Several problems were found in 2014: the radiopure feedback resistors made from silicon exhibited a large parasitic capacitance and our own custom development of 0.5-1 GΩ resistors made e.g. from TiN films or amorphous Ge did not mature fast enough; the last batch of SF291 JFETs had a high mortality rate of 50 % by electro-static discharges - especially during handling in a glove box. Due to these problems we compared in a commissioning test in January 2015 the planned readout with the one used in Phase I (the entire amplifier positioned 35 cm above the string). The performance difference between the two solutions can be small for both energy resolution and pulse shape analysis. It was therefore decided to switch to the simpler version.

Mounting of the full detector array was further delayed by leakage current problems of the detectors. About half of the detectors received from the manufacturer in 2014 exhibited a high current when taken out of the vacuum storage containers. Our normal procedure for curing with a methanol bath did not work this time and detectors were sent back to Canberra. Another problem is related to the orientation of the isolating groove between the p^+ and n^+ contacts. Half of the BEGe detectors mounted in pairs (Fig. 7 left) had the groove facing upwards. Particulates can fall in the groove and lead to instabilities. Modifications of the handling procedures could not solve the problem and hence a new detector mount was designed where all grooves now face downwards (Fig. 7 right). In July 2015, 22 working BEGe detectors and 5 semi-coaxial detector

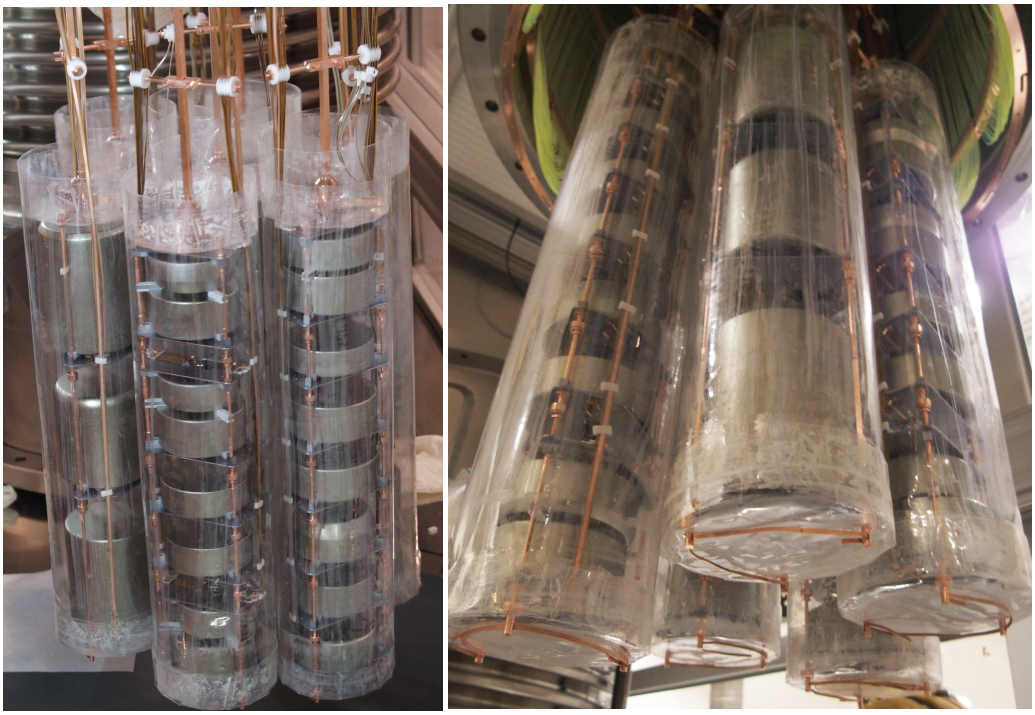

Figure 8: Pictures taken of the entire germanium detector array.

were installed - still in the original detector holders. Five of the detectors with groove facing upwards showed the above mentioned problem with higher leakage current and some additional problems reduced the number of working detectors to 18. The data collected in this configuration was large enough to have a first estimate of the performance of a large array.

After new holders were fabricated (for all but 5 pairs) and all repaired detectors arrived from

the manufacturer, the entire array was assembled (see Fig. 8) and Phase II data taking started on December 20, 2015.

Visible in Fig. 8 are also the so called mini shrouds surrounding each detector string. They are made from nylon (provided by the Borexino collaboration) and covered with TPB as wavelength shifter. This cylinder prevents ^{42}K (progeny of ^{42}Ar) to drift from outside of the cylinder to the detector surface. This β emitter was already in Phase I an important background. The previous mini shroud of copper is now replaced by a nylon version which is transparent: the wavelength shifted argon scintillation light from background decays inside the mini shroud volume can be detected this way.

All detectors can be biased to operational voltage. Currently three detectors (one natural and two BEGe detectors) are used for anti-coincidence only. This is a great success considering the problems experienced during the long commissioning phase. Fig. 9 shows the energy resolution (FWHM) of the installed detectors. For the coaxial detectors the resolution is often better than in Phase I while some BEGe detectors have a resolution larger than expected. The possible reasons are under study.

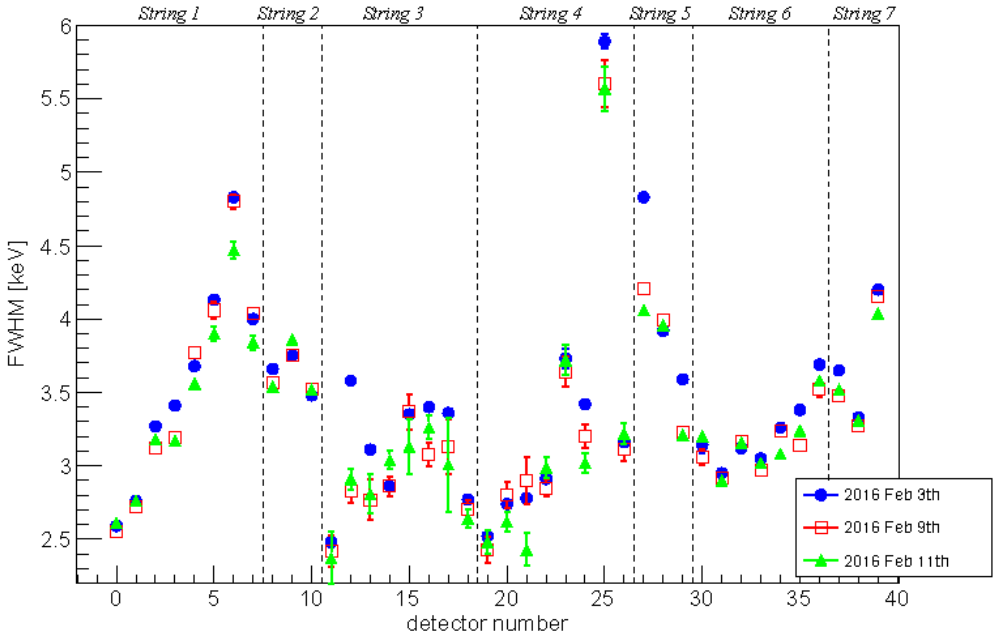

Figure 9: FWHM at 2614.5 keV for three calibration runs in February 2016.

5 Conclusions

The analysis of Phase I data resulted in several new publications in 2015 like searches for new decay modes of ^{76}Ge. Compared to previous experiments limits could be improved between a factor of 5 (for Majoron decays) and two orders of magnitude (two neutrino decays to excited states).

The hardware for Phase II was completed and the second data taking phase of GERDA has started on December 20, 2015. Compared to Phase I the detector mass is doubled due

to the new additional BEGe detectors. This detector type exhibits much better background discrimination by pulse shape analysis. Together with the operational liquid argon scintillation veto we expect the background to be reduced by an order of magnitude compared to Phase I to 0.001 cts/(keV·kg·yr).

6 List of Publications

Publications in 2015

[1] *$2\nu\beta\beta$ decay of ^{76}Ge into excited states with* GERDA *Phase I*,
M. Agostini, M Allardt, A M Bakalyarov, M Balata, I Barabanov, N Barros, L Baudis, C Bauer, N Becerici-Schmidt, E Bellotti, S Belogurov, S T Belyaev, G Benato, A Bettini, L Bezrukov, T Bode, D Borowicz, V Brudanin, R Brugnera, D Budjas, A Caldwell, C Cattadori, A Chernogorov, V D'Andrea, E V Demidova, A di Vacri, A Domula, E Doroshkevich, V Egorov, R Falkenstein, O Fedorova, K Freund, N Frodyma, A Gangapshev, A Garfagnini, C Gooch, P Grabmayr, V Gurentsov, K Gusev, A Hegai, M Heisel, S Hemmer, G Heusser, W Hofmann, M Hult, L V Inzhechik, J Janicsko Csathy, J Jochum, M Junker, V Kazalov, T Kihm, I V Kirpichnikov, A Kirsch, A Klimenko, K T Knöpfle, O Kochetov, V N Kornoukhov, V V Kuzminov, M Laubenstein, A Lazzaro, V I Lebedev, B Lehnert, H Y Liao, M Lindner, I Lippi, A Lubashevskiy, B Lubsandorzhiev, G Lutter, C Macolino, B Majorovits, W Maneschg, E Medinaceli, Y Mi, M Misiaszek, P Moseev, I Nemchenok, D Palioselitis, K Panas, L Pandola, K Pelczar, A Pullia, S Riboldi, N Rumyantseva, C Sada, M Salathe, C Schmitt, B Schneider, J Schreiner, O Schulz, B Schwingenheuer, S Schönert, A-K Schütz, O Selivanenko, M Shirchenko, H Simgen, A Smolnikov, L Stanco, M Stepaniuk, C A Ur, L Vanhoefer, A A Vasenko, A Veresnikova, K von Sturm, V Wagner, M Walter, A Wegmann, T Wester, H Wilsenach, M Wojcik, E Yanovich, P Zavarise, I Zhitnikov, S V Zhukov, D Zinatulina, K Zuber, and G Zuzel,
J. Phys. G: Nucl. Part. Phys. **42** (2015) 115201.

[2] *Double-beta decay with majoron emission in* GERDA *Phase I*,
S. Hemmer for the GERDA collaboration,
Eur. Phys. J. Plus **130** (2015) 139.

[3] *Enhancement of light yield and stability of radio-pure tetraphenyl-butadiene based coatings for VUV light detection in cryogenic environments*,
L. Baudis, G. Benato, R. Dressler, F. Piastra, I. Usoltsev, and M. Walter,
J. of Instrumentation **10** (2015) P09009.

[4] GERDA*: Results and perspectives*,
C. Cattadori for the GERDA collaboration,
In Proc. *Neutrino Oscillation Workshop*,
Nucl. and Particle Physics Procs. **265-266** (2015) 38, Otranto, Italy, 7-13 September 2014, 2015.

[5] *Improvement of the energy resolution via an optimized digital signal processing in* GERDA *Phase I*,
M. Agostini, M. Allardt, A. M. Bakalyarov, M. Balata, I. Barabanov, N. Barros, L. Baudis, C. Bauer, N. Becerici-Schmidt, E. Bellotti, S. Belogurov, S. T. Belyaev, G. Benato, A. Bettini, L. Bezrukov, T. Bode, D. Borowicz, V. Brudanin, R. Brugnera, D. Budjas, A. Cald-

well, C. Cattadori, A. Chernogorov, V. D'Andrea, E. V. Demidova, A. di Vacri, A. Domula, E. Doroshkevich, V. Egorov, R. Falkenstein, O. Fedorova, K. Freund, N. Frodyma, A. Gangapshev, A. Garfagnini, P. Grabmayr, V. Gurentsov, K. Gusev, A. Hegai, M. Heisel, S. Hemmer, G. Heusser, W. Hofmann, M. Hult, L. V. Inzhechik, J. Janicsko Csathy, J. Jochum, M. Junker, V. Kazalov, T. Kihm, I. V. Kirpichnikov, A. Kirsch, A. Klimenko, K. T. Knöpfle, O. Kochetov, V. N. Kornoukhov, V. V. Kuzminov, M. Laubenstein, A. Lazzaro, V. I. Lebedev, B. Lehnert, H. Y. Liao, M. Lindner, I. Lippi, A. Lubashevskiy, B. Lubsandorzhiev, G. Lutter, C. Macolino, B. Majorovits, W. Maneschg, E. Medinaceli, M. Misiaszek, P. Moseev, I. Nemchenok, D. Palioselitis, K. Panas, L. Pandola, K. Pelczar, A. Pullia, S. Riboldi, N. Rumyantseva, C. Sada, M. Salathe, C. Schmitt, B. Schneider, S. Schönert, J. Schreiner, A.-K. Schütz, O. Schulz, B. Schwingenheuer, O. Selivanenko, M. Shirchenko, H. Simgen, A. Smolnikov, L. Stanco, M. Stepaniuk, C. A. Ur, L. Vanhoefer, A. A. Vasenko, A. Veresnikova, K. von Sturm, V. Wagner, M. Walter, A. Wegmann, T. Wester, H. Wilsenach, M. Wojcik, E. Yanovich, P. Zavarise, I. Zhitnikov, S. V. Zhukov, D. Zinatulina, K. Zuber, and G. Zuzel,
Eur. Phys. J. **C75** (2015) 255.

[6] *Improvement of the* GERDA *Ge Detectors Energy Resolution by an Optimized Digital Signal Processing*,
G. Benato, V. D'Andrea, C. Cattadori, and S. Riboldi, In Proc. *TAUP 2013*, Physics Procedia **61** (2015) 673, edited by Wick Haxton and Frank Avignone, Elsevier, 2015.

[7] *LArGe: active background suppression using argon scintillation for the* GERDA *$0\nu\beta\beta$-experiment*,
M. Agostini, M. Barnabe-Heider, D. Budjas, C. Cattadori, A. Gangapshev, K. Gusev, M. Heisel, M. Junker, A. Klimenko, A. Lubashevskiy, K. Pelczar, S. Schönert, A. Smolnikov, and G. Zuzel,
Eur. Phys. J. **C75** (2015) 506.

[8] *Limit on neutrinoless double beta decay of ^{76}Ge by* GERDA,
GERDA collaboration:, M. Agostini, M. Allardt, E. Andreotti, A.M. Bakalyarov, M. Balata, I. Barabanov, M. Barabè Heider, N. Barros, L. Baudis, C. Bauer, N. Becerici-Schmidt, E. Bellotti, S. Belogurov, S.T. Belyaev, G. Benato, A. Bettini, L. Bezrukov, T. Bode, V. Brudanin, R. Brugnera, D. Budjás, A. Caldwell, C. Cattadori, A. Chernogorov, F. Cossavella, E.V. Demidova, A. Domula, V. Egorov, R. Falkenstein, A. Ferella, K. Freund, N. Frodyma, A. Gangapshev, A. Garfagnini, C. Gotti, P. Grabmayr, V. Gurentsov, K. Gusev, K.K. Guthikonda, W. Hampel, A. Hegai, M. Heisel, S. Hemmer, G. Heusser, W. Hofmann, M. Hult, L.V. Inzhechik, J. Janicskó Csàthy, J. Jochum, M. Junker, T. Kihm, I.V. Kirpichnikov, A. Kirsch, A. Klimenko, K.T. Knöpfle, O.Kochetov, V.N. Kornoukhov, V.V. Kuzminov, M. Laubenstein, A. Lazzaro, V.I. Lebedev, B. Lehnert, H.Y. Liao, M. Lindner, I. Lippi, A. Lubashevskiy, B. Lubsandorzhiev, G. Lutter, A.A. Machado, C. Macolino, B. Majorovits, W. Maneschg, M. Misiaszek, I. Nemchenok, S. Nisi, C. O'Shaughnessy, L. Pandola, K. Pelczar, G. Pessina, A. Pullia, S. Riboldi, N. Rumyantseva, C. Sada, M. Salathe, C. Schmitt, J. Schreiner, O. Schulz, B. Schwingenheuer, S. Schönert, E. Shevchik, M. Shirchenko, H. Simgen, A. Smolnikov, L. Stanco, H. Strecker, M. Tarka, C.A. Ur, A.A. Vasenko, O. Volynets, K. von Sturm, V. Wagner, M. Walter, A. Wegmann, T. Wester, M. Wojcik, E. Yanovich, P. Zavarise, I. Zhitnikov, S.V. Zhukov, D. Zinatulina, K. Zuber, and G. Zuzel, In Proc. *TAUP2013*, Physics Procedia **61** (2015) 828, edited by Wick Haxton and Frank Avignone, Elsevier, 2015.

[9] *Phase II upgrade of the* GERDA *experiment for the search of neutrinoless double beta decay*, B. Majorovits for the GERDA collaboration, In Proc. *TAUP 2013*, Physics Procedia **61** (2015) 254, edited by Wick Haxton and Frank Avignone, Elsevier, 2015.

[10] *Production, characterization and operation of* ^{76}*Ge enriched BEGe detectors in* GERDA, M. Agostini, M. Allardt, E. Andreotti, A. M. Bakalyarov, M. Balata, I. Barabanov, N. Barros, L. Baudis, C. Bauer, N. Becerici-Schmidt, E. Bellotti, S. Belogurov, S. T. Belyaev, G. Benato, A. Bettini, L. Bezrukov, T. Bode, D. Borowicz, V. Brudanin, R. Brugnera, D. Budjas, A. Caldwell, C. Cattadori, A. Chernogorov, V. D'Andrea, E. V. Demidova, A. Domula, V. Egorov, R. Falkenstein, K. Freund, N. Frodyma, A. Gangapshev, A. Garfagnini, C. Gotti, P. Grabmayr, V. Gurentsov, K. Gusev, A. Hegai, M. Heisel, S. Hemmer, G. Heusser, W. Hofmann, M. Hult, L. V. Inzhechik, L. Ioannucci, J. Janicsko. Csathy, J. Jochum, M. Junker, V. Kazalov, T. Kihm, I. V. Kirpichnikov, A. Kirsch, A. Klimenko, K. T. Knöpfle, O. Kochetov, V. N. Kornoukhov, V. V. Kuzminov, M. Laubenstein, A. Lazzaro, V. I. Lebedev, B. Lehnert, H. Y. Liao, M. Lindner, I. Lippi, A. Lubashevskiy, B. Lubsandorzhiev, G. Lutter, C. Macolino, B. Majorovits, W. Maneschg, M. Misiaszek, I. Nemchenok, S. Nisi, C. O'Shaughnessy, D. Palioselitis, L. Pandola, K. Pelczar, G. Pessina, A. Pullia, S. Riboldi, N. Rumyantseva, C. Sada, M. Salathe, C. Schmitt, J. Schreiner, O. Schulz, A.- K. Schuetz, B. Schwingenheuer, S. Schönert, E. Shevchik, M. Shirchenko, H. Simgen, A. Smolnikov, L. Stanco, H. Strecker, C. A. Ur, L. Vanhoefer, A. A. Vasenko, K. Von Sturm, V. Wagner, M. Walter, A. Wegmann, T. Wester, H. Wilsenach, M. Wojcik, E. Yanovich, P. Zavarise, I. Zhitnikov, S. V. Zhukov, D. Zinatulina, K. Zuber, and G. Zuzel, Eur. Phys. J. **C75** (2015) 39.

[11] *Results on* $\beta\beta$ *decay with emission of two neutrinos or Majorons in* ^{76}*Ge from* GERDA *Phase I*,
GERDA collaboration, M. Agostini, M. Allardt, A. M. Bakalyarov, M. Balata, I. Barabanov, N. Barros, L. Baudis, C. Bauer, N. Becerici-Schmidt, E. Bellotti, S. Belogurov, S. T. Belyaev, G. Benato, A. Bettini, L. Bezrukov, T. Bode, D. Borowicz, V. Brudanin, R. Brugnera, D. Budjas, A. Caldwell, C. Cattadori, A. Chernogorov, V. D'Andrea, E. V. Demidova, A. di Vacri, A. Domula, E. Doroshkevich, V. Egorov, R. Falkenstein, O. Fedorova, K. Freund, N. Frodyma, A. Gangapshev, A. Garfagnini, P. Grabmayr, V. Gurentsov, K. Gusev, A. Hegai, M. Heisel, S. Hemmer, G. Heusser, W. Hofmann, M. Hult, L. V. Inzhechik, J. Janicskó Csáthy, J. Jochum, M. Junker, V. Kazalov, T. Kihm, I. V. Kirpichnikov, A. Kirsch, A. Klimenko, K. T. Knöpfle, O. Kochetov, V. N. Kornoukhov, V. V. Kuzminov, M. Laubenstein, A. Lazzaro, V. I. Lebedev, B. Lehnert, H.Y. Liao, M. Lindner, I. Lippi, A. Lubashevskiy, B. Lubsandorzhiev, G. Lutter, C. Macolino, B. Majorovits, W. Maneschg, E. Medinaceli, M. Misiaszek, P. Moseev, I. Nemchenok, D. Palioselitis, K. Panas, L. Pandola, K. Pelczar, A. Pullia, S. Riboldi, N. Rumyantseva, C. Sada, M. Salathe, C. Schmitt, B. Schneider, S. Schönert, J. Schreiner, A.-K. Schütz, O. Schulz, B. Schwingenheuer, O. Selivanenko, M. Shirchenko, H. Simgen, A. Smolnikov, L. Stanco, M. Stepaniuk, C.A. Ur, L. Vanhoefer, A. A. Vasenko, A. Veresnikova, K. von Sturm, V. Wagner, M. Walter, A. Wegmann, T. Wester, H. Wilsenach, M. Wojcik, E. Yanovich, P. Zavarise, I. Zhitnikov, S. V. Zhukov, D. Zinatulina, K. Zuber, and G. Zuzel,
Eur. Phys. J. **C75** (2015) 416.

other papers

[12] GERDA collaboration, Eur. J. Phys. C73 (2013) 2330

[13] GERDA collaboration, Jour. Phys. G40 (2013) 035110

[14] GERDA collaboration, Eur. J. Phys. C74 (2104) 2764

GINGER/G-GranSasso-RD Annual Report 2015

J. Belfi[a], N. Beverini[a,b], F. Bosi[a], G. Carelli[a,b], A. Di Virgilio[a], E. Maccioni[a,b], R. Santagata[a,c], A. Simonelli[a,b,d], and G. Terreni[a]
A. Ortolan[e], D. Orlandi[f], Michela Paris[f] and C. Zarra[f]
C. Altucci[g,h], A. Porzio[g,i], R. Velotta[g,h]
A. Beghi[l,m], D. Cuccato[l,m], A. Donazzan[l,m], G. Naletto[l,m], M.G. Pelizzo[l,n]
M.L. Ruggiero[o,p] and A. Tartaglia[o]
G. De Luca[q], and G. Saccorotti[r]

[a] INFN-Pisa- Italy
[b] University of Pisa-Italy
[c] Present address: LPL (Universitéï£¡ Paris 13, Sorbonne Paris Citï£¡ - CNRS)
[d] Present address: LMU, Muenchen, Germany
[e] LNL -INFN Padova-Italy
[f] LNGS-INFN Assergi, Italy
[g] INFN-Napoli-Italy
[h] University of Naples, Italy
[i] CNR-SPIN Napoli-Italy
[l] INFN-Padova, Italy [m] DEI-Univ. of Padua, Padova-Italy
[n] CNR- IFN Padua-Italy
[o] Politecnico di Torino-Italy
[p] INFN-Torino-Italy
[q] INGV L'Aquila, Italy
[r] INGV Pisa, Italy

Abstract

Large ring laser gyroscopes (with a perimeter of several meters) are capable of measuring angular rotations with precision better that a fraction of $prad/s$, not far from what is necessary for General Relativity tests (about 10^{-14} rad/s). The GINGER (Gyroscopes IN General Relativity) project is based on an array of ring lasers; its aim is to overcome this limit and realize an earth based apparatus to test GR. A ring laser by himself has enough sensitivity, it provides a continuous data taking, and the frequency response is valid as well down to very low frequency. Environmental disturbances induced by atmospheric events can limit this apparatus, this is why an underground location can be a suitable choice for GINGER. The prototype GINGERino, a square ring laser with 3.6m side, has been installed inside LNGS and put in operation in 2015. It has shown that it can run unattended for weeks with a typical sensitivity below nrad/s for 1 s measurement, the integration time is of the order of 100 s, limited by the backscatter noise. This noise is mainly due to the mirrors which are not yet top quality; an improved set of mirrors will be installed in 2016. So far three engineering runs have been pursued, the preliminary analysis is reported, and the future program sketched.

1 Introduction

Ring laser gyroscopes (RLG) [1] are, at present, the most precise sensors of absolute angular velocity for an Earth based apparatus. They are based on the Sagnac effect arising from a rigidly rotating ring laser cavity. They are essential in estimating rotation rates relative to the local inertial frame in many contexts ranging from inertial guidance to angle metrology, from geodesy to geophysics and as well as sensors for the realization of inertial platforms. The Gross ring "**G**" at the Wettzell Geodetic Observatory has obtained a resolution on the Earth rotation rate of 3×10^{-9} (about 15×10^{-14} rad/s with 4 hours integration time) [1, 2]. Such an unprecedented sensitivity shows that this class of instrument is suited to probe the spatio-temporal structure of the local gravity field. Earth rotation is, actually, precisely measured by an international system of very long baseline interferometers (VLBI). VLBI has demonstrated highly accurate and stable determinations of the universal time, mainly because its very precise observations of extragalactic radio sources provide access to a nearly inertial celestial reference frame. RLG is an instrument whose outputs are directly linked to the instantaneous axis of rotation of the Earth. Furthermore one obtains a continuous set of measurements, which is not yet available for VLBI. A good agreement between VLBI and ring laser has been achieved by measuring and comparing the low frequency Chandler– and Annual– Wobble, a free oscillation of the Earth [3]. The remaining discrepancy is due to the fact that local tilts of **G**, a single component ring laser, currently cannot be measured with a sufficient long-term stability. An improvement in sensitivity and a full 3-dimensional detection of the Earth rotational velocity vector would allow RLG to integrate efficiently the data produced by VLBI and, possibly, measure the Lense–Thirring effect. GINGER (Gyroscopes IN GEneral Relativity) will aim at measuring the gravitomagnetic (Lense–Thirring) effect of the rotating Earth by means of an array of high sensitivity and accuracy ring lasers. In the weak–field approximation of Einstein's equations, the response ν seen by a RLG located in a laboratory on the Earth surface, with co–latitude θ, and with the axis contained in the meridian plane at an angle ψ with respect to the zenith, can be written as:

$$\nu = 4\frac{S}{\lambda}\Omega_E[\cos(\theta+\psi) - 2\frac{GM_E}{c^2R_E}\sin\theta\sin\psi + \frac{GI_E}{c^2R_E^3}(2\cos\theta\cos\psi + \sin\theta\sin\psi)] \ , \qquad (1)$$

where S is a geometric scale factor for the RLG, G the Newton's gravitational constant, $\Omega_E = 7.29 \times 10^{-5}$ rad/s the Earth's instantaneous angular rotation speed, M_E the Earth's mass, R_E the Earth's average radius, and $I_E \approx \frac{2}{5}M_ER_E^2$ the Earth's moment of inertia. The first term corresponds to the standard Sagnac signal; the second one, known as geodetic or De Sitter precession, is produced by the motion of the laboratory in the curved space–time around the Earth and, the third one, known as Lense-Thirring precession (LT) and characterized by a dipolar structure, is produced by the rotating mass of the Earth and is proportional to the Earth angular momentum [4]. It is possible to show that the ring laser signal depends on PPN parameters γ and α_1; detailed calculations and comparison with alternative theories of relativity are reported in the appendix A. The last two terms of eq. [1] are both relativistic but their contributions can be discriminated by a vectorial reconstruction of the rotation speed. They are smaller than the classical Sagnac effect by a factor of $\approx 10^{-9}$, that is of the order of magnitude of the ratio between R_E and the Schwarzschild radius of the Earth $2GM_E/c^2$. These effects should be observed as a difference between the rotation rate observed by the array of RLGs in the rotating frame of the laboratory, and the length of the day determined in the "fixed stars" inertial frame by IERS (International Earth Rotation and Reference System) through VLBI. Registering a perturbation that amounts to 1 part in a billion of the Earth rotational rate, requires an unprecedented sensitivity of the apparatus. An array of at least three ring lasers would allow us to vectorially

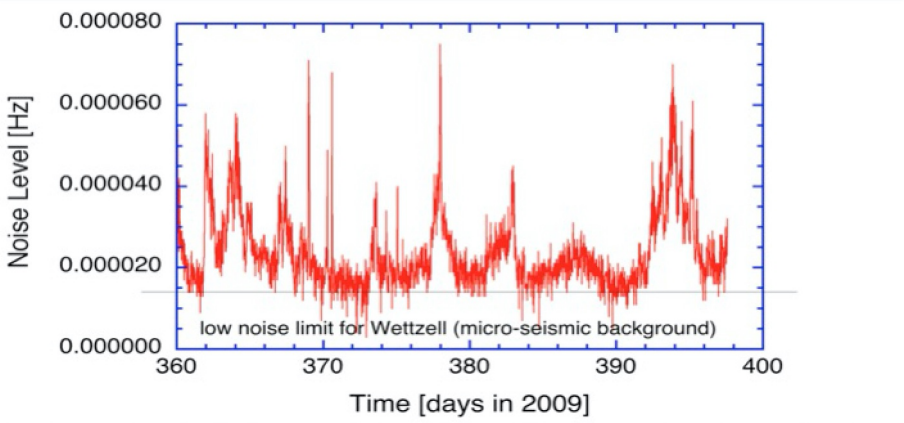

Figure 1: Local disturbances like top soil wind, microseisms, variable hydrology effects are seen at the Geodetic Observatory of Wettzell by the **G** ring laser as extra noise above the actual instrument limit. (Courtesy of U. Schreiber and A. Gebauer)

measure the Earth's angular velocity and, having at disposal the time series of the daily estimate of the Earth rotation vector from the IERS Service (http://www.iers.org), it would be possible to isolate the Geodetic and Lense-Thirring contributions. An underground location, far from external disturbances as rain, wind etc., is essential for this challenging experiment, and LNGS (Laboratori Nazionali del GranSasso, the underground INFN National laboratory) may be a suitable location. Moreover, in such a case the external disturbances cannot be neglected as shown in Fig. 1 where the disturbances recorded by **G** in Wettzell are clearly visible [5].

LNGS underground laboratory exhibits a very high natural thermal stability and, being deep underground, it is not affected by top soil disturbances. Moreover, being a very large laboratory, it seems feasible, if needed, to further shield GINGER in order to reduce the anthropic disturbances. In order to check how much the underground location is an advantage for GINGER, a single axis apparatus called GINGERino, has been installed inside LNGS. This installation is a prototype dedicated to GINGER and to the utilization of RLG for fundamental science, but at the same time provides unique information for geophysics. When the sensitivity will be good enough it should also provide local measurements relevant for geodesy, as daily and semidiurnal polar motion. The Earth rotation rate is a very important parameter, in particular it is connected with the variation of the atmospheric angular momentum, see fig 2.

The construction of GINGERino has been completed by the end of 2014. In spring 2015 it has been taking data for the first time, and a second run in October 2015. In the following the apparatus will be described, and the very preliminary data will be reported and discussed. In the conclusions the near future development will be sketched. At the end two appendices are added:

- Appendix A reports the detailed calculation of the ring laser signal taking into account the PPN parameters, and a discussion about the modified theories of gravity.
- Appendix B describes the 2015 work on the two prototypes GP2 and GEMS. GP2 is the prototype dedicated to the control of one hetero-lithic ring laser and GEMS is a prototype of the external metrology system to provide signal to control the geometry of the ring lasers array.

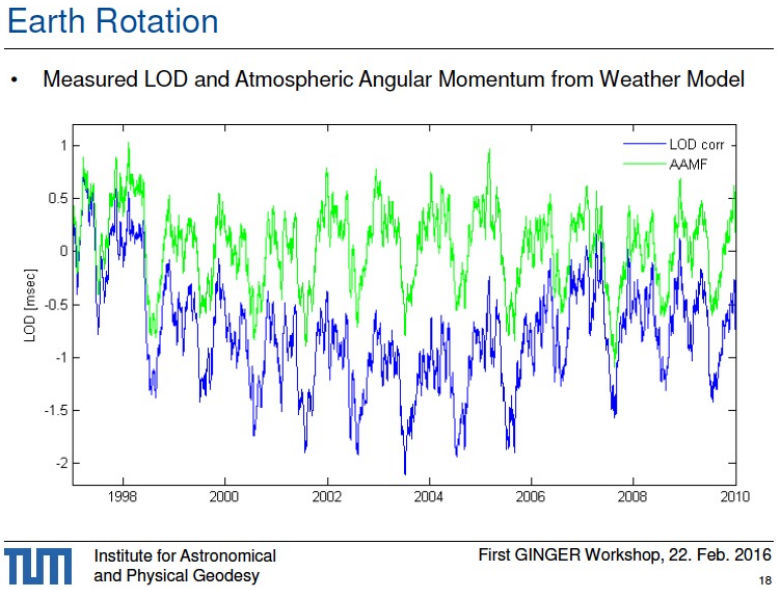

Figure 2: Comparison of the measured LOD (Length Of Day) and the atmospheric angular momentum estimated with the weather model. 1 ms is 1 part 10^8 of the whole length of the day. Courtesy of U. Hugentobler.

2 The GINGERino Apparatus

The whole GINGERino consists of a 3.6 m in side square ring laser and few high sensitivity co-located seismic instruments. These are tilt meters with nrad resolution (2-K High Resolution Tiltmeter (HRTM), Lipmann) and high performance seismometers (Trillium 240s and Guralp CMG 3TD-360 s). This combination of different instruments will improve the knowledge of the behavior of the location, and be essential in the interpretation of geophysical data. In the following the different components will be described together with data acquisition and analysis.

2.1 The ring laser and the granite monument

The Gross ring **G** is based on a monolithic mechanical design which cannot be extended to form an array. In order to circumvent this engineering limitation, we have been developing an heterolithic mechanical structure since several years. This concept has been used, so far, in three prototypes: G-Pisa (no more in operation) [6, 7], GP2 (actually running at INFN Pisa) [8, 9] and GINGERino. GINGERino (see Fig. 3.) uses the mechanics of G-Pisa which is made up of 4 mirror boxes connected by vacuum pipes. Each mirror can be independently moved, with sub-micrometer resolution, so to align the optical cavity. Two piezoelectric translators can be used to stabilize the perimeter in order to compensate for the thermal expansion of the cavity, avoiding laser mode hopping and increasing the device duty cycle. The perimeter active control of the prototype G-Pisa has been successfully tested in the past [7]. The ring laser is tightly attached to a cross structure made of black African granite, composed of a central octagonal massive block (3 tons), and four lightened arms each weighting $\approx 800\,kg$ (see Fig. 4). The granite structure is screwed to a reinforced concrete block integral to the underneath bedrock. The African black granite has been chosen because it can be machined with high precision and

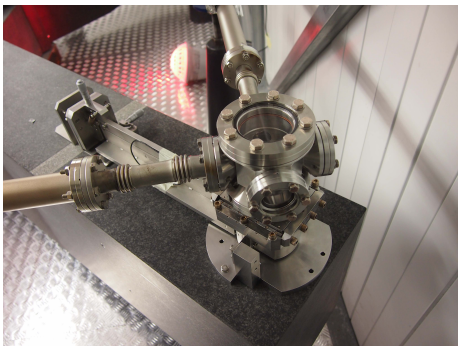

Figure 3: Left: The main structure of GINGERino is shown: it is composed of the G-Pisa mechanical structure with longer vacuum tubes, attached to a granite cross, which is attached to the bedrock with a concrete solid structure. Detail of one of the four mirror boxes, the two output viewports and the micro-metric system to tilt the mirrors are well visible.

has quite a low thermal expansion coefficient (7×10^{-6} $/^oC$). The advantages of a single support for the mirrors are: a) a better definition of the geometry and planarity since the granite can be very precisely machined; b) the whole set-up is attached to its center and the whole granite cross is inside the same thermal bath. The installation area was at a temperature of 7 ^oC with a relative humidity close to the dew point all the year round. The whole installation is now protected by a large anechoic box. Infrared lamps are used to increase the temperature inside the box thus reducing the relative humidity from more than 90% down to $\approx 50-60\%$. So far, this infrastructure has been running for several months, and has shown that it keeps the GINGERino area at a temperature around $14-18$ ^oCdegrees Celsius. We will investigate later if this system needs to be improved with additional shielding and/or an active temperature control.

3 Sensitivity of the apparatus

A first set of data have been taken late spring 2015. Until September 2015, the timing was not synchronised with GPS. The measured cavity ring-down time was $\simeq$ 250 ms. From a direct estimate of the Sagnac frequency by means of the Hilbert transform of the interferogram, we deduced an instrumental resolution of $0.1 nrad/sec/\sqrt{Hz}$ in the range $(10^{-2} - 1)$ Hz (see Fig. 5). As clearly visible in Fig 6, the long term stability of the instrument was limited to 100 sec, mainly by radiation backscattering on the mirrors. GINGERino was operated for weeks unattended, see fig. 7

4 Second and third run and comparative analysis with seismometers

In October 2015, after a failure that have polluted the mirrors, we have restarted GINGERino by using a novel set of mirrors with a measured ring-down time of the cavity around 150 ms, about a factor 2 worse than our first run. At the same time we successfully implemented the synchronization with GPS, all the pipes of the ring laser have been decoupled from the floor, the vacuum pump has been taken away, and the monitor of the gain tube has been inserted. In Fig. 8, typical power spectra from the two runs are compared. One of the mirrors exhibited a bright spot on the border of the laser beam, which severely affected the intensity of backscattered

Figure 4: Left: GINGERino. Right: The anechoic box seen from Node A.

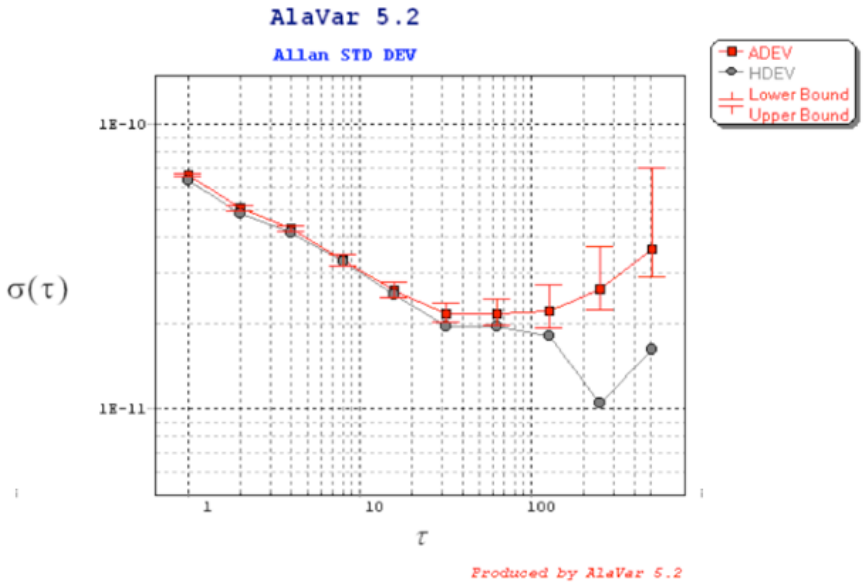

Figure 5: Allan standard deviation of GINGERino as a function of integration time (no backscattering subtraction), data with reduced backscattering have been selected. In this picture the Allan is in rad/s, it shows the best sensitivity of 20 prad/s, with 30 s of integration time.

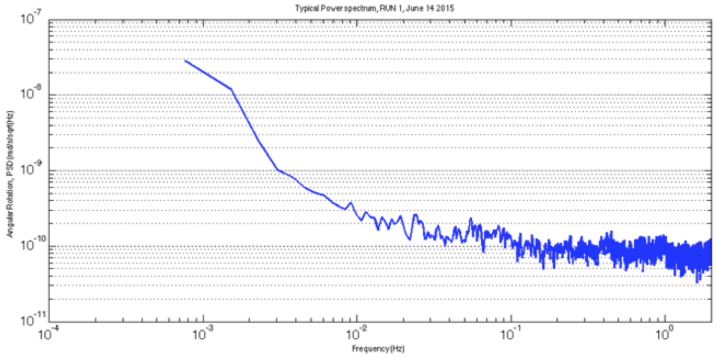

Figure 6: Angular velocity resolution of GINGERino, directly estimated from the interferogram, as a function of the frequency. The instrument is able to resolve $0.1 nrad/sec/\sqrt{Hz}$ in the range $(10^{-2} - 1)Hz$. In this measurement the information has been filtered of $+/-2Hz$ around the Sagnac frequency.

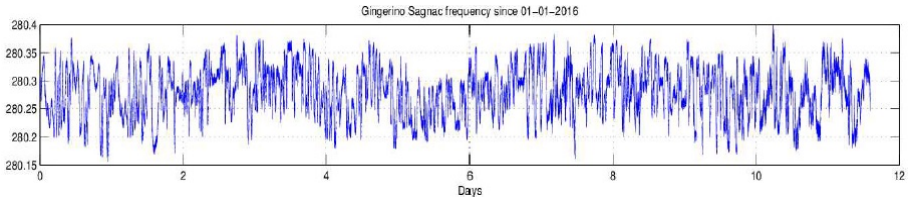

Figure 7: Typical behavior of the Sagnac frequency, the average value 280 Hz is compatible with the Sagnac frequency of the earth rotation rate and the latitude of LNGS

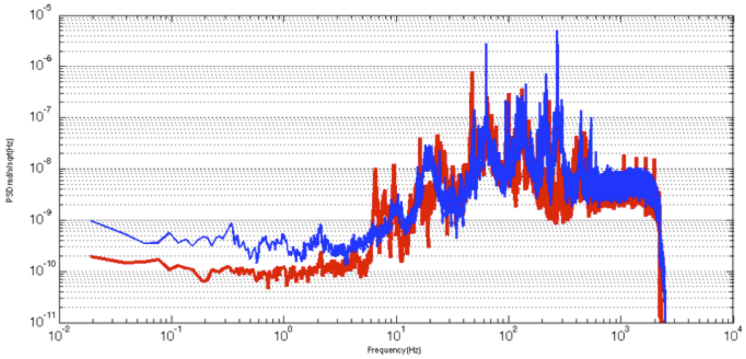

Figure 8: Typical Power Spectral Densities of the interferogram from run 1 (red) and run 2 (blue). The sensitivity at low frequency of the run 2 is not as good as in run 1. This is due to the lower mirrors quality. However, there is an improvement in the high frequency part of the spectrum, due to an improvement of the isolation of the instrument from the floor.

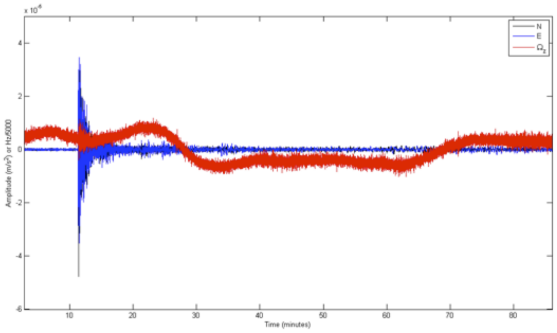

Figure 9: Teleseismic event of the Vanuatu earthquake. The timing between ring laser (red curve) and seismometers shows a good synchronization. The two instruments are acquired by two different acquisition systems, in particular the seismometers are acquired by the INGV network GAIA.

light; later on this mirror has been replaced with a mirror with similar losses, but more uniform diffusion. After the insertion of the getters pump, which prevent the ageing of the He-Ne gas mixture, in January 2016 a third run has been started, and the data taking has begun of February, and is still going on at the time of writing. In section 5 the analysis of 5 days with the Kalman filter is reported. Mirrors are crucial part of the apparatus because of the roles of the ring down time and backscattering in limiting the RLG sensitivity. In order to make the laser running, reflectivity above 99.995% is required, and the backscattering noise (which pollutes the low frequency response) decreases reducing the losses of the mirrors. The goal for the mirrors is to achieve a reflectivity higher than99.999% with a transmission higher than 0.5 ppm, to have enough output power. A new set of mirrors are in preparation, and it will be ready by spring 2016. Moreover, it is necessary to center the maximum of the reflectivity profile at 632.8 nm so to avoid competition with other Neon lines which are few nano-meters apart. At the present stage, we don't have a facility to check the reflectivity of each mirror, so that we can only check them with the RLG. Since the reflectivity is the main parameter, we plan to set up a facility to measure the reflectivity and the losses of each mirror. This facility consists of L-shaped triangular cavity and will be installed in the clean room at INFN Pisa. The upgrade in GPS timing has allowed a direct comparison between the RLG data and the seismometers that are independently acquired. In particular, we have been able to see in the Sagnac signal the effect of the Vanuatu earthquake happened on Tuesday, October 20, 2015 21:52 UTC (see Fig. 9).

4.1 Application of the Kalman filter to 5 days of data

The strategy for ring laser data analysis has been extensively discussed in previous papers [10], where we have shown how and why backscattering noise can be efficiently subtracted, by post-processing the data, applying Kalman filtering. For this purpose several service signals have been acquired during the third run. The ring-down time of the cold optical cavity was measured as 253 μs. From a direct estimate of the Sagnac frequency by AR2 algorithm, we found that the raw sensitivity of the instrument is still in the range nano-rad/sec at few seconds of integration time.

We carefully analyzed 5 days of data when GINGERino showed a stable behavior without laser mode jumps. Our routine for the calibration and identification of laser parameters was run on the time series of mono-beams, interferogram, and monitor of the laser discharge.

On February the 3^{rd}, we performed the laser calibration using the following spectroscopic parameters which were already available: plasma temperature $T_p = 365$ K; gas pressure $p = 5.6$ mbar; isotopic concentration of $^{20}Ne-^{22}Ne$ gas mixture $k_{^{20}Ne} = 50\%$. The reference parameters for the GINGERino setup inside the LNGS facility are: ring side length $L = 3.6$ m, laser and angle between the earth rotation vector and the normal of the ring $\theta = 42.45$. These numbers translate into an expected Sagnac frequency of 280.1 Hz, which we used for the setup of digital filters in the analysis of interferogram, clockwise and counter-clockwise mono-beam intensities.

We first calibrate the mono-beam intensities and the gain probe in Lamb units, by measuring the multimode threshold of the laser and using a gain calibration ramp [10]. The multimode mean voltage values for the intensities and the mean modulation of the interferogram at multimode, are $V_{m1} = 1.67$ V, $V_{m2} = 1.195$ V, and $V_{Im} = 0.165$ V, respectively. We calibrated the gain monitor with a linear input/output model $G = aV_p + b$. The fit parameters were estimated as $a = 0.0258\, V^{-1}$ and $b = 1.2446$, with relative errors of 1.1×10^{-3} and 8×10^{-4}, respectively. Fig.10 shows the experimental points and the results of the fit. The calibrated single pass gain allows us to estimate the mono-beam intensities in Lamb units. In addition, we estimated the modulation and phase differences of mono-beams by means of digital lock-in filters tuned to the Sagnac frequency. Then we use these quantities to estimate the Lamb parameters $\alpha_{1,2}$ (excess gain minus losses), $r_{1,2}$ (backscattering amplitudes), β (self saturation, almost proportional to the laser single pass gain), and $\varepsilon_{1,2}$ (backscattering phases) at the rate of 1 sample every 10 seconds. The results for the calibrated gain and the estimated laser parameters are reported in Fig.11. It is worth noticing that the timeseries of $\alpha_{1,2}$ and β are much more stable than the time-series of $r_{1,2}$ and $\varepsilon_{1,2}$.

Provided with the laser parameters, we applied the Kalman routine to the time-series of intensities and interferogram of all the 5 days for the computation of the backscattering BSK. Then we fit the computed backscattering to the linear input/output model $AR2 = a\, BSK + b$. The coefficients of the linear fit are $a = 1.103$, $b = 280.317$, with relative errors of 9×10^{-4} and 3.5×10^{-5}, respectively.

The residuals of the fit showed an improved sensitivity, and the corrected Sagnac frequency is more precise, as reported in Fig. 12 and Fig.13.

However, the study of the residuals showed that the stability of mono-beam intensities and Sagnac frequency is affected by some residual fluctuations, which are probably due to cavity deformations. It is worth noticing that the control of perimeter length was not yet implemented in this run. As a consequence, some extra noise is present in the Sagnac frequency in the $[10^{-2} \div 10^{1}]$ Hz band. Therefore the backscattering subtraction on the complete run shows suboptimal performances with respect to the Allan standard deviation, see Fig. 14. However, we analyzed a subset of 3 h of the data in which GINGERino showed a fairly stable behavior. Notice that the rms amplitude of fluctuations of Sagnac frequency after the backscattering subtraction decreases from 14 mHz to 0.225 mHz and to 0.14 mHz, for integration times of 10, and 350 sec, respectively. In any case, these promising results on backscattering subtraction are still preliminary. In the future runs, we will provide the perimeter stabilization of GINGERino and, hopefully, we will be able to subtract backscattering more efficiently and to improve the relative stability of GINGERino. The goal is to measure Earth rotation with a relative precision of $10^{-7} \div 10^{-8}$, which is the precision required to observe daily polar motion.

5 Analysis of the seismometers

In order to have clear picture of the residual seismic noise of the site, we have performed a comprehensive analysis of three seismometers. The three pictures below (Fig.s 15, 16 and 17)

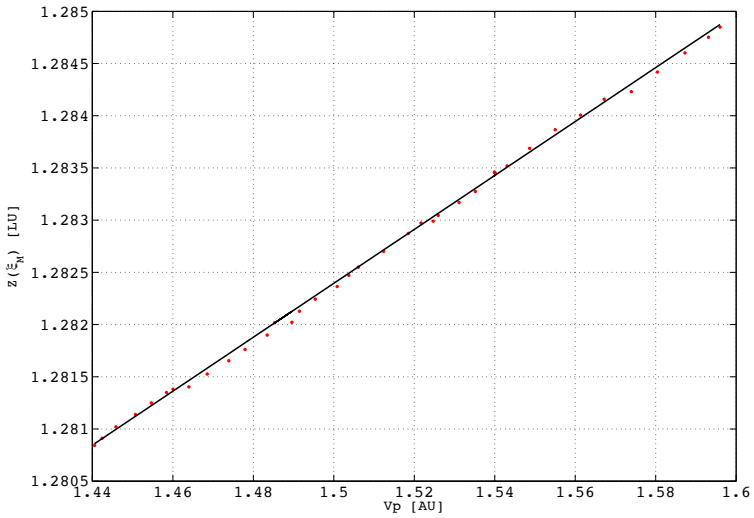

Figure 10: Calibration of the single pass gain G as a linear function of the plasma discharge voltage V_p.

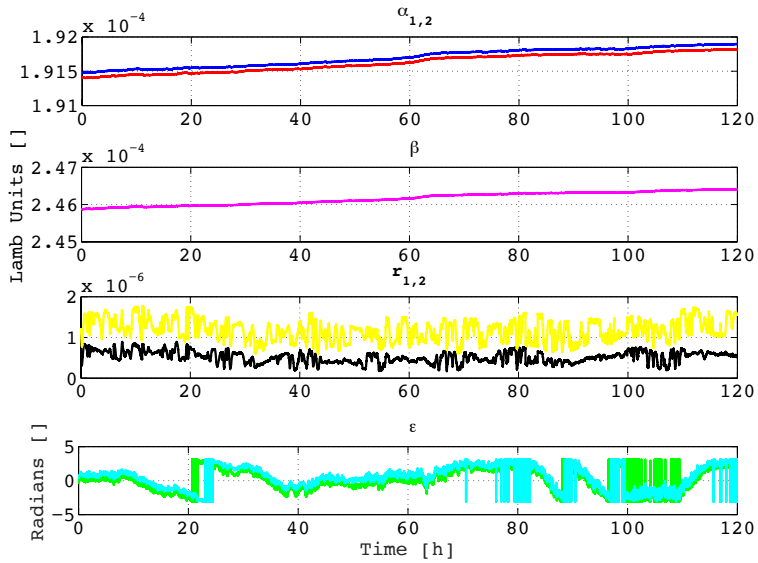

Figure 11: Time plots of the Lamb parameters $\alpha_{1,2}$, β, $r_{1,2}$ and $\varepsilon_{1,2}$ for the 5 days of analysis.

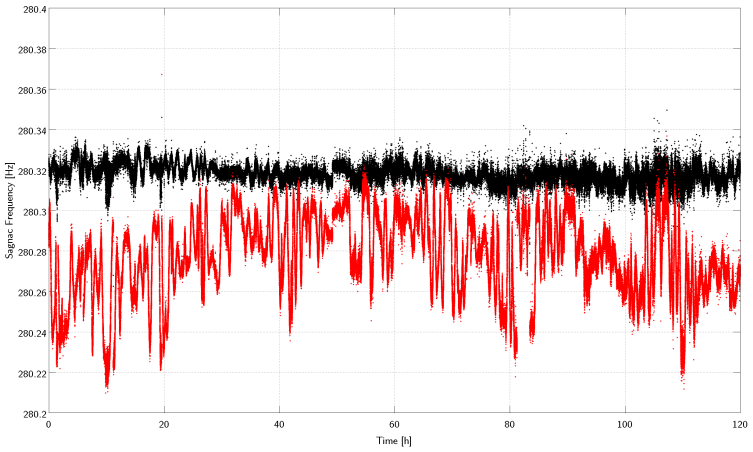

Figure 12: Time comparison of the Sagnac frequency AR2 estimates with (black) and without (red) the backscattering subtraction.

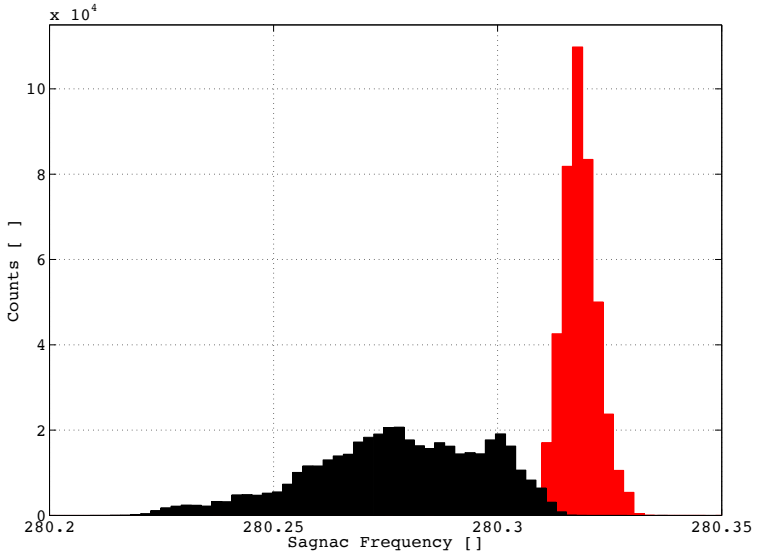

Figure 13: Histograms of the Sagnac frequency AR2 estimates with (red) and without (black) the backscattering subtraction.

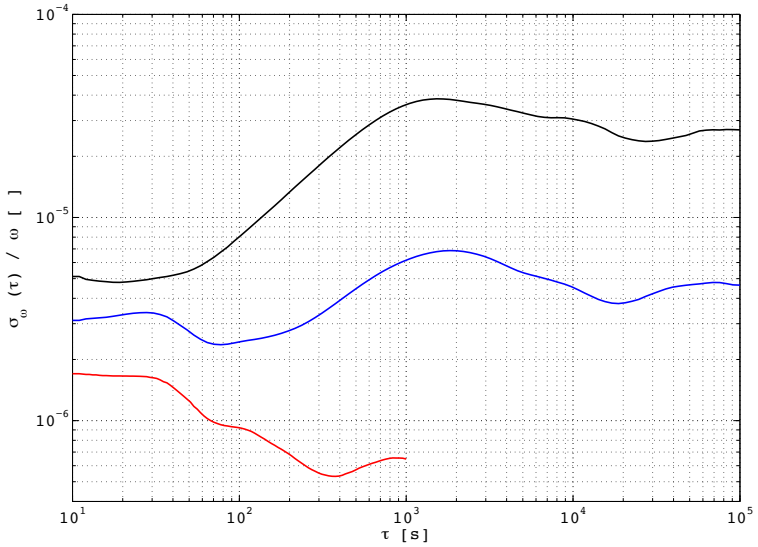

Figure 14: Relative Allan deviation of the Sagnac frequency of GINGERino as a function of time. Black line: AR2 algorithm. Blue line: AR2 with backscattering subtraction. Red line: AR2 with backscattering subtraction over 3 hours of best typical behavior of GINGERino.

show the seismic noise power spectra vs. seismic wave periods, for the three components of the acceleration (in units of $m^2/s^4/Hz$ (dB)): vertical Z, horizontal N (North) and horizontal (East). The continuous lines are the two spectrum of the low and high noise model for the Earth (NLNM and NHLM, after Peterson 1993 [11]). Our typical spectrum is close to the NLNM and shows a very good behavior across the spectral region for primary and secondary microseisms, but exhibits larger and unwanted noise at low frequency (high periods) for the N and E components. This is a point of concern for the future development of GINGER that is mainly interested at low frequency, and it is necessary to understand if this noise is intrinsic to the lab, or if it can be eliminated. A deeper analysis including the polarisation for horizontal components of acceleration has shown that the excess horizontal noise is directional and directed along the tunnel (see Fig. 18). We actually believe that this effect is induced by the air motion around the seismometers. Further investigation, by possibly isolating the apparatus from air

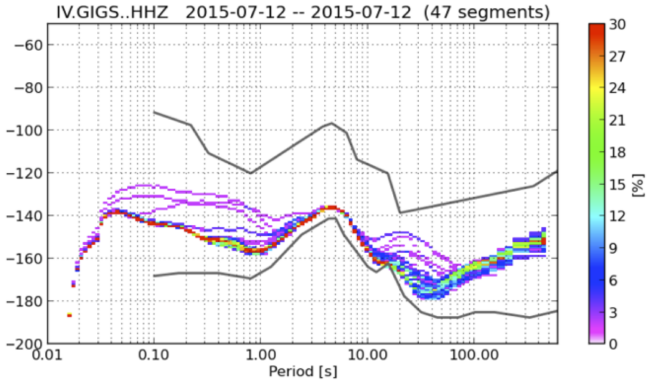

Figure 15: Typical power spectrum of the vertical component.

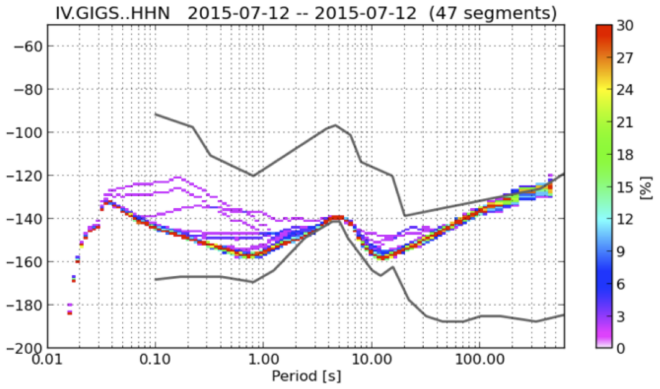

Figure 16: Typical power spectrum of the horizontal N component.

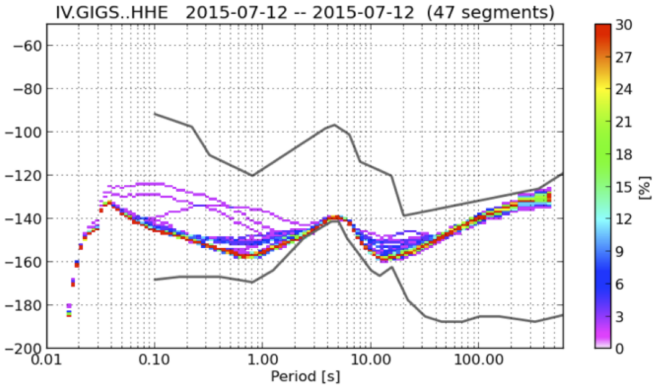

Figure 17: Typical power spectrum of the horizontal E component.

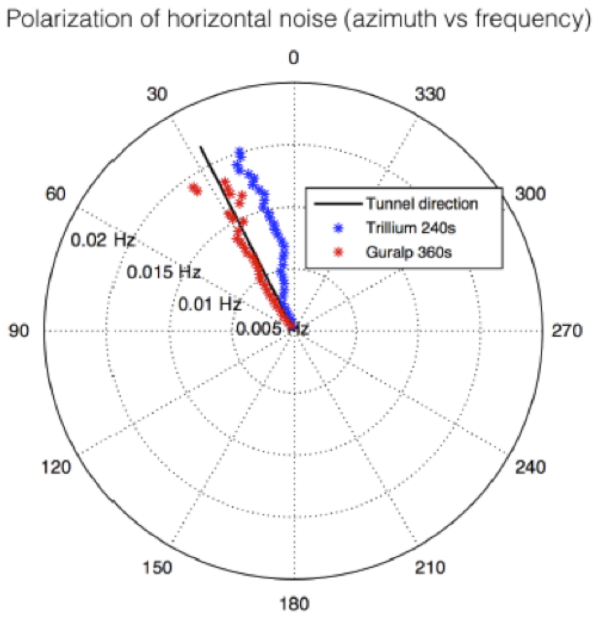

Figure 18: Reconstruction of the polarization of the horizontal noise of the two seismometers. Their relative alignment is within 5 degrees, they show the disturbances propagates mainly along the tunnel.

Figure 19: Typical trend of the pressure inside the room of GINGERino

flow or inducing extra air flow in controlled conditions, will be necessary for a stronger evidence. It is well known that the noise level of the horizontal components of seismic sensors is much higher than the level of the vertical ones. It is often assumed that the tilt of the seismometer's monument due to local pressure variation – besides other meteorological effects – is responsible for that effect, mainly in the frequency range below 10 mHz (Beauduin, R., et al. "The effects of the atmospheric pressure changes on seismic signals or how to improve the quality of a station." Bulletin of the Seismological Society of America 86.6 (1996): 1760–1769.). Shielding against air-pressure variations is essential for long-period observations. Variations of the buoyancy force on the proof-mass of vertical component sensors are caused by variations of air-density due to air-pressure variations. The amplitude of such forces can easily exceed the amplitude of the tides, if the instrument is not shielded appropriately. The analysis of the data taken from the two installed seismometers has shown that this tilting noise is directed along the tunnel, and a possible interpretation is that this is induced by the air motion around the seismometers and the whole anechoic box. This air flow due to forced air convection inside the tunnel may lead to high pressure variations when it encounters the GINGERino box that acts as a membrane. It is also well known that the deformation caused by non-isotropic variations of air-pressure on the casing of the seismometer (i.e. turbulencies) can result in tilts. As an indirect proof of this hypothesis the environmental pressure monitors has shown a large variability over time (see Fig. 19). Day/Night and weekdays/week-end variations are evident and very well correlated with the

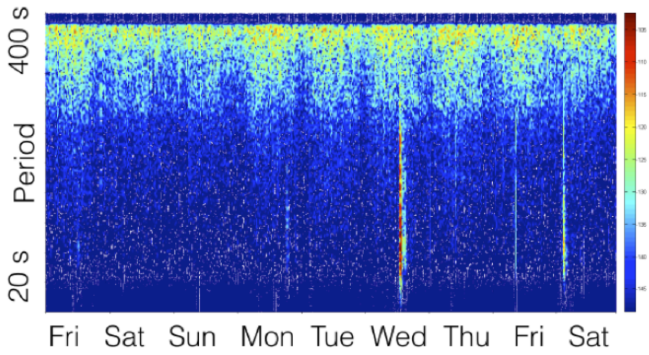

Figure 20: Seismometers: typical horizontal signals in function of frequency and week day.

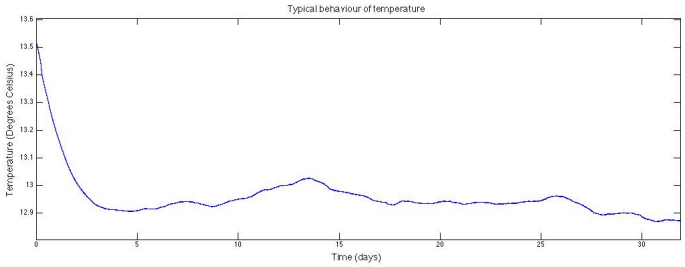

Figure 21: Typical behavior of the temperature monitor: after the operation the environment takes few days to reach the turmoil equilibrium

TF analysis of the seismic noise on horizontal component parallel to the tunnel. In Fig. 20 the analysis done for days of year from 164 to 172 is reported.

6 Environmental Monitors

GINGERino is protected by an anechoic box. The location in between Node A and Node B has several advantages, since it is very well isolated from the man made disturbances of the laboratory, but it is a very wet place. We have measured more than 90% of relative humidity and a temperature around 6 C^o. In order to reduce the relative humidity below 70% we have installed few infrared lamps inside the box and leave the system reach a thermal equilibrium point around 16 C^o. The standard procedure is to operate around GINGERino for one week and then leave it operating stand alone. It usually takes few days to reach a stable thermal equilibrium, see Fig. 21. The data taken when the system is at the thermal equilibrium are the ones valuable for the analysis. The pressure is the parameter of environment which has a large variability (see Fig. 19), we are investigating if it induces disturbances in the ring laser data. One tilt meter with sensitivity of a few nano-radiants and bandwidth of 1 mHz has been installed on top of the granite monument, in order to detect local subsidence. Fig. 22 shows the typical behavior, it exhibits the typical tilt induced by the diurnal and semidiurnal tides of the Moon, while the very low frequency trend is an artifact of the tilt-meter.

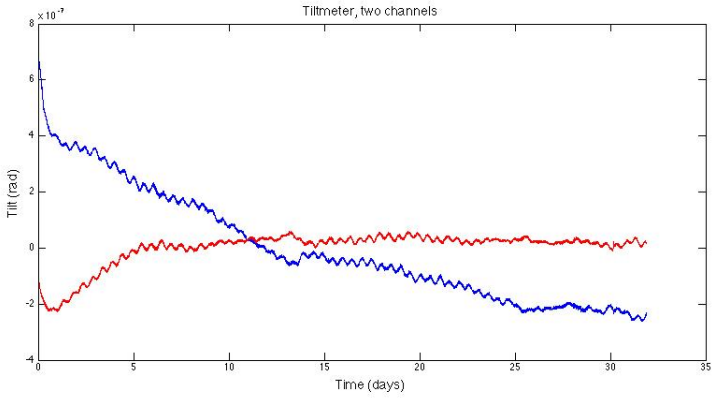

Figure 22: The two channels of the tilt meter. The diurnal and semidiurnal polar motions are visible. The very low frequency trend of the instrument is not a real subsidence of the floor, it is an artifact of the tilt-meter

7 Conclusions

GINGERino has been constructed inside LNGS and at the moment it is under study in order to improve the sensitivity and the long term stability. In 2015, several mechanical improvements have been made in order to make the RLG cavity stiffer and to improve its isolation from external disturbances. The instrument has been in data taking during the spring and in October 2015. In the first, second and third runs the ring-down times of the cavity were of the order of 240μs, 150μs, and 250μs, respectively. The quality of the cavity depends on the mirrors, but unfortunately the mirrors of the first run have been damaged during a failure in the vacuum system. The sensitivity curve in the three cases is around 10^{-10} rad/s, compatible with the actual instrument shot noise and ring-down times. The main limitation comes from the backscattering noise, which limits down to tens of seconds the integration time of the apparatus. In the third run we succesfully calibrated the laser dynamics parameters. In 2016 the effort will be dedicated to increase the ring-down time of the cavity, possible up to $1ms$, getting mirrors of higher quality so to also reduce the backscattering. A novel set of higher quality mirror are in preparation, they are expected to be installed before summer 2016. The quality of the mirrors we are aiming for have losses of a few part per million, which is the status of the art for dielectric coating.

Notwithstanding this technical limitation GINGERino has already given few clear indication on the site quality toward the bigger GINGER project. The analysis of RLG data and co-located seismometers and other environmental monitors has shown that pressure is the parameter with higher variability. A first evidence of the role of this variations on the low frequency disturbances seen by the seismometer has been found. We will investigate if the pressure variations limit the long term stability of the apparatus of GINGERino. There is evidence that the seismometers are disturbed by the pressure variations. Few tele seismic events have been detected by GINGERino, coming from far away earthquakes; the analysis of those events are in progress.

8 Acknowledgement

The progress around the apparatus of GINGERino is possible thanks to the continuous support of the people of LNGS, we hanks the support of: Gabriele Bucciarelli, Nicola Massimiani, Ercolino Tatarelli and the people of "servizio facchinaggio". We are grateful to Donato Orlandi and his

collaborators: Antonio Croce and Davide Giusti. They have realized the part to improve the support of the discharge and the vacuum tubes of GINGERino. We have to thank as well the Computing teams of LNGS and Pisa: in particular Sandra Parlati, Nazarene Taborgna, Silvia Arezzini, Alberto Ciampa and Enrico Mazzoni. Regarding the support of the Pisa Section we are grateful to Alessandro Soldani, Andrea Di Sacco, Antonio Orsini, Antonino Ragonesi.

9 Appendix A: The ring laser signal: The PPN approach

The aim of the GINGER experiment is to measure the gravitational field of the Earth, up to post-Newtonian order, by mean of a ring laser. Actually it is important to stress that this would be *the first measurement* of the General Relativistic gravitomagnetism of the gravitational field of the Earth, performed in a terrestrial laboratory.

A sufficiently general expression of the gravitational field of the rotating Earth (see e.g. [12]) is

$$\begin{aligned} ds^2 \quad &= G_{\mu\nu}\, dX^\mu dX^\nu = (1-2U(R))dT^2 - (1+2\gamma U(R))\,\delta_{ij} dX^i dX^j + \\ 2 &\left[\frac{(1+\gamma+\alpha_1/4)}{R^3}(\boldsymbol{J}_\oplus \wedge \boldsymbol{R})_i - \alpha_1 U(R) W_i\right] dX^i dT, \end{aligned} \tag{2}$$

where $-U(R)$ is the Newtonian potential, $\boldsymbol{J}_\oplus$ is the angular momentum of the Earth, W_i is the velocity of the reference frame in which the Earth is at rest with respect to mean rest-frame of the Universe; γ and α_1 are post-Newtonian parameters that measure, respectively, the effect of spatial curvature and the effect of preferred frames. The background metric (2) is referred to an Earth Fixed Inertial (ECI) frame, where Cartesian geocentric coordinates are used, such that $\boldsymbol{R}$ is the position vector and $R \doteq \sqrt{\sum_i X_i^2} = \sqrt{X^2+Y^2+Z^2}$.

It is possible to show (see e.g. [13]) that the Sagnac time delay in a terrestrial laboratory turns out to be

$$\Delta\tau = \frac{4\,(\boldsymbol{\Omega}_\oplus + \boldsymbol{\Omega}')\cdot \mathbf{S}}{c^2}, \tag{3}$$

where $\mathbf{S}$ is the vector associated to the area enclosed by the light path; in particular, $\dfrac{4\boldsymbol{\Omega}_\oplus \cdot \mathbf{S}}{c^2}$ is the purely kinematic Sagnac term, due to the rotation of the Earth, while $\dfrac{4\boldsymbol{\Omega}' \cdot \mathbf{S}}{c^2}$ is the gravitational correction $\boldsymbol{\Omega}' = \boldsymbol{\Omega}_G + \boldsymbol{\Omega}_B + \boldsymbol{\Omega}_W + \boldsymbol{\Omega}_T$, where

$$\boldsymbol{\Omega}_G = -(1+\gamma)\,\boldsymbol{\nabla} U(R) \wedge \boldsymbol{V}, \tag{4}$$

$$\boldsymbol{\Omega}_B = -\frac{1+\gamma+\alpha_1/4}{2}\left(\frac{\boldsymbol{J}_\oplus}{R^3} - \frac{3\boldsymbol{J}_\oplus \cdot \boldsymbol{R}}{R^5}\boldsymbol{R}\right), \tag{5}$$

$$\boldsymbol{\Omega}_W = \alpha_1 \frac{1}{4}\boldsymbol{\nabla} U(R) \wedge \boldsymbol{W}, \tag{6}$$

$$\boldsymbol{\Omega}_T = -\frac{1}{2}\boldsymbol{V} \wedge \frac{d\boldsymbol{V}}{dT}. \tag{7}$$

In detail, we have the four contributions: i) the geodetic or de Sitter precession $\boldsymbol{\Omega}_G$ is due to the motion of the laboratory in the curved space-time around the Earth; ii) the Lense-Thirring or gravito-magnetic precession $\boldsymbol{\Omega}_B$ is due to the angular momentum of the Earth; iii) $\boldsymbol{\Omega}_W$ is due to

the preferred frames effect; and iv) the Thomas precession $\mathbf{\Omega}_T$ is related to the angular defect due to the Lorentz boost. The terms in (4)-(7) must be evaluated along the laboratory world-line (hence, they are constant in the local frame), whose position and velocity in the background frame are $\boldsymbol{R}$ and $\boldsymbol{V}$, respectively.

A ring laser converts the time differences (3) into the frequency difference

$$\Delta f = \frac{4}{\lambda P}\ \left(\mathbf{\Omega}_\oplus + \mathbf{\Omega}'\right) \cdot \mathbf{S}, \tag{8}$$

where P is the perimeter and λ is the laser wavelength.

It is important to emphasize that, for the very nature of the measurement performed, a ring laser is able to detect, in principle, *all the contributions*[1] (4)-(7),

9.1 Beyond the PPN approach

Modified theories of gravity introduce perturbations of the gravitational field of the Earth that, in general, cannot be described within the PPN scheme. So, quite generally, we are led to suppose that the space-time metric (2) could be perturbed in the form

$$G_{00} \to G_{00} + \delta G_{00}, \quad , G_{ij} \to G_{ij} + \delta G_{ij}, \quad G_{0i} \to G_{0i} + \delta G_{0i} \tag{9}$$

where the perturbation terms $\delta G_{\mu\nu}$ are determined by the specific modified gravity model.

Roughly speaking, we may say that the the geodetic term $\mathbf{\Omega}_G$ is sensitive to modifications of both G_{00} and G_{ij}, while the Lense-Thirring term $\mathbf{\Omega}_B$ is sensitive to modification of the G_{0i} term. So, in principle, a measurement performed by a terrestrial ring laser could be used to explore the effects of *all* the modified terms of the metric.

Notice that this is not true, for instance, for the LAGEOS/LARES experiment, which has been designed to measure *only* the gravito-magnetic field of the Earth, that is the G_{0i} term[2] of the metric (2). In other words, the measurements that could be performed by GINGER are *complementary* to those of LAGEOS/LARES.

As an example of modified gravity model, we may consider **Horava-Lifshits gravity** (a four-dimensional theory of gravity which is power-counting renormalizable and, hence, can be considered as a candidate for the ultraviolet completion of GR). In particular, if we denote by θ the colatitude of the laboratory, and by α the angle between the radial direction and the normal vector the interferometer plane, the geoedetic term is modified according to (see e.g. [14])

$$-2\frac{GM}{c^2R}\Omega_\oplus \sin\theta \sin\alpha \to \left(1 + \frac{G^*}{G}a_1 - \frac{a_2}{a_1}\right)\frac{G^*M}{c^2R}\sin\theta\sin\alpha \tag{10}$$

while the Lense-Thirring one by

$$\frac{GI_\oplus}{c^2R^3}\Omega_\oplus\left(2\cos\theta\cos\alpha + \sin\theta\sin\alpha\right) \to \frac{G^*I_\oplus}{c^2R^3}\Omega_\oplus\left(2\cos\theta\cos\alpha + \sin\theta\sin\alpha\right) \tag{11}$$

In the above equations a_1, a_2 are coupling constants of the theory and G^* is the Newtonian constant in the Horava-Lifshits theory, that could, in principle, differ from the GR one. So, we see that the modification of the two terms are different in this modified gravity model: GINGER could, in principle, constrain the constants G^*, a_1, a_2 while the measurements performed

[1] Their sum constitutes the *total* gravito-magnetic field in a terrestrial laboratory.

[2] LARES measures the gravito-magnetic field of asymptotically inertial observers.

by LARES do not depend on a_1, a_2.

A similar situation happens in **extended theories of gravity**: in [15] the authors consider the weak field limit (in order to describe with sufficient accuracy the weak field of the Earth) of a generic scalar-tensor-higher-order model and show that both the geodetic and the Lense-Thirring terms are modified, by somewhat complicated combinations of terms that depend on the effective masses m_R, m_Y, m_ϕ of the model. In particular, $\mathbf{\Omega}_G \to \mathbf{\Omega}_G + \mathbf{\Omega}_G^{EG}$, where

$$\mathbf{\Omega}_G^{(\mathrm{EG})} = -\Big[g(\xi,\eta)(m_R\tilde{k}_R r+1)\,F(m_R\tilde{k}_R\mathcal{R})\,e^{-m_R\tilde{k}_R r} + \frac{8}{3}(m_Y r+1)\,F(m_Y\mathcal{R})\,e^{-m_Y r} + \frac{1}{3} - g(\xi,\eta)](m_R\tilde{k}_\phi r+1)F(m_R\tilde{k}_\phi\mathcal{R})\,e^{-m_R\tilde{k}_\phi r}\Big]\frac{\mathbf{\Omega}_G}{3}\ . \quad (12)$$

and $\mathbf{\Omega}_B \to \mathbf{\Omega}_B + \mathbf{\Omega}_B^{EG}$, where

$$\mathbf{\Omega}_B^{(\mathrm{EG})} = -e^{-m_Y r}(1 + m_Y r + {m_Y}^2 r^2)\,\mathbf{\Omega}_B\ ,$$

Once again, notice that the modifications of the two terms are different, and that GINGER could be able to test both of them.

Another example of modified gravity model that could be tested, in principle, by GINGER is the **Standard Model Extension**, in which violations of Lorentz symmetry are allowed for both gravity and electromagnetism: actually, these violations could be signals of new physics effects deriving from a still unknown underlying quantum theory of gravity [**?**]. There are 9 coefficients $\bar{s}^{\mu\nu}$ that parameterize the effects of Lorentz violation in the gravitational sector, under the assumption of spontaneous Lorentz-symmetry breaking. In particular, in [16] it is shown that additional contributions deriving from Lorentz violation are present in the gravitational field of a point-like source of mass M, that to lowest order approximation are

$$G_{00} = 1 - 2U(R)\left[1 + \frac{3}{2}\bar{s}^{00}\right], \quad (13)$$

$$G_{0j} = -U(R)\left[\bar{s}^{0j}\right]. \quad (14)$$

We have modifications of the de Sitter contribution, due to (13), and of the gravito-magnetic contribution, due to (14).

Eventually, also **Chern-Simons gravity** [17] introduces peculiar modifications of the ring laser signal with respect to General Relativity.

10 Appendix B: Geometry Control: GP2 and GEMS

10.1 GP2 1.6× 1.6 m^2 ring laser

Resolving the Earth rotation rate below the level of one part per billion, requires to control the ring laser geometrical scale factor K_s to the same level of accuracy. Being $K_s = \frac{4A}{\lambda P}$, the stabilization of the only laser cavity perimeter P, directly related to the ring laser optical frequency emission, is not sufficient. In fact, also the area A enclosed by the beam path must be controlled. The aim is to reduce the fluctuation associated with the deformation of the optical cavity, stabilizing with a sub-nanometer accuracy the variation of the mirror inter-distances.

More specifically, the beam circulating inside a cavity with four spherical mirrors has 12 degrees of freedom in space, corresponding to the 3 coordinates in space of each of the four

mirrors. Tracing out the three rigid translations and rotations, we have 6 remaining degrees of freedom determining the cavity shape. Our basic idea is to constrain these degrees of freedom by exploiting the symmetry properties of a closely regular square shape. In particular, we proposed [**?**] an active stabilization approach. This is done by injecting the two diagonal Fabry-Pérot resonators, formed by the two couples of opposite cavity mirrors with the same ultra-stable reference laser, and correct the position of the cavity mirrors by means of piezoelectric nanometric transducers. In this way the stability of the laser wavelength is transferred to the square diagonals and the cavity is affected only quadratically by the perturbations on the mirrors positions along the residual 4 degrees of freedom. These last can be eventually optimized by controlling the cavity perimeter length. In fact, once the fixed diagonals length constraint is considered, the regular square configuration corresponds to a saddle point for the perimeter length function. The experimental setup installed at the INFN in Pisa is shown in Fig.23.

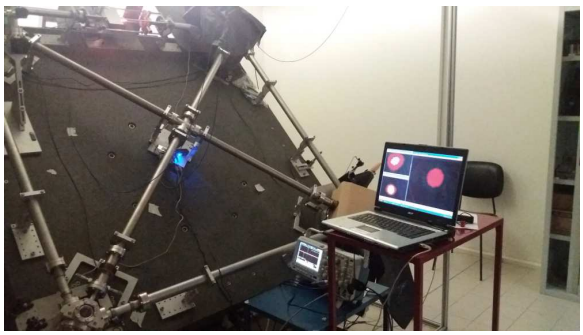

Figure 23: GP2 ring laser is oriented at the maximum signal, i.e. with the laser plane perpendicular to the Earth's rotation axis. Three webcams are used for monitoring the beam profiles of three laser beams: the two modes resonating in the diagonals and the ring laser emission itself.

The experimental technique for the diagonal cavities control is based on the multi-frequency phase modulation of the reference laser, and is described in detail in **??**. This provides the estimate of both the cavity resonance frequency and the free-spectral range of the two resonators, so that an absolute length measurement can be achieved. In Fig. 24 is reported the optical scheme of the geometry control apparatus.

A sub-nanometer length stabilization of the diagonals cavities has been obtained with a signal integration time of few hundred seconds. The feedback signals controlling the two diagonal cavity lengths are reported in Fig. 25. Both signals follow the room temperature fluctuation in the laboratory, that to date is not provided by a temperature stabilization system. The switch off of the air-conditioning/heating, at $t \sim 1.2$ hours, is visible and clearly affect the trend of the two signals. The difference between the two signal corrections, plotted in the same graph, accounts for time-dependent temperature gradients in the laboratory, differential mechanical relaxations, and also slightly different mechanical responses of the piezoelectric translator stages.

A length metrology technique has been provided, and its compatibility with a He-Ne square ring laser gyroscope has been demonstrated. To date, the main limit to the use of this tool are the uncontrolled environmental conditions in the laboratory, and the anthropic noise of the building during working hours.

10.2 GEMS

A control scheme of the scale factor of a single ring is at the moment under development and test at INFN of Pisa with a prototype called GP2 [18]. Monitoring of relative angles between different

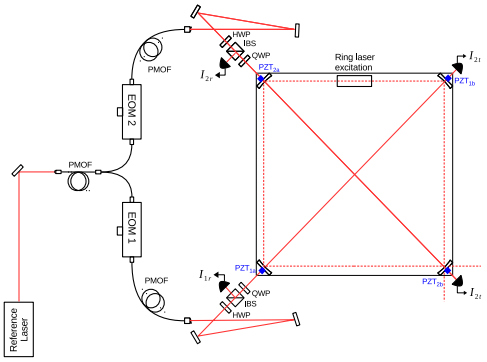

Figure 24: Optical setup for the interrogation of the diagonal Fabry-Perot. EOM: Electro-Optic Modulator. PBS: Polarizing Beam Splitter. IBS: Intensity Beam Splitter. PMOF: Polarization Maintaining Optical Fiber. HWP: Half Wave Plate. QWP: Quarter Wave Plate. PZT: Piezoelectric Transducer. F: neutral filter.

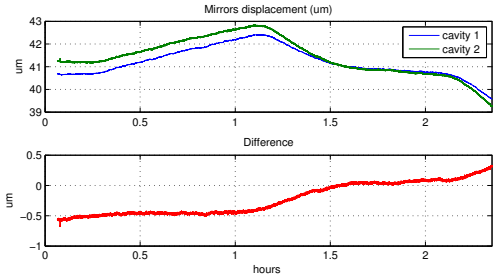

Figure 25: Closed-loop corrections to both mirrors forming the GP2 diagonal cavities. Upper graph: displacement correction applied to the opposite mirrors of the two cavities. Lower graph: correction difference.

rings was originally founded on higher order modes of the ring cavity [19], but it was then realized that an independent metrology technique had to be developed, something independent on any ring laser dynamics. Therefore a third approach, based on an external metrology system is now under development. This metrology system will be closely matched to the main instrument, providing real-time measurements of its geometrical frame and acting as the first element of a feedback control loop. This external metrology could be applied to the control of each ring and to the monitoring of the angles between different rings.

The best real world example of this alternative technique is represented by the "External Metrology Truss" [20, 21] devised by NASA's Jet Propulsion Laboratory (JPL) for its discontinued Space Interferometric Mission [22]. This device was supposed to provide reliable distance measurements for the accurate monitoring of the baseline length of a stellar interferometer aimed to planet finding. The truss was made up of a network of laser heterodyne interferometers, working together to keep the spacecraft geometry constantly well known to the $10\,pm$ precision. A common light source was provided by a fiber coupled $1319\,nm$ Nd:YAG DPSS laser. Source light was split in half and each part sent to an acousto-optic modulator, where a frequency offset was introduced between the halves: a reference and a measurement beam were created in this way and, after proper splitting, sent to every interferometer via PM optical fibers. Each interferometer (beam-launcher) laid on a compact and portable Zerodur® base, where all the optics

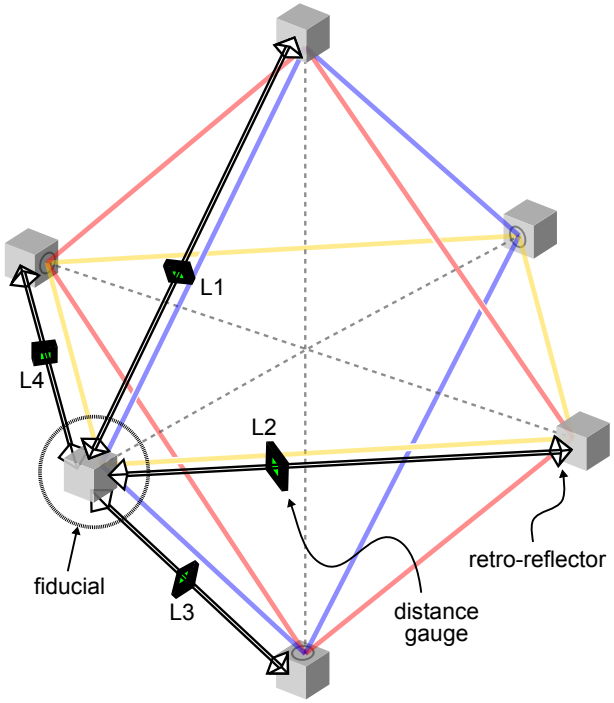

Figure 26: Simplified structure of the external metrology truss matched with GINGER (octahedral version).

were firmly fixed. This breadboard was placed between two of the many fiducials laying on the spacecraft. The fiducials were made by multiple corner-cube retro-reflectors, rigidly connected to appropriate reference points of the truss to be monitored. Single distance measurements were retrieved by detecting the phase shift between two heterodyne beatings: the reference beating, generated by direct recombination of the source lights, and the measurement beating, generated by recombination between the source light and the measurement beam, which had travelled along a racetrack between the fiducials. Together with this main displacement monitoring system, there existed some other subsystems working to provide additional features and reliability:

- a frequency tuning system for the laser source, devoted to two-colors interferometry for the determination of the absolute distance between the fiducials [20];
- a pointing dithering system which protected against misalignments of the interferometer with respect to the axis ideally connecting the fiducials [23].

For a detailed description of the beam laucher we refer to [24].

10.3 Full system concept and GEMS

Basically, the idea is to adapt the JPL concept to the case of GINGER, which will then rely on an effective geometry monitoring system. Moreover, this external metrology system will send its data to a feedback control loop, whose actuators will be multi-axial piezo-electric translational stages carrying all the ring laser mirrors.

If for example an octahedral shape is chosen for GINGER, every fiducial (one for each vertex) could be ideally composed by a single bulk substrate featuring both the ring laser super-mirror, which is shared by 3 ring lasers, and 4 corner retro-reflectors, one for each edge leaving from the

given vertex. Then the external metrology truss would be ideally set up by placing 12 compact distance gauges along the corresponding edges of the octahedron (26). A dedicated vacuum system will be necessary to guarantee measurements independent on any ring laser dynamics. Extremely precise manufacturing of the fiducials will be essential as well, together with their geometrical characterization.

Moreover, depending on the number of available interferometers and the type of physically craftable fiducials (either simple one-direction backreflectors, or multidirectional ones), an array of cross measurements can be realized to over-constraint the "rigidity" of the ring laser array. Then, thanks to a detailed mathematical model of the geometry of the ring laser and a multivariable control scheme, it will be possible to drive suitable nano-positioning actuators to properly move the mirrors and actively control all the relevant dimensions of the cavities. In such a way, it will be possible to keep GINGER's geometry locked within the required accuracy, independently of any environmental disturbances.

The first step towards the realization of this device is the construction of its fundamental element, i.e. the compact heterodyne laser interferometer.

Single gauge prototype design

Starting from what was outlined by JPL, the first working example of a distance gauge for GINGER will be a simplified prototype: its preliminary design will let us evaluate parts behavior, alignment issues and links between single components and overall system performances. The prototype will lie on a vibration isolated optical table and work in a standard air environment, certainly without claim to reach the final desired precision. The goal for this first step is to be able to measure relative shifts between fiducials with sub-micron precision.

The prototype's optical design mostly follows what was conceived for SIM, at least with respect to its basic working principle and the means of splitting between reference and measurement beams. Source light comes from a continuous wave Nd:YAG DPSS laser featuring a $> 1\,km$ coherence length and analog frequency tunability; its $1064\,nm$ beam is fiber coupled right after exiting the device and routed to a 50:50 fiber splitter by means of PM single mode fibers. Each half is then sent to a in-fiber acousto-optic modulator which shifts its optical frequency by respectively $150\,MHz$ and $150.1\,MHz$. Finally, both beams travel through refractive fiber collimators and are ready to proceed across the free-space section of the distance gauge. The simplified optical schematic of a single interferometer is showed in 27.

10.4 The racetrack

Spatial separation between measurement and reference beams is provided by a gold-coated double mirror, operating at 45° angle of incidence. A 3D model of this mirror showed non trivial footprint issues due to the 45° incidence angle and the necessity to keep a wide enough clear aperture on both sides of the mirror. We chose a $2\,in$ diameter in order to avoid beam shading by mounts 28. The 45° tilted hole lets the reference beam walk through and reach the recombination beam-splitter (beam-combiner) immediately after; instead, the annular part of the beam is sent along the racetrack, made up by the drilled mirror itself and 4 auxiliary gold mirrors. These additional gold mirrors are set up in two prealigned fixed pairs, as to form two 2D retro-reflectors which will act as distance fiducials; one of them is placed on a nano-positioning translational stage in order to carry out performance tests of the prototype. Furthermore, we plan to place properly shaped masks along the $8\,m$ test distance for a better spatial isolation of the reference and measurement beams, given that a mixing of them badly compromises the distance measurements.

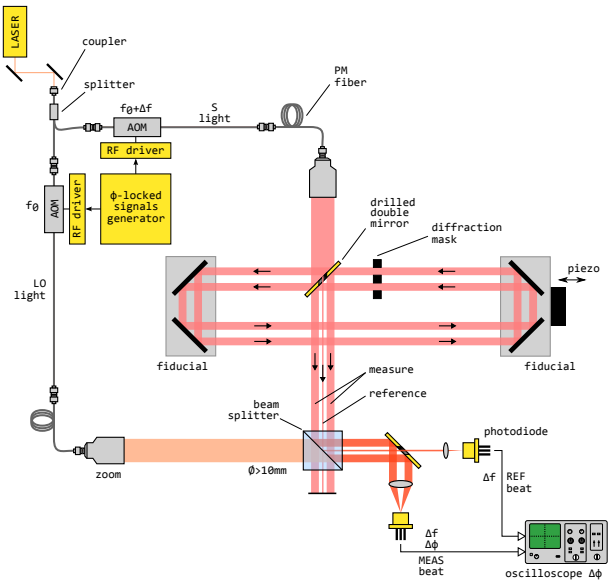

Figure 27: Schematic of the distance gauge prototype.

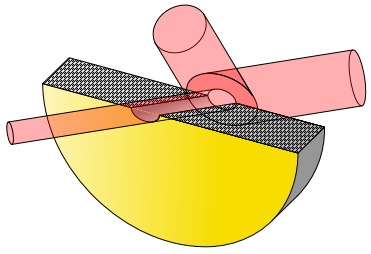

Figure 28: 3D layout of the double mirror picking off the measurement beam.

10.5 The heterodyne interferometer

Except for the so called "racetrack", the setup is similar to that of a standard Mach-Zehnder interferometer. Actually this is the optical path that the reference beams (central part of each source beam) follow before recombinating and giving birth to a reference light beating. The measurement beam is picked out by means of the double sided mirror. As already mentioned, this mirror spatially splits one of the source beams in two parts: the inner part, propagating straight through the hole along the Mach-Zehnder path, and the outer part, with a ring shaped section, hitting the mirror and travelling along the racetrack. In fact, this beam measures the distance between the fiducials by making a loop: the beam goes to the first fiducial (on the left) and hits it off-center; the reflected beam is offset and goes past the gauge to hit the second fiducial on the right; then the beam is reflected and offset a second time and lines up again with the double-sided mirror; finally the beam hits the back side of the drilled mirror and proceeds down to the beam-combiner. With respect to its reference counterpart, the beam travelling along the racetrack gathers a phase delay directly proportional to the relative displacement between the fiducials. A measurement light beating is therefore generated by the recombination between the outer parts of the source beams. We recall that the reference and measurement lights are spatially separated, reducing the risk of signals intermixing if compared to polarized light solutions [24].

A second drilled mirror provides for the deflection of the measurement beating on a detector different from the reference one. Both of these detectors are transimpedance amplified photodiodes with switchable gain and their generated voltage signals are sent to an oscilloscope, on which first rough phase measurements will be performed. A suitable digital phasemeter will be used for high resolution sampling.

References

[1] Karl Ulrich Schreiber and Jon-Paul R. Wells. Invited review article: Large ring lasers for rotation sensing. *Review of Scientific Instruments*, 84(4):1, 2013.

[2] T. et al. Nilsson. Combining vlbi and ring laser observations for determination of high frequency earth rotation variation. *Journal of Geodynamics*, 62(12):69–73, 12 2012.

[3] K. U. et al. Schreiber. How to detect the chandler and the annual wobble of the earth with a large ring laser gyroscope. *Physical Review Letters*, 107(17), 10 2011.

[4] F. Bosi, G. Cella, A. Di Virgilio, A. Ortolan, A. Porzio, S. Solimeno, M. Cerdonio, J. P. Zendri, M. Allegrini, J. Belfi, N. Beverini, B. Bouhadef, G. Carelli, I. Ferrante, E. Maccioni, R. Passaquieti, F. Stefani, M. L. Ruggiero, A. Tartaglia, K. U. Schreiber, A. Gebauer, and J. P. R. Wells. Measuring gravitomagnetic effects by a multi-ring-laser gyroscope. *Physical Review D*, 84(12), 2011.

[5] A. et al. Gebauer. High-frequency noise caused by wind in large ring laser gyroscope data. *Journal of Seismology*, 16(4):777–786, 08 2013.

[6] J. Belfi, N. Beverini, F. Bosi, G. Carelli, A. Di Virgilio, E. Maccioni, A. Ortolan, and F. Stefani. A 1.82 m(2) ring laser gyroscope for nano-rotational motion sensing. *Applied Physics B-Lasers and Optics*, 106(2):271–281, 2012.

[7] Jacopo Belfi, Nicolo Beverini, Filippo Bosi, Giorgio Carelli, Angela Di Virgilio, Dmitri Kolker, Enrico Maccioni, Antonello Ortolan, Roberto Passaquieti, and Fabio Stefani. Per-

formance of "g-pisa" ring laser gyro at the virgo site. *Journal of Seismology*, 16(4):757–766, 2012.

[8] PhD Thesis University of Siena: Santagata, R. Sub-nanometer length metrology for ultra-stable ring laser gyroscopes. 2015.

[9] R. Santagata, A. Beghi, J. Belfi, N. Beverini, D. Cuccato, A. Di Virgilio, A. Ortolan, A. Porzio, and S. Solimeno. Optimization of the geometrical stability in square ring laser gyroscopes. *Classical and Quantum Gravity*, 32(5), 2015.

[10] D. Cuccato, A. Beghi, J. Belfi, N. Beverini, A. Ortolan, and A. Di Virgilio. Controlling the non-linear intracavity dynamics of large he-ne laser gyroscopes. *Metrologia*, 51(1):97–107, 2014.

[11] J. Peterson. Observations and modeling of seismic background noise. *U.S. Geol. Surv. Open-File Rept.*, 93(322), 1993.

[12] Clifford M. Will. The confrontation between general relativity and experiment. *Living Reviews in Relativity*, 9(3), 2006.

[13] Ruggiero M.L. Sagnac effect, ring lasers and terrestrial tests of gravity. *Galaxies*, (3):84–102, 2015.

[14] Ninfa Radicella, Gaetano Lambiase, Luca Parisi, and Gaetano Vilasi. Constraints on covariant horava-lifshitz gravity from frame-dragging experiment. *Journal of Cosmology and Astroparticle Physics*, 2014(12):014, 2014.

[15] S. Capozziello, G. Lambiase, M. Sakellariadou, A. Stabile, and An. Stabile. Constraining models of extended gravity using gravity probe b and lares experiments. *Phys. Rev. D*, 91:044012, Feb 2015.

[16] Quentin G Bailey. Lorentz-violating gravitoelectromagnetism. *Physical Review D*, 82(6):065012, 2010.

[17] Daiki Kikuchi, Naoya Omoto, Kei Yamada, and Hideki Asada. Possible altitudinal, latitudinal, and directional dependence of the relativistic sagnac effect in chern-simons modified gravity. *Physical Review D*, 90(6):064036, 2014.

[18] J. Belfi, N. Beverini, M. Calamai, G. Carelli, E. Maccioni, A. Di Virgilio, R. Santagata, A. Porzio, D. Cuccato, A. Ortolan, and S. Solimeno. Absolute control of the scale factor in gp2 laser gyroscope: Toward a ground based detector of the lense-thirring effect. In *European Frequency and Time Forum & IEEE International Frequency Control Symposium (EFTF/IFC), 2013 Joint*, pages 795–798, 2013.

[19] F. Bosi, G. Cella, A. Di Virgilio, A. Ortolan, A. Porzio, S. Solimeno, M. Cerdonio, J. P. Zendri, M. Allegrini, J. Belfi, N. Beverini, B. Bouhadef, G. Carelli, I. Ferrante, E. Maccioni, R. Passaquieti, F. Stefani, M. L. Ruggiero, A. Tartaglia, K. U. Schreiber, A. Gebauer, and J-P. R. Wells. Measuring gravitomagnetic effects by a multi-ring laser gyroscope. *Physical Review D*, 84:122002(23), 2011.

[20] P. G. Halverson, A. Kuhnert, J. Logan, M. Regehr, S. Shaklan, R. Spero, F. Zhao, and T. Chang. Progress towards picometer accuracy laser metrology for the space interferometry mission. In *Proceedings of ICSO 2000, 4th International Conference on Space Optics*, pages 417–428. NASA JPL, 2000.

[21] P. G. Halverson, O. Alvarez-Salazar, A. Azizi, F. Dekens, B. Nemati, and F. Zhao. Progress towards picometer accuracy laser metrology for the space interferometry mission - update for icso 2004. In *Proceedings of ICSO 2004, 5th International Conference on Space Optics*, pages 515–522. NASA JPL, 2004.

[22] B. Nemati. Sim planetquest: Status and recent progress. In *Proceedings of SPIE: Advances in Stellar Interferometry*, volume 6268. NASA JPL, 2006.

[23] J. E. Logan, P. G. Halverson, M. W. Regehr, and R. E. Spero. Automatic alignment of a displacement-measuring heterodyne interferometer. *Applied Optics*, 41:4314–4317, 2002.

[24] L. B. Ames, B. Barrett, R. Bell, L. Dries, K. Dutta, P. G. Halverson, B. Holmes, E. T. Kvamme, D. F. Leary, P. Perkins, M. Scott, T. E. Van Eck, and F. Zhao. Sim external metrology beam launcher (qp) development. In *Proceedings of SPIE: Interferometry in Space*, volume 4852, pages 347–354. NASA JPL, 2003.

LUCIFER: Low-background Underground Cryogenic Installation For Elusive Rates

J.W.Beeman[a], F.Bellini[b,c], L.Cardani[b,c], N.Casali[f,g], M.Clemenza[h,i], I.Dafinei[c], S.Di Domizio[j,k], F.Ferroni[b,c], L.Gironi[h,i], A.Giuliani[l], C.Gotti[h,i], M.Maino[h,i], S.Nagorny[n], S.Nisi[g], C.Nones[m], L.Pagnanini[n], L.Pattavina[g], G.Pessina[i], G.Piperno[b,c], S.Pirro[g], E.Previtali[i], C.Rusconi[i], K.Schaeffner[n], C.Tomei[c], M.Vignati[b,c]

[a] Lawrence Berkeley National Laboratory, Berkeley, California 94720, USA
[b] Dipartimento di Fisica - Sapienza Università di Roma I 00185 Roma - Italy
[c] INFN - Sezione di Roma 00185 Roma - Italy
[e] INFN - Sezione di Pavia I 27100 Pavia - Italy
[f] Dipartimento di Fisica - Università degli Studi dell'Aquila I 67100 L'Aquila - Italy
[g] INFN - Laboratori Nazionali del Gran Sasso I 67010 Assergi (Aq) - Italy
[h] Dipartimento di Fisica - Università di Milano Bicocca I 20126 Milano - Italy
[i] INFN - Sezione di Milano Bicocca I 20126 Milano - Italy
[j] INFN - Sezione di Genova I 16146 Genova - Italy
[k] Dipartimento di Fisica - Università di Genova I 16126 Genova - Italy
[l] Centre de Spectrométrie Nucléaire et de Spectrométrie de Masse, 91405 Orsay, France
[m] CEA, Irfu, SPP Centre de Saclay, F-91191 Gif-sur-Yvette, France
[n] Gran Sasso Science Institute, L'Aquila I-67100 - Italy

Abstract

In the field of fundamental particle physics, the neutrino has become more and more important in the last few years, since the discovery of its mass. In particular, the ultimate nature of the neutrino (if it is a Dirac or a Majorana particle) plays a crucial role not only in neutrino physics, but also in the overall framework of fundamental particle interactions and in cosmology. The only way to disentangle its ultimate nature is to search for the neutrinoless double beta decay ($0\nu\beta\beta$). The idea of LUCIFER is to combine the standard bolometric technique employed in $0\nu\beta\beta$ experiments with the bolometric light detection technique used in cryogenic dark matter experiments. The bolometric technique allows an extremely good energy resolution while its combination with the scintillation detection offers an ultimate tool for background rejection. The goal of LUCIFER is not only to build the first array of enriched scintillating bolometers but also to demonstrate the feasibility of a background-free experiment, proving the potentiality of this technique, and to establish the most stringent limit on the effective neutrino mass using ^{82}Se $0\nu\beta\beta$. We report on activities carried out in 2015 (and the activities foreseen for 2016?).

1 Introduction

Bolometers are cryogenic particle detectors in which the energy, released by an interacting particle, is measured by a very sensitive thermometer provided that the heat capacity of the absorber is reasonably small. This can be achieved cooling down the system at cryogenic temperatures of the order of tens of mK.

Bolometers offer a wide choice of absorber materials, at the same time being able to achieve an energy resolution competitive with that of Ge diodes (namely of the order of 5 keV FWHM at 3 MeV). The freedom in the choice of the absorber provides the unique opportunity of selecting the $0\nu\beta\beta$ isotope without the limitations usually induced by the experimental technique.

Unlike other solid-state devices, however, bolometers are not ionization detectors but phonon detectors. As a consequence they are almost equally sensitive to any kind of particle, despite the way energy is released. In other words electrons, α-particles, and nuclear recoils -depositing the same amount of energy in the detector- produce a pulse with the same amplitude and shape. The CUORICINO [1] detector demonstrated that the background in the region of interest is dominated by radioactive contaminations on the surfaces facing the detectors. Alpha particles produced by these contaminants can lose a fraction of their energy in the host material and the rest in the detector, thus producing a flat background from the energy of the decay (several MeV) down to the $0\nu\beta\beta$ region.

Scintillating bolometers, proposed also for $0\nu\beta\beta$ surveys [2], allow to overcome this disadvantage by providing the possibility to distinguish α interactions (background only) from β/γ interactions (background and signal).

The interesting feature of scintillating bolometers is that the ratio between the two signals (*light/heat*) depends on the particle mass and charge. Particles like βs and γs have the same light emission (conventionally referred as the Light Yield (LY), i.e. the fraction of particle energy emitted in photons) which is typically different from the light emission of α particles or neutrons. Consequently, the simultaneous read out of the heat and light signals allows particle discrimination.

If the scintillating crystal contains a $0\nu\beta\beta$ candidate, the $0\nu\beta\beta$ signal (i.e. the energy deposition produced by the two electrons emitted after the decay) can be distinguished from an α signal, and only βs and γs can give a sizable contribution to the background that limits the experimental sensitivity. The feasibility of this technique is today widely proven. Scintillating bolometers containing Ca, Mo, Cd and Se have been successfully tested, coupled to a thin Ge wafer operated as bolometer for the light read-out [3, 4, 5, 6]. Presently those that look most promising for a $0\nu\beta\beta$ large scale experiment are ZnSe and $ZnMoO_4$.

2 The LUCIFER detector

The LUCIFER set-up consists of an array of detectors, arranged in a tower-like structure, as schematized in Fig. 1. The single tower will consist of cylindrical crystals of 44 mm diameter and 55 mm height, interleaved with Ge-wafer light detector. The crystal is held in position by means of six S-shaped Teflon pieces fixed to two cylindrical Cu frames. The frames are held together through three Cu columns. The crystal is surrounded (without being in thermal contact) with a reflecting plastic foil (3M Vikuiti) in order to increase the light collection efficiency. Each crystal is faced to two light detectors, and at the same time, a single light detector looks at two crystals. The final detector will be made of 5 independent towers, all coupled to a comment Cu top-plate. The tower will be installed in the same dilution cryostat that hosted the Cuoricino experiment,

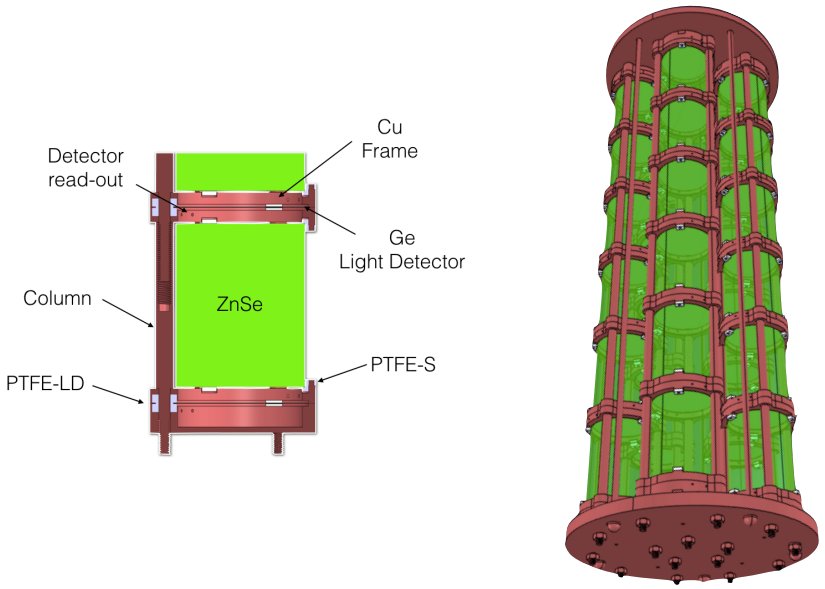

Figure 1: Rendering of the LUCIFER detector set-up.

with major upgrades, for improving the detector duty cycle and reducing microphonism noise induced on the detectors.

The key point of the experiment will be the crystal growth made with enriched isotope, as it will be discussed later in the text. With the enriched material being extremely expensive, any loss during the various stages of purification and production must be minimized.

2.1 Natural crystals

Because of its high content in Se (56%), as well as its good bolometric and scintillating properties, ZnSe has always been an interesting candidate for the search of the $0\nu\beta\beta$ of ^{82}Se ($Q_{\beta\beta}$=2997.9 keV [7]).

The largest ZnSe bolometer ever realized, a 431 g crystal grown at ISMA (Ukraine), was recently characterized in terms of energy resolution, internal contaminations and particle identification capabilities [8].

The FWHM energy resolution was found to be 13.4±1.0 keV at 1461 keV and 16.3±1.5 keV at 2615 keV. However, starting from the consideration that light and heat are two *correlated* estimates of the particle energy, we developed an analysis algorithm that allowed to improve considerably the energy resolution by removing this correlation. This algorithm, whose details are described in [8], resulted in a FWHM energy resolution of 12.2±0.8 keV at 1461 keV and 13.4±1.3 keV at 2615 keV.

Various bolometric measurements were performed in order to assess the scintillation properties of ZnSe at cryogenic temperatures. In Fig. 2 (left) the detected scintillation light is reported as a function of the heat released in the crystals. In order to study the discrimination power between β/γ and α events, an uranium α source covered with a thin mylar foil was placed close to the ZnSe surface. The mylar foil degrades the energy of the emitted αs, producing a flat

continuum of events at low energy (red circles in the plot). Using a ^{228}Th γ-source (outside the cryostat) and the "internal" α source, we were able to investigate the discrimination potential in the $0\nu\beta\beta$ energy region.

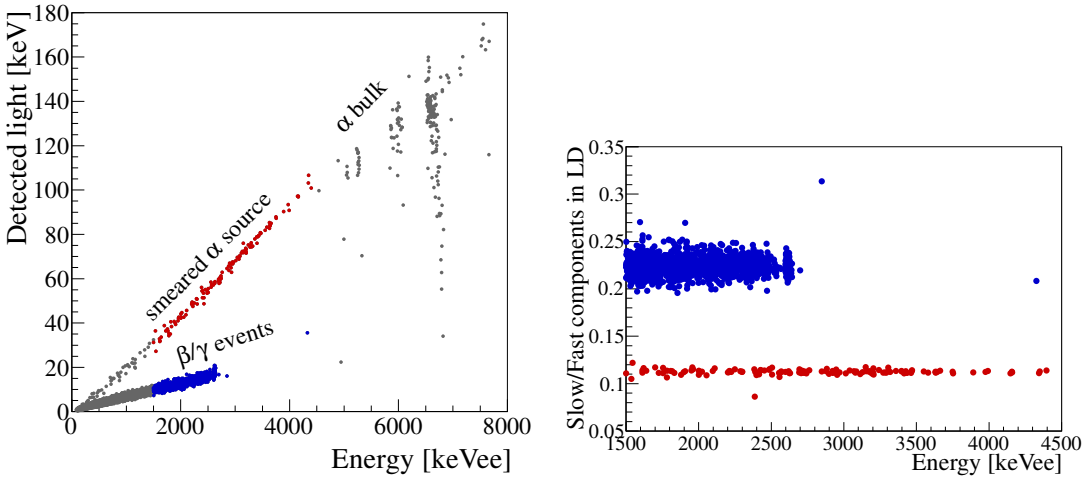

Figure 2: Particle discrimination in ZnSe. The light emitted by the ZnSe crystal (left) and the shape of the same light pulses (right) are reported as a function of the energy released in the ZnSe bolometer. A ^{228}Th γ-source was used to produce β/γ events (blue) up to 2615 keV (^{208}Tl), while a smeared α source was placed under the crystal to provide a continuum of αs extending to lower energies (red). The (heat-channel) x-axis is (energy) calibrated using the most intense γ peaks. The blue and red points of the upper plot are determined by a cut on the bottom plot.

Looking at Fig. 2 (left), we observed that the events produced by the γ-source (blue) lie in a different region with respect to α particles with the same energy. The LY of β/γ events resulted in $\mathrm{LY}_{\beta/\gamma} = 6.42 \pm 0.01$ keV/MeV, irrespective of the energy deposit. The LY of α particles was studied separately for surface and internal α contaminations, resulting in $\mathrm{LY}_{\alpha}^{surf} = 29.70 \pm 0.17$ keV/MeV and $\mathrm{LY}_{\alpha}^{bulk} = 26.62 \pm 0.86$ keV/MeV. Several tests showed that the difference in the LY of bulk/surface events can not be ascribed to self-absorption in the crystal or to an energy dependence of the effects. Therefore, the origin of this behaviour must reside in an effectively larger light production on the crystal surface or in non-uniformities in the light collection.

The larger LY of α events with respect to β/γ in ZnSe crystals is not yet understood and, in principle, could affect the discrimination capability. A poor efficient light collection for α particles, indeed, can generate α events leaking in the β/γ band increasing the background in the region of interest (see Fig. 2 left).

In order to overcome this problem, we developed an analysis algorithm which is sensitive to the difference in the pulse shape of αs and β/γs (see details in [8]). Each pulse was fitted using a model that takes into account the development of the phonon signals, the thermistor and electronics response, and the scintillation process, that can not be considered instantaneous. Applying this algorithm to the heat and light pulses of ZnSe, we discovered that a poor particle discrimination can be obtained using the heat channel alone. The shape of the light pulses, on the contrary, is very sensitive to the type of interacting particles (see Fig. 2 right).

Thanks to the pulse shape discrimination, it is possible to identify and reject the α interaction

with very high efficiency, thus strongly reducing the background in the energy region of interest.

3 Assembly

During the 2015 the mechanical configuration of the tower was designed and the all high purity copper Cu and PTFE pieces were produced. The selection of the materials was done using the same criteorions adopted for CUORE. The mechanical design was conceived in order to maximise the volume occupancy inside the Hall A cryostat, to optimise the light collection and to decrease the amount of dead materials close to the detectors. Specifically designed tools for the final detector assembly were developed and they are now under construction. In order to prepare the final detector each NTD sensor is bonded using 25 μm gold wires and glued on ZnSe crystals and Ge light detectors. For the bonding procedure an approach very similar to that already tested in CUORE will be applied. Regarding the gluing procedure, specific designed tools were realized. In particular a semi-automatic gluing platform was built in order to optimize the deposition of the glue spots on crystals and NTDs. The gluing system is enclosed in a dedicated glow box to minimize the radon and radon daughter deposition on the crystal surfaces.

4 Enriched crystals

In 2015, big efforts were devoted to the development of synthesis and purification processes of $Zn^{82}Se$ powder, able to preserve the high purity of the starting materials (namely Zn and ^{82}Se) and the high production yield.

After the complete refining of these different processes at the ISMA institute in Karkhiv (Ukraine), the enriched Selenium produced by the URENCO Company and the selected high-purity Zinc were shipped to Ukraine by land transportation, in order to minimize cosmic-ray activation. The very delicate process involved in the synthesis of the ZnSe molecule was organized and optimized at ISMA with the direct support of the LUCIFER collaboration and in summer 2015 the process was tested on natural Zn and Se metals with very successful results. Starting from this point, in September 2015 the preparation of the $Zn^{82}Se$ was started with good production yield. Using the implemented set-up the conversion of the 27 kg of raw materials (enriched Selenium and Zinc) into $Zn^{82}Se$ powder was completed in December 2015.

In parallel to the synthesis, the final process for the crystal growth was implemented. After a couple of growing tests with natural material that showed a net improvement in ZnSe crystal quality and reproducibility, the production of the $Zn^{82}Se$ was started. The crystal growths for the LUCIFER experiment are planned to be completed before the end of February 2016.

The final mechanical process of the $Zn^{82}Se$ crystals will be made in Italy, at Gran Sasso Laboratory (LNGS). To perform this final process, all the needed tools and consumables are ready and preliminary tests were done to optimize the complete treatment of the crystal surfaces.

In order to test the complete crystal production process and to certify the crystal quality a cryogenic measurement started in November 2015 in the hall C cryostat of the LNGS underground laboratory. The bolometric performances of the ZnSe detector was tested with good results. Specifically, the measurement allowed the analysis of: energy resolution, light emission of the crystals for α and γ/β interactions; preliminary analysis of the radioactive contamination of the enriched crystals were also obtained.

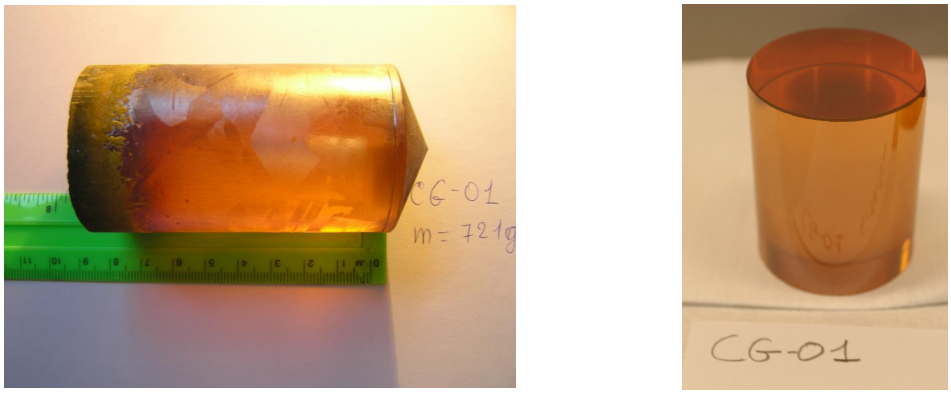

Figure 3: Photo of the first $Zn^{82}Se$ ever produced. Left: photo of the ingot grown at ISMA. Right: photo of the crystal after the cutting and polishing processes.

5 Material assay

The main background sources for the LUCIFER experiment will be: i) high energy γ emission from ^{214}Bi - up to 3.2 MeV - and ii) pile-up events from ^{208}Tl γ cascade. Even if the background induced by these sources can be suppressed, as discussed in [10], still it can not be completely neglected. The two previously mentioned nuclides are produced by the decay of the natural chain of primordial ^{238}U and ^{232}Th. A thorough material selection is mandatory in order to reduce as much as possible their concentration in the $Zn^{82}Se$ crystals. In order to allow an almost zero-background investigation [11, 12], ^{238}U and ^{232}Th contaminations inside the final crystal must be at the level of tens of μBq/kg or better.

5.1 Highly pure ^{82}Se

The entire enrichment process for the production of 15 kg of ^{82}Se for the LUCIFER experiment was carried out at URENCO, Stable Isotope Group in Almelo, in the Netherlands. In order to be able to achieve the required experimental sensitivity, the use of enriched Se is mandatory, given the relatively low natural isotopic abundance of 8.73% [13]. The enrichment is performed through a well established procedure: centrifugal enrichment. A dedicated line of centrifuges was employed for the enrichment of gaseous SeF_6, that was fully separated from the one used for the ^{235}U enrichment.

The production of enriched Se consists of 3 main steps:

1- procurement of SeF_6 gas;

2- centrifugal enrichment of $^{82}SeF_6$;

3- conversion of $^{82}SeF_6$ gas to ^{82}Se metal.

The starting material is natural SeF_6 gas, purchased by URENCO from an external supplier, which is fed into a cascade of centrifuges. The outcome of the process is $^{82}SeF_6$ enriched gas at a $\geq 95\%$ level. The subsequent step is the conversion from gas to metal, which is performed through a series of chemical reactions [14]. The final product is enriched ^{82}Se metal.

In Table 1 the abundance of the different selenium isotopes after the enrichment process, measured with ICP-MS are reported. The values reported in the table are the average over the 70 conversion processes weighted for their relative mass, while the uncertainty refers to the

Table 1: Isotopic abundance of natural (recommended values [13]) and enriched selenium. The values for the enriched isotope are averaged over 70 different gas-to-metal conversion processes, weighted for their relative mass.

	^{74}Se	^{76}Se	^{77}Se	^{78}Se	^{80}Se	^{82}Se
Natural Se [%]	0.87	9.36	7.63	23.78	49.61	8.73
Enriched Se [%]	<0.01	<0.01	<0.01	<0.01	3.67±0.14	96.33±0.31

spread in the enrichment. As it is shown in the table, an enrichment above 95% on ^{82}Se is ensured on all the samples, in some cases an enrichment level up to 97.7% was achieved. For the sake of comparison, we report also the recommended natural occurring values [13].

The investigation on the internal radioactive contamination of enriched Se metal for the LUCIFER experiment was carried out with γ-spectroscopy using a HP-Ge detector located in the underground Laboratory of LNGS.

The internal contaminations of the sample, as well as their concentrations, are listed in Table 2. No evidence of nuclides from the natural chains of ^{235}U/^{238}U and ^{232}Th are detected, in agreement with the ICP-MS measurements (see Table **??**). We report the limits of detectability for long-lived β/γ-emitters of the decay chains. Limits are set at an extremely low level - hundreds of μBq/kg, and they are competitive with values reported on other raw materials used for the crystal growth of $\beta\beta$ decay detectors [15, 16, 17].

Table 2: Internal radioactive contamination for 2.5 kg of 96.3% enriched ^{82}Se metal beads. Limits are computed at 90% C.L. The measurement was carried out on October 2014.

Chain	Nuclide	Activity [μBq/kg]	Concentration [ppb]
^{232}Th			
	^{228}Ra	< 61	< 0.015
	^{228}Th	< 110	< 0.026
^{238}U			
	^{226}Ra	< 110	< 0.009
	^{234}Th	< 6200	< 0.500
	^{234m}Pa	< 3400	< 0.280
^{235}U	^{235}U	< 74	< 0.13
	^{40}K	< 990	< 32
	^{60}Co	< 65	$< 1.6{\cdot}10^{-12}$
	^{75}Se	110±40	$(2.0\pm0.7)\cdot10^{-13}$

5.2 Highly pure Zinc

The metal Zinc employed for the growth of $Zn^{82}Se$ crystals was purchased from Kharkov Institute of Physics and Technology (Kharkov, Ukraine). Here, starting from commercially available Zinc, a serie of complex purification processes, involving melting filtration and distillation is carried out in order to purify the final material.

The chemical and radioactive purity of the Zn used in LUCIFER were investigated using gamma spectroscopy, with HP-Ge detectors, and ICP mass spectrometry. The performance of the detector in terms of bolometric signal and background in the ROI are strongly influenced by the presence of contaminants, from chemical elements and nuclides respectively.

The overall impurities amount to less than 10 ppm, thus ensuring highly performing bolometers after the crystal growth.

6 Light detectors

The needed light detectors will be made of Ge wafers configured as bolometers. One side of the Ge wafer will be prepared with an anti-reflecting coating in order to maximize the light detection efficiency. All the wafers were prepared in 2013 and the anti-reflecting coating process was also defined. Radioactivity test on Ge surfaces were done in order to evaluate possible background components that will be due to surface treatments, i.e. coating deposition. The results obtained indicate that surfaces are very clean, from the radioactive point of view. The deposition of SiO_2 for the anti-reflection coating is under preparation and all the light absorbers will be ready at the beginning of 2016.

The light detector prototypes were tested in a cryogenic measurement, together with ZnSe scintillating bolometers. They featured excellent baseline energy resolution, FWHM of 40 eV, and they allow for an efficient scintillation light detection. The expected light signal at the ^{82}Se Q-value is expected to be about 20 keV, thus much larger than the detector energy resolution.

7 NTD thermistors

Neutron Transmutation Doped thermistors (NTD) are semi-conductor devices doped close to the metal to insulator transition. The best technique available for producing a uniform doping is to produce the dopant by bombarding the Ge crystal with a high flux of thermal neutrons.

The detector performance are strictly related to the characteristics of the NTDs, namely the doping level. The thermal signal from ZnSe crystals and light detectors will be read out using NTDs that must be optimized for such specific application. Dedicated studies have demonstrated that the total needed neutron fluence for the NTDs doping for LUCIFER's applications is $4.33x10^{18}$ n/cm^2.

The irradiation at the nuclear reactor of the germanium wafer, the preparation and the definition of the contacts on the two sides of the Ge wafer were completed during the 2014. In the last months of 2015 the shape and the preparation of the final thermistor for the Lucifer experiment were defined. In particular to optimize the sensitivity and the heat capacity of the two parts, ZnSe crystals and Ge light detector, it was decided that the shape of the NTD sensor must be: 2.8x3x1 mm^3 for the crystals and 2.8x2x0.5 mm^3 for the light detectors. This choice was done in order to minimize the contribution to the heat capacity that the full doped NTD will gives specifically for the light detector.

To prepare the final sensors it is necessary to cut the irradiated Ge wafer in the correct shapes, then the single chip must be polished on surfaces and at the end it is necessary to etch

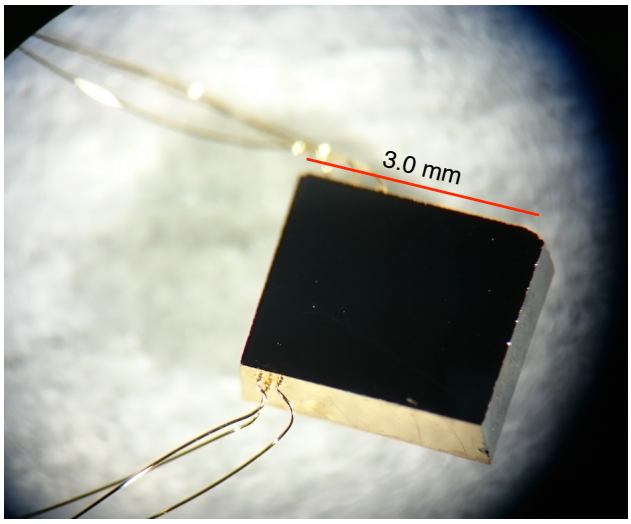

Figure 4: NTD thermistor for the read-out of $Zn^{82}Se$ scintillating bolometer. Dimensions: 2.8x3x1 mm^3.

the NTD surfaces to minimize possible parasitic currents. A factory will cut and polish the NTDs for the experiment and the final etching will be performed in LNGS. The production of all the needed NTD sensors will start soon and it will be completed in the first months 2016.

8 Electronics and Data Acquisition

The electronic read-out is conceived to meet the following criterions: negligible radioactive background, low noise and very good stability. It is located at room temperature and a set of twisted connecting wires are routed. To suppress interference and cross-talk the input stage of the front-end is differential, with a pair of JFET transistors custom designed for having a small gate current, making negligible the parallel noise [18]. It includes a second stage, close to the input stage and to the cryogenic set-up, and an antialiasing filter, close to the DAQ. Every channel shows a very small thermal drift, of the order of a few ppm/°C, thanks to a very stable power supply system designed for this purpose [19]. The system is instrumented with heating injectors (highly stable both in time and temperature) that allow to feed short current pulses to heater resistors glued on each crystal for gain stabilization [20]. The electronics set-up includes the detector biasing system that enables a channel by channel energy conversion gain maximisation.

The data acquisition (DAQ) system is based on commercial digitizer boards from National Instruments, NI-PXI628x. These feature 18-bit ADCs, configurable sampling frequency up to 500 kHz, and configurable input range up to +/-10 V. They can digitize up to 16 analog signals in differential input configuration. The DAQ boards are contained in one or more PXI chassis that can be controlled remotely via computer. The data link between DAQ chassis and computers consist in an optical fiber connection which provides proper data transmission bandwith and a complete electrical decoupling between the computers and the detectors. The bolometer waveforms are digitized with sampling frequencies in the range $(1 \div 2)$ kHz for both heat and light detectors.

The complete bolometer data streams are transferred from the PXI chassis to the computers,

and the triggers are implemented in the software [22]. This approach allows to implement arbitrarily complex signal detection algorithms, the only constraint being the computing resources. Among the other advantages, it is easy to save the light detector waveform in correspondence of a heat detector trigger, or viceversa. Triggered events are saved in a custom format based on the ROOT data analysis framework. Each event contains information on the waveforms of the triggering bolometer and of the light detector in a window of configurable length, the event time and other ancillary information. The DAQ system gives the possibility to save continuous data streams of the bolometer waveforms, irrespective of the presence of triggers.

Finally the DAQ system includes high level communication interfaces with the Electronic System. These interfaces are exploited by interactive control panels and by software algorithms for the automatic characterization of the detectors. These procedures consist in measuring the signal to noise ratio of the detectors as a function of the applied bias current and have the purpose of finding the optimal working point for each bolometer.

The whole electronic and DAQ chains were tested in several measurements performed in the Hall C cryostat with scintillating bolometers. The front end electronics are under production and the complete set of read out channels will be ready in Spring 2016 together with the DAQ system

9 Acknowledgements

This work was made in the frame of the LUCIFER experiment, funded by the European Research Council under the European Union's Seventh Framework Programme (FP7/2007-2013)/ERC grant agreement n. 247115.

10 List of Publications

J. W. Beeman *et al.* [LUCIFER Collaboration], "Double-beta decay investigation with highly pure enriched ^{82}Se for the LUCIFER experiment," Eur. Phys. J. C **75**, no. 12, 591 (2015) doi: 10.1140/epjc/s10052-015-3822-x.

N. Casali *et al.* [LUCIFER Collaboration], "TeO_2 bolometers with Cherenkov signal tagging: towards next-generation neutrinoless double beta decay experiments," Eur. Phys. J. C **75**, no. 1, 12 (2015) doi: 10.1140/epjc/s10052-014-3225-4.

References

[1] E.. Andreotti et al., Astropart. Phys. **34** (2011) 822.

[2] S. Pirro et al.,Phys. Atom. Nucl **69**, (2006) 2109.

[3] C. Arnaboldi et al., Astrop. Phys. **34**, (2011) 797.

[4] C. Arnaboldi et al., JINST **5**, (2010) P11007.

[5] C. Arnaboldi et al., Astrop. Phys. **34**, (2010) 143.

[6] C. Arnaboldi et al., Astrop. Phys. **34**, (2011) 344

[7] D. Lincoln et al., Phys. Rev. Lett. **110**, (2013) 012501.

[8] J.W. Beeman et al., J. Inst. **8**, (2013) P05021

[9] J.W. Beeman et al., J. Inst. **8**, (2013) P07021.

[10] J.W. Beeman et al., J. Inst. **8**, (2013) P05021

[11] C. Arnaboldi et al., Astropart. Phys. **34**, (2011) 344.

[12] L. Cardani, PhD thesis, Sapienza Università di Roma (Rome, Italy), 2013.

[13] M. Berglund and M.E. Wieser, Pure Appl. Chem. **83**, (2011) 397.

[14] P. Benetti et al., Proceedings of the 12th International Workshop on Separation Phenomena in Liquids and Gases (SPLG-12), Paris, France, June 2012.

[15] C. Arnaboldi et al., J. Cryst. Growth **312**, (2010) 2999.

[16] H. Bhang et al., J. Phys.: Conf. Ser. **375**, (2012) 042023.

[17] GERDA Coll., Eur. Phys. J. C **75**, (2015) 39.

[18] C. Arnaboldi et al., IEEE Tran. on Nucl. Sc. **51**, (2004) 2975.

[19] A. Alessandrello et al., IEEE Tran. on Nucl. Sc. **44**, (1997) 416.

[20] C. Arnaboldi et al., IEEE Tran. on Nucl. Sc. **50**, (2003) 979.

[21] A. Alessandrello et al., Cryog. **37**, (1997) 27.

[22] G. Piperno et al., JINST **6**, (2011) P10005.

LUNA: Laboratory for Underground Nuclear Astrophysics

M. Aliotta[a], D. Bemmerer[b], A. Best[c], A. Boeltzig[d], C. Broggini[e], C. Bruno[a], A. Caciolli[f], F. Cavanna[g], G. F. Ciani[d], P. Corvisiero[g], T. Davinson[a], R. Depalo[f], G. D'Erasmo[p], A. Di Leva[h], Z. Elekes[i], F. Ferraro[g], E. M. Fiore[p], A. Formicola[c], Zs. Fülöp[i], S. Gazzana[c], G. Gervino[j], A. Guglielmetti[k], C. Gustavino[l], Gy. Gyürky[i], G. Imbriani[h], L. Leonzi[c], M. Lugaro[o], P. Marigo[f], V. Mossa[p], M. Junker[c], I. Kochanek[c], R. Menegazzo[e], F. R. Pantaleo[p], V. Paticchio[p], R. Perrino[p], D. Piatti[f], P. Prati[g], L. Schiavulli[p], E. Somorjai[i], O. Straniero[m], F. Strieder[n], T. Szücs[b], M. P. Takács[b], D. Trezzi[k], A. Valentini[p], S. Zavatarelli[g]
Spokesperson: P. Prati

[a]University of Edinburgh, Edinburgh, United Kingdom
[b]Helmholtz-Zentrum Dresden-Rossendorf, Dresden, Germany
[c]INFN, Laboratori Nazionali del Gran Sasso (LNGS), Assergi (AQ), Italy
[d]Gran Sasso Science Institute (GSSI), L'Aquila, Italy
[e]INFN, Padova, Italy
[f]Università degli Studi di Padova and INFN, Padova, Italy
[g]Università degli Studi di Genova and INFN, Genova, Italy
[h]Università degli Studi di Napoli "Federico II", and INFN, Napoli, Italy
[i]Institute for Nuclear Research (MTA ATOMKI), Debrecen, Hungary
[j]Università degli Studi di Torino and INFN, Torino, Italy
[k]Università degli Studi di Milano and INFN, Milano, Italy
[l]INFN, Roma, Italy
[m]Osservatorio Astronomico di Collurania, Teramo, and INFN Napoli, Italy
[n]Institut für Experimentalphysik III, Ruhr-Universität Bochum, Bochum, Germany
[o]Monarch University Budapest, Budapest, Hungary
[p]Università degli Studi di Bari and INFN, Bari, Italy

Abstract

Aim of the LUNA experiment is the direct measurement of the cross section of nuclear reactions relevant for stellar and primordial nucleosynthesis. The year 2015 was dedicated to the measurement of the ^{22}Ne(p,γ)^{23}Na, ^{23}Na(p,γ)^{24}Mg and ^{18}O(p,γ)^{19}F reactions; data analysis on ^{17}O(p,α)^{14}N and ^{18}O(p,α)^{15}N was completed as well. The ^{22}Ne(p,γ)^{23}Na reaction was studied with a windowless gas target circulated with ^{22}Ne enriched gas. Both a couple of high resolution HpGe detectors and a 4π segmented BGO crystal were used to determine the strength of several resonances and of the direct capture component at astrophysical energies. The two other reactions were studied by a solid target set-up and again the high efficiency BGO detector. The LUNA MV project was pursued in parallel to the LUNA activities and new progresses were obtained.

1 The $^{17}O(p,\alpha)^{14}N$ reaction

The $^{17}O(p,\alpha)^{14}N$ reaction (Q_{val}=1.2 MeV) plays a key role in several astrophysical scenarios, and in AGB stars in particular [1, 2, 3]. At energies of astrophysical interest its reaction rate is dominated [4] by a narrow and isolated resonance at E_p=70 keV. This resonance has been studied several times in the past, using both direct and indirect methods, as summarised in ref. [5]. However, the picture painted in the literature is still not completely satisfying. The uncertainty in the resonance strength is not negligible (≈20%). Furthermore, published strength values obtained with direct measurements have all been retracted or reanalysed [5].
An experimental campaign aimed at measuring the E_p=70 keV resonance in $^{17}O(p,\alpha)^{14}N$ was recently completed at the underground LUNA accelerator. We exploited the low background in the underground environment in order to carry out a direct investigation of this weak ($\omega\gamma \approx$ neV) resonance employing the thick-target yield technique. Protons were accelerated on a solid Ta_2O_5 target and alpha particles detected at backward angles using an array of silicon detectors. The setup was commissioned using the well-known E_p=193 keV resonance in $^{17}O(p,\alpha)^{14}N$ [6]. A clear peak was observed at E_p=71.5 keV at the expected energies, as shown in Fig. 1. The green dotted lines indicate the region of interest that was estimated *a priori* from the energy of the alpha peak from E_p=193 keV resonance in $^{17}O(p,\alpha)^{14}N$ [6]. The alpha peak from the E_p=70 keV resonance appears where expected and has a signal significance higher than 5 sigma. Results of the analysis [7] indicate a resonance strength that is significantly higher than reported in previous investigations. Because of the importance of this resonance [4], we expect our results to have significant astrophysical consequences in a number of scenarios [8, 9].

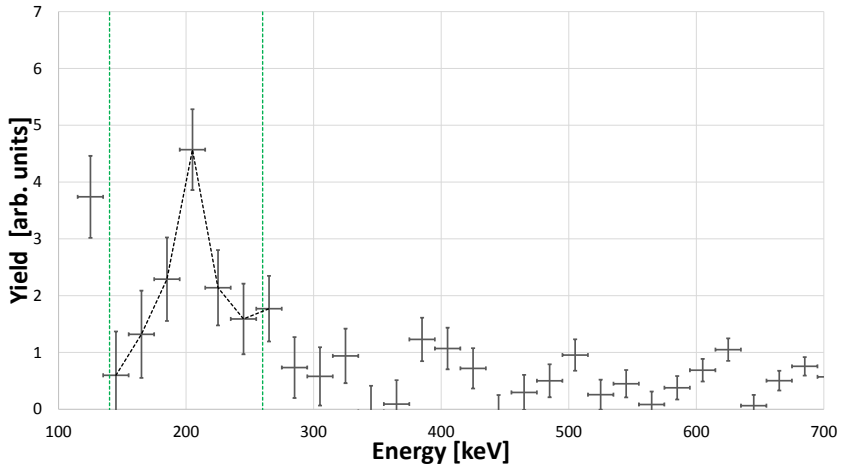

Figure 1: The spectrum acquired at E_p=71.5 keV for $^{17}O(p,\alpha)^{14}N$, after subtraction of the natural background. The green dotted lines indicate the expected peak position, calculated *a priori*.

2 The $^{18}O(p,\alpha)^{15}N$ reaction

The $^{18}O(p,\alpha)^{15}N$ reaction (Q_{val}=3.98 MeV) plays a role in Giant Branch Stars [1, 2, 3, 10] where it influences the abundance of the rare ^{18}O isotope. Our investigation was carried out employing the same setup commissioned for the $^{17}O(p,\alpha)^{14}N$ campaign [6]. We measured the

excitation function of the $^{18}O(p,\alpha)^{15}N$ reaction from E_p=360 keV to E_p=60 keV, the lowest energy achieved to date corresponding to a cross-section of the order of the picobarn. In order to extrapolate our measurements to even lower energies, thus reaching the Gamow window region in AGB stars, we will employ the powerful R-matrix formalism [11] to perform a single fit to our data and to data acquired at higher energies (i.e. not accessible at the LUNA-400kV machine), using a small set of physically meaningful parameters. Fig. 2 shows a preliminary comparison between an R-matrix calculation (not a fit) and the data we acquired. This calculation and our data are in good agreement. Data analysis is still in progress.

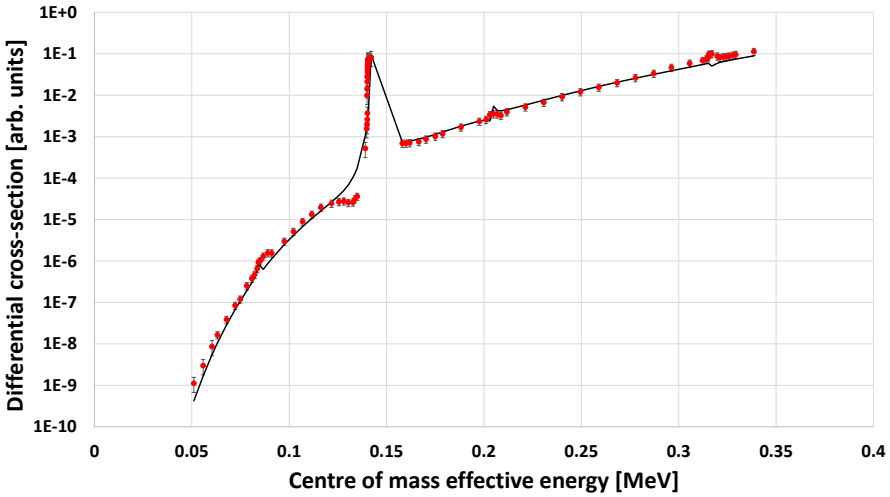

Figure 2: Preliminary comparison between data acquired at LUNA at 135° (red points) and an R-matrix calculation (black line). The agreement is good, but could be improved.

3 Study of the $^{22}Ne(p,\gamma)^{23}Na$ reaction

3.1 Science case

The $^{22}Ne(p,\gamma)^{23}Na$ reaction is included in the hydrogen burning neon-sodium (NeNa) cycle. This cycle affects the nucleosynthesis of neon and sodium isotopes, and it plays a key role in the study of the surface composition of Red Giant Branch stars (Gamow peak 30-100 keV), the composition of the ejecta from Asymptotic Giant Branch Stars and classical novae (Gamow peak 100-600 keV) [12] and possibly in the simmering phase prior to the explosion of a type Ia supernova [13].

The $^{22}Ne(p,\gamma)^{23}Na$ is the NeNa cycle reaction with the most uncertain cross section. In the energy range relevant for astrophysics, the $^{22}Ne(p,\gamma)^{23}Na$ reaction rate was poorly known because of the contribution of a large number of resonances, many of which were never observed directly [14, 15], before the experiment performed at LUNA in 2015. The mere existence of several of these energy levels, e.g. the ones corresponding to the E_p = 215, 104, and 70 keV resonances, is even doubted [16].

An experimental campaign structured in two phases was started in 2013 to measure directly the resonance strength of several resonances below 400 keV. The data taking for the first phase is concluded and the results has been published in 2015 [17]. The second phase will be finished in the early 2016, but some of the preliminary results will be already presented here.

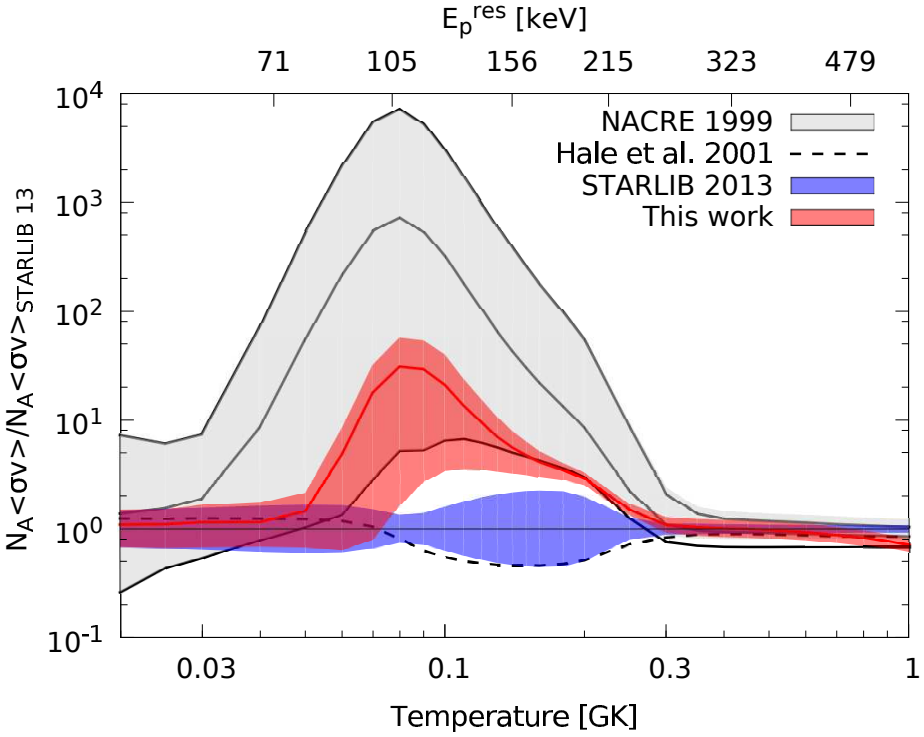

Figure 3: Thermonuclear reaction rate of [17], NACRE Collaboration [14], Hale et al. [18], and the STARLIB group [19] normalized to the STARLIB group [19].

3.2 Phase I (HPGe): Study of selected resonances with a HPGe detector

First phase of the data taking of the ^{22}Ne(p,γ)^{23}Na reaction with enriched neon-22 gas was concluded in fall 2014. Immediately afterwards, the setup was removed to make space for phase II. Several resonances have been observed for the first time during phase I of the experiment. The thermonuclear reaction rate obtained with these new LUNA results [17] is shown in fig. 3 compared with previous rates reported in literature. Detailed branching schemes have been developed for several of the new resonances, and in two cases, even a coincidence analysis of the two HPGe detectors was possible. The comparison of the new LUNA data with previous, surface-based direct and indirect results impressively confirms the validity of the LUNA approach of direct, low-energy cross section measurements deep underground. The results of this first phase are also described and discussed in a recent paper [17], which was selected for the Editors Suggestion in Physical Review Letters.

3.3 Phase II (BGO): Direct capture and low-energy resonances with a BGO detector

In phase II of the experiment, a high-luminosity BGO borehole detector is used in order to address several low-energy resonances and the direct capture component, as well. The typical γ-ray detection efficiency of 70% of this detector [24] will enable either a positive confirmation or a severe upper limit for the low-energy resonances that make up much of the discrepancy between the Iliadis and NACRE reaction rates (fig. 3). A new cylindrical interaction chamber has been designed, provided with a water-cooled, electrically-insulated collimator. A copper calorimeter with 200 W operating power was developed, including the NI CompactRIO control system and its LabVIEW software, so that the beam current is sampled every second and integrated over the duration of the run. A copy of the interaction chamber was made, provided with tubes and flanges. Thanks to this test chamber we measured the gas pressure and temperature along the beam direction in different positions (inside the chamber, the collimator and the connecting pipe) so that the density profile without the beam can be obtained. The pressure profile is shown in fig. 4. The DAQ is based on the CAEN V1724 digitizer (8 Channel, 14 bit, 100 MS/s) and it is performed in list mode, so that offline coincidence analysis is possible. The efficiency have been measured by means of four radioactive sources (^{7}Be, ^{137}Cs, ^{60}Co and ^{88}Y) and the well known E_p=278 keV resonance of the ^{14}N$(p,\gamma)^{15}$O reaction. The final setup commissioning was completed in the early 2015.

During the whole 2015 the data taking of this phase was completed. The non resonant contribution to the S-factor was measured in an energy range from 200 keV up to 360 keV and the two purported resonances at 70 and 105 keV, for which only upper limits exist from the HPGe phase, have been studied in detail. The data analysis is still ongoing.

4 Solid target measurements

Currently two measurement campaigns run on the solid target beam line and the beam time is shared according to the experimental requirements. Setup and DAQ are shared between the two experiments and are discussed in the following section. The individual measurements are described subsequently.

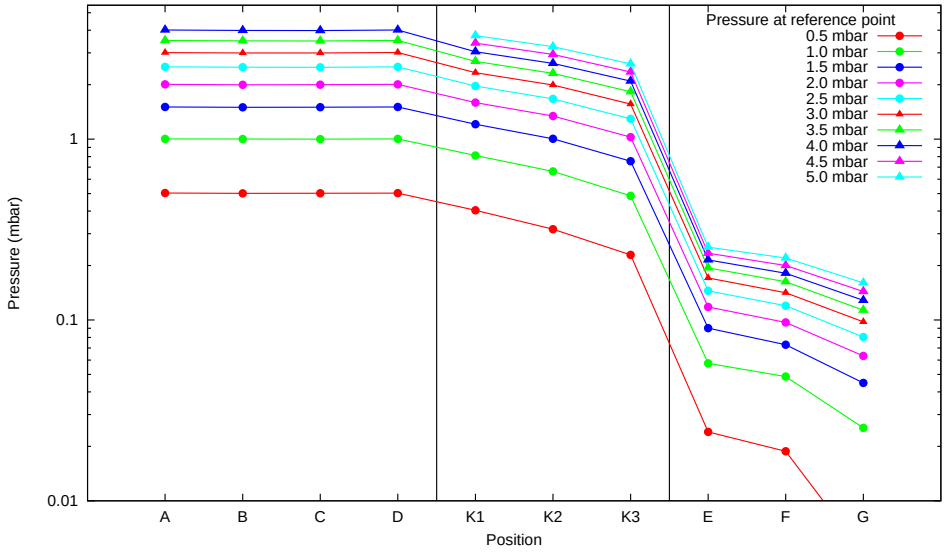

Figure 4: Pressure profile in the setup for phase II of the ^{22}Ne(p,γ)^{23}Na experiment. Positions A-D are inside the target chamber proper, K1-K3 inside the collimator tube at the target chamber entrance, and E-G in the tube connecting the target chamber to the first stage of the differential pumping system.

4.1 Hardware

A newly designed lead shielding for the solid target setup was installed. It provides 10 cm of lead around the BGO detector setup, or 15 cm of lead around a germanium detector that can be placed in the 0° or the 55° position with respect to the beam axis. Thanks to the custom design, access to the target chamber is provided without the need to disassemble the shielding.

Background measurements of the unshielded BGO detector have been studied, and the contributions in the (high-energy) region of interest for the currently investigated reactions have been identified to be dominated by neutron-induced events. First background measurements with the shielding in place have been performed with the BGO detector (see figure 5) and with a HPGe detector at the 0 position. For the BGO setup the background mainly improved in the region of environmental gamma rays and the region of pile-up events up to approximately 6 MeV.

A further reduction of the high-energy neutron-induced background appears feasible using a layer of a few centimeters of borated polyethylene. This might open opportunities for the future to investigate or reinvestigate reactions that were previously limited in sensitivity by the background rate in the BGO detector.

An additional upgrade to the setup was the installation of a new digital DAQ system for the BGO setup. It is shared by all experiments at LUNA that currently employ the BGO detector.

4.2 ^{23}Na(p, γ)^{24}Mg

Focus of the study on the ^{23}Na(p,γ) is the resonance at $E_{\mathrm{c.m.}} = 138$ keV that is potentially relevant for the nucleosynthesis in AGB stars. Only an upper limit has been determined for this resonance so far, with a hint of an observation [25].

The reaction Q value is 11.7 MeV, which, together with the expected weakness of the resonance, suggests the use of the high-efficiency LUNA 4 π BGO detector to detect this resonance.

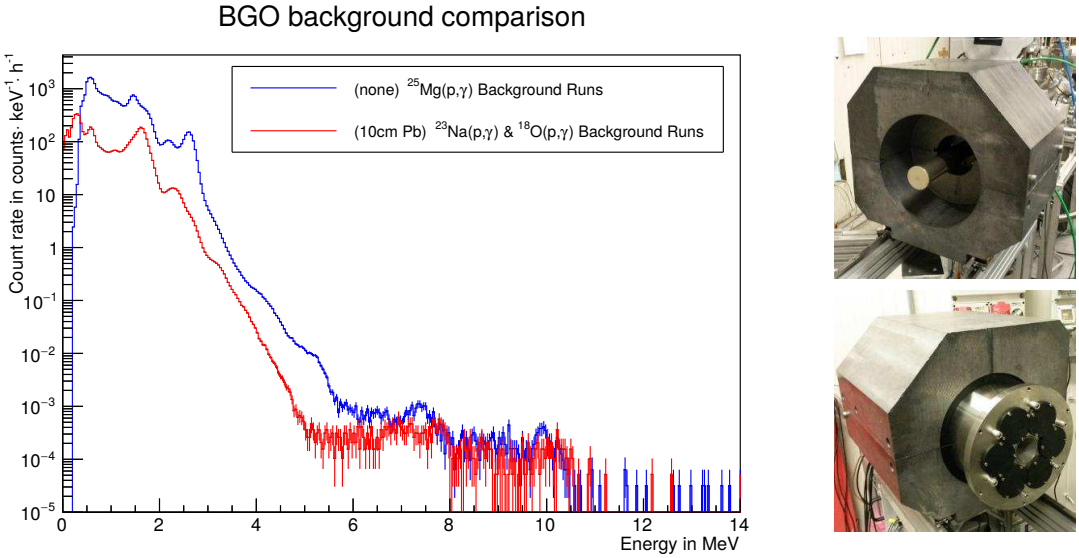

Figure 5: *Left:* Comparison of the environmental background spectrum for the BGO detector setup acquired during the ^{25}Mg(p,γ) campaign and with the current setup with the lead shielding and new DAQ system installed. *Right:* The two halves of the opened lead shielding with the BGO detector sitting inside.

The summing capabilities of this setup have been successfully exploited in the past for measurements of the reactions ^{14}N(p, γ)^{15}O and ^{25}Mg(p, γ)^{26}Al. A HPGe detector detector will be used for measurements at higher energies to determine the non-resonant component of the cross section and measure the branchings of stronger resonances.

First measurements focused on the characterization of various targets (evaporated Na_2WO_4, Na_2SiO_3 and NaCl) from different production sites and batches. The Na_2WO_4 targets showed the best behavior and were selected for the main experiment; to further improve the homogeneity of the targets they were stored in a protective atmosphere to avoid oxidization and accumulation of moisture. Target stability under beam was sufficient.

The low-energy data show beam-induced background from the reaction ^{11}B(p, γ)^{12}C, which exhibits a strong and 5 keV broad resonance at E_p = 162 keV. This resonance's main gamma decay branch involves the emission of a 11.7 MeV gamma-ray, leading to strong background in the expected signal region of the $E_{\mathrm{c.m.}}$ = 138 keV resonance in ^{23}Na(p, γ)^{24}Mg. A detailed analysis of the acquired spectra is underway.

The suspected source for this beam-induced background is the copper cold finger that provides electron suppression and acts as a trap for residual carbohydrates in the beam line vacuum. It extends to a very close distance to the target and it can not be excluded that it is hit by a small fraction of the proton beam. To eliminate this possible background component a new cold finger has been acquired and coated with Nickel on the inside. Additionally, guided by beam optics calculations, new beam-defining apertures have been installed in the beam line to better constrain the beam.

The BGO phase of this campaign has been concluded. The upcoming beamtime will be the first to use the HPGe detector setup for both reactions. With this setup also the ^{11}B(p, γ)^{12}C rate after the modifications described above is to be studied. If a reduction of this rate can be observed, a period in the beam time schedule has been left free to remount the BGO setup and

do a final one-week measurement searching for the $E_{\mathrm{c.m.}} = 138\,\mathrm{keV}$ resonance.

4.3 $^{18}\mathrm{O}(\mathrm{p},\gamma)^{19}\mathrm{F}$

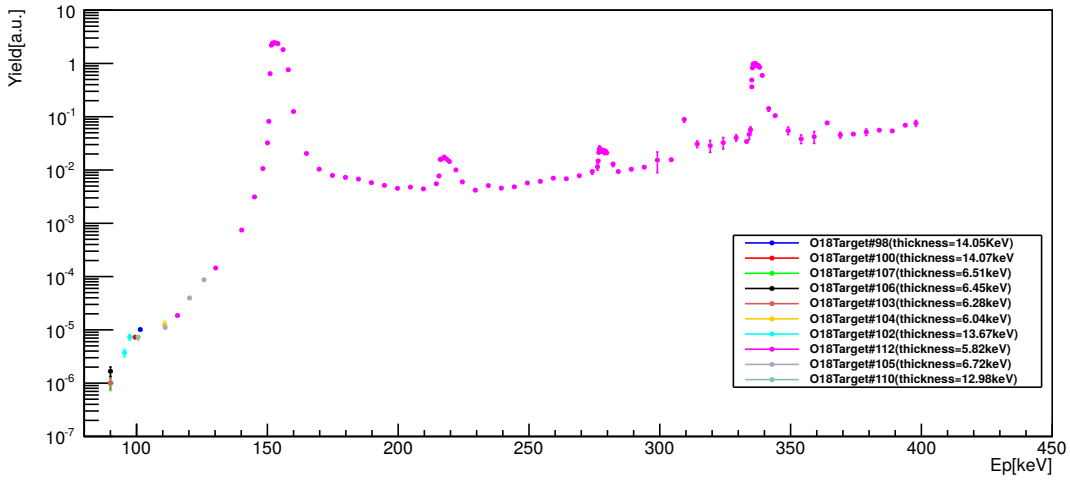

Figure 6: Yield (arbitrary units) of the $^{18}\mathrm{O}(\mathrm{p},\gamma)^{19}\mathrm{F}$ reaction.

A strong $^{18}\mathrm{O}(\mathrm{p},\gamma)^{19}\mathrm{F}$ resonance at 90 keV could provide an explanation for observed oxygen depletion in presolar grains. So far only an experimental upper limit and a theoretical estimate with a very large uncertainty exist [26, 27]. Additionally, the energy of the resonant state is only known to $\pm$ 3 keV, which leads to significant uncertainties in the stellar reaction rate. A direct measurement of the resonant strength and an improvement of the energy uncertainty are desirable.

The targets for the $^{18}\mathrm{O}(\mathrm{p},\gamma)^{19}\mathrm{F}$ campaign were prepared using the anodizing procedures established in previous experiments and showed favorable target profiles. The rest of the setup has been described above.

$^{18}\mathrm{O}(\mathrm{p},\gamma)^{19}\mathrm{F}$ has a Q-value of 8 MeV, which makes it another good candidate for a BGO measurement. A complete excitation curve has been measured with this detector from 400 keV to 90 keV in steps of approximately 10 keV. Resonances at 334 keV, 275 keV, 217 keV and 151 keV were scanned and the energy region between 90 and 110 keV was intensely studied to reveal the 90 keV resonance strength. The BGO phase has been concluded and the DC component and resonance branchings will be studied using a HPGe detector in the next beam time. The analysis of the BGO data is ongoing. An experimental yield curve is shown in figure 6.

5 LUNA-MV

The LUNA MV accelerator will provide intense beams of H^+, $^4\mathrm{He}^+$, $^{12}\mathrm{C}^+$ e $^{12}\mathrm{C}^{++}$ in the energy range: 200 keV - 3.5 MeV. The tender for the LUNA-MV accelerator has been published in April 2015. At the deadline (August 31th, 2015), two quotations have been received (from NEC and High Voltage Engineering). In September 2015, the tender committee was appointed by the President of INFN and it was composed by: P. Martella (INFN-LNGS, chair), A. Di Leva (Univ. of Naples and INFN), L. Giuntini (Univ. of Florence and INFN), A. Gugliemetti (Univ. of Milan and INFN), V. Rigato (INFN-LNL). The committee met several times and selected

the offer presented by High Voltage Engineering Europe (HVEE). The firm offered a Singletron accelerator with terminal voltage between 0.2 and 3.5 MV and equipped with a ECR source. This way the machine will produce H, He and C beams with maximum intensities of 1000, 500 and 200 mA, respectively. The contract should be signed within March 2016; by November 2017 the accelerator will be built and tested by the Contractor. Delivery at LNGS is scheduled for January 2018. Finally, by July 2018 the accelerator will be installed and tested at LNGS. The whole procedure is under the responsibility of the RUP (Responsible of the Procedure), G. Imbriani (University and INFN Napoli) while the designer and DEC (Executive Work Director) is M. Junker (INFN-LNGS).
As for the infrastructure, the final solution for the building and shielding, has been identified by GEANT4 simulations in a 80 cm concrete thickness, both for the walls and the roof of the new experimental hall. The shielding performance has been checked independently by MCNP at the INFN central radioprotection service (LNF-ISMEL) under the supervision of Dr. A. Esposito. Finally, in the extreme and worst conditions (in terms of intensity and energy of the neutron produced inside the experimental hall), the neutron flux outside the shielded area will be much lower than 10^{-6} cm^{-2} s^{-1}. The total footprint of the new experimental hall has been fixed (i.e. $27 \times 12.5\,\mathrm{m}^2$ for the shielded area plus $4.2 \times 12.5\,\mathrm{m}^2$ for the enslaved technical building).
A working group, coordinated by C. Broggini (INFN-Padua), has been launched in October 2015 to prepare a detailed proposal for the first 5 years of activity of the LUNA-MV facility. The WG will conclude its activity within June 2016 and the proposal will be first approved by the LUNA Collaboration and then submitted to the LNGS-SC and to funding agencies. The procedure toward a formal Collaboration Agreement among the LUNA-Institutions has been started.

References

[1] K.M. Nollett *et al.*, Astrophys. J. **582** (2003) 1036

[2] M. Lugaro *et al.*, A&A 461 (2007) 657

[3] S. Palmerini *et al.*, ApJ. 764 (2013) 128

[4] M.Q. Buckner *et al.*, Phys. Rev. C **91** (2015) 015812

[5] M.L. Sergi *et al.*, Phys. Rev. C **91** (2015) 065803

[6] C.G. Bruno *et al.*, Eur. Phys. J. A **51** (2015) 94

[7] C.G. Bruno *et al.*, Phys. Rev. Lett., *in preparation*

[8] O. Straniero *et al.*, *in prepration*

[9] M. Lugaro *et al.*, *in preparation*

[10] H. Lorenz-Wirzba et al., Nuc. Phys. A 313 (1979) 346

[11] P. Descouvemont and D. Baye, Rep. Prog. Phys. **73** (2010) 036301

[12] C. Iliadis, A. Champagne, J. José, S. Starrfield, and P. Tupper, Astrophys. J. Suppl. Ser. **142**, 105 (2002).

[13] D. A. Chamulak, E. F. Brown, F. X. Timmes, and K. Dupczak, Astrophys. J. **677**, 160 (2008), 0801.1643.

[14] C. Angulo *et al.*, Nucl. Phys. A **656**, 3 (1999).

[15] C. Iliadis, R. Longland, A. E. Champagne, and A. Coc, Nucl. Phys. A **841**, 251 (2010).

[16] R. B. Firestone, Nucl. Data Sheets **108**, 1 (2007).

[17] F. Cavanna *et al.*, Phys. Rev. Lett. **115**, 252501 (2015).

[18] S. E. Hale *et al.*, Phys. Rev. C **65**, 015801 (2001).

[19] A. L. Sallaska *et al.*, Astrophys. J. Suppl. Ser. **207**, 18 (2013).

[20] R. Longland *et al.*, Phys. Rev. C **81**, 055804 (2010).

[21] J. Görres, C. Rolfs, P. Schmalbrock, H. P. Trautvetter, and J. Keinonen, Nucl. Phys. A **385**, 57 (1982).

[22] J. Görres *et al.*, Nucl. Phys. A **408**, 372 (1983).

[23] F. Cavanna *et al.*, Eur. Phys. J. A **50**, 179 (2014), 1411.2888.

[24] C. Casella *et al.*, Nucl. Inst. Meth. A **489**, 160 (2002).

[25] J. M. Cesaratto *et al.*, Phys. Rev. C 88 (2013) 065806

[26] M. Q. Buckner *et al.*, Phys. Rev. C 86 (2012) 065804

[27] H. T. Fortune, Phys. Rev. C 88 (2013) 015801

6 List of Publications

- *"Resonance strengths in the $^{17,18}O(p,\alpha)^{14,15}N$ reactions and background suppression underground. Commissioning of a new setup for charged-particle detection at LUNA"*,
  C. G. Bruno, D. A. Scott, A. Formicola, M. Aliotta, T. Davinson, M. Anders, A. Best, D. Bemmerer, C. Broggini, A. Caciolli, F. Cavanna, P. Corvisiero, R. Depalo, A. Di Leva, Z. Elekes, Zs. Fülöp, G. Gervino, C. Griffin, A. Guglielmetti, C. Gustavino, Gy. Gyürky, G. Imbriani, M. Junker, R. Menegazzo, E. Napolitani, P. Prati, E. Somorjai, O. Straniero, F. Strieder, T. Szücs, D. Trezzi
  Eur. Phys. J A 51 (2015) 94.

- *"Three new low-energy resonances in the $^{22}Ne(p,\gamma)^{23}Na$"*,
  F. Cavanna, R. Depalo, M. Aliotta, M. Anders, D. Bemmerer, A. Best, A. Boeltzig, C. Broggini, C. G. Bruno, A. Caciolli, P. Corvisiero, T. Davinson, A. Di Leva, Z. Elekes, F. Ferraro, A. Formicola, Zs. Fülöp, G. Gervino, A. Guglielmetti, C. Gustavino, Gy. Gyürky, G. Imbriani, M. Junker, R. Menegazzo, V. Mossa, F. R. Pantaleo, P. Prati, D. A. Scott, E. Somorjai, O. Straniero, F. Strieder, T. Szücs, M. P. Takács, D. Trezzi

- *"Low-energy resonances in the $^{22}Ne(p,\gamma)^{23}Na$ reaction directly observed at LUNA"*,
  F. Cavanna, R. Depalo
  EPJ Web of Conferences (CGS15), 93 03004 (2015)

- *"The LUNA experiment at Gran Sasso Laboratory: Studying stars by going underground"*,
  A. Guglielmetti
  AIP Conference Proceedings 1681, (2015) 050001

- *"Rivelazione di neutroni in esperimenti di astrofisica nucleare: studio e caratterizzazione di scintillatori liquidi organici"*
  G. F. Ciani
  Tesi di Laurea Magistrale, Università degli studi di Bari

- *"Neutron detection in nuclear astrophysics experiments: study of organic liquid scintillators"*
  G. F. Ciani
  Journal of Physics: Conference Series, 689, 1

- *"Nuclear Astrophysics with LUNA"*
  C. Broggini
  submitted to Journal of Physics: Conference Series

- *"Background modeling and shielding of a Bismuth Germanium Oxide (BGO) detector underground"*
  A. Boeltzig
  submitted to Journal of Physics: Conference Series

- *"Status of the direct measurements of $^{18}O(p,\gamma)$ and $^{23}Na(p,\gamma)$ cross sections at astrophysical energies at LUNA"*
  A. Boeltzig
  submitted to Journal of Physics: Conference Series

- *"Cross section measurements for $^{23}Na(p,\gamma)^{24}Mg$"*
  A. Boeltzig
  Journal of Physics: Conference Series 689 (2016) 0120

- *"Low-Energy resonances in the $^{22}Ne(p,\gamma)^{23}Na$ reaction directly observed at LUNA"*
  R. Depalo
  submitted to Journal of Physics: Conference Series

- *"Towards the study of $^{2}H(p,\gamma)^{3}He$ reaction in the Big Bang Nucleosynthesis energy range in LUNA"*
  I. Kochanek
  submitted to Journal of Physics: Conference Series

- *"LUNA: present status and future prospects"*
  A. Caciolli
  submitted to Nucleus Nucleus 2015 Conference

- *"Looking the Universe from Deep Underground"*
  D. Trezzi
  PoS (2015) 041

- *"Nuclear Cosmology Deep Underground"*
  D. Trezzi
  Acta Physica Polonica

- *"Study of the $^{2}H(p,\gamma)^{3}He$ reaction in the Big Bang Nucleosynthesis energy range at LUNA"*
  D. Trezzi
  submitted to Journal of Physics: Conference Series

- *"A direct measurement of the $^{22}Ne(p,g)^{23}Na$ reaction down to the energies of astrophysical interest"*
  F. Cavanna
  PhD thesis, Università degli studi di Genova

- *"The neon-sodium cycle: Study of the $^{22}Ne(p,g)^{23}Na$ reaction at astrophysical energies"*
  R. Depalo
  PhD thesis, Università degli studi di Padova

- *"Studio della reazione $^{22}Ne(p,g)^{23}Na$ a energie astrofisiche"*
  D. Piatti
  Tesi di Laurea Magistrale, Università degli studi di Padova

7 Conference and seminar contributions

- P. Prati, "The LUNA-MV project: status and perspectives", invited talk 13th symposium on the origin matter and evolution of galaxies, Beijing, (China) 24-27.06.2015

- P. Prati, "Status and perspective for ^{22}Ne(α,n)^{25}Mg", invited talk at GIANTS 2015, Padova (Italy) 28-30.04.2015

- A. Caciolli, "LUNA: present status and future prospects, invited talk at Nucleus Nucleus 2015 Conference", LNS-Catania, (Italy) 21-26.06.2015

- A. Guglielmetti, "The LUNA experiment at Gran Sasso Laboratory: studying stars by going underground", invited seminar at Warsaw University (Poland) 2015

- A. Guglielmetti, "Status and future of LUNA", invited talk at GIANTS 2015, Padova (Italy) 28-30.04.2015

- A. Guglielmetti, "The LUNA experiment at Gran Sasso laboratory: studying stars by going underground", invited talk at Nuclear Structure and Dynamics, Portorose (Slovenia) 15-19.06.2015

- A. Guglielmetti, "L'esperimento LUNA ed il progetto LUNA MV ai Laboratori Nazionali del Gran Sasso", relazione su invito al 101esimo Congresso Nazionale SIF, Roma, 21-25.09.2015

- R. Depalo, "Latest results from LUNA", invited talk at Nuclear Physics in Astrophysics VII Conference York, (Great Britain) 18-22.05.2015

- A. Best, "Underground Nuclear Astrophysics", invited talk at XXI International School on Nuclear Physics and Applications & International Symposium on Exotic Nuclei, Varna (Bulgaria) 06-12.09.2015

- D. Trezzi, 'Looking the Universe from Deep Underground", invited talk at 54th International Winter Meeting on Nuclear Physics, Bormio (Italy) 25-29.01.2016

- G. Imbriani, "Status and perspective of ^{13}C(α,n)^{16}O", VIII Meeting of the Italian Groups of Theoretical and Experimental Nuclear Astrophysics, Padova (Italy) 28-30.04.2015,

- C. Broggini, "Nuclear Astrophysics with LUNA", invited lecture at the 8th Summer School on Experimental Nuclear Astrophysics, S.Tecla (Italy) 13-20.09.2015

- C. Broggini, "LUNA experiment: status and perspectives", invited talk at the Spes one-day workshop Nuclear Astrophysics at Spes, Caserta, Italy 12-13.11.2015

- C. Broggini, "Astrofisica Nucleare al Gran Sasso", relazione su invito al 101esimo Congresso Nazionale SIF, Roma, 21-25.09.2015

- Zs. Fülöp, "Nuclear astrophysics experiments underground", invited talk at International Conference on Precision Physics and Fundamental Physical Constants (FFK-2015) Budapest, (Hungary) 12-16.10.2015

- A. Formicola, "Nuclear processes in stars reproduced in underground laboratories", invited talk at Twelfth Conference on the Intersections of Particle and Nuclear Physics-CIPANP 2015, Vail Colorado, 19-24.05.2015

- A. Formicola, "Experimental challenges in Underground Nuclear Astrophysics Laboratory", invited talk at the Conference on Science at the Sanford Underground Research Facility (CoSSURF), 17-20.05.2015

- D. Trezzi, "Nuclear Cosmology Deep Underground", talk at XXIV Mazurian lakes conference on Physics, Piaski (Poland) 06-13.09.2015

- D. Trezzi, "Studying the Universe from Deep Underground", seminar at Osservatorio Astronomico di Brera, Merate (Italy) 15.04.2015

- F. Ferraro, "Direct measurement of the ^{22}Ne(p,γ)^{23}Na reaction cross section at LUNA", talk at the 8th Summer School on Experimental Nuclear Astrophysics, S.Tecla (Italy) 13-20.09.2015

- F. Cavanna, "Underground Nuclear Astrophysics at Gran Sasso Laboratories", talk at European Nuclear Physics Conference (EuNPC 2015), Groningen (Netherlands) 31.084.09.2015

- A. Boeltzig, "Status of the direct search for the E(c.m.) = 138 keV resonance in ^{23}Na(p,γ)^{24}Mg at LUNA", talk at European Nuclear Physics Conference (EuNPC 2015), Groningen (Netherlands) 31.084.09.2015

- A. Boeltzig, "Status of the direct measurements of ^{18}O(p,γ) and ^{23}Na(p,γ) cross sections at astrophysical energies at LUNA", talk at the 8th Summer School on Experimental Nuclear Astrophysics, S.Tecla (Italy) 13-20.09.2015

- A. Boeltzig, "Cross Section Measurements for ^{23}Na(p,γ) at LUNA", talk at 6th Young Researcher Meeting L'Aquila (Italy), 12-14.10.2015

- C. Bruno, "Direct underground measurement of the ^{17}O(p,α)^{14}N reaction at LUNA", talk at Nuclear Physics in Astrophysics VII Conference York, (Great Britain) 18-22.05.2015

- R. Depalo, "Low-Energy resonances in the ^{22}Ne(p,γ)^{23}Na reaction directly observed at LUNA", talk at the 8th Summer School on Experimental Nuclear Astrophysics, S.Tecla (Italy) 13-20.09.2015

- I. Kochanek, "Towards the study of ^{2}H(p,γ)^{3}He reaction in the Big Bang Nucleosynthesis energy range in LUNA", talk at the 8th Summer School on Experimental Nuclear Astrophysics, S.Tecla (Italy) 13-20.09.2015

- G. Gervino, "Ultra-sensitive γ-ray spectroscopy set-up for investigating primordial lithium problem", FRONTIER DETECTORS FOR FRONTIER PHYSICS 13th Pisa Meeting on Advanced Detectors, Isola d'Elba 24-30.05.2015 (Italy)

- A. Best, "^{18}O(p,γ)^{19}F and ^{23}Na(p,γ)^{24}Mg at LUNA contributed talk at the 2016 meeting of the APS Prairie Section at the University of Notre Dame, Indiana in November

- A. Boeltzig, "Direct Cross Section Measurements for Astrophysics at LUNA", poster at Excellence in Detectors and Instrumentation Technologies (EDIT) School Frascati, (Italy) 20-29.10.2015

- A. Boeltzig, "Background modeling and shielding of a Bismuth Germanium Oxide (BGO) detector underground", poster at Nuclear Physics in Astrophysics VII Conference York, (Great Britain) 18-22.05.2015

- G. F. Ciani, "Neutron detection in nuclear astrophysics experiments: study of organic liquid scintillators ", poster at 6th Young Researcher Meeting L'Aquila (Italy), 12-14.10.2015

- V. Mossa, "Study of the ^{2}H(p,γ)^{3}He reaction in the Big Bang Nucleosynthesis energy range at LUNA", poster at 54th International Winter Meeting on Nuclear Physics, Bormio (Italy) 25-29.01.2016

- D. Trezzi, "Study of the ^{2}H(p,γ)^{3}He reaction in the Big Bang Nucleosynthesis energy range at LUNA", poster at Nuclear Physics in Astrophysics VII Conference York, (Great Britain) 18-22.05.2015

- C. Bruno, "Going underground to study stars", poster at School of Physics and Astronomy Postgraduate Poster Evening, Edinburgh University (UK), 10.2015, First prize

2015 LVD STATUS REPORT

The LVD Collaboration

N.Yu.Agafonova[7], M.Aglietta[8], P.Antonioli[1], V.V.Ashikhmin[7], G.Badino[8], G.Bari[1], R.Bertoni[8], E.Bressan[1], G.Bruno[5], V.L.Dadykin[7], E.A.Dobrynina[9], R.I.Enikeev[7], W.Fulgione[8], P.Galeotti[8], M.Garbini[1], P.L.Ghia[2], P.Giusti[1], F.Gomez[8], E.Kemp[3], V.B.Korchaguin[7], A.S.Mal'gin[7], A.Molinario[8], R.Persiani[1], I.A.Pless[6], A.Romero[8], V.G.Ryasny[7], O.G.Ryazhskaya[7], O.Saavedra[8], G.Sartorelli[1], M.Selvi[1], I.R.Shakyrianova[7], G.C.Trinchero[8], C.Vigorito[8], V.F.Yakushev[7], A.Zichichi[1*]

[1] *University of Bologna and INFN-Bologna, Italy*
[2] *CNRS-IN2P3, Paris, France*
[3] *University of Campinas, Campinas, Brazil*
[5] *INFN-LNGS, Assergi, Italy*
[6] *Massachusetts Institute of Technology, Cambridge, USA*
[7] *Institute for Nuclear Research, Russian Academy of Sciences, Moscow, Russia*
[8] *INFN-Torino, INAF-OATO, Torino and University of Torino, Italy*
[*] *Spokesperson of the LVD experiment*

Abstract

The Large Volume Detector (LVD) has been continuously taking data since 1992 at the INFN Gran Sasso National Laboratory. LVD is sensitive to neutrino bursts from gravitational stellar collapses with full detection probability over the Galaxy. We have searched for neutrino bursts in LVD data taken in 8340 days of operation (8124 with $M_{act} \geq$300 ton). No evidence of neutrino signals has been found since 9 June 1992 to 29 February 2016. The 90% C.L. upper limit on the rate of core-collapse and failed supernova explosions out to distances of 25 kpc is found to be 0.10 y^{-1}, this being the most stringent limit ever achieved by the observation of supernovae through neutrinos in the entire Galaxy.

LVD is one of the three founding members of the Supernovae Early Warning System (SNEWS) project, the network of neutrino observatories whose aim is to provide the astronomical community with a prompt ad confident alert of the occurrence of a galactic supernova event. We actively participate in the network since 2005 when it became operational.

1 Introduction

The detection of neutrinos from the optically bright supernova in the Large Magellanic Cloud, SN1987A [Hirata et al.(1987), Bionta et al.(1987), Alekseev et al.(1987)] and [Aglietta et al.(1987)][1], led to important inferences on the physics of core collapse supernovae. It experimentally proved the critical role of neutrinos in the explosion of massive stars, as suggested more than 50 years ago [Gamow and Shoenberg(1940)],
[Zel'dovich and Guseinov(1965)], [Colgate and White(1966)], [Nadyozhin(1977)]. While a complete understanding of the physics involved is still lacking [Woosley & Janka(2005)] the SN1987A event helped to establish some aspects of the theory, namely the total energy radiated, the neutrinos temperatures and the duration of the radiation pulse (see e.g. [Loredo and Lamb(2002), Pagliaroli, Vissani, Costantini and Ianni(2009)]).

However, only a small number of neutrinos could be detected in that occasion, ≈ 20. Thus, it was not possible to study the detailed features of the neutrino emission, which is expected to carry important information on the dynamics of the explosion. Such a small number was due not only to the source distance (about 50 kpc from the Earth) but also to the relatively small dimensions of the detectors existing at that time. In fact, the need for larger and more sensitive neutrino detectors to study one of the most powerful and rare events occurring in the Galaxy had already become evident in the scientific community even before SN 1987A. The extremely low frequency (present estimates give a rate between one every 10 yr and one every 100 yr) implies that long-term observations using powerful neutrino detectors are of essence to detect explosions of massive stars. Also, the observation of neutrinos from SN 1987A was guided by the optical observation. However, the core-collapse rate in the Galaxy exceeds that of observable optical supernovae because light can be partially or totally absorbed by dust in the Galactic plane. In recent times this point has been discussed by [Adams et al.(2013)] with the conclusion that large long-term neutrino detectors are the most suited to observing the Galaxy searching for core-collapse supernovae explosions. Neutrino detectors are also sensitive to collapsing objects that fail to explode, becoming black holes (so-called failed supernovae), because those are expected to emit a neutrino signal even stronger, although shorter in time, than from core-collapse supernovae [Nakazato et al.(2008)].

In addition, the prompt identification of a neutrino signal could provide astronomers with an early alert of a supernova occurrence (SuperNova Early Warning System, SNEWS,
[Antonioli et al.(2004)] of which LVD is a founding member) allowing one to study phenomenons like the shock break out, a flash of radiation as the shock wave breaks out from the surface of the star [Klein and Chevalier(1978), Falk(1978)], and to detect the signal due to the emission of gravitational waves
[Pagliaroli, Vissani, Coccia and Fulgione(2009)].

Based on the pioner idea by [Domogatsky and Zatsepin(1965)], several neutrino detectors have been observing the Galaxy in the last decades to search for stellar collapses, namely Super-Kamiokande [Ikeda et al.(2007)], Baksan [Novoseltseva et al.(2011)], MACRO
[Ambrosio et al.(2004)], AMANDA [Ahrens et al.(2002)], SNO [Aharmim et al.(2011)]. None of them has found evidence of supernovae explosions, thus setting limits to the rate of collapses. The longest duration experiment is Baksan: it has provided the most stringent limit in terms of rate (0.09 per year at 90% C.L. based on 26 years of operation) but given the limited size its sensitivity to the whole Galaxy is controversial. In turn, the most sensible detector, Super-Kamiokande (fully efficient up to 100 kpc), sets a limit to the rate of 0.32 per year at 90%

[1]The explanation of five signals recorded by the LSD detector about 5 hours earlier with respect to the other three experiment still remains controversial.

C.L.

The results of the search for supernova neutrino bursts based on the data taken by the Large Volume Detector (LVD) [Aglietta et al.(1992)] in more than 20 yr of operation in the INFN Gran Sasso National Laboratory (LNGS) in Italy have been published in 2015 [Agafonova et al.(2015)]. Results of this analysis are summarized and updated in Section 2. Finally, in Section **??**, present conditions of the detector and its possible developments are discussed.

2 Core Collapse SN Monitor

SN neutrinos can be detected in LVD through charged current (CC) and neutral current (NC) interactions on proton, Carbon nuclei and electrons of the liquid scintillator. The scintillator detector is supported by an iron structure, whose total mass is about 850 t. This can also act as a target for neutrinos and antineutrinos, as the product of interactions in iron can reach the scintillator and be detected [Agafonova et al.(2007)]. The total target thus consists of 8.3 x 10^{31} free protons, 4.3 x 10^{31} C nuclei and 3.39 x 10^{32} electrons in the scintillator and of 9.7 x 10^{30} Fe nuclei in the support structure.

The main neutrino reaction in LVD is the inverse beta decay (IBD), as it can be seen in Table 1, where all other relevant neutrino interaction channels are shown too and their relevance in detecting neutrinos from collapsing stars has been evaluated by using a conservative model based on the observations of neutrinos from the SN1987A [Pagliaroli, Vissani, Costantini and Ianni(2009)].

Table 1: Neutrino interaction channels in LVD. Cross sections of different interactions are obtained referring to [Strumia and Vissani(2010)] for interaction 1, [Fukugita et al.(1988)] for interactions 2-4, [Bahcall et al.(1995)] for interaction 5 and [Kolbe and Langanke(2001)] and [Toivanen et al.(2001)] for interactions 6-8.

ν interaction channel	E_ν threshold	%	
$\bar{\nu}_e + p \rightarrow e^+ + n$	(1.8 MeV)	(88%)	(1)
$\nu_e + {}^{12}C \rightarrow {}^{12}N + e^-$	(17.3 MeV)	(1.5%)	(2)
$\bar{\nu}_e + {}^{12}C \rightarrow {}^{12}B + e^+$	(14.4 MeV)	(1.0%)	(3)
$\nu_i + {}^{12}C \rightarrow \nu_i + {}^{12}C^* + \gamma$	(15.1 MeV)	(2.0%)	(4)
$\nu_i + e^- \rightarrow \nu_i + e^-$	(-)	(3.0%)	(5)
$\nu_e + {}^{56}Fe \rightarrow {}^{56}Co^* + e^-$	(10. MeV)	(3.0%)	(6)
$\bar{\nu}_e + {}^{56}Fe \rightarrow {}^{56}Mn + e^+$	(12.5 MeV)	(0.5%)	(7)
$\nu_i + {}^{56}Fe \rightarrow \nu_i + {}^{56}Fe^* + \gamma$	(15. MeV)	(2.0%)	(8)

LVD consists of an array of 840 scintillator counters, 1.5 m^3 each, viewed from the top by three photomultipliers (PMTs). It is a modular detector. This modularity allows LVD to achieve a very high duty cycle, that is essential in the search of unpredictable sporadic events. On the one hand, the three independent data acquisition systems, one per tower, minimize (in practice, nullify) the probability of a complete shutdown of the experiment. On the other hand, failures involving one or more counters do not affect other counters. LVD can thus be serviced during data-taking by stopping only the part of the detector (down to individual counters) that needs maintenance. The modularity of the detector results in a "dynamic" active mass M_{act}.

LVD has been in operation since 9 June 1992, its mass increasing from 300 t (about one full "tower") to its final one, 1000 t, in January 2001. The trigger logic (extensively described in

[Agafonova et al.(2007)]) is based on the 3-fold coincidence of the PMTs in a single counters. Given the relevance of the IBD reaction, the trigger has been optimized for the detection of both products of this interaction, namely the positron and the neutron. Each PMT is thus discriminated at two different threshold levels, the higher one, $\mathcal{E}_{\rm H}$, at present set to 4 MeV for all counters, being also the main trigger condition for the detector array. The lower one ($\mathcal{E}_{\rm L} \simeq 0.5$ MeV) is in turn active only in a 1 ms time-window following the trigger, allowing the detection of (n, p) captures. Once a trigger is identified, the charge and time of the three summed PMTs signals are stored in a memory buffer. The time is measured with a relative accuracy of 12.5 ns and an absolute one of 100 ns [Bigongiari et al.(1990)]. One millisecond after the trigger, all memory buffers are read out, independently in the three towers.

The method used in LVD to search for neutrino bursts from gravitational stellar collapses essentially consists in searching, in the time series of single counter signals (events), for a sequence (cluster) whose probability of being simulated by fluctuations of the counting rate is very low. The higher the event frequency, the higher is the probability of a "background-cluster', given by accidental coincidences. At the trigger level, the bulk of events in LVD is due to natural radioactivity products both from the rock surrounding the detector and from the material that constitutes the detector itself and to atmospheric muons. A set of cuts, described in detail in [Agafonova et al.(2015)] aims at reducing such a background while isolating signals potentially due to neutrinos. After the background reduction, the counting rate is decreased by a factor of about 400.

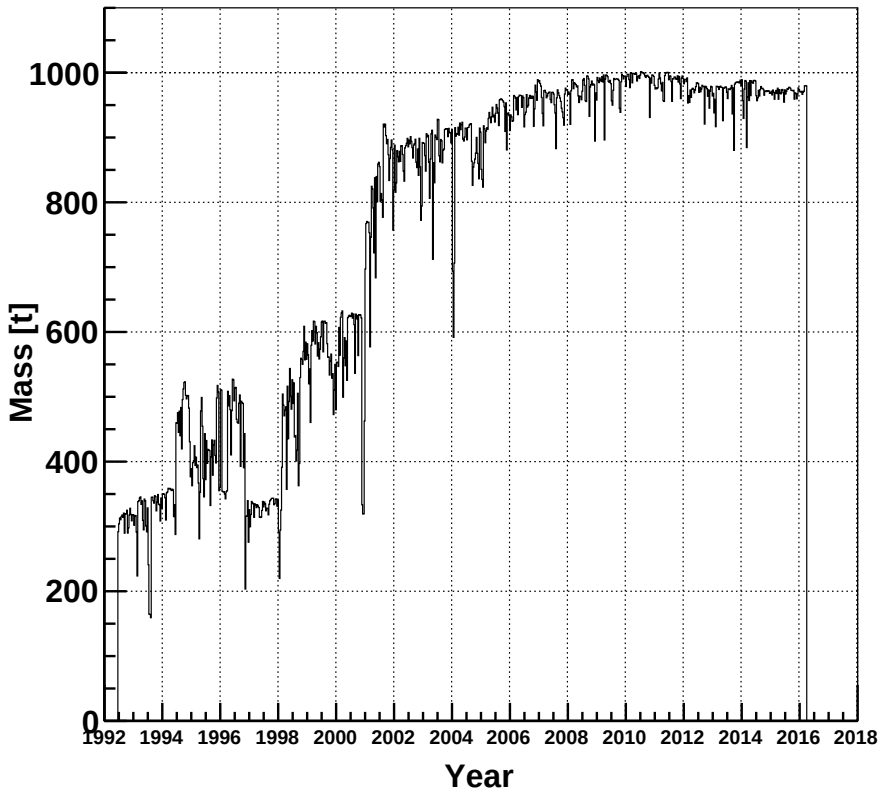

Figure 1: LVD active mass as a function of time in the period from June 1992 to March 2016.

The active detector mass, M_{act}, resulting after applying the quality cuts, is shown in Figure 1, as a function of time in the data period since June 1992 to March 2016.

During this time the active mass has been larger than 300 t in 8124 days, corresponding to a live time larger than 94% (> 99 % since 2001). 300 t is the minimal mass that allows LVD to be sensitive to neutrino bursts over the whole Galaxy. The number of events collected in this period and passing the cuts is 14974216. The distribution of time intervals between successive events is shown in Figure 2 (blue histogram). Due to the variable detector configuration, the differences in time have been normalized to account for the active mass at the time of the events. The normalization is done by equalizing the event rate (f, that depends on the active mass) to a reference one, $f_{\rm ref}$, that corresponds to the average one when the whole array (1000 t) is in operation, i.e., $\delta t_{\rm norm} = \delta t \cdot f / f_{\rm ref}$, with $f_{\rm ref} = 0.03$ s^{-1}. LVD events behave as a stochastic time series well described by the Poisson statistics as proved by the quality of the fit to a Poisson distribution (shown in the figure as a dashed black line).

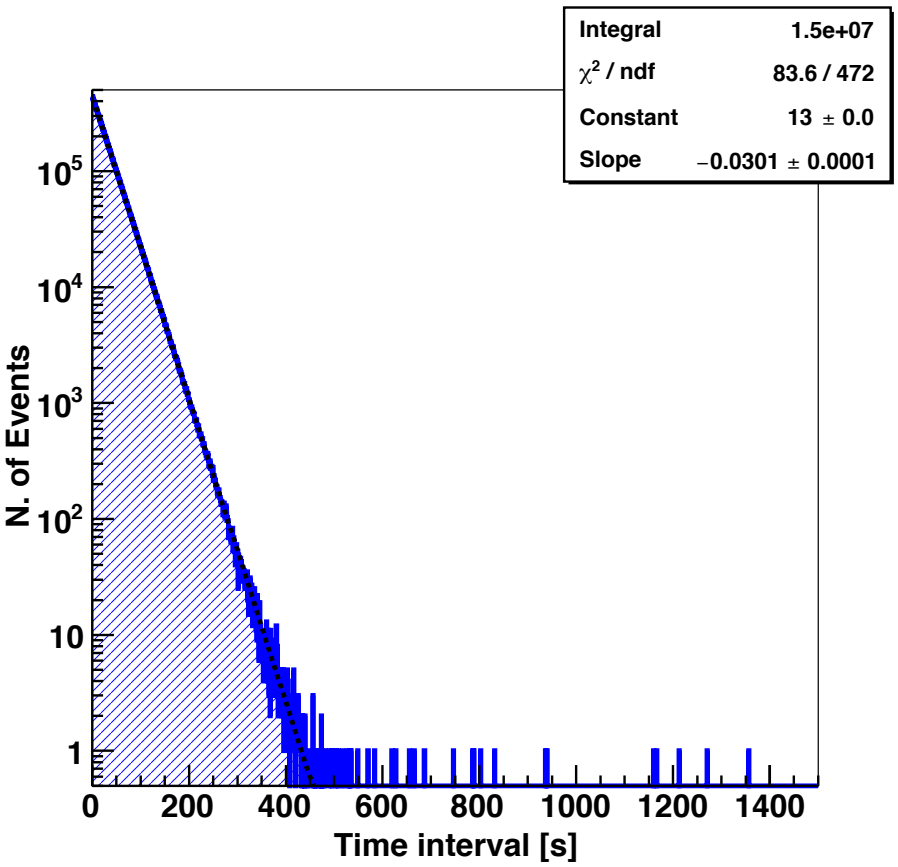

Figure 2: Distribution of normalized time intervals between successive events passing the selections described in the text. The normalization is done by equalizing the counting rate at the time of each event to the average one. The dashed black line shows the result of a Poissonian fit to the distribution.

The search for neutrino bursts in LVD data is essentially a two-steps process.
In the first step, we analyze the entire time series[2] to search for cluster of events. The rationale

[2]We choose here not to exploit the capability of LVD to detect both products of the IBD reaction. Indeed,

of the search is that each event could be the first of a possible neutrino burst. As we do not know a priori the duration of the burst, we consider all clusters formed by each event and the n successive ones, with n from 1 to all those contained inside a time window $\Delta t_{max} = 100$ s. The duration of each cluster is given by the time difference Δt between the first event and the last one of each sequence. The analysis is then applied iteratively, starting from the next one, to all LVD events. The advantage of the described analysis, where all clusters with durations up to 100 s are considered, is that it is unbiassed with respect to the duration of the possible neutrino burst, unknown a priori. Moreover, the choice of $\Delta t_{max} = 100$ s is very conservative as it well exceeds the expected duration of a neutrino burst from core collapse supernovae and even more that from failed supernovae.

The second step of the process consists in deciding if one or more among the detected clusters are neutrino-bursts candidate. To this aim, we associate to each of them (characterised by $m_i, \Delta t_i$) a quantity that we call imitation frequency F_{im_i}. This represents the frequency with which background fluctuations can produce clusters of any duration, between 0 and Δt_{max}, with the same or lower probability than that of the individual cluster. As shown in [Fulgione et al.(1996)], this quantity, which depends on $(m_i, \Delta t_i)$, on the background rate, f_{bk_i} and on the maximum cluster duration chosen for the analysis, Δt_{max}, can be written as:

$$F_{im_i} = f_{bk}^2 \Delta t_{max} \sum_{k \geq m_i - 2} P(k, f_{bk_i} \Delta t_i) \quad (1)$$

Given the duration of the LVD data set (more than 20 years), we choose 1/100 y^{-1} as imitation-frequency threshold, F_{im}^{th}. That means that a cluster $(m_i, \Delta t_i)$ is considered as a candidate neutrino burst if:

$$\sum_{k \geq m_i - 2} P(k, f_{bk} \Delta t_i) < \frac{F_{im}^{th}}{f_{bk}^2 \cdot \Delta t_{max}} \quad (2)$$

where $P(k, f_{bk} \Delta t_i)$ is the Poisson probability to have k events in the time window Δt_i if f_{bk} is the average background frequency.

The introduction of the imitation frequency has a double advantage. From the viewpoint of the search for neutrino bursts, it allows us to define a priori the statistical "significance" of each cluster in terms of frequency. Also, it allows us to monitor the performance of the search algorithm and the stability of the detector[3] by increasing the imitation-frequency threshold. Namely, we study the time distribution of clusters (i.e., the difference in time between clusters) having imitation frequency less than 1/day, 1/week and 1/month. The occurrence of clusters with different F_{im} over 8124 days of measurement is uniform as can be seen in Figure 3. It shows the F_{im} of all detected clusters as a function of time. Clusters above the black, green, blue lines are those with $F_{im} < 1$ day^{-1}, $week^{-1}$, $month^{-1}$, respectively.

The capability of LVD to detect in real-time (i.e., "on-line") a supernova event is extensively discussed in [Agafonova et al.(2008)]. In that case a fixed time-window (i.e., 20 s) is used in the burst-search algorithm. In turn, for the so-called "off-line" analysis we do not fix a priori

as discussed in [Agafonova et al.(2012)], the algorithm applied to all selected events is more sensitive than when applied to events with the IBD signature. It becomes slightly more efficient if we apply it to a mixture of unsigned and signed events, but at the price of loss of simplicity and of independence from models. Finally, by using all events the algorithm is sensible not only to possible neutrino interactions in the liquid scintillator but also in the iron structure [Imshennik & Ryazhskaya(2004)].

[3]The performance of the selection procedure and its capability to discriminate a burst from background fluctuations has also been hardware tested, by generating clusters of signals in a subset of counters equipped with a LED system.

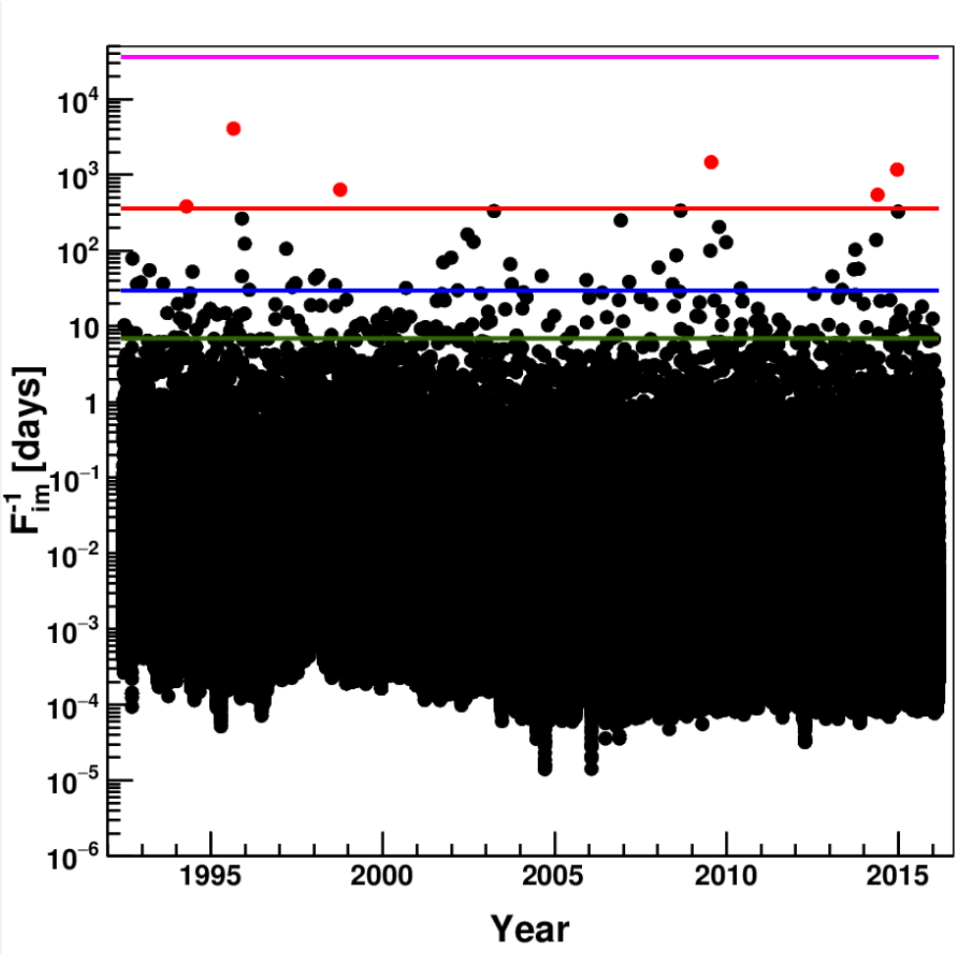

Figure 3: Distribution of detected clusters versus time between June 1992 and December 2013. Red dots represent clusters with imitation frequency less than $F_{im} = 1$/year. Black green, blue, red and purple lines correspond to $F^{th}_{im} = 1/$ day, $F^{th}_{im} = 1/$ week, $F^{th}_{im} = 1/$ month, $F^{th}_{im} = 1/$ y, $F^{th}_{im} = 1/100$ y, respectively.

the duration of the burst, i.e., we consider all possible durations up to 100 s. Consequently, we extend here our previous study to account for this choice. As in [Agafonova et al.(2008)], we discuss the sensitivity to the identification of a neutrino burst in terms of the maximum detectable distance of the supernova explosion.

To estimate the characteristics of a neutrino signal in LVD from a gravitational stellar collapse we exploit the parametrization of the neutrino flux proposed by

[Pagliaroli, Vissani, Costantini and Ianni(2009)]. That is based on the analysis of neutrinos observed at the occurrence of SN1987A and it includes the impact of neutrino oscillations too. The adopted model can be summarized as follows:

- the neutrino emission occurs in two main stages:[4] ν_e and $\bar{\nu}_e$ are emitted during the accretion phase (≈ 500 ms), determining in part the future evolution of the core collapse [O'Connor and Ott(2011)];

[4] ν_e emitted in shock breakout, when ν_e produced in electron captures (neutronization) are released, play a secondary role in the detector sensitivity.

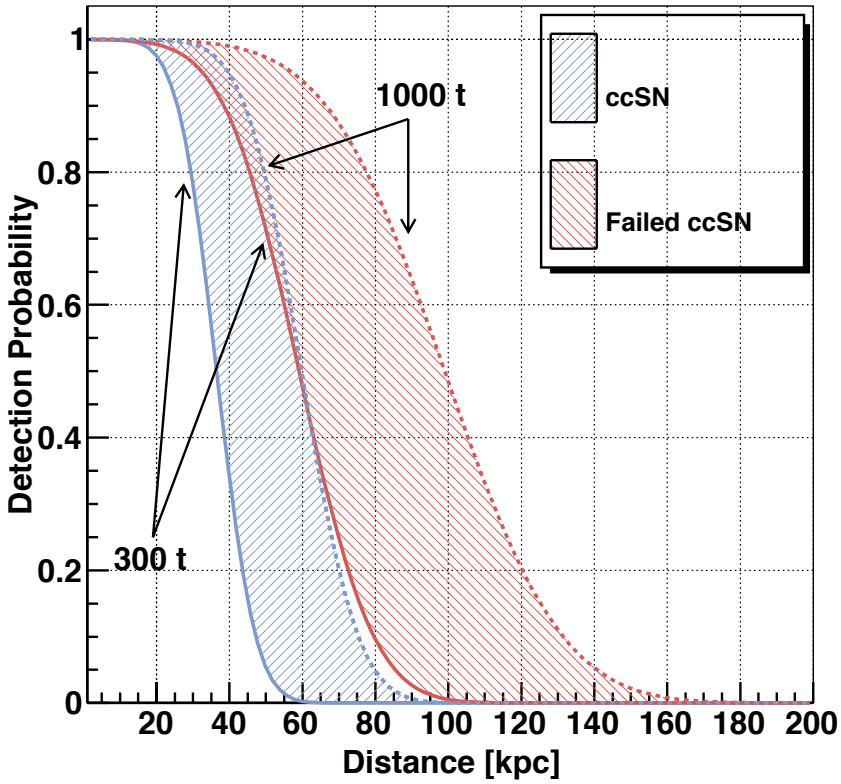

Figure 4: LVD detection probability versus source distance for the imitation frequency of 1/100 y^{-1} (see text). The blue and red bands correspond to the case of standard core collapse (ccSN) and failed supernovae, respectively. The solid (dashed) line represents an active mass of 300 (1000) t.

neutrinos and antineutrinos, ν_i and $\bar{\nu}_i$, of all flavors are emitted during the thermal cooling;
- the total neutrino signal is expected to develop on a time scale of about 10 s, being 90% (50%) the fraction of detected events in the first 10 s (1 s);
- the time averaged temperatures of emitted neutrinos are: 10.7 MeV for ν_e, 12.0 MeV for $\bar{\nu}_e$ and 14.2 MeV for $\nu_{\mu,\tau}, \bar{\nu}_{\mu,\tau}$;
- Mikheev-Smirnov-Wolfenstein (MSW) oscillations effects on neutrinos crossing the matter of the collapsing star [Wolfenstein(1978)], [Mikheev and Smirnov(1985)] are taken into account, while ν-ν interactions are neglected [Agafonova et al.(2007)]. The normal mass hierarchy scenario has been conservatively assumed together with the most recent values of θ_{12} and mass squared differences Δm^2_{12} and Δm^2_{23} (see e.g. [Strumia and Vissani(2010)] for a review). In this scenario the non null value for θ_{13} mixing angle [An et al.(2012)] has no significant impact on the expected neutrino signal.

By simulating neutrino events in LVD generated according to the described model, we estimate the detection probability as a function of the distance of the gravitational stellar collapse from the Earth. We find that a total of more than 300 events would trigger LVD for a collapse 10 kpc away: events are shared among all interaction channels as shown in Table 1. This number

becomes more than 260 taking into account the chosen energy cut at 10 MeV[5]. The detection probability as a function of the distance of the collapse is shown in Figure 4 for the chosen imitation frequency of 1/100 y^{-1}. The blue band corresponds to the case of standard core collapse supernovae: the solid (dashed) line represents an active mass of 300 (1000) t.

We also evaluate the detection probability in the case of stellar collapses ending into black-holes, so-called failed supernovae, by using a similar procedure as above. This is shown as a red band in the same Figure 4 (similarly, the two boundary lines represent a mass of 300 t and 1000 t). In this case, we take as reference the predictions of [Nakazato et al.(2008)] by choosing the most conservative one in terms of neutrino emission. Namely, we assume a progenitor of 40 solar masses, a burst duration shorter than 500 ms, a total emitted energy in neutrinos of 1.3 10^{53} ergs and the inverted neutrino mass hierarchy.

We can conclude that the LVD efficiency in detecting supernovae or failed supernovae explosions is more than 95% for distances less then 25 kpc when the detector active mass is larger than 300 t.

By analyzing the time series of 14974216 events we get 30673501 clusters with multiplicity $m \geq 2$ and $\Delta t \leq 100$ s. For each cluster, we evaluate the imitation frequency, F_{im}^{th}, following eq.1. Those are shown in Figure 3 as a function of time. In the figure the purple line represents the expectations for a F_{im}^{th} of 1/100 y^{-1}, i.e., the threshold for considering a cluster as a neutrino-burst candidate. None of the observed clusters passes such threshold, the maximum detected significance being $(F_{im})^{-1} = 11.16$ y associated to a cluster of 7 events during about 5 seconds. For the sake of completeness, we have carefully inspected all clusters with $F_{im} \leq 1$/month (51 of them). Their energy spectra have been examined as well as the number of low-energy delayed signals that might be the signature of IBD interactions (see Section 2). All 51 clusters are fully compatible with chance coincidences among background signals. The characteristics of the 6 most significant among them ($F_{im} \leq 1$/year) are reported in Table 2. Besides the date, we show the conditions of the detector at the time of the cluster, i.e., active mass and background frequency. The properties of the clusters are listed in the last five columns: multiplicity, duration, imitation frequency, average energy of events and number of IBD candidate events. The distance corresponding to 90% detection probability is also shown: that is derived from the blue curve in Figure 4 account taken of the active mass. We note that for all four clusters it is well above 25 kpc.

We conclude that no evidence is found for core collapse or failed supernovae during the considered data-taking period. Account taken of the live-time of 8124 days, we obtain a limit on the rate of gravitational collapses out to 25 kpc of less than 0.103 per year at 90% C.L.

3 List of Publications

1. **Implication on the Core Collapse Supernova Rate from 21 Years of Data of the Large Volume Detector**, The LVD Collaboration, ApJ, 802, 47 (arXiv:1411.1709v2).

2. **Search for SN neutrino bursts with LVD**, C.Vigorito for the LVD Collaboration, The

[5] As anticipated in Section 3.3, the described simulation allows us to evaluate too the possible impact of topological cuts on a real neutrino burst. It results that even in the worst possible experimental conditions, i.e., for a source at 25 kpc and a minimal detector active mass, $M_{act} = 300$ t, the probability to mistakenly reject counters, modules or groups due to statistical fluctuations of an uniform distribution, thus downgrading an authentic cluster, remains always $< 3 \cdot 10^{-4}$.

Table 2: Characteristics of clusters with significance $F_{im} < 1 \cdot y^{-1}$: time of occurrence (UTC), active mass (M_{act}), background rate (f_{bk}), distance corresponding to 90% detection probability ($D_{90\%}$), multiplicity (m), duration (Δ t), inverse of imitation frequency (F_{im}^{-1}), average events energy ($\bar{E}$), number of IBD candidates (N_{IBD})

n.	UTC	M_{act}[t]	$f_{bk}[s^{-1}]$	$D_{90\%}$[kpc]	m	Δt[s]	F_{im}^{-1}[y]	$\bar{E}$ [MeV]	N_{IBD}
1	1994 16-04 10:40:49.263	346	$1.08 \cdot 10^{-2}$	29.5	7	18.88	1.06	26.5	2
2	1995 27-08 16:18:10.478	431	$1.85 \cdot 10^{-2}$	35.0	7	5.49	11.16	36.2	1
3	1998 07-10 15:41:41.775	552	$1.40 \cdot 10^{-2}$	30.6	12	90.05	1.76	32.2	3
4	2009 18-07 07:39:20.517	976	$2.40 \cdot 10^{-2}$	40.4	12	42.71	4.02	14.6	1
5	2014 25-05 03:54:14.555	959	$2.78 \cdot 10^{-2}$	36.8	14	61.56	1.49	22.6	4
6	2014 18-12 20:21:28.787	937	$2.33 \cdot 10^{-2}$	45.9	8	9.98	3.22	18.8	3

References

[Adams et al.(2013)] Adams Scott M. et al., 2013, ApJ, 778:164

[Agafonova et al.(2007)] Agafonova N.Yu. et al., 2007, APh, 27, 254-270; [hep-ph/069305].

[Agafonova et al.(2008)] Agafonova N.Yu. et al., 2008, APh, 28, 516

[Agafonova et al.(2012)] Agafonova N.Yu. et al., 2012, PhRvL, 109-7, 070801

[Agafonova et al.(2015)] Agafonova N.Yu. et al., 2015, ApJ, 802, 47

[Aglietta et al.(1987)] Aglietta, M. et al., 1987, EPL, 3, 1315

[Aglietta et al.(1992)] Aglietta, M. et al., 1992, NcimA, 105, 1793

[LSD Collaboration(1992)] M.Aglietta *et al.*, 1992, APh, 1, 1-9.

[Ahrens et al.(2002)] Ahrens, J., et al. 2002, APh, 16, 345

[Aharmim et al.(2011)] Aharmim B. et al., 2011, ApJ, 728:83

[Alekseev et al.(1987)] Alekseev, E. N., et al., 1987, JETPL, 45, 589

[Ambrosio et al.(2004)] Ambrosio, M., et al. 2004, EPJC, 37, 265

[An et al.(2012)] An, F. P., et al., 2012, PhRvL, 108, 171803

[Antonioli et al.(1991)] P. Antonioli, W. Fulgione, P. Galeotti and L. Panaro, 1991, NIMPA, 309, 569.

[Antonioli et al.(2004)] Antonioli, P., et al., 2004, NJPh, 6, 114

[Bahcall et al.(1995)] Bahcall, J.N., Kamionkowski M. and Sirlin, A., 1995, PhRvD, 51, 6146

[Bigongiari et al.(1990)] Bigongiari A., Fulgione W., Passuello D., Saavedra O., Trinchero G., 1990, NIMPA, 288, 529.

[Bionta et al.(1987)] Bionta, R. M., et al. (IMB collaboration), 1987, PhRvL, 58, 1494

[Colgate and White(1966)] Colgate S.A. and White R.H., 1996, ApJ, 143, 626

[Domogatsky and Zatsepin(1965)] Domogatsky G.V. and Zatsepin G.T., 1965, in 9th ICRC Conf. Proc., Vol.1 1030

[Falk(1978)] Falk S.W., 1978, ApJ, 225, L133

[Fukugita et al.(1988)] Fukugita M., Kohyama Y., Kubodera K.,1988, PhLB, 212, 139

[Fulgione et al.(1996)] Fulgione W., Mengotti-Silva N., and Panaro L., 1996, NIMPA, 368, 512

[Gamow and Shoenberg(1940)] Gamow G. and Shoenberg M., 1940, PhRv, 58, 1117

[Hirata et al.(1987)] Hirata, K., et al., 1987, PhRvL, 58, 1490

[Ikeda et al.(2007)] Ikeda, M., et al., 2007, ApJ, 669, 519

[Imshennik & Ryazhskaya(2004)] Imshennik, V.S. & Ryazhskaya, O., 2004, AstL, 30, 14

[Loredo and Lamb(2002)] T.J. Loredo, D.Q. Lamb, 2002, PhRvD, 65, 063002

[LVD Collaboration(1993-2013)] LVD Collaboration, 1993-2013, in ICRC Conf. Proc.

[Klein and Chevalier(1978)] Klein R.I. and Chevaliere R.A. 1978, ApJL, 223, L109

[Kolbe and Langanke(2001)] Kolbe E., Langanke K., 2001, PhRvC, 63, 025802

[Mikheev and Smirnov(1985)] Mikheev, S. P., & Smirnov, A. Y. 1985, SvJNP, 42, 913

[Nadyozhin(1977)] Nadyozhin D.K., 1977, ApSS, 49, 399 and 1978, 53,131

[Nakazato et al.(2008)] Nakazato K., Sumiyoshi K., Suzuki H. and Yamada S., 2008, PhRvD, 78, 083014

[Novoseltseva et al.(2011)] Novoseltseva, R. V., Boliev, M. M., Volchenko, V. I., et al. 2011, Proc. 32nd ICRC (Beijing), 4, 153

[O'Connor and Ott(2011)] E. OConnor and C. D. Ott, 2011, ApJ, 730, 70

[Pagliaroli, Vissani, Costantini and Ianni(2009)] Pagliaroli G., Vissani F., Costantini M.L., Ianni A., 2009, AsPh, 31, 163

[Pagliaroli, Vissani, Coccia and Fulgione(2009)] Pagliaroli G., Vissani F., Coccia E., Fulgione W. 2009, PhRvL, 103, 031102

[Strumia and Vissani(2010)] Strumia A. and Vissani F., arXiv:hep-ph/0606054v3

[Toivanen et al.(2001)] Toivanen J., Kolbe E., Langanke K., Martinez-Pinedo G. and Vogel P., 2001, NuPhA, 694, 395

[Wolfenstein(1978)] Wolfenstein, L. 1978, PhRvD, 17, 2369

[Woosley & Janka(2005)] Woosley S. and Janka T., 2005, NatPh 1, 147-154

[Zel'dovich and Guseinov(1965)] Zel'dovich, Ya. B., and Guseinov, O. Kh. 1965, SPhD, 10, 524

OPERA

N. Agafonova[1], A. Aleksandrov[2], O. Altinok[3], A. Anokhina[4], S. Aoki[5], A. Ariga[6], T. Ariga[6], D. Autiero[7], A. Badertscher[8], A. Bagulya[9], A. Bendhabi[10], A. Bertolin[11,*], C. Bozza[12], T. Brugière[7], R. Brugnera[13,11], F. Brunet[14], G. Brunetti[15,16,7], S. Buontempo[2], A. Cazes[7], L. Chaussard[7], M. Chernyavskiy[9], V. Chiarella[17], A. Chukanov[18], N. D'Ambrosio[19], F. Dal Corso[11], G. De Lellis[20,2], P. del Amo Sanchez[14], Y. Déclais[7], M. De Serio[21], F. Di Capua[2], A. Di Crescenzo[20,2], D. Di Ferdinando[16], N. Di Marco[22,a], S. Dmitrievski[18], M. Dracos[23], D. Duchesneau[14], S. Dusini[11], T. Dzhatdoev[4], J. Ebert[24], O. Egorov[25], R. Enikeev[1], A. Ereditato[6], L. S. Esposito[8], J. Favier[14], T. Ferber[24], R. A. Fini[21], D. Frekers[26], T. Fukuda[27], A. Garfagnini[13,11], G. Giacomelli[15,16] †, M. Giorgini[15,16,b], C. Göllnitz[24], J. Goldberg[28], D. Golubkov[25], L. Goncharova[9], Y. Gornushkin[18], G. Grella[12], F. Grianti[29,17], A. M. Guler[3], C. Gustavino[39], C. Hagner[24], K. Hamada[27], T. Hara[5], M. Hierholzer[24], A. Hollnagel[24], K. Hoshino[27], M. Ieva[21], H. Ishida[30], K. Jakovcic[31], C. Jollet[23,*], F. Juget[6], M. Kamiscioglu[3], K. Kazuyama[27], S. H. Kim[32,d], M. Kimura[30], N. Kitagawa[27], B. Klicek[31], J. Knuesel[6], K. Kodama[33], M. Komatsu[27], U. Kose[13,11], I. Kreslo[6], H. Kubota[27], C. Lazzaro[8], J. Lenkeit[24], I. Lippi[11], A. Ljubicic[31], A. Longhin[13,11,e], P. Loverre[34,39], G. Lutter[6], A. Malgin[1], G. Mandrioli[16], K. Mannai[10], J. Marteau[7], T. Matsuo[30], V. Matveev[1], N. Mauri[15,16,e], E. Medinaceli[16], F. Meisel[6], A. Meregaglia[23,*], P. Migliozzi[2], S. Mikado[30], S. Miyamoto[27], P. Monacelli[39], K. Morishima[27], U. Moser[6], M. T. Muciaccia[35,21], N. Naganawa[27], T. Naka[27], M. Nakamura[27], T. Nakano[27], D. Naumov[18], V. Nikitina[4], K. Niwa[27], Y. Nonoyama[27], S. Ogawa[30], N. Okateva[9], A. Olchevski[18], M. Paniccia[17], A. Paoloni[17], B. D. Park[32,f], I. G. Park[32], A. Pastore[35,21], L. Patrizi[16], E. Pennacchio[7], H. Pessard[14], K. Pretzl[6], V. Pilipenko[26], C. Pistillo[6], N. Polukhina[9], M. Pozzato[15,16], F. Pupilli[22], R. Rescigno[12], T. Roganova[4], H. Rokujo[5], G. Romano[12], G. Rosa[34,39], I. Rostovtseva[25], A. Rubbia[8], A. Russo[20,2], V. Ryasny[1], O. Ryazhskaya[1], O. Sato[27], Y. Sato[36], A. Schembri[19], W. Schmidt-Parzefall[24], H. Schroeder[37], L. Scotto Lavina[20,2,g], A. Sheshukov[18], H. Shibuya[30], G. Shoziyeov[4], S. Simone[35,21], M. Sioli[15.16], C. Sirignano[13,11], G. Sirri[16], J. S. Song[32], M. Spinetti[17], L. Stanco[11], N. Starkov[9], M. Stipcevic[31], T. Strauss[8,h], P. Strolin[20,2], S. Takahashi[27], M. Tenti[15,16], F. Terranova[17], I. Tezuka[36], V. Tioukov[2], P. Tolun[3], A. Trabelsi[10], T. Tran[7], S. Tufanli[3,h], P. Vilain[38], M. Vladimirov[9], L. Votano[17], J. L. Vuilleumier[6], G. Wilquet[38], B. Wonsak[24] V. Yakushev[1], C. S. Yoon[32], T. Yoshioka[27], J. Yoshida[27], Y. Zaitsev[25], S. Zemskova[18], A. Zghiche[14] and R. Zimmermann[24].

1. INR-Institute for Nuclear Research of the Russian Academy of Sciences, RUS-117312 Moscow, Russia
2. INFN Sezione di Napoli, I-80125 Napoli, Italy
3. METU-Middle East Technical University, TR-06531 Ankara, Turkey
4. SINP MSU-Skobeltsyn Institute of Nuclear Physics of Moscow State University, RUS-119992 Moscow, Russia
5. Kobe University, J-657-8501 Kobe, Japan

† deceased

6. Albert Einstein Center for Fundamental Physics, Laboratory for High Energy Physics (LHEP), University of Bern, CH-3012 Bern, Switzerland
7. IPNL, Université Claude Bernard Lyon 1, CNRS/IN2P3, F-69622 Villeurbanne, France
8. ETH Zurich, Institute for Particle Physics, CH-8093 Zurich, Switzerland
9. LPI-Lebedev Physical Institute of the Russian Academy of Sciences, RUS-117924 Moscow, Russia
10. Unité de Physique Nucléaire et des Hautes Energies (UPNHE), Tunis, Tunisia
11. INFN Sezione di Padova, I-35131 Padova, Italy
12. Dipartimento di Fisica dell'Università di Salerno and INFN, I-84084 Fisciano, Salerno, Italy
13. Dipartimento di Fisica dell'Università di Padova, I-35131 Padova, Italy
14. LAPP, Université de Savoie, CNRS/IN2P3, F-74941 Annecy-le-Vieux, France
15. Dipartimento di Fisica dell'Università di Bologna, I-40127 Bologna, Italy
16. INFN Sezione di Bologna, I-40127 Bologna, Italy
17. INFN - Laboratori Nazionali di Frascati dell'INFN, I-00044 Frascati (Roma), Italy
18. JINR-Joint Institute for Nuclear Research, RUS-141980 Dubna, Russia
19. INFN - Laboratori Nazionali del Gran Sasso, I-67010 Assergi (L'Aquila), Italy
20. Dipartimento di Scienze Fisiche dell'Università Federico II di Napoli, I-80125 Napoli, Italy
21. INFN Sezione di Bari, I-70126 Bari, Italy
22. Dipartimento di Fisica dell'Università dell'Aquila and INFN, I-67100 L'Aquila, Italy
23. IPHC, Université de Strasbourg, CNRS/IN2P3, F-67037 Strasbourg, France
24. Hamburg University, D-22761 Hamburg, Germany
25. ITEP-Institute for Theoretical and Experimental Physics, RUS-117259 Moscow, Russia
26. University of Münster, D-48149 Münster, Germany
27. Nagoya University, J-464-8602 Nagoya, Japan
28. Department of Physics, Technion, IL-32000 Haifa, Israel
29. Università degli Studi di Urbino "Carlo Bo", I-61029 Urbino, Italy
30. Toho University, J-274-8510 Funabashi, Japan
31. IRB-Rudjer Boskovic Institute, HR-10002 Zagreb, Croatia
32. Gyeongsang National University, ROK-900 Gazwa-dong, Jinju 660-300, Korea
33. Aichi University of Education, J-448-8542 Kariya (Aichi-Ken), Japan
34. Dipartimento di Fisica dell'Università di Roma "La Sapienza" and INFN, I-00185 Roma, Italy
35. Dipartimento di Fisica dell'Università di Bari, I-70126 Bari, Italy
36. Utsunomiya University, J-321-8505 Tochigi-Ken, Utsunomiya, Japan
37. Fachbereich Physik der Universität Rostock, D-18051 Rostock, Germany
38. IIHE, Université Libre de Bruxelles, B-1050 Brussels, Belgium
39. INFN Sezione di Roma1, I-00185 Roma, Italy
a. Now at INFN - Laboratori Nazionali del Gran Sasso, I-67010 Assergi (L'Aquila), Italy
b. Now at INAF/IASF, Sezione di Milano, I-20133 Milano, Italy
c. Now at Dipartimento di Fisica dell'Università di Roma "La Sapienza" and INFN, I-00185 Roma, Italy
d. Now at Pusan National University, Geumjeong-Gu Busan 609-735, Korea
e. Now at INFN - Laboratori Nazionali di Frascati dell'INFN, I-00044 Frascati (Roma), Italy
f. Now at Asan Medical Center, 388-1 Pungnap-2 Dong, Songpa-Gu, Seoul 138-736, Korea
g. Now at SUBATECH, CNRS/IN2P3, F-44307 Nantes, France
h. Now at Albert Einstein Center for Fundamental Physics, Laboratory for High Energy Physics (LHEP), University of Bern, CH-3012 Bern, Switzerland

Abstract

The OPERA neutrino detector at the underground Gran Sasso Laboratory (LNGS) was designed to perform the first detection of neutrino oscillations in appearance mode through the study of $\nu_\mu \to \nu_\tau$ oscillations. The apparatus consists of a lead/emulsion-film target complemented by electronic detectors. It is placed in the high-energy long-baseline CERN to LNGS beam (CNGS) 730 km away from the neutrino source. Runs with CNGS neutrinos were successfully conducted in 2008, 2009, 2010, 2011 and 2012 for a total luminosity of 18×10^{19} p.o.t. (*proton on target*). In November 2012 the CNGS run has been stopped and subsequently the beam line has been dismounted. The emulsion analysis has continued during 2013, 2014 and 2015. At the beginning of 2015 the decommissioning of the OPERA detector has started. After a brief description of the beam and of the experimental apparatus we report on the data and related analysis results.

1 Introduction

The solution of the long-standing solar and atmospheric neutrino puzzles has come from the hypothesis of neutrino oscillations. This implies that neutrinos have non vanishing and non-degenerate mass eigenstates, and that their flavor eigenstates involved in weak interaction processes are a superposition of the mass eigenstates. Several experiments carried on in the last decades with solar and reactor neutrinos, as well as with atmospheric and accelerator neutrinos, contributed to build-up our present understanding of neutrino mixing. Atmospheric neutrino oscillations have been studied mainly by the Kamiokande, MACRO, Super-Kamiokande and SOUDAN2 experiments. Long baseline experiments with accelerator neutrinos (K2K and MINOS) confirmed the oscillation scenario first pointed out by the Super-Kamiokande experiment supporting the $\nu_\mu \to \nu_\tau$ oscillation channel for atmospheric neutrinos, while the CHOOZ and Palo Verde reactor experiments excluded the $\nu_\mu \to \nu_e$ channel as the dominant one. However, the direct appearance of a different neutrino flavor is still an important open issue. This is the main goal of the OPERA experiment [1] that uses the long baseline (L=730 km) CNGS neutrino beam from CERN to LNGS. The challenge of the experiment is to measure the appearance of ν_τ from ν_μ oscillations in an almost pure muon-neutrino beam. This requires the detection of the short-lived τ lepton ($c\tau = 87.11$ μm) produced in the charged-current interaction of a ν_τ. This sets two conflicting requirements: a large target mass needed to have sufficient statistics and an extremely high accuracy detector technique to observe the short-lived τ lepton. The τ is identified by the detection of its characteristic decay topologies either in one prong (electron, muon or hadron) or in three prongs. The τ track is measured with a large-mass active target made of 1 mm thick lead plates (target mass and absorber material) inter-spaced with thin nuclear emulsion films (high-accuracy tracking devices). This detector is historically called Emulsion Cloud Chamber (ECC). Among past applications it was successfully used in the DONUT experiment for the first direct observation of the ν_τ.

The OPERA detector [2] is made of two identical Super Modules (SM) each consisting of a target section of about 625 tons made of lead/emulsion-film ECC modules (hereafter called "bricks"), of a scintillator tracker detector (TT) needed to trigger the read-out and pre-localize neutrino interactions within the target, and of a muon spectrometer (Figure 1). A single SM has longitudinal dimensions of about 10 m. The detector is equipped with an automatic machine (the Brick Manipulator System, BMS) that allows the on-line removal of bricks from the detector. Ancillary facilities exist for the handling, the development and the scanning of the emulsion films. The film scanning is performed with two independent types of scanning microscopes: the European Scanning System (ESS) in Europe and the S-UTS in Japan.

A target brick consists of 56 lead plates of 1 mm thickness interleaved with 57 emulsion films [3]. The plate material is a lead alloy with a small calcium content to improve its mechanical properties [4]. The transverse dimensions of a brick are 12.8 $\times$ 10.2 cm^2 and the thickness along the beam direction is 7.9 cm (about 10 radiation lengths). The construction of more than 150,000 bricks for the neutrino target has been accomplished by an automatic machine, the Brick Assembly Machine (BAM) operating underground in order to minimize the number of background tracks from cosmic-rays and environmental radiation. The bricks have been inserted in the detector target by the BMS and housed in a light support structure placed between consecutive TT walls. The support structure has been designed with the requirement of minimizing the material along the neutrino beam direction in order to reduce to the 0.1% level the number of interactions in regions not instrumented with emulsion films or scintillators. In order to reduce the emulsion scanning load the use of Changeable Sheets (CS) [5], successfully applied in the CHORUS experiment, was extended to OPERA. Tightly packed doublets of

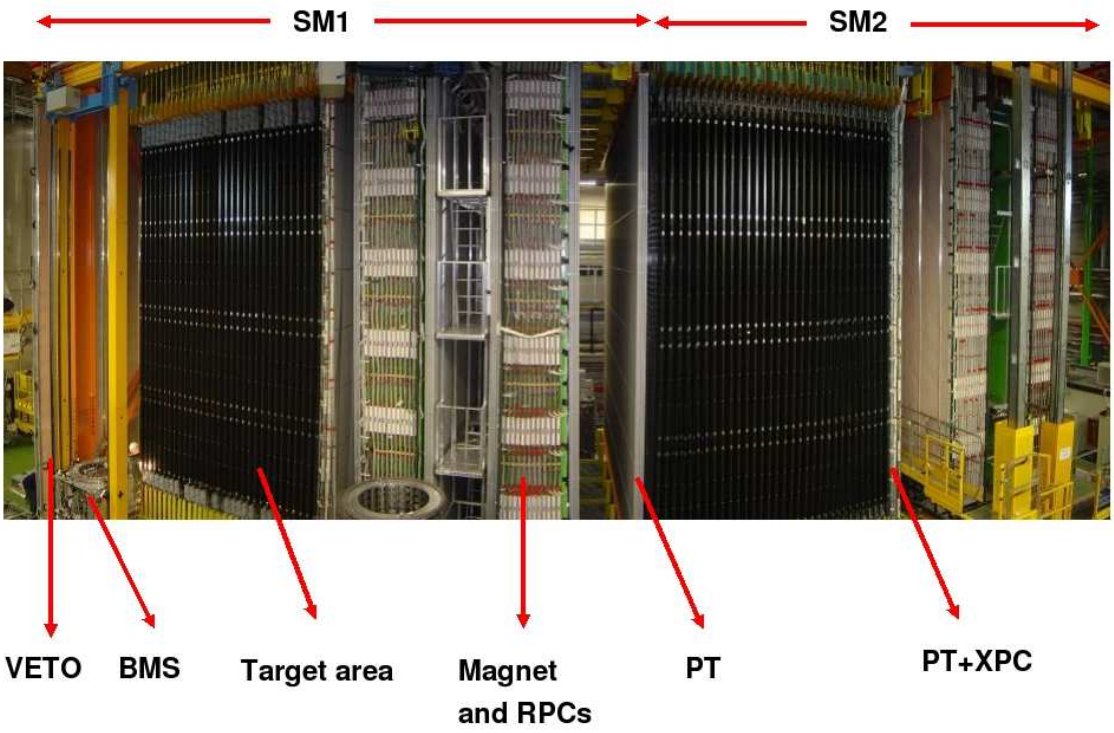

Figure 1: Fish-eye view of the OPERA detector. The upper horizontal lines indicate the position of the two identical supermodules (SM1 and SM2). The "target area" is made of walls filled with ECC bricks interleaved with planes of plastic scintillators (TT). Arrows also show the position of the VETO planes, the drift tubes (PT), the RPC with diagonal strips (XPC), the magnets and the RPC installed between the magnet iron slabs. The Brick Manipulator System (BMS) is also visible. See [2] for more details.

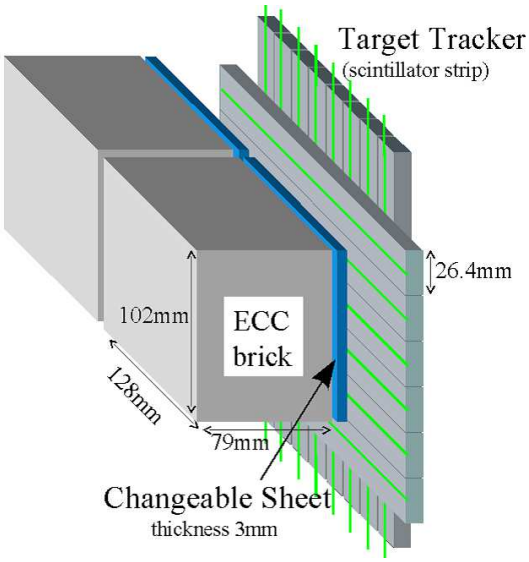

Figure 2: Schematic view of two bricks with their Changeable Sheet and target tracker planes.

emulsion films are attached to the downstream face of each brick and can be removed without opening the brick. Charged particles from a neutrino interaction in the brick cross the CS and produce signals in the TT scintillators. Following these signals the brick is extracted and the CS developed underground and analyzed in the scanning facilities at LNGS and in Nagoya. The information of the CS is used for a precise prediction of the position of the tracks in the most downstream films of the brick, hence guiding the so-called *scan-back* vertex finding procedure.

The brick, CS and TT layout [5] is schematically shown in Figure 2.

2 Evidence of $\nu_\mu \to \nu_\tau$ appearance in the CNGS beam with direct τ detection

The CNGS neutrino beam was designed and optimized for the study of $\nu_\mu \to \nu_\tau$ oscillations in appearance mode, by maximizing the number of charged current (CC) ν_τ interactions at the LNGS site. For a detailed description of the CNGS beam we refer to [2].

After the beam commissioning run in 2006, the CNGS run started on September 2007 at rather low intensity. The first event inside the OPERA target was observed on October 3^{rd}.Longer runs took place in 2008, 2009, 2010, 2011 and 2012. On December 2012 the last CNGS neutrinos were delivered to LNGS. A long shutdown took place at CERN in 2013 and 2014 for the upgrade of LHC, and the CNGS beam has been decommissioned. The decommissioning of the OPERA detector has started at the beginning of 2015.

A first ν_τ interaction candidate with a one-prong topology was found in 2010 [6].

A second ν_τ interaction candidate was found in 2011 with a three-prong topology and presented in 2012 [7] (Fig.4).

A third ν_τ interaction candidate was found in 2012 in the muonic decay channel and officially presented in 2013 [8] (Fig.5).

A fourth ν_τ interaction candidate was found in 2014 with a one prong decay topology [10] (Fig.6).

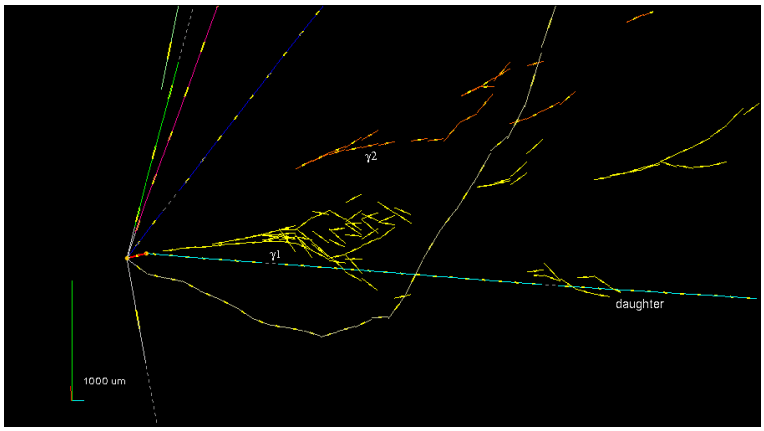

Figure 3: The first OPERA tau candidate (see [6] for details).

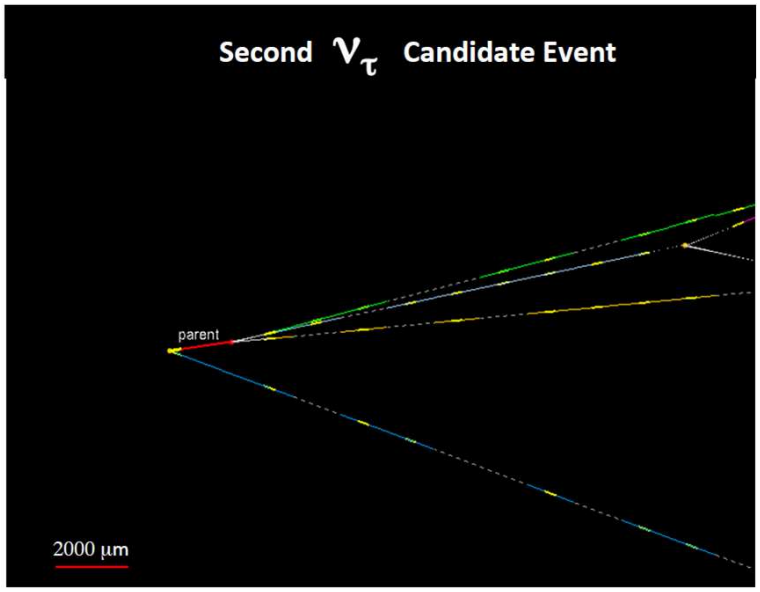

Figure 4: The second OPERA tau candidate; in this candidate event the tau decays into three prongs (see [7] for details).

A fifth ν_τ interaction candidate was found in 2015 with a one prong decay topology [13] (Fig.7).

The five candidate events found, together with a conservative background estimation, mostly due to charm candidates with undetected muon, give a significance of 5.1 sigma for the direct detection of $\nu_\mu \to \nu_\tau$ oscillations [13] .

3 Status of the event analysis and plan for 2015

(Fig.8) shows the history of the data analysis as a function of time, from the beginning of data taking (2008 run) up to now. The upmost line shows the number of events reconstructed in the target with the Target Tracker detectors (TT), then the number of events with at least

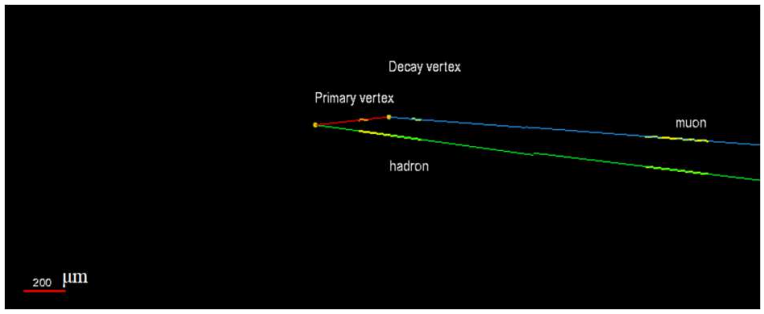

Figure 5: The third OPERA tau candidate; in this candidate event the short track is seen to decay leptonically into one muon which stops in the spectrometer.

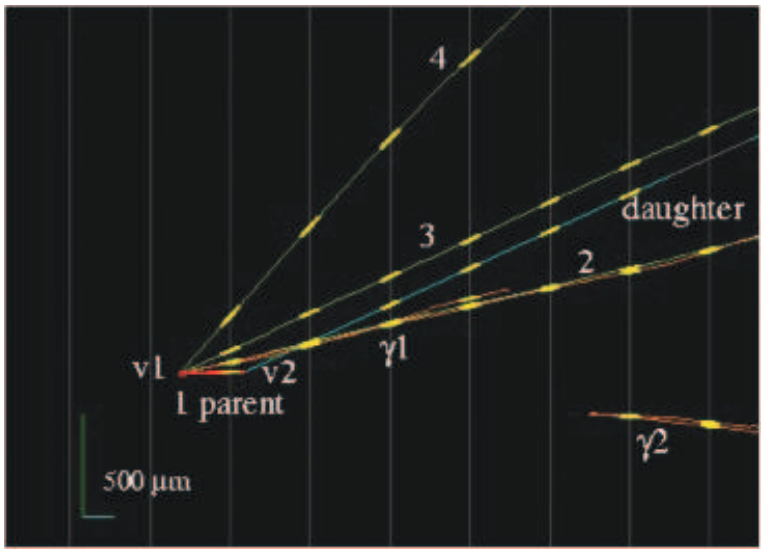

Figure 6: The fourth OPERA tau candidate event. In this event the short parent track is seen to decay into a daughter particle which is consistent to be a hadron, from momentum/range measurements. None of the tracks originating from the primary vertex is consistent with being a muon.

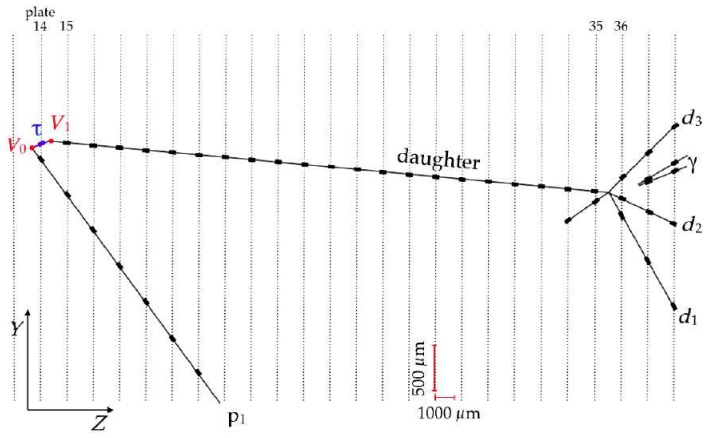

Figure 7: The fifth OPERA tau candidate event. In this event the short parent track decays into a daughter particle which is consistent to be a hadron, since it interacts in the same brick . The other particle, originating from the primary vertex (V0), is also consistent to be a hadron since it is seen to interact in the downstream brick

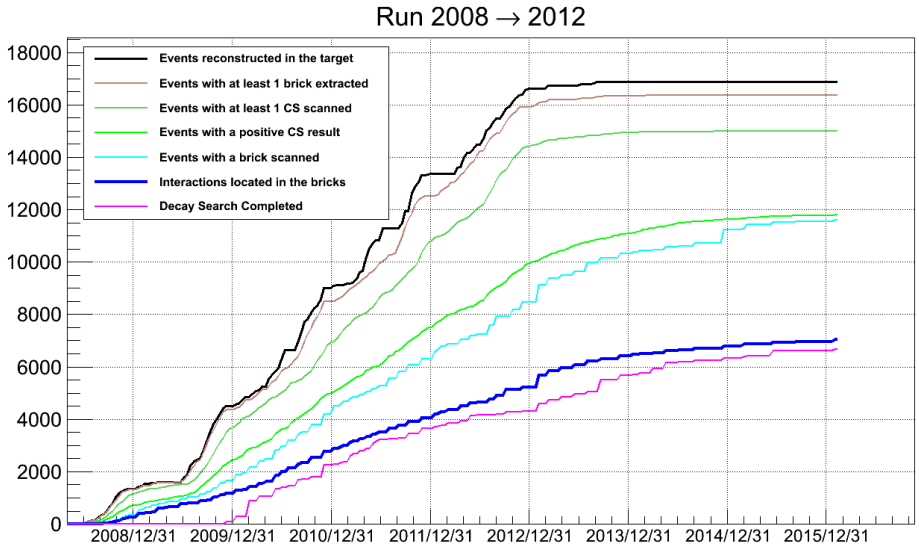

Figure 8: OPERA data analysis as function of time. The upmost line shows the number of events reconstructed in the target, then the number of events with at least one extracted brick is shown and the number of events with at least one CS pair scanned. The next two curves indicate the number of events with positive signal found in the CS and the number of events with at least one brick scanned. The lowest two lines indicate the number of events with the neutrino interaction found in the brick and the number of events whith the decay search completed.

one brick extracted is shown, and subsequently the number of events with at least one pair of CS scanned. The next line shows the number of events with positive result in the CS and subsequently the number of events with at least one brick scanned is shown. The last two lines show the number of interactions found and measured in the bricks and the number of events with the decay search completed. The total number of neutrino interactions reconstructed in the target by the electronic detectors is 16872, while the number of located interactions in the bricks is 7041.

The scanning and analysis of the extracted bricks, will continue during 2016 in order to complete the search for ν_τ events collected in the last years and not yet found. All the most probable event bricks and the second probable bricks have been measured and analyzed. During the year 2016 the remaining third and fourth most probable bricks (for those events which have not been confirmed in the first and second brick) will be developed and analyzed.

References and list of publications

[1] M. Guler *et al.*, OPERA proposal, CERN/SPSC 2000-028, SPSC/P318, LNGS P25/2000.

[2] R. Acquafredda *et al.* [OPERA Collaboration] "The OPERA experiment in the CERN to Gran Sasso neutrino beam", JINST 4:P04018,2009.

[3] T. Nakamura *et al.*, "The Opera Film: New Nuclear Emulsion For Large-Scale, High-Precision Experiments," Nucl. Instrum. Meth. A **556** (2006) 80.

[4] A. Anokhina *et al.* [OPERA Collaboration], "Study of the effects induced by lead on the emulsion films of the OPERA experiment,"

JINST **3** P07002 (2008).

[5] A. Anokhina *et al.* [OPERA Collaboration], "Emulsion sheet doublets as interface trackers for the OPERA experiment," JINST **3** (2008) P07005

[6] N. Agafonova *et al.* [OPERA Collaboration], "Observation of a first ν_τ candidate in the OPERA experiment in the CNGS beam," Phys. Lett. *B691* , 138 (2010).

[7] N. Agafonova *et al.* [OPERA Collaboration], New result on $\nu_\mu \to \nu_\tau$ appearance with the OPERA Experiment in the CNGS beam." JHEP11 *1301* , 036 (2013)

[8] N. Agafonova *et al.*[OPERA Collaboration],"Evidence for $\nu_\mu \to \nu_\tau$ appearance in the CNGS neutrino beam with the OPERA experiment." Phys.Rew. D 89 051102(R),(2014)

[9] N. Agafonova *et al.* [OPERA Collaboration]"Measurement of TeV atmospheric muon charge ratio with the full OPERA data." Eur.Phys. J. C 74, 2933 (2014)

[10] N. Agafonova *et al.*[OPERA Collaboration],"Observation of tau neutrino appearance in the CNGS beam with the OPERA experiment." PTEP 2014, no. 10, 101C01 (2014)

[11] N. Agafonova *et al.*[OPERA Collaboration],"Procedure for short-lived particle detection in the OPERA experiment and its application to charm decays

Eur.Phys.J.C 74, no. 8,2986 (2014)

[12] N. Agafonova *et al.*[OPERA Collaboration],"Limits on muon neutrino to tau neutrino oscillations induced by a sterile neutrino state, obtained by OPERA at the CNGS beam." JHEP *06* , 069 (2015)

[13] N. Agafonova *et al.*[OPERA Collaboration],"Discovery of ν_τ appearance in the CNGS neutrino beam with the OPERA experiment."Phys. Rev.Lett. *115* , 121802 (2015)

THEORY GROUP

The LNGS theory group is organized in five working subgroups, local nodes of the INFN research network: AAE, High-energy astrophysics; INDARK, Inflation, dark matter and the large-scale structure of the universe; NPQCD, Non-Perturbative quantum chromodynamics; NUMAT, Nuclear matter and compact stellar objects; TASP, Theoretical astroparticle physics. The local coordinators are indicated in bold face in the members list.

There is a long-standing tradition of collaboration between the LNGS theory group and several experimental groups. In this report, we briefly describe the activities of the theory group in 2015.

Members of the group: A. Addazi, R. Aloisio, L. Ambrogi, Z. Berezhiani, V. Berezinsky, R. Biondi, P. Blasi, A. Breccione Mattucci, S. Carignano, M. D'Angelo, G. Di Carlo, G. Di Panfilo, D. Ejlli, A.T. Esmaili, P. Giammaria, A. Mammarella, **M. Mannarelli**, G. Morlino, A. Palladino, G. Pagliaroli, A. Parisi, L. Pilo, S. Recchia, F. Tonelli, F.L. Villante, F. Vissani.

More information can be found at: `http://theory.lngs.infn.it/index.html`

NPQCD

Member: **G. Di Carlo**.
– Collaboration with V. Azcoiti, E. Follana (Zaragoza University) and A. Vaquero (Zaragoza University and Cyprus Inst.).

Scientific work

Our main interest is the study of gauge theories with sign problem using Lattice QCD simulations.

During 2015 we have worked on the spectral flow with the Adams' operator [1] and we started an extensive simulation of the Schwinger's model with an imaginary theta term, to study the (possible) disappearance of the (first order) phase transition at $\theta = \pi$ for small enough values of the fermionic mass. Preliminary results are promising and the full simulation and analysis will continue through 2016. We are also starting the study of same system for quenched QCD, to investigate the theta dependence of the model, including finite temperature effects and using various definitions of the topological charge.

AAE

Members: A. Addazi, **Z. Berezhiani**, R. Biondi, D. Ejlli

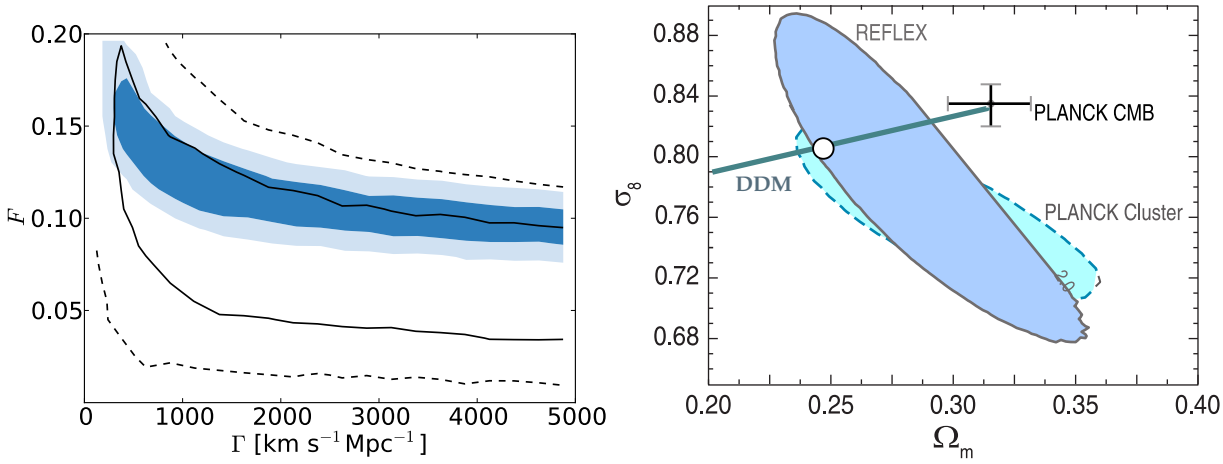

Figure 1: Left panel: one and two sigma likelihood contours for our model parameters. Solid and dashed lines correspond to a dataset consisting of JLA sample of SN Ia and HST measurements of h, on top of the best fit Planck model parameters. Addition of Planck cluster data results in much narrower shaded area. Right panel: Ω_m and σ_8 derived from cluster counts and from CMB. Line marked DDM shows trend of these parameters when F and Γ are varied in our model. White circle represents a model with $F = 0.1$ and $\Gamma = 2000$ as an example.

– Collaborations with A. D. Dolgov (Univ. Ferrara), I. Tkachev (INR Moscow), A. Vainshtein (ITP, Minneapolis, USA), Yu. Kamyshkov (Univ. Tennessee, USA), R. Bernabei, P. Belli, A. Incichitti, M. Bianchi (Univ. Roma II), R. Cerulli (LNGS), S. Capozziello, G. Esposito (Univ. Naples)

Scientific work

The research activity has been mainly focused on the following topics and the following results were obtained:

- Decaying dark matter and its tests with the CMB and BAO data: It was shown that emerging tension between the direct astronomical measurements at low redshifts and cosmological parameters deduced from the Planck measurements of the CMB anisotropies can be alleviated if the dark matter consists of two fractions, a stable dominant part and a smaller unstable fraction, F, with decay rate Γ. At the recombination $F \sim 5 - 10$ per cent if it has decayed by now, i.e. Γ is larger than the present Hubble constant, see Fig. 1. In this way, in the decaying dark matter model the Hubble constant $h \simeq 0.70 \pm 0.01$ is obtained from the Planck and BAO data, which mitigates between the Planck result $h = 0.6727 \pm 0.0066$ for standard ΛCDM model and $h = 0.738 \pm 0.024$ from the direct measurements by the Hubble Space Telescope [2].

- Direct detection of dark matter particles: The long-standing annual modulation effect measured by the DAMA Collaboration is examined in the context of asymmetric mirror dark matter, assuming that dark atoms interact with target nuclei in the detector via kinetic mixing $\frac{\epsilon}{2} F^{\mu\nu} F'_{\mu\nu}$ between mirror and ordinary photons, see the left panel of Fig. 2.

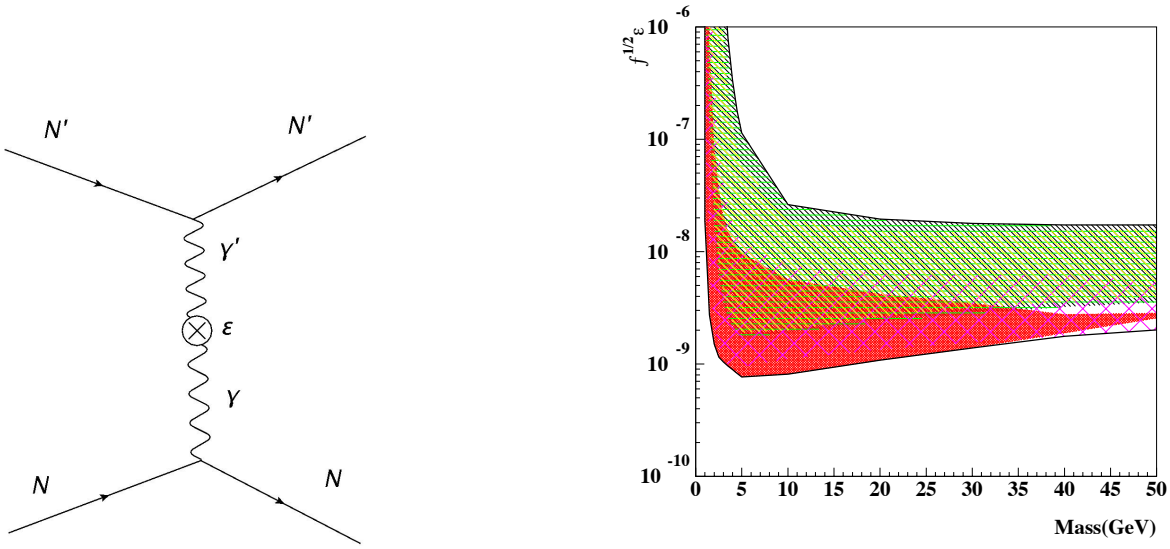

Figure 2: Left panel: Mirror Nucleus-Nucleus Rutherford-like interaction through the photon-mirror photon kinetic mixing portal. Right panel: Allowed regions for the $\sqrt{f}\epsilon$ parameter, f being the dark matter density in units of 0.5 GeV/cm63, as function of mirror nucleus mass $M_{A'}$, obtained by marginalizing all the models for each considered scenario. These allowed intervals identify the $\sqrt{f}\epsilon$ values corresponding to C.L. larger than 5σ from the *null hypothesis*, that is $\sqrt{f}\epsilon = 0$. The five scenarios defined in the text can be recognized on the basis of different hatching of the allowed regions; the black line is the overall boundary.

In the right panel of Fig. 2 we report the relevant ranges for the kinetic mixing parameter obtained taking into account various existing uncertainties in nuclear and particle physics quantities as well as characteristic density and velocity distributions of dark matter in different halo models [3].

- Supersymmetric Grand Unification at the LHC: The magic couple of SUSY and GUT still appears the most elegant and predictive physics concept beyond the Standard Model. Since up to now LHC found no evidence for supersymmetric particles it becomes of particular relevance to determine an upper bound of the energy scale they have to show up. In particular, we have analyzed a generic SUSY-GUT model assuming one step unification like in SU(5), and adopting naturalness principles, we have obtained general bounds on the mass spectrum of SUSY particles. We claim that if a SUSY gauge coupling unification takes place, the lightest gluino or Higgsino cannot have a mass larger than about 20 TeV. Such a limit is of interest for planning new accelerator machines [4].

INDARK

Members: A. Breccione Mattucci, **L. Pilo** and F.L. Villante.
– Collaboration with G. Ballesteros (CERN and IPh CEA Saclay) M. Crisostomi (ICG-Portsmouth)

D. Comelli (INFN-Ferrara) K. Koyama (ICG-Portsmouth) F. Nesti, (Boskovic Institue-Zagreb)
M. Pinsonneault (Ohio State Univ.) G. Tasinato(Swansea Univ.)

Scientific work

The research activity has been focused on the following topics:

- Study of the branches of Lorentz invariant massive gravity [25]. The basic building block for Lorentz-invariant and ghost-free massive gravity is the square root of the combination $g^{-1}\eta$, where g^{-1} is the inverse of the physical metric and η is a reference metric. Since the square root of a matrix is not uniquely defined, it is possible to have physically inequivalent potentials corresponding to different branches. It can be shown that around the Minkowski background, the only perturbatively well-defined branch is the potential proposed by de Rham, Gabadadze and Tolley (dRGT). On the other hand, if Lorentz symmetry is broken spontaneously, other potentials exist with a standard perturbative expansion. One can show this explicitly building new Lorentz-invariant, ghost-free massive gravity potentials for theories that in the background preserve rotational invariance but break Lorentz boosts.

- Alternative matter coupling in bigravity [26, 27]. We have studied cosmology in the bigravity formulation of the dRGT model where matter couples to both metrics. At linear order in perturbation theory two mass scales emerge: an hard one from the dRGT potential, and an environmental dependent one from the coupling of bigravity with matter. At early time, the dynamics is dictated by the second mass scale which is of order of the Hubble scale. The set of gauge invariant perturbations that couples to matter follow closely the same behavior as in GR . The remaining perturbations show no issue in the scalar sector, while problems arise in the tensor and vector sectors. During radiation domination, a tensor mode grows power-like at super-horizon scales. More dangerously, the only propagating vector mode features an exponential instability on sub-horizon scales. We discuss the consequences of such instabilities and speculate on possible ways to deal with them.

- The effective field theory that describes the low-energy physics of self-gravitating media is formulated in terms of four derivatively coupled scalar fields that can be identified with the internal comoving coordinates of the medium [28]. Imposing SO(3) internal spatial invariance, the theory describes supersolids. Stronger symmetry requirements lead to superfluids, solids and perfect fluids, at lowest order in derivatives. In the unitary gauge, massive gravity emerges, being thus the result of a continuous medium propagating in spacetime. Our results can be used to explore systematically the effects and signatures of modifying gravity consistently at large distances. The dark sector is then described as a self-gravitating medium with dynamical and thermodynamic properties dictated by internal symmetries. These results indicate that the divide between dark energy and modified gravity, at large distance scales, is simply a gauge choice.

- Phenomenology of kev-sterile neutrinos as potential dark matter candidates. Determination of the galaxy structure in scenarios with fermionic warm dark matter. Limit on the mass of kev-sterile neutrinos from dwarf spheroidal galaxies.

TASP

Members: R. Aloisio, V. Berezinsky, P. Blasi, M. D'Angelo, A.T. Esmaili, P. Giammaria, G. Morlino, A. Palladino, S. Recchia, **F.L. Villante**, F. Vissani.
– Collaboration with P.D. Serpico (Laboratoire de Physique Theorique d'Annecy-le-Vieux, Francia), A. Serenelli (IEEC-CSIC, Spagna), F. Aharonian (Dublin Institute for Advanced Studies, Irlanda), V. Dokuchaev (INR, Moscow), Yu. Eroshenko (INR, Moscow)

Scientific work

The research activity has been focused on the following topics:

- Neutrino physics and astronomy: Studies of the possible sources and of the characteristic signatures of a cosmic population of very high energy neutrinos; Analysis and interpretation of the high-energy IceCUBE data; Phenomenology of kev-sterile neutrinos as potential dark matter candidates. Determination of the galaxy structure in scenarios with fermionic warm dark matter; Study of the spectrum of supernova neutrinos in ultra-pure scintillators, in particular, in connection to the possibility to observe neutral current events; Study of new expectations and uncertainties on neutrinoless double beta decay, in particular in view of the renormalisation of the couplings of the nucleons in nuclear medium; Quantitative study of the solar composition problem. Analysis of the role of a future CNO solar neutrino measurement. Limits to the properties of non standard weakly interacting particles from solar data global fits.
- Cosmic ray physics: Study of the propagation of very high energy cosmic ray in extragalactic environment; comparison between different numerical simulations; Analysis and interpretation of Pierre Auger Observatory experimental data (energy spectrum and observables related to chemical composition; Non linear effects in cosmic ray physics; Effects of intergalactic magnetic fields in the physics of ultra high energy cosmic rays; Dark matter models and indirect detection of dark matter.

NUMAT

Members: S. Carignano, M. Mannarelli, **G. Pagliaroli**, A. Parisi, F. Tonelli and F. Vissani.
– Collaboration with L. Pilo, F.L. Villante, A. Palladino, F. Tonelli, A. Boeltzig, S. Marcocci, M. Viel and S. Dell'Oro, R. Casalbuoni (University of Florence and INFN), R. Gatto (University of Geneve).

Scientific work

The scientific achievements concern several aspects of neutrino physics and compact stars.

- Astrophysical neutrinos: We deeply investigated the potential of High Energy Neutrinos recently observed by the IceCube detector. In particular, we analyzed the HESE events observed by IceCube, aiming to probe the initial flavor of cosmic neutrinos. We include

for the first time the passing muons observed by IceCube in the analysis. Our result corroborates the hypotheses that cosmic neutrinos have been seen and their flavor matches expectations derived from the neutrino oscillations [49, 32]. Moreover, we used these data to constrain non-radiative neutrinos decay channels both in normal and inverted mass hierarchy [37]

- Properties of neutrinos: We investigated the potential relevance of the analysis of Palanque-Delabrouille et al. [JCAP 02 (2015) 045] to the neutrinoless double beta decay search. In this analysis we indicate that the allowed values for the Majorana effective mass turn out to be < 75 meV at 3σ C.L. with a tremendous impact on the possibility of detecting such a signal [40].

- Properties of ultra-dense matter: We analyzed various aspects of pion and kaon condensation in the framework of chiral perturbation theory. Considering a system at vanishing temperature and varying the isospin chemical potential and the strange quark chemical potential we reproduce known results about the phase transition to the pion condensation phase and to the kaon condensation phase. However, we obtain mesonic mixings and masses in the condensed phases that are in disagreement with the results reported in previous works [50].

- Within a large collaboration involving gravitational waves detectors, Ligo and Virgo, and neutrinos detectors, LVD, Borexino and IceCube, we started developing techniques and strategies for a joint analysis of Neutrinos and Gravitational Waves emitted during core collapse Supernovae. This is the Phase I of a structured proposal submitted and accepted by several detectors (neutrino detectors and GW detectors) to increase the detection probability for these complex astrophysical events.

Conferences, seminars and other activities

- ETH Miniworkshop on Dark Matter, 27 Feb. 2015, ETH Zurich, Switzerland (Z. Berezhiani invited Lecture)

- IFAAE2015: "Incontri di Fisica delle Alte Energie 2015", 8-10 Apr. 2015, Roma Tor Vergata, Italy (R. Biondi talk)

- SW9: Int. Workshop "Hot Topics in Modern Cosmology", 27 Apr -1 May 2015, Cargese, France (Z. Berezhiani plenary talk and R. Biondi talk)

- ACFC 2015: WE-Heraeus-Seminar on Astrophysics, Clocks and Fundamental Constants (Z. Berezhiani invited Lecture)

- NG14: XIV Marcel Grossman Meeting, 12-18 July 2015, La Sapienza, Rome (Z. Berezhiani invited talk at DM2 Session and A. Addazi talk)

- Int. Workshop "Crossroads of Neutrino Physics", 20 July-14 Aug. 2015, MITP, Mainz, Germany (Z. Berezhiani talk)

- KSM 2015: 2nd Karl Schwarzschild Meeting on Gravitational Physics 20-24 July 2015, Frankfurt, Germany (A. Addazi talk)

- 3rd NNbar at ESS Workshop, 27-28 Aug. 2015, Chalmers Univ., Gothenburg, Sweden (Z. Berezhiani invited talk)
- CFA Lectures "Hot Topics in Astroparticle Physics", 14-25 Sept. 2015, LNGS, Assergi, Italy (Z. Berezhiani invited talk, A. Addazi talk and R. Biondi talk)
- Int. Conference "Challenges in Contemporary Elementary Particle Physics and Quantum Field Theory" 30 Oct.-1 Nov. 2015, Tbilisi, Georgia (Z. Berezhiani invited talk)
- Extented theories of gravity, 2-20 March 2015, Nordita, Stockolm. (L. Pilo invited talk)
- Hot topics in Modern Cosmology, 27 April-1 May 2015, Cargese. (L. Pilo talk)
- 14th Marcel Grossmann meeting, 12-18 July 2015, Rome. (L. Pilo talk)
- Gravity @ all scales, 24-28 August 2015,Nottingham. (L. Pilo invited talk)
- Split School of High Energy Physics, 14-18 September 2015, Split. (L. Pilo invited talk)
- VIII Incontro di Astrofisica Nucleare Teorica e Sperimentale (GIANTS 2015), 28-30 April 2015, Padova, Italy. (F. Villante invited talk).
- 17th Lomonosov Conference on Elementary Particle Physics, 20-26 August 2015, Moscow, Russia (F. Villante invited review talk).
- Neutrinos and Dark Matter in Nuclear Physics (nDM 2015) June 1-5, 2015, Jyvaskyla, Finland. (F. Villante invited talk).
- Nuclear Astrophysics Virtual Institute (NAVI) Physics Days 26-27 February 2015, GSI, Darmstadt, Germany. (F. Villante invited talk).
- Next Generation Nucleon Decay and Neutrino Detector (NNN15)", 28-31 October 2015, Stony Brook University, USA. (F. Villante invited talk).
- Searching for the Sources of Galactic Cosmic Rays (SuGAR 2015), 21-23 Jan 2015. Geneva, Switzerland. (P. Blasi invited talk).
- Searching for the Sources of Galactic Cosmic Rays (SuGAR 2015), 21-23 Jan 2015. Geneva, Switzerland. (M. D'Angelo talk).
- 16th International Workshop on Neutrino Telescopes (Neutel 2015), 02-06 Mar 2015. Venice, Italy (F. Vissani invited talk)
- 16th International Workshop on Neutrino Telescopes (Neutel 2015), 02-06 Mar 2015. Venice, Italy (S. Dell'Oro and S.Marcocci and F. Vissani poster)
- Neutrino Oscillation Workshop (NOW 2014), 07-14 Sep 2014. Conca Specchiulla, Otranto, Lecce, Italy (R.Aloisio invited talk)
- 14th International Conference on Topics in Astroparticle and Underground Physics (TAUP 2015) 07-11 Sep 2015. Torino, Italy (G. Pagliaroli talk)
- 16th Workshop on Statistical Mechanics and Nonperturbative Field Theory (SM&FT 2015) 09-11 Dec 2015. Bari, Italy (M.Mannarelli talk)

- Colloquium at Lecce, Universitá del Salento (F. Vissani)
- Lectures at Inst. Balseiro, Bariloche for "Programa Maldacena de Profesores Invitados" (F. Vissani)
- Lectures on Neutrino Physics for the PhD of Milan U. (F. Vissani)
- 7th Very Large Volume Neutrino Telescope Workshop (VLVnT 2015) 14-16 Sep 2015. Rome, Italy (F. Vissani talk)
- Seminar in the conference in memory of Professor Giorgio Giacomelli, Bologna (F. Vissani)
- Lectures on Neutrino Physics for the PhD of GSSI (F. Vissani)

Activity in INFN and International organizations

R. Aloisio is a member of the GSSI Scientific Board.

G. Pagliaroli and A. Parisi organized the "Lectures on Magnetar" within the Center for Astroparticle Physics (CFA).

G. Pagliaroli, Z, Berezhiani and R. Biondi organized the series of lectures "Hot Topics in Astroparticle Physics" within the CFA.

A. Mammarella and G. Pagliaroli organized the series "Lectures on double beta decay" within the CFA.

V. Berezinsky is a member of Council "Cosmic Ray Research" (Russia), a member of Int. Advisory Board of JEM-EUSO, a member of Int. Scientific Advisory Committee of Gigaton Volume Detector of High Energy Neutrinos.

M. Mannarelli and G. Pagliaroli have been coordinating the activities of the CFA.

L. Pilo is member of the Doctorate Collegium of the Physics Dept. and of the Doctorate Commission, University of L'Aquila.

F.L. Villante has been a member of the Scientific Board of the CFA.

F. Vissani is the physics area coordinator and Chair of the GSSI Astroparticle Physics PhD Committee, co-organizer of the LNGS seminars, observer in Comm.II on behalf of Comm.IV, referee for the INFN National Permanent Committees II on non-accelerator physics; member of the scientific committee for the ICRANet-INFN agreement; associate editor of European Physical Journal C.

Publications in journals

[1] V. Azcoiti, G. Di Carlo, E. Follana, and A. Vaquero, "Topological Index Theorem on the Lattice through the Spectral Flow of Staggered Fermions," *Phys. Lett.*, vol. B744, pp. 303–308, 2015.

[2] Z. Berezhiani, A. D. Dolgov, and I. I. Tkachev, "Reconciling Planck results with low redshift astronomical measurements," *Phys. Rev.*, vol. D92, no. 6, p. 061303, 2015.

[3] A. Addazi, Z. Berezhiani, R. Bernabei, P. Belli, F. Cappella, R. Cerulli, and A. Incicchitti, "DAMA annual modulation effect and asymmetric mirror matter," *Eur. Phys. J.*, vol. C75, no. 8, p. 400, 2015.

[4] Z. Berezhiani, M. Chianese, G. Miele, and S. Morisi, "Chances for SUSY-GUT in the LHC Epoch," *JHEP*, vol. 08, p. 083, 2015.

[5] Z. Berezhiani, "Shadow dark matter, sterile neutrinos and neutrino events at IceCube," *Nucl. Part. Phys. Proc.*, vol. 265-266, pp. 303–306, 2015.

[6] A. Addazi and S. Capozziello, "External stability for Spherically Symmetric Solutions in Lorentz Breaking Massive Gravity," *Int. J. Theor. Phys.*, vol. 54, no. 6, pp. 1818–1829, 2015.

[7] A. Addazi, "'Exotic vector-like pair' of color-triplet scalars," *JHEP*, vol. 04, p. 153, 2015.

[8] A. Addazi and M. Bianchi, "Un-oriented Quiver Theories for Majorana Neutrons," *JHEP*, vol. 07, p. 144, 2015.

[9] A. Addazi and G. Esposito, "Nonlocal quantum field theory without acausality and nonunitarity at quantum level: is SUSY the key?," *Int. J. Mod. Phys.*, vol. A30, no. 15, p. 1550103, 2015.

[10] A. Addazi and M. Bianchi, "Neutron Majorana mass from Exotic Instantons in a Pati-Salam model," *JHEP*, vol. 06, p. 012, 2015.

[11] A. Addazi, "Chaotization Inside Quantum Black Holes," *Electron. J. Theor. Phys.*, vol. 12, no. 34, pp. 89–106, 2015.

[12] A. Addazi, "Neutron-Antineutron oscillation as a test of a New Interaction," *Nuovo Cim.*, vol. C38, no. 1, p. 21, 2015.

[13] R. Biondi, "Dark Matter and IceCube Neutrinos," *Nuovo Cim.*, vol. C38, no. 1, p. 31, 2015.

[14] D. Ejlli, "Axion production and CMB spectral distortion in cosmological tangled magnetic field," *Eur. Phys. J.*, vol. C75, no. 8, p. 397, 2015.

[15] Z. Berezhiani and A. Vainshtein, "Neutron-Antineutron Oscillation as a Signal of CP Violation," 2015.

[16] Z. Berezhiani, "Neutron-antineutron Oscillation and Baryonic Majoron: Low Scale Spontaneous Baryon Violation," 2015.

[17] A. Addazi, "More about Neutron Majorana mass from Exotic Instantons: an alternative mechanism in Low-Scale String theory," 2015.

[18] A. Addazi, "Dynamical R-parity violations from exotic instantons," 2015.

[19] A. Addazi, "Neutron-antineutron transition as a test-bed for dynamical CPT violations," 2015.

[20] A. Addazi, "Unitarization and Causalization of Non-local quantum field theories by Classicalization," 2015.

[21] A. Addazi, "Direct generation of a Majorana mass for the Neutron from Exotic Instantons," 2015.

[22] A. Addazi, "Quantum chaos inside Black Holes," 2015.

[23] A. Addazi, "Neutron-Antineutron transitions from exotic instantons: how fast they might be and further implications," in *14th Marcel Grossmann Meeting on Recent Developments in Theoretical and Experimental General Relativity, Astrophysics, and Relativistic Field Theories (MG14) Rome, Italy, July 12-18, 2015*, 2015.

[24] A. Addazi, "Chaotization inside Quantum Black Holes," 2015.

[25] D. Comelli, M. Crisostomi, K. Koyama, L. Pilo, and G. Tasinato, "New Branches of Massive Gravity," *Phys. Rev.*, vol. D91, no. 12, p. 121502, 2015.

[26] D. Comelli, M. Crisostomi, K. Koyama, L. Pilo, and G. Tasinato, "Cosmology of bigravity with doubly coupled matter," *JCAP*, vol. 1504, p. 026, 2015.

[27] M. Crisostomi, D. Comelli, and L. Pilo, "On the Cosmology of Massive Bigravity," *Nuovo Cim.*, vol. C38, no. 1, p. 30, 2015.

[28] G. Ballesteros, D. Comelli, and L. Pilo, "Massive and modified gravity as self-gravitating media," 2016.

[29] M. Mannarelli, G. Pagliaroli, A. Parisi, L. Pilo, and F. Tonelli, "Torsional oscillations of nonbare strange stars," *Astrophys. J.*, vol. 815, no. 2, p. 81, 2015.

[30] M. L. Ahnen *et al.*, "Limits to dark matter annihilation cross-section from a combined analysis of MAGIC and Fermi-LAT observations of dwarf satellite galaxies," *JCAP*, vol. 1602, no. 02, p. 039, 2016.

[31] M. L. Ahnen *et al.*, "Very-high-energy gamma-rays from the Universe's middle age: detection of the z=0.940 blazar PKS 1441+25 with MAGIC," *Astrophys. J.*, vol. 815, no. 2, p. L23, 2015.

[32] A. Palladino, G. Pagliaroli, F. L. Villante, and F. Vissani, "Double pulses and cascades above 2 PeV in IceCube," *Eur. Phys. J.*, vol. C76, no. 2, p. 52, 2016.

[33] A. Esmaili and A. Yu. Smirnov, "Discrete symmetries and mixing of Dirac neutrinos," *Phys. Rev.*, vol. D92, no. 9, p. 093012, 2015.

[34] M. L. Ahnen *et al.*, "Very high-energy γ-ray observations of novae and dwarf novae with the MAGIC telescopes," *Astron. Astrophys.*, vol. 582, p. A67, 2015.

[35] P. Blasi, E. Amato, and M. D'Angelo, "High-Energy Cosmic Ray Self-Confinement Close to Extra-Galactic Sources," *Phys. Rev. Lett.*, vol. 115, no. 12, p. 121101, 2015.

[36] R. Aloisio, P. Blasi, and P. Serpico, "Nonlinear cosmic ray Galactic transport in the light of AMS-02 and Voyager data," *Astron. Astrophys.*, vol. 583, p. A95, 2015.

[37] G. Pagliaroli, A. Palladino, F. L. Villante, and F. Vissani, "Testing nonradiative neutrino decay scenarios with IceCube data," *Phys. Rev.*, vol. D92, no. 11, p. 113008, 2015.

[38] A. Esmaili and P. D. Serpico, "Gamma-ray bounds from EAS detectors and heavy decaying dark matter constraints," *JCAP*, vol. 1510, no. 10, p. 014, 2015.

[39] R. Aloisio, D. Boncioli, A. di Matteo, A. F. Grillo, S. Petrera, and F. Salamida, "Cosmogenic neutrinos and ultra-high energy cosmic ray models," *JCAP*, vol. 1510, no. 10, p. 006, 2015.

[40] S. Dell'Oro, S. Marcocci, M. Viel, and F. Vissani, "The contribution of light Majorana neutrinos to neutrinoless double beta decay and cosmology," *JCAP*, vol. 1512, no. 12, p. 023, 2015.

[41] G. Morlino, M. Lyutikov, and M. J. Vorster, "Mass-loading of bow shock pulsar wind nebulae," *Mon. Not. Roy. Astron. Soc.*, vol. 454, no. 4, pp. 3886–3901, 2015.

[42] A. Palladino and F. Vissani, "The natural parameterization of cosmic neutrino oscillations," *Eur. Phys. J.*, vol. C75, p. 433, 2015.

[43] R. Aloisio, S. Matarrese, and A. V. Olinto, "Super Heavy Dark Matter in light of BICEP2, Planck and Ultra High Energy Cosmic Rays Observations," *JCAP*, vol. 1508, no. 08, p. 024, 2015.

[44] K. Kotera, E. Amato, and P. Blasi, "The fate of ultrahigh energy nuclei in the immediate environment of young fast-rotating pulsars," *JCAP*, vol. 1508, no. 08, p. 026, 2015.

[45] M. Cardillo, E. Amato, and P. Blasi, "On the cosmic ray spectrum from type II Supernovae expanding in their red giant presupernova wind," *Astropart. Phys.*, vol. 69, pp. 1–10, 2015.

[46] G. Morlino and S. Gabici, "Cosmic ray penetration in diffuse clouds," *Mon. Not. Roy. Astron. Soc.*, vol. 451, no. 1, pp. L100–L104, 2015.

[47] M. D'Angelo, L. Fedeli, A. Sgattoni, F. Pegoraro, and A. Macchi, "Particle acceleration and radiation friction effects in the filamentation instability of pair plasmas," *Mon. Not. Roy. Astron. Soc.*, vol. 451, no. 4, pp. 3460–3467, 2015.

[48] N. Vinyoles, A. Serenelli, F. L. Villante, S. Basu, J. Redondo, and J. Isern, "New axion and hidden photon constraints from a solar data global fit," *JCAP*, vol. 1510, no. 10, p. 015, 2015.

[49] A. Palladino, G. Pagliaroli, F. Villante, and F. Vissani, "What is the Flavor of the Cosmic Neutrinos Seen by IceCube?," *Phys. Rev. Lett.*, vol. 114, no. 17, p. 171101, 2015.

[50] A. Mammarella and M. Mannarelli, "Intriguing aspects of meson condensation," *Phys. Rev.*, vol. D92, no. 8, p. 085025, 2015.

The XENON100 and XENON1T Experiments in 2015

E. Aprile[a]*, J. Aalbers[d], F. Agostini[b,c], D. Alexander[m], M. Alfonsi[e], F. Amaro[j], M. Anthony[a], F. Arneodo[h], P. Barrow[i], L. Baudis[i], B. Bauermeister[s], L. Bellizzi[p], L. Benabderrahmane[h], T. Berger[m], A. Breskin[f], P. Breur[d], A. Brown[d], E. Brown[m], S. Bruenner[n], G. Bruno[b], R. Budnik[f], A. Buss[l], L. Bütikofer[o], J. Calven[s], J. M. R. Cardoso[j], M. Cervantes[k], D. Cichon[n], D. Coderre[o], J. Conrad[s], A. P. Colijn[d], J. P. Cussonneau[p], S. D'Amato[i], M. P. Decowski[d], P. Di Gangi[c], S. Diglio[p], A. Di Giovanni[h], P. de Perio[a], E. Duchovni[f], G. Eurin[n], J. Fei[u], A. D. Ferella[s], A. Fieguth[l], D. Franco[i], W. Fulgione[b], A. Gallo Rosso[b], F. Gao[u], M. Garbini[c], C. Geis[e], A. Gmür[i], M. Galloway[i], L. W. Goetzke[a], L. Grandi[t], Z. Greene[a], C. Grignon[e], C. Hasterok[n], E. Hogenbirk[d], J. Howlett[a], R. Itay[f], B. Kaminsky[o], G. Kessler[i], A. Kish[i], H. Landsman[f], R. F. Lang[k], D. Lellouch[f], L. Levinson[f], Q. Lin[a], F. Linde[d], S. Lindemann[n], M. Lindner[n], F. Lombardi[u], J. A. M. Lopes[j], A. Manfredini[f], I. Maris[h], T. Marrodán Undagoitia[n], J. Masbou[p], F. V. Massoli[c], D. Masson[k], D. Mayani Paras[i], M. Messina[a], K. Micheneau[p], A. Molinario[q], M. Murra[l], J. Naganoma[r], K. Ni[u], U. Oberlack[e], P. Pakarha[i], B. Pelssers[s], R. Persiani[p], F. Piastra[i], J. Pienaar[k], M. Piro[m], V. Pizzella[n], G. Plante[a], N. Priel[f], L. Rauch[n], S. Reichard[k], C. Reuter[k], A. Rizzo[a], S. Rosendahl[l], N. Rupp[n], J. M. F. dos Santos[j], R. Saldanha[t], G. Sartorelli[c], M. Scheibelhut[e], S. Schindler[e], S. Schneider[l], J. Schreiner[n], M. Schumann[o], L. Scotto Lavina[p], M. Selvi[c], P. Shagin[r], E. Shockley[t], H. Simgen[n], A. Stein[g], D. Thers[p], A. Tiseni[d], G. Trinchero[q], C. Tunnell[d], N. Upole[t], M. Vargas[l], M. von Sivers[o], H. Wang[g], Y. Wei[i], C. Weinheimer[l] C. Wittweg[l], J. Wulf[i], J. Ye[u], Y. Zhang[a], and T. Zhu[a]
(The XENON Collaboration)

*Spokesperson

[a] Physics Department, Columbia University, New York, NY, USA
[b] INFN-Laboratori Nazionali del Gran Sasso and Gran Sasso Science Institute, L'Aquila, Italy
[c] Department of Physics and Astrophysics, University of Bologna and INFN-Bologna, Bologna, Italy
[d] Nikhef and the University of Amsterdam, Science Park, Amsterdam, Netherlands
[e] Institut für Physik & Exzellenzcluster PRISMA, Johannes Gutenberg-Universität Mainz, Mainz, Germany
[f] Department of Particle Physics and Astrophysics, Weizmann Institute of Science, Rehovot, Israel
[g] Physics & Astronomy Department, University of California, Los Angeles, CA, USA
[h] New York University in Abu Dhabi, Abu Dhabi, United Arab Emirates
[i] Physics Institute, University of Zürich, Zürich, Switzerland
[j] Department of Physics, University of Coimbra, Coimbra, Portugal
[k] Department of Physics and Astronomy, Purdue University, West Lafayette, IN, USA
[l] Institut für Kernphysik, Wilhelms-Universität Münster, Münster, Germany
[m] Department of Physics, Applied Physics and Astronomy, Rensselaer Polytechnic Institute, Troy, NY, USA
[n] Max-Planck-Institut für Kernphysik, Heidelberg, Germany
[o] Albert Einstein Center for Fundamental Physics, University of Bern, Bern, Switzerland
[p] SUBATECH, Ecole des Mines de Nantes, CNRS/In2p3, Université de Nantes, Nantes, France
[q] INFN-Torino and Osservatorio Astrofisico di Torino, Torino, Italy
[r] Department of Physics and Astronomy, Rice University, Houston, TX, USA
[s] Department of Physics, University of Stockholm, Sweden
[t] Department of Physics, University of Chicago, Chicago, IL, USA
[u] Department of Physics, University of California, San Diego, CA, USA

Abstract

The XENON collaboration operates the XENON100 and XENON1T dark matter experiments at Gran Sasso Underground Laboratory. Important results and significant progress have been achieved from these two experiments in 2015. The XENON100 published leptophilic dark matter search results with its ultra-low electronic recoil background. The long period stable operation of XENON100 also makes it possible for the experiment to search for annual modulated signals for the first time and to publish a result that significantly constrain the dark matter interpretation of the DAMA modulation signals. The XENON1T experiment has completed its construction and assembly in the latter half of the year, marked by an inauguration event on Nov.11, 2015. All subsystems for XENON1T have been under series of testing and verification in order for a smooth start of dark matter search in early 2016.

1 Introduction

The XENON collaboration uses dual-phase xenon time-projection chambers (TPC) to search for dark matter at LNGS. They have led the development of increasing larger and more sensitive detectors, probing deeper into the parameter space of varieties of dark matter models. The XENON100 experiment has completed its dark matter search data taking but is still being operated as a testbed for novel calibration sources to be used in XENON1T. The XENON1T experiment is being commissioned. With 3.5-ton of ultra-pure liquid xenon filled in the detector, XENON1T will keep pushing the dark matter search sensitivity towards a possible discovery. This report summarises the current status of both XENON100 and XENON1T and their achieved results and milestones in 2015.

2 XENON100

2.1 Operation status

Following XENON100's dark matter search run in 2014, several important results were released in 2015 regarding leptophilic dark matter models and the annual modulation signals using the low energy electronic recoil events. The detector is continuously being used for testing various calibration sources developed for XENON1T. We have been taking data to study the detector calibration with ^{88}YBe, ^{83m}Kr, ^{220}Rn from a ^{228}Th source, and CH_3T (tritiated methane). Analyses of these calibration data to understand the detector performance and calibration procedures are currently on-going.

2.2 Published Results

2.2.1 Exclusion of Leptophilic Dark Matter

Dark Matter in the form of Weakly Interacting Massive Particles (WIMPs) is typically expected to induce nuclear recoils in a terrestrial detector target with an annually modulated rate due to the motion of the Earth around the Sun. Although such a modulation has been observed by the DAMA/LIBRA collaboration using sodium iodine [4], it is difficult to interpret it as a dark matter signal, given the null results from other experiments. Experimental anomalies like annual modulation signal observed in the DAMA/LIBRA project cannot be explained by traditional dark matter scattering on atomic nuclei, but could be accommodated if dark matter scatters predominantly off electrons or if most of the energy is release in the form of photons.

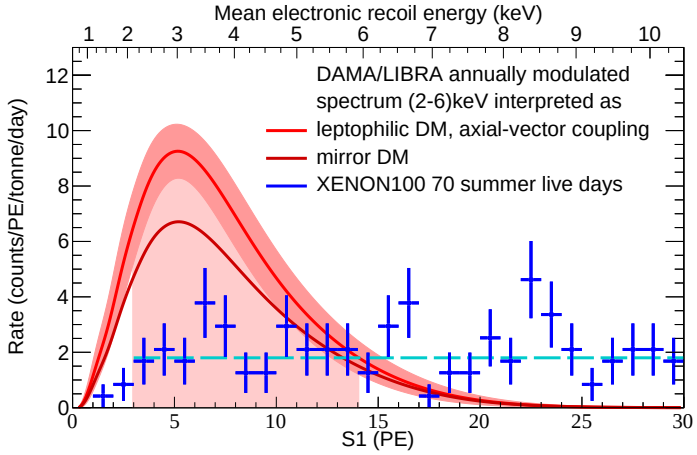

Figure 1: **Contrasting XENON100 data with DAMA/LIBRA**. The DAMA/LIBRA modulated spectrum (red), interpreted as WIMPs scattering through axial-vector interactions, as it would be seen in the XENON100 detector. The 1σ band includes statistical and systematic uncertainties. The DAMA/LIBRA modulated spectrum interpreted as luminous dark matter is very similar, whereas the interpretation as mirror dark matter is indicated separately (dark red). The (blue) data points are XENON100 data from the 70 summer live days with their statistical uncertainty.

For a long time, it was considered unfeasible to test such a leptophilic model (Dark Matter interacting with electrons) since the scattering of Dark Matter particles off electrons or the emission of photons is much more difficult to distinguish from radioactive backgrounds that are

present in any actual detector. Thanks to careful design and selection of materials, XENON experiment is setting the new gold standards in low background experiments.

In an article recently published in the Science magazine [5] we interpret data from the XENON100 detector that were acquired between February 28, 2011 and March 31, 2012 for a total exposure of 224.6 live days and 34 kg fiducial mass. We have previously searched this data set for spin-independent [1] and spin-dependent [6] WIMP-induced nuclear recoils as well as for axion-induced electronic recoils [2].

At low energies the XENON100 background is dominated by forward-scattered Compton events, resulting in a flat spectrum with a rate of 5.3 $events/(keV \cdot tonne \cdot day)$ in the fiducial volume [7]. The total rate in the XENON detector is more than two orders of magnitude lower than the average background rate reported by DAMA/LIBRA in the same energy interval, and it is even smaller than their reported annual modulation amplitude of (11.2 ± 1.2) $events/(keV \cdot tonne \cdot day)$ [4]. In the analysis we considered the most challenging scenario to exclude namely when the constant spectrum is fully attributed to background and only the modulated part is attributed to a 100% modulated dark matter signal.The dark matter-induced rate would then be zero on December 2nd, and twice the measured modulation amplitude on June 2nd. It follows that there is an optimized time interval to consider for best sensitivity.

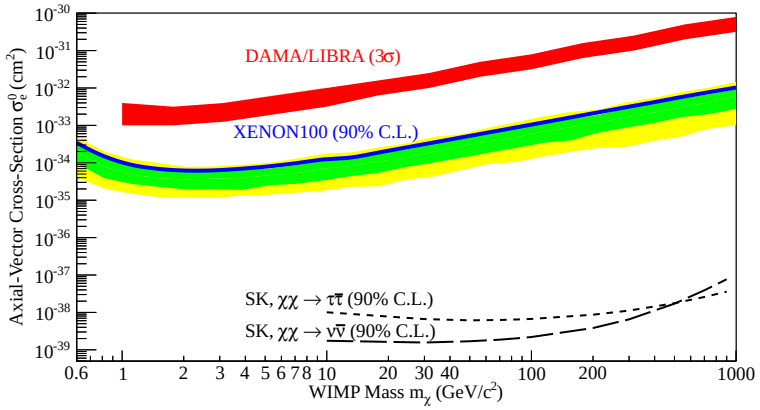

Figure 2: **Parameter space for WIMPs coupling to electrons through axial-vector interactions.** The XENON100 upper limit (90% confidence level) is indicated by the blue line, along with the green/yellow bands indicating the $1\sigma/2\sigma$ sensitivity. For comparison, we also show the DAMA/LIBRA allowed region (red) and the constraint from Super-Kamiokande (SK) using neutrinos from the Sun, by assuming dark matter annihilation into $\tau\bar{\tau}$ or $\nu\bar{\nu}$, both calculated in [8].

We contrast the DAMA/LIBRA signal interpreted as Dark Matter according to three representative models: WIMPS coupling to electrons through axial-vector interaction [8], Multicomponent Dark Matter with a sub-Gev particle [9] and a model that features a dark matter particle with ∼keV mass splitting between states connected by a magnetic dipole moment operator [10]. The deposited electronic recoil energy in XENON100 is estimated from the S1 signal, measured in photoelectrons (PE), using the NESTv0.98 model [3].

The level of exclusion was based on a comparison of the integral counts without any background substraction. We exclude leptophilic models as explanation for the long-standing DAMA/LIBRA signal, such as couplings to electrons through axial-vector interactions at a 4.4σ confidence level, mirror dark matter at 3.6σ, and luminous dark matter at 4.6σ. Fig. 1 shows the incompatibility of XENON100 electronic recoil spectrum and the expected signals according to two of these

models. The time interval considered is 70 summer live days, which corresponds to the period of optimal sensitivity.

Also a profile likelihood analysis was performed to constrain the cross section $\sigma^0_{\chi e} \equiv G^2 m_e^2/\pi$ for WIMPs coupling to electrons through axial-vector interactions. To this end, we drop the assumption of a 100% modulated rate and use the entire 224.6 live days data set, results are shown in Fig. 2.

2.2.2 XENON100 Annual Modulation Signal Search

One possible explanation of the annual modulation observed by DAMA/LIBRA is that it is induced by WIMP-electron interactions, for example via axial-vector couplings of WIMPs to electrons. This hypothesis was strongly challenged by an annual modulation analysis of XENON100 data published in PRL in August 2015 [11]. In this study, the stability of the rate of electronic recoil (ER) events from science run II of XENON100 [1], consisting of 225 live-days of data taken over the course of 397 actual days, was quantified using an unbinned profile likelihood (PL) analysis.

A careful study of the detector stability ruled out the possibility that variations of the thermodynamic state of the detector influence these ER rates. The 15 parameters investigated showed very small overall variations. For example, the LXe temperatures varied by less that 0.17°C, and the LXe levels by 220 μm. A correlation analysis was performed to quantify the correlations between the various detector parameters and the ER rates. Although two parameters, the LXe temperature and level, were found to give a significant correlation with ER rate, subsequent detailed analyses showed they in fact have no significant impact on the ER rate.

The extremely low rate of ER events in XENON100 is known to be dominated by γ and β rays produced by the decay of various radioactive backgrounds. Those with half-lives relevant for an annual modulation study, ^{60}Co, ^{222}Rn, and ^{85}Kr, were studied in detail. The change in the level of ^{60}Co, based on a Monte Carlo (MC) simulation using the measured activity, was determined to have a negligible impact on the ER rate. Direct measurements of ^{222}Rn made *in situ* using α decays and $\beta - \gamma$ delayed coincidence events also show the variations therein have a negligible impact on the ER rate, as is confirmed by a correlation analysis. It was determined, however, that the level of ^{85}Kr in the LXe grew linearly over the course of the run due to an air leak. As a result, a total increase in the rate of (0.10 ± 0.02) events per day in the low-E range is expected over the course of one year.

The stability of the three classes of ER events was studied using an unbinned PL method, incorporating the variation of the cut acceptance and the linearly increasing background from ^{85}Kr.

A MC simulation was used to assess the discovery potential of the PL analysis, and to verify its sensitivity to annual modulation signals. The study shows that the PL method should be sensitive to periods between 7 and 500 days, and that a modulation with an amplitude of 2.7 events/(keV $\cdot$ tonne $\cdot$ day) would be identified with an average local significance near 3σ.

The PL analysis of run II science data, Fig.3, shows a rising significance at long periods, with local significances at one year of 2.8σ and 2.5σ for low-energy single scatter (SS) and multiple scatter (MS) events, respectively. SS events in the high-E range also show a rising significance, but with a local significance at one year of 1.4σ. Binned cross checks using χ^2 and Lomb-Scargle periodgram methods are in agreement with the results of the PL analysis.

The best-fit parameters and uncertainties are determined from PL scans. Fig.4 shows the corresponding confidence level contours as a function of modulation amplitude for an assumed annual modulation signal in the low-E SS data. The simulations show that the rise in significance

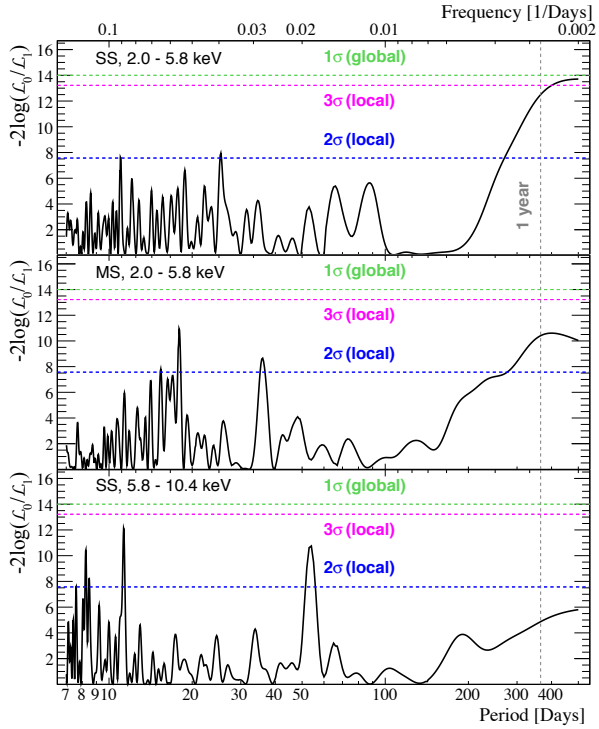

Figure 3: $-2\log(\mathcal{L}_0/\mathcal{L}_1)$ as a function of modulation period for SS in the low-E region (top), MS in the low-E region (middle) and SS in the high-E region (bottom).

at long periods in the low-E SS and MS data could be explained by a modulating component with a period greater than 300 days. However, the best-fit phase disagrees with the expected phase from a standard dark matter halo (152 days) at a level of $2.5\,\sigma$ based on the 1D PL scan as shown in top panel of Fig.4. Furthermore, the rise in significance at long periods is evident in both SS and MS data, also disfavouring a WIMP interpretation.

We directly compare the XENON100 time-dependent rate information with the expected DAMA/LIBRA annual modulation signal in our detector, the expected S1 spectrum in XENON100 is derived from the DAMA/LIBRA residual modulation spectrum (Fig. 8 in [4]) following the approach described in [5], assuming the signals are from WIMP-electron scattering through axial-vector coupling [8, 5]. The expected annual modulation amplitude in the low-E range in XENON100 is then calculated as $(11.5 \pm 1.2(\text{stat}) \pm 0.7(\text{syst}))$ events/(keV $\cdot$ tonne $\cdot$ day), with statistical uncertainty from the reported DAMA/LIBRA spectrum and systematic uncertainty from the energy conversion in XENON100. The resulting PL analysis of our data disfavours the expected DAMA/LIBRA annual modulation by $4.8\,\sigma$.

2.2.3 Ongoing analyses

There are several ongoing analyses based on the data already published in 2013. These include the low-mass WIMP analysis using only the charge signal for energy estimation, the inelastic nuclear recoil analysis and the full livetime analysis using the combination of earlier science data with currently blinded run III (154 live days and totalling 479 live days spanning 4 years). We have completed the signal and background modelling, background rejection, and uncertainties entering into the limit calculations. The current dark matter cross section limits as well as the annual modulation analysis will be updated soon.

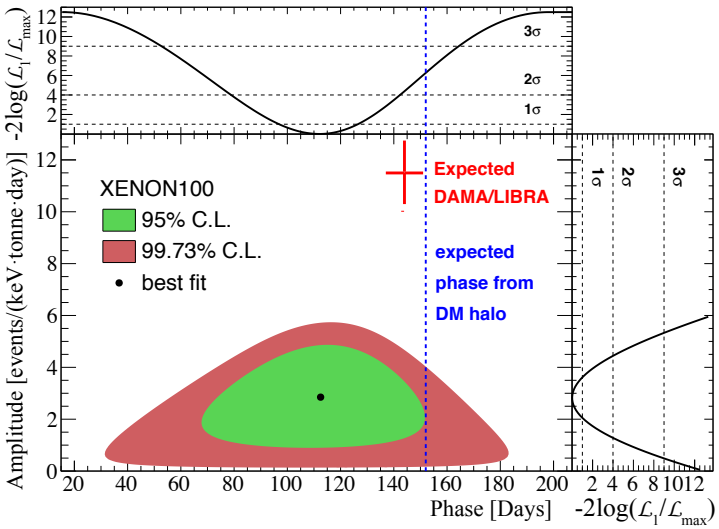

Figure 4: The XENON100 best-fit, 95% and 99.73% confidence level contours as a function of amplitude and phase relative to January 1, 2011 for period $P = 1$ year. The expected DAMA/LIBRA signal with statistical uncertainties only and the phase expected from a standard dark matter (DM) halo are overlaid for comparison. Top and side panels show $-2\log(\mathcal{L}_1/\mathcal{L}_{max})$ as a function of phase and amplitude, respectively, along with two-sided significance levels.

XENON100 is currently still taking data and is being used as a low background test bench for a series of calibration and proof of principle measurements preparatory for XENON1T. We have been taking data to study the detector calibration with ^{88}YBe, ^{83m}Kr, ^{220}Rn from a ^{228}Th source, and CH_3T (tritiated methane). The XENON1T DAQ system has been tested on XENON100. A pioneering method for Rn distillation from xenon has been proven successful. The analyses are ongoing and publications of these important test results are forseen.

3 XENON1T

XENON1T is the current generation of XENON dark matter detectors that use the two-phase xenon time projection chamber to search for dark matter. The detector has a total target mass of about 3.5-ton and a fiducial mass of at least 1-ton. With an ultra-low electronic recoil background rate of 1.8×10^{-4} evt/keV/kg/day and an expected electronic recoil rejection of 99.75% with a 40% nuclear recoil acceptance, XENON1T will reach a spin-independent sensitivity of WIMP-nucleon cross section of 1.6×10^{-47} cm^2 at $m_\chi = 50$GeV/c^2 after a two ton-year exposure. The XENON1T detector is currently being commissioned at Gran Sasso Underground Laboratory.

General Commissioning, Schedule In 2015, a flurry of activity at multiple institutions in parallel, and at LNGS in particular, has greatly advanced the XENON1T experiment towards operation. Guided by the collaboration's Technical Coordinator (E. Aprile) and the on-site Commissioning Manager (M. Messina) as well as the Working Group Coordinators, the parallel streams of production, assembly, and commissioning of subsystems have been coming together. We discuss the multitude of milestones achieved in 2015 below, and restrict ourselves here to some bullet points and the general statement that all systems are coming together in time or with little delay, and, most importantly, within specifications. Despite numerous challenges, no road blocks have been encountered in the entire system. The TPC has been assembled and

integrated with the cryostat and the PMT arrays are completely tested. XENON1T has been officially inaugurated to start the commissioning phase on November 11, 2015.

The gas system and Krypton cryogenic distillation column have been commissioned and operated successfully. Upon filling, xenon gas has been analyzed to check for chemical purity. The cryogenic cooling system and the ReStoX xenon recovery and storage system have been verified to fulfill specifications. Stable operation of over 2 t of liquid xenon in the cryostat and 3 t in the entire system including ReStoX have been demonstrated under automated control of the Slow Control system.

An initial measurement of the integral Rn level emanating from all the inner surfaces, such as TPC materials, cryostat walls, cables, etc. are completed. At the same time, we tested the new deionized water plant to fill the tank, and have the cryostat immersed in water for the first time.

We expect to fill the TPC with liquid xenon (LXe) and start the commissioning of the inner detector in Spring 2016. It is worth noting that one week of XENON1T science data should be sufficient to reach the current best limit reported by LUX. A paper on XENON1T sensitivity based on detailed Monte Carlo simulations, and informed by material screening results, is submitted [15]. Software for XENON1T has been prepared and tested extensively using XENON100 data to ensure fast turn around of the dark matter search results once the physics data comes out.

In the following, we provide an overview of the achieved progress of XENON1T subsystems towards the completion of the entire detector assembly and testing.

Cryostat, Cryogenics, ReStoX and Slow Control System One of the major achievements is the successful commissioning of the combined subsystems of the vacuum-insulated double-shell cryostat in the water shield, the cryogenic cooling system, the cryogenic xenon recovery and storage system ReStoX, and their interplay controlled by the Slow Control System (SCS). The achievable cooling power of the main cooling system (pulse tube refrigerator) was measured to be 250 W at 175 K, slightly higher than expected. The cryostat leveling mechanism has been tested. A buoyancy-control system supporting the empty cryostat is now ready. ReStoX is a 2.1 m-diameter spherical double-walled stainless steel pressure vessel able to store a total of 7.6 t of xenon in supercritical, liquid or solid state. Its large capacity will be sufficient for the XENONnT upgrade phase. Cooling is provided by two LN_2-based systems: a 3 kW condenser inside the sphere for standard operation and cooling lines around the sphere for fast LXe recovery from the detector in case of emergency. The heat load is limited to 48 W.

We have successfully filled all 3.5 t of xenon into ReStoX and maintain a pressure of about 1 bar absolute. Over 2 t of LXe were transferred to the cryostat to perform numerous tests on filling, cooling, recirculation, and recovery. One test was targeted to the question on how well a sudden pressure increase in the cryostat can be relieved by opening a gaseous xenon (GXe) line to ReStoX. The test shows that the relieving capacity of the GXe tube to ReStoX is adequate, provided ReStoX is operated at its standby pressure of 1 bar. In another test, 10 mbar of N2 were introduced into the insulation vacuum. Once the cryostat pressure reached a preset value, the LXe transfer valve opens and about 50 kg of Xe were transferred from the cryostat to ReStoX within less than one hour, relieving the cryostat pressure.

For these tests and the cryogenic operation of XENON1T, the SCS is essential and has been accordingly developed further and commissioned. Based on commercial industry standards, the SCS employs a networked architecture of controller units with a central supervisory control and data acquisition computer (SCADA). The core PLCs and touch panels for the cryogenics,

Figure 5: Left: XENON1T cryostat suspended by the support structure inside the water tank. Right: Assembled TPC in the cleanroom of Lab2.

ReStoX and purification systems and a preliminary alarm interface are operational. Interfaces to some of the remaining XENON systems (e.g., recirculation system) are being developed.

Purification, Distillation Column and Rn Removal The LXe purification system is installed in its final position underground and connected to all other systems including the distillation column. Two QDrive pumps have been installed in the system and successfully tested at recirculation speeds up to 50 slpm for short-term operation, meeting the designed specs. Both pumps have been equipped with external fans (in addition to chilled water) to maintain lower operating temperatures. A temperature sensor and an accelerometer have been installed on each pump, and interfaced to the slow control (SC) to monitor them and ensure safe operation. An automated shutdown routine has been implemented to turn off and isolate each pump from the remaining system in the event of abnormal performance. A permanent bake-out system has been installed on the gas lines of the purification system, which includes dedicated temperature controllers and sensors for each heating tape. Additionally, the same heating system has been installed on the gas lines connecting the purification system to other subsystems, and is nearly complete.

In September 2015, the purification system together with ReStoX, the cryostat and the bottle storage, has been used for the commissioning of the distillation column. During this test, xenon gas was circulated at 30 slpm between the purification system and the cryostat in order to investigate whether the Kr concentration changes over time or not. This result will be a good probe of the leak tightness of the system. During this run, the phase 2 cryogenic distillation column (full height 5 m, package height 3 m) [13] has been fully commissioned. A total of 210 kg of xenon gas has been successfully distilled from bottles into ReStoX at the nominal speed of 3 kg/h. This is the first longterm operation of the phase 2 column over several days. The system was still controlled by a LabView-based slow control software. Ongoing work is implementing the transition to the SCADA-based XENON1T Slow Control System. The distillation of the full xenon inventory will be done in 2016 before Dark Matter search data taking begins. Operating at nominal speed, 3.5 tons of xenon gas will be distilled within less than two months.

PMTs and Time Projection Chamber All the XENON1T PMTs, including spare units, were delivered by Hamamatsu in autumn 2015. After the testing procedures at room and LXe

temperatures were completed, the tubes with the best performance were selected for installation into the top and bottom arrays. Prior to their installation in a clean room environment, the PMTs and all the array components, including the copper and PTFE parts, the bases and cables, were cleaned following standard procedures. After the successful tests of the assembled tubes with their bases and cables in the clean room (Fig. 6), the complete arrays were packaged and transported to LNGS. After another round of PMT tests, the arrays were installed into the TPC in the clean room above ground. Once the full TPC was integrated into the cryostat in the underground clean room inside the water tank, and the cryostat closed, the PMTs were turned on one by one and signals from each tube were observed. The current focus is on the *in situ* gain calibration and on the tuning of the LED light, which is brought into the TPC by means of optical fibres. In addition, we are completing the PMT data base, that stores the main parameters, the radioactivity levels, and test results for each tube.

In parallel to this work, we have started to develop, together with Hamamatsu, a tube with even lower radioactivity for XENONnT. In the following months, we plan to test some of the new tubes at cryogenic temperatures and to screen their components with HPGe detectors and with ICP-MS.

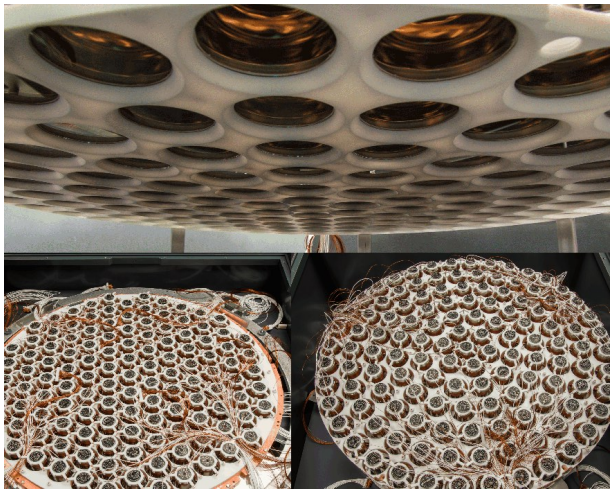

Figure 6: The XENON1T PMT arrays.

The XENON1T TPC has a height and diameter of 96 cm, and will enclose a target mass of 2.0 t of LXe out of the total 3.5 t. The sensitive volume will be viewed by a total of 248 PMTs. The detector is entirely made from low-background materials such as OFHC copper, virgin-grade PTFE and selected low-background stainless steel. In 2015, all the components have been fabricated and come together, and have been assembled at LNGS in recent weeks. The design foresees two options for level control, of which a diving bell similar to XENON100 will be tested initially. Four precision level meters have been installed around the top electrodes, and a readout board is expected to be completed by the end of December. All electrodes (cathode and bottom screening mesh: wires; all other electrodes are etched mesh electrodes) were fabricated, cleaned and installed in the TPC (Fig. 7, left). A mechanical weakness in the original design of the resistive chain has been caught during testing and replaced by a more robust design. A final test on the assembled TPC just showed that all resistor contacts survived the move from Lab2 under ground.

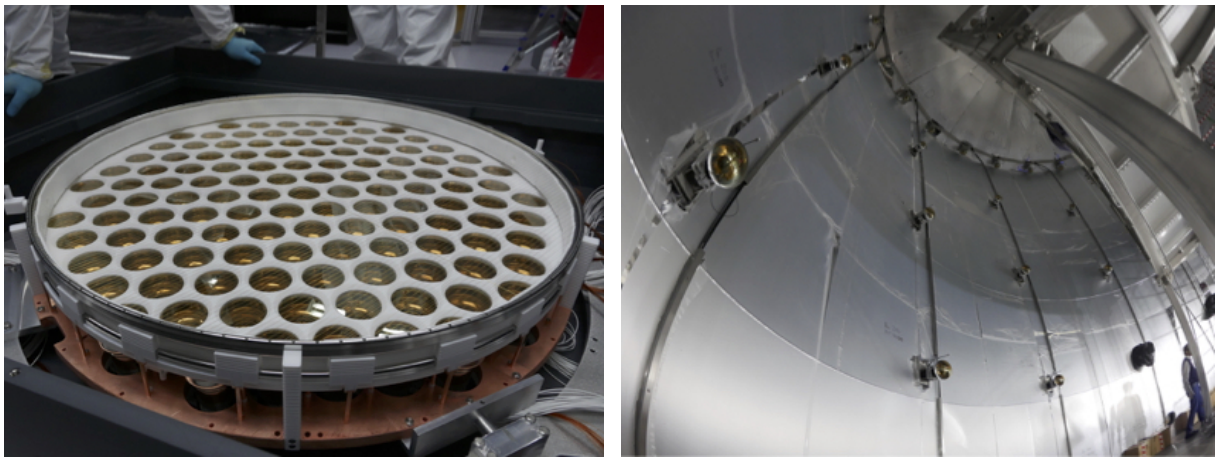

Figure 7: Left: Assembly of the Bottom PMT array with screening mesh and cathode. Right: Muon veto system with reflective foil (behind protective foil).

Data acquisition and Electronics, Muon Veto and Computing The two large subsystems of the trigger-less DAQ system, DaqReader (asynchronous front-end readout including DAQ control) and EventBuilder (online trigger), have been extensively operated and tested both independently and together. The full hardware (front end, computers, network) has been installed in October. The web interface is configured to use the LNGS LDAP authentication server locally. Final tests regarding DAQ/muon veto integration are completed.

One important test of the DAQ was a readout test of the XENON100 detector using the full DAQ system, performed in the summer. It was very successful, and helped us debug some remaining issues. There are two trigger parts, the pretrigger/event-builder and high level trigger. The coincident pretrigger/event-builder is used for chunking up the data, and is more than fast enough. The high level trigger can operate at 600 Hz processing events. The development of the data processor 'pax' is in its final stages, with programming support from the NL eScience Center. The class based ROOT output has been completed.

The muon veto system [14] is completed (Fig. 7, right). All 84 PMTs have been installed, and the protective foil has been removed in preparation of water filling. The commissioning of the muon veto will start during a water filling test, which starts in parallel with the Rn emanation measurement. The fibers of the PMT calibration system have been connected to LED boxes. The readout electronics was tested and has been installed in the data acquisition room. The development of the muon veto DAQ software has seen great advances in recent months. It has been developed in close collaboration with the TPC DAQ working group. A muon veto DAQ server has recently been bought and installed, and is now being used in the ongoing DAQ tests.

Calibration The calibration systems for XENON1T have been commissioned. This includes a system of multiple timing belts used to accurately position external calibration sources around the cryostat. Internal calibration sources 83mKr and CH3T have been successfully tested on XENON100 and will be used on XENON1T. The novel ^{220}Rn calibration source has also been successfully tested on XENON100 and is yielding important information using its alpha, beta and gamma decays. Calibration of XENON1T with the same source is foreseen. The deuterium-deuterium neutron generator has been accurately characterized.

Material Screening Nearly all construction materials for the XENON1T detector have been screened in terms of radioactivity and Rn emanation. The PMTs were screened using the Gator HPGe detector at LNGS. Its large measuring cavity and ultra-low background allow us to measure 15 PMTs simultaneously, reaching an acceptable sensitivity within ∼15 days in order to match the Hamamatsu production rate (30 PMTs/month). Results have been reported in a recently accepted paper [12], the low-background specifications for XENON1T have been met. An important part of the screening campaign has been focused on Rn emanation measurements. These measurements indicate that Rn may be the dominant intrinsic electronic recoil background, yet still at an acceptable level of $10\,\mu$Bq/kg.

Monte Carlo and Sensitivity We performed a detailed Monte Carlo simulation of the XENON1T experiment with a GEANT4 model. Considering the contaminations of the detector construction materials, measured through a screening campaign performed with Ge and mass spectrometry techniques, and the contaminants intrinsic to the LXe, we estimated both the ER and NR backgrounds.

Selecting single scatter events in the (1, 12) keV range, assuming a 1 t FV, the total ER background rate is $(1.80 \pm 0.15) \cdot 10^{-4}$ $(\mathrm{kg \cdot day \cdot keV})^{-1}$, a factor ~ 30 lower than in XENON100 [7], which corresponds to (720 ± 60) $(\mathrm{t \cdot y})^{-1}$ before applying any discrimination selection. The most relevant contribution, about 85% of the total, comes from the assumed 10 μBq/kg of ^{222}Rn, while the one from the materials is of the same order of those coming from ^{85}Kr and elastic scattering of solar neutrinos ($\sim 5\%$ each).

The NR background has been studied in the energy region (4, 50) keV, which corresponds to the same S1 range used for ER when taking into account the different response of LXe to ER and NR. Using the measured radio-activities of materials, we estimated a rate of (0.6 ± 0.1) $(\mathrm{t \cdot y})^{-1}$ from radiogenic neutrons. Due to the performance of the water Cherenkov muon veto, the background from muon-induced neutrons is reduced to less than $1 \cdot 10^{-2}$ $(\mathrm{t \cdot y})^{-1}$. A different approach is needed for the NR background from coherent scattering of neutrinos: indeed their rate in the same energy region is very small, $(1.8 \pm 0.3) \cdot 10^{-2}$ $(\mathrm{t \cdot y})^{-1}$. Given their very steep energy spectrum, it is relevant to calculate their contribution after the conversion from energy into the signal seen in the detector, to correctly take into account the fluctuations due to the small number of detected photons at low energies.

The LCE for the S1 signal has been calculated with a MC simulation of the propagation of photons inside the TPC, considering the effects of the refractive index, the absorption length in LXe, the transparency of the various electrodes and the reflectivity of PTFE. Assuming realistic values for all these parameters, the resulting LCE averaged over the whole TPC active volume is 35%. This corresponds to a light yield at zero field of 7.7 PE/keV (4.6 PE/keV at 530 V/cm) at 122 keV γ energy.

We have studied the WIMP signal and the expected backgrounds by converting energy depositions from ERs and NRs into observable signals, taking into account the detector resolution. Considering as reference a 99.75% ER discrimination with a corresponding 40% NR acceptance, the background in the (3, 70) PE S1 range is (1.62 ± 0.15) $(\mathrm{t \cdot y})^{-1}$ from ER, (0.22 ± 0.04) $(\mathrm{t \cdot y})^{-1}$ from NR of radiogenic neutrons, and (0.23 ± 0.04) $(\mathrm{t \cdot y})^{-1}$ from NR of neutrino coherent scattering. The uncertainties reflect only those coming from the knowledge of the sources of background, and not those from the LXe response which have been directly included in the sensitivity estimation. The spectra of the various backgrounds, together with those from some reference WIMP signals, are shown in figure 8.

We calculated the XENON1T sensitivity using the Profile Likelihood Ratio method, without any ER/NR discrimination cut. The main systematic uncertainty comes from $\mathcal{L}_{\mathrm{eff}}$, treated as

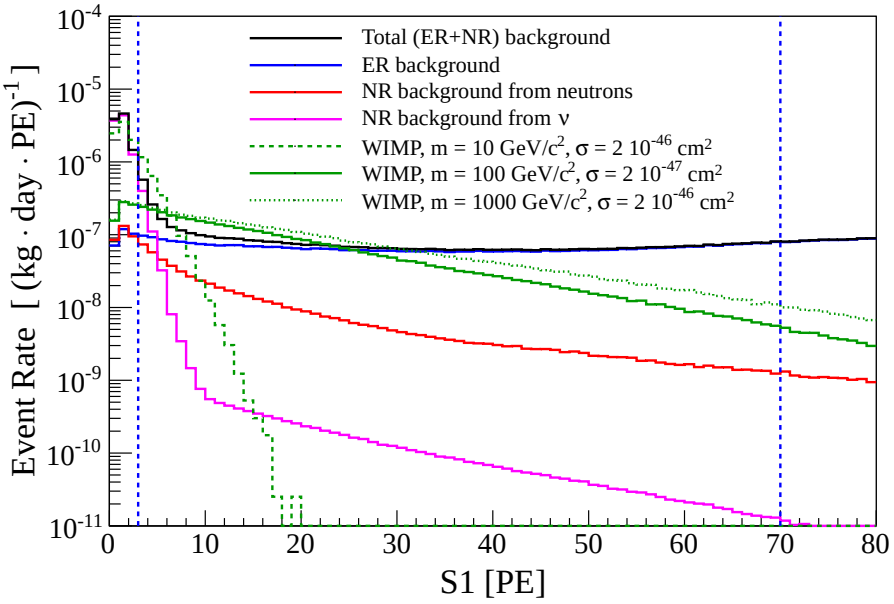

Figure 8: Spectrum of the total background as a function of S1 (black) and of its components: ERs (blue), NRs from radiogenic neutrons (red) and NRs from CNNS (purple). NR spectra for three examples of WIMP signals (green): mass $m_\chi = 10$ GeV/c^2 and cross section $\sigma = 2 \cdot 10^{-46}$ cm^2 (dashed), $m_\chi = 100$ GeV/c^2 and $\sigma = 2 \cdot 10^{-47}$ cm^2 (solid), $m_\chi = 1000$ GeV/c^2 and $\sigma = 2 \cdot 10^{-46}$ cm^2 (dotted). The vertical dashed blue lines delimit the S1 region used in the sensitivity calculation. In this plot we select the events with S2 $>$ 150 PE, and assume a 99.75% ER rejection with a flat 40% NR acceptance.

a nuisance parameter affecting both the signal from WIMPs and the NR backgrounds. After a 2 y measurement in 1 t FV, we obtain the sensitivity shown in figure 9, where the median value of the spin-independent WIMP-nucleon cross section reaches a minimum of $1.6 \cdot 10^{-47}$ cm^2 at m$_\chi$=50 GeV/c^2.

We also estimated the sensitivity of XENONnT, a future upgrade to XENON1T, which will be hosted in the same experimental area and will contain up to 7 t of LXe. Considering a FV where the ER and NR backgrounds from the detector materials are suppressed to a negligible level and assuming an improved purification from intrinsic contaminants, the most relevant background comes from ERs and NRs from solar neutrinos. Assuming a 20 t·y exposure, the sensitivity reaches $1.6 \cdot 10^{-48}$ cm^2 at m$_\chi$=50 GeV/c^2, an order of magnitude better than XENON1T.

In conclusion, with the XENON1T and XENONnT experiments we will be able to reach an unprecedented sensitivity to galactic dark matter particles, more than two orders of magnitude with respect to the currently running experiments. This will allow us to probe the region of electroweak parameter space favored by theoretical calculations in supersymmetric and other WIMP models.

4 Conclusions

The XENON collaboration keeps making progress towards the detection of dark matter particles using liquid xenon. The XENON100 experiment has produced new results regarding

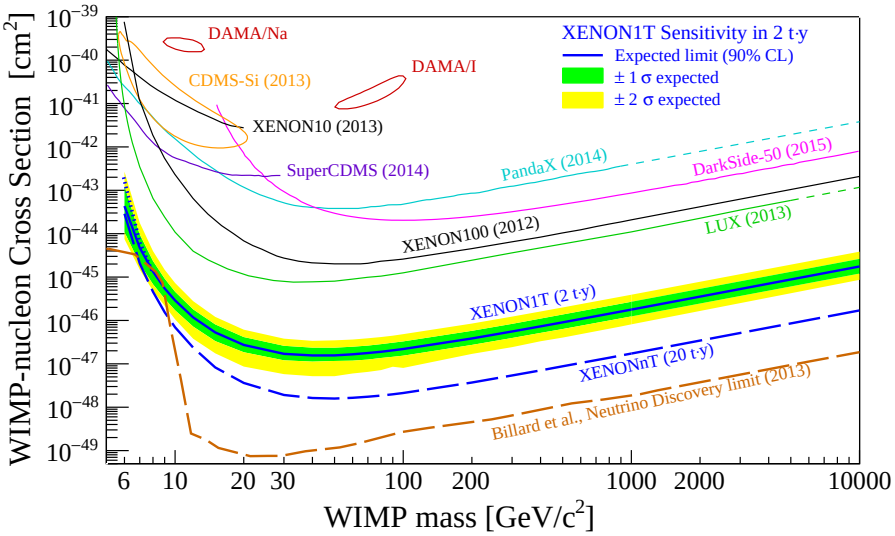

Figure 9: XENON1T sensitivity (90% C.L.) to spin-independent WIMP-nucleon interaction: the solid blue line represents the median value, while the 1σ and 2σ sensitivity bands are indicated in green and yellow respectively. The dotted blue line, visible at low WIMP masses, shows the XENON1T sensitivity assuming $\mathcal{L}_{\text{eff}} = 0$ below 3 keV. The XENONnT median sensitivity is shown with the dashed blue line. We refer to [15] for references of other experimental results and the neutrino discovery limit shown in the plot.

leptophilic dark matter and constraining the annual modulation signals in the electron recoil data. The XENON1T has completed its construction and is under commissioning. Upon the start of XENON1T in early 2016, we expect significant improvement in the sensitivity to search for WIMP dark matter and keep exploring the untouched parameter space for dark matter candidates in theories beyond the Standard Model.

5 List of Publications

The XENON Collaboration published the following papers during 2015:

- "Exclusion of Leptophilic Dark Matter Models using XENON100 Electronic Recoil Data", E. Aprile *et al.* [XENON Collaboration], Science, vol. 349 no. 6250 pp. 851-854 (2015)
- "Search for Event Rate Modulation in XENON100 Electronic Recoil Data", E. Aprile *et al.* [XENON Collaboration], Phys. Rev. Lett. 115, 091302 (2015)
- "Lowering the radioactivity of the photomultiplier tubes for the XENON1T dark matter experiment", E. Aprile *et al.* [XENON Collaboration], Eur.Phys.J. C75 (2015) 11, 546
- "Physics reach of the XENON1T dark matter experiment", E. Aprile *et al.* [XENON Collaboration], arXiv:1512.07501, submitted to JCAP.

References

[1] E. Aprile *et al.* [XENON Collaboration], Phys. Rev. Lett. **109**, 181301 (2012) [arXiv:1207.5988 [astro-ph.CO]].

[2] E. Aprile *et al.* [XENON Collaboration], Phys.Rev. **D90** (2014) 6, 062009. [arXiv:1404.1455v2 [astro-ph.CO]].

[3] M. Szydagis, N. Barry, K. Kazkaz, J. Mock, D. Stolp, M. Sweany, M. Tripathi, S. Uvarov, N. Walsh, and M. Woods, JINST 6, P10002 (2011).

[4] R. Bernabei *et al.*, *Eur.Phys.J.* **C73**, 2648 (2013).

[5] E. Aprile et al., [XENON Collaboration], Science 349, 851(2015).

[6] E. Aprile *et al.*, [XENON Collaboration], *Phys.Rev.Lett.* **111**, 021301 (2013).

[7] E. Aprile *et al.*, [XENON Collaboration], *Phys.Rev.* **D83**, 082001 (2011).

[8] J. Kopp, V. Niro, T. Schwetz, J. Zupan, *Phys.Rev.* **D80**, 083502 (2009).

[9] R. Foot, *Int.J.Mod.Phys.* **A29**, 1430013 (2014).

[10] B. Feldstein, P. W. Graham, S. Rajendran *Phys.Rev.* **D82**, 075019 (2010).

[11] E. Aprile *et al.* [XENON Collaboration], Phys. Rev. Lett. **115**, 091302 (2015), [arxiv::1507.07748].

[12] E. Aprile *et al.* [XENON Collaboration], Eur.Phys.J. C75 (2015) 11, 546

[13] S. Rosendahl et al., JINST 9 (2014) 10010.

[14] E. Aprile *et al.* [XENON Collaboration], JINST **9** (2014) 11006.

[15] E. Aprile *et al.* [XENON Collaboration], arXiv:1512.07501, submitted to JCAP.

Cosmic Silence

E. Fratini[a,b], M.F. Fischietti[a,c], G. Simone[a], E. Bortolin[b], C. De Angelis[b], G. Esposito[b], P. Fattibene[b], C. Nuccetelli[b], C. Quattrini[b], M. A. Tabocchini[a,b,*], E. Alesse[c], A. Tessitore[c], F. Zazzeroni[c], M. Balata[d], L. Ioannuci[d], A. Esposito[e], M. Chiti[e], O. Frasciello[e], L. Satta[a,e,*], M. Pavan[f], G. Cenci[g]

[a]Museo Storico della Fisica e Centro Studi e Ricerche Enrico Fermi
[b]Istituto Superiore di Sanitá, Technology and Health Department, and INFN-Roma1 Gr. coll. Sanitá, 00161 Roma, Italy
[c]LAquila University, Department of Biotechnological and Applied Clinical Sciences
[d]INFN - Gran Sasso National Laboratory
[e]INFN - Frascati National Laboratory
[f]La Bicocca University of Milan
[g]La Sapienza University of Rome, "C. Darwin"Department of Biology and Biotechnologies
(*) Spokepersons

Abstract

The molecular mechanisms involved in the biological response to environmental radiation are still little known and need to be investigated. The Silence Cosmic project, funded by the Istituto Nazionale di Fisica Nucleare (INFN) and Centro Fermi (Italy), tries to give a contribution in this field by investigating the influence of the environmental radiation on the metabolism and the response to genotoxic stress capability of *in vitro* biological systems. *In vivo* experiments are also planned in the near future using the fruit fly *Drosophila melanogaster* and, eventually, mice. The experimental approach is based on the set up of parallel experiments in different environmental conditions: at the underground Gran Sasso National Laboratory (LNGS) of the INFN, where the radiation background is strongly reduced, and in reference laboratories located at the ISS and at the University of LAquila. In order to allow a comprehensive interpretation of the obtained results in terms of biophysical mechanisms, a radiation field characterization in the experimental sites is ongoing. This will step forward by means of two approaches, namely dedicated measurements of the n and gamma components, and Monte Carlo simulations with MCNP6 and FLUKA codes. Moreover, we will use GEANT 4 to simulate the flux and dose values on target.

1 Introduction

Environmental radiation represents a constant daily stimulus that has been incorporated in the biology of living organisms during evolution, with the development of defense mechanisms well preserved during phylogeny. In order to investigate if modulation of radiation environment can modify the biochemistry of biological systems and their response to genotoxic agents, in the late 90s Satta et al. designed an experiment consisting in twin set-up of yeast cultures in a laboratory where the environmental radiation is strongly reduced and in a reference laboratory. To this purpose, they took advantage of the unique opportunity represented by the Gran Sasso underground laboratory of the Italian National Institute of Nuclear Physics (INFN), where the cosmic radiation is almost absent and neutron flux reduced by a 103 factor with respect to external values [1-3]. Since then, studies performed on cells of different origins (yeast, rodent and human) have indicated that cell cultured at the LNGS underground laboratory are less preserved from DNA damage, and show reduced Reactive Oxygen Species (ROS) scavenging power than those cultured in an external reference laboratory at the Istituto Superiore di Sanit (ISS, Rome) [4-8]. The Cosmic Silence Project aims to deepen the investigation of the molecular mechanisms involved in environmental radiation response by using sensitive *in vitro* (A11 hybridoma cells derived from transgenic pKZ1 mouse model) and *in vivo* (*Drosophila melanogaster* and pKZ1 transgenic mice) models, showing different levels of complexity in the phylogenetic tree [9-10]. Recent data on A11 cells, obtained after incubation of cells for some weeks in the reference laboratory and in the underground laboratory, in the presence or absence of shielding around the cell culture incubator, corroborate the hypothesis that environmental radiation contributes to the development and maintenance of defence mechanisms. Moreover, the data indicate that a gamma component increase of the environmental radiation does not significantly influence the biological response. To get more insight on the radiation-induced mechanisms underlying the observed effects, a deep characterization of the radiation field in the different environments is ongoing. As soon as the new animal housing facility will be set up underground at LNGS, hopefully at the beginning of 2016, *in vivo* experiments will start using the fruit fly *Drosophila melanogaster*.

2 Characterization of the radiation field in the different experimental sites

The Cosmic Silence project requires a characterization of the radiation field in the environments where the *in vitro* and the *in vivo* experiments are carried out. To this purpose measurements have been planned in the different sites of interest, namely in the underground laboratories of Gran Sasso (INFN) and in the ground laboratories at LAquila University and at ISS.

Neutrons measurements
Neutrons are generally detected through nuclear reactions that result in prompt charged particles such as protons, alpha particles, and so on. Because the cross section for neutron interactions in most materials is a strong function of neutron energy, rather different techniques have been developed for neutron different energy regions. A widely used detector for slow neutrons is the BF3 proportional tube. In this device, boron trifluoride serves as both the target for slow neutron conversion into secondary particle as well as a proportional gas. Neutron background has been measured inside the "Silenzio Cosmico" laboratory using a Boron trifluoride detector by Centronic (50 mm tube diameter, 1070 mm active length, 70 cm Hg). BF3 detector was exposed in horizontal and vertical position obtaining the following results:

Position	**Fast component** $ncm^{-2}s^{-1}$	**Thermal component** $ncm^{-2}s^{-1}$	**Ambient dose equivalent rate** $nSvh^{-1}$
Vertical positon	$5.74E-05$	$0.9E-06$	0.12
Horizontal position	$2.4E-04$	$1.54E-04$	0.32

There is no good explanation of the difference between the horizontal and vertical position. It could be a geometrical effect. In fact, the horizontal position could "see" a higher surface in the bypass. Such effect should disappear if measurement would be performed in the LNGS halls. In order to measure the whole neutron spectrum, including epithermal and fast components, two additional sets of measurements were arranged, both in Hall A and in the Pulex area. In these latter cases, the BF3 detector was wrapped up with 1.5 mm of Cadmium and 12.5 cm of polyethylene, respectively. Fig.1 reports the results in terms of mean values and associated standard errors. They seem to clearly confirm the above mentioned hypothesis of a "geometric effect", being the results of n counts in Hall A fully independent on the detector orientation, within the experimental error.

The possible inter comparison with measurements performed by other authors so far, is rather difficult for several reasons:

- differences in measurements' positions;
- differences in distances from the concrete and in humidity;
- differences in detectors used and in the measured spectra regions.

The results in vertical position would seem to agree with the measurements of $3E-05$ $ncm^{-2}s^{-1}$ reported by other authors [11]. We planned further measurements of neutron background, both in the bypass of the Pulex area and in another hall, aimed at a more deep understanding of the experimental results shown above and, possibly, at a clearer discrimination

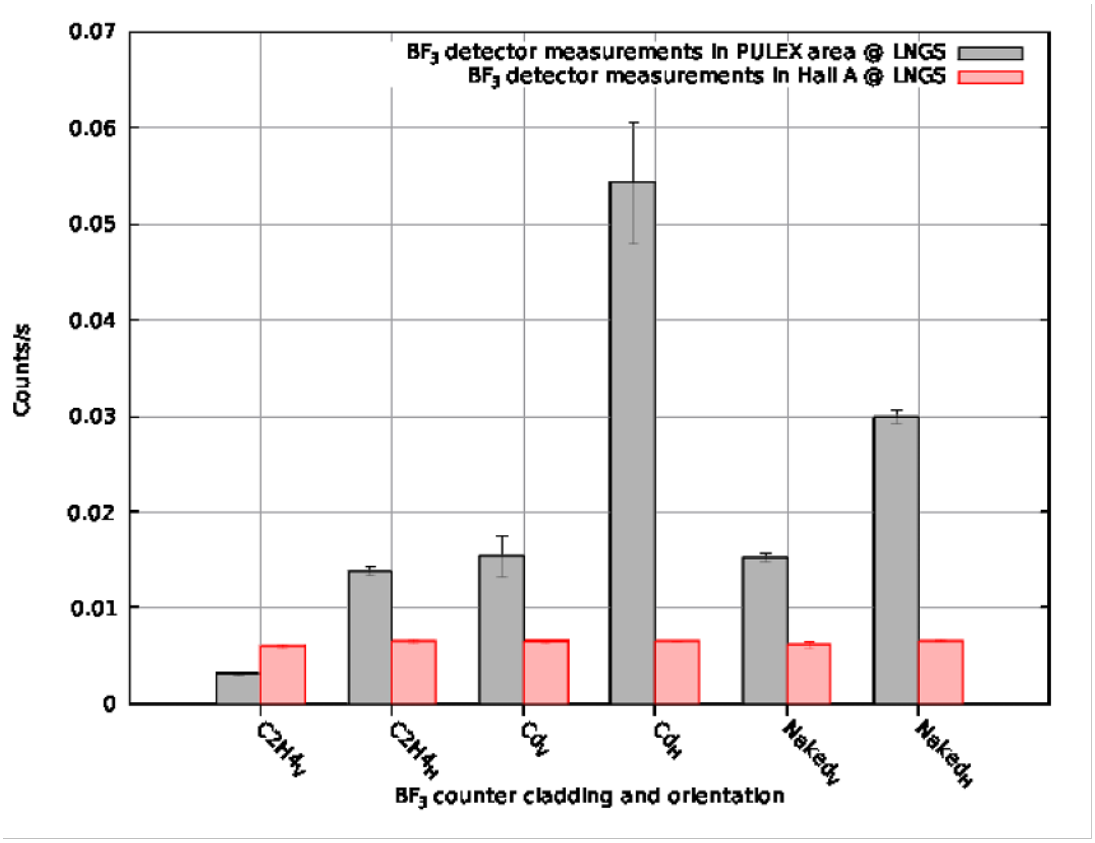

Figure 1: Preliminary results of neutron counts measured at LNGS: Pulex area, in grey; Hall A in red. BF3 detector orientation is indicated by subscripts "V" and "H". The three detector configurations are indicated as "C2H4" for polyethylene cladding, "Cd" for Cadmium one and "Naked" for the bare one.

of the presumed geometric effect previously discussed. For this purpose, we will carry out a dedicated simulation campaign by means of Monte Carlo codes MCNP6 and FLUKA, which will provide theoretical estimations of the background radiation field experimental data can be compared to.

Gamma component measurements

The dosimeters used to evaluate the gamma background dose rate were the Lithium fluoride TLD700H, selected on the base of their high radiation sensitivity, as reported in literature. Thermoluminescence readouts were performed with a Harshaw 3500 TL reader by heating the TLDs from 100 to 240°C with a rate of 10°C/s; preheat (2 minutes at 100°C) and annealing (15 minutes at 240°C) were carried out with the PTW-TLDO oven controlled by a programmable microprocessor. During the time stability study the TLDs were stored in the dark inside a lead housing to reduce the room radiation background exposure. A preliminary check of the dosimetric characteristics of the thermoluminescence dosimeters selected for the study, namely batch variability, radiation sensitivity, fading behavior and re-use effect, was carried out during the first phase of the experiment. The results confirmed the suitability of TLD700H for the experiment. In particular, the tests confirmed they have high radiation sensitivity and reduced long time signal fading: they could detect doses of the order of a few μGy and guarantee a signal

stability for at least 14 weeks. The cited features were crucial to detect the background dose rates of the different experimental sites in particular those recorded in the LNGS underground laboratories. Monitoring measurements were conducted using sets of five TLDs kept inside a tissue culture flask and placed in the different sites previously identified. At LNGS underground laboratories three cell incubators with different characteristics, were monitored: one located inside a $5cm$ thick iron shield, one without shielding and a third one, containing tablets of KCl to enhance the gamma rays contribution to radiation background due to K-40. TLDs were placed inside and, in one case, also outside the incubators hosting the cell cultures. In the ground laboratories at the University of LAquila, sets of TLDs were kept inside and outside of a cage for mice; at the ISS one incubator was monitored. In each site, three different measurement sessions were performed over a period of about 1.5 years (September 2014-March 2016). Each measurement session lasted a period of time ranging from 28 to 98 days. The TL responses were converted in dose by using a dose-response curve obtained by irradiating six different sets of TLDs in the range (4-350) μGy with a Cs-137 source available at LNF- INFN. Preliminary data analysis indicates that the background dose rate at ISS (inside the cell culture incubator) is about 70 times that at underground LNGS (shielded incubator) and the dose rate at the University of LAquila (in the mouse cage) is about 4 times that at the LNGS outside the incubators. No significant differences between the response of the dosimeters inside and outside of the mice cage were observed.
The incubator containing KCl tablets showed an enhanced radiation background, being the dose rate about 20 times that one inside of the shielded incubator. Comparing the results obtained with dosimeters put inside and outside the unshielded incubator, it seems that the incubator itself produces a shielding effect of about 20%. Further measurements are planned for analyzing the gamma radiation energy spectrum and the activity concentration of gamma radiation emitting radionuclides by gamma spectroscopy with an HpGe.

Radon
Radon activity concentration in air will be measured and monitored using an Alfaguard instrument during the biological experiments.

GEANT4 simulations
In view of a detailed evaluation of the composition and spectrum of the background radiation in the low and in the reference radiation environments, we planned to complement the experimental measurements with GEANT4 simulations. To this purpose, we started a collaboration with the Milano-Bicocca University, in order to implement the modelling of the Cosmic Silence installation using a Montecarlo simulation code, called ARBY, for arbitrary geometries based on GEANT4. This collaboration will be very helpful for the final design and control of the underground "Cosmic Silence" facility. The goal is to predict the dose to the target starting from particle fluxes. The input of simulation is the γ-ray flux, measured underground (from HPGe measurement done in Hall A), and the neutron flux, measured underground (from data reported in literature and from the data collected in the framework of the collaboration). The output of simulation will be the flux and dose values on target. Up to now the LNGS geometry was implemented. A validation of the simulation against a known standard benchmark will be also needed (dose evaluation in standard conditions) to verify or calibrate the predictions.

Catalase (Cat): catalyzes the decomposition of hydrogen peroxide to water and oxygen

Superoxide dismutases (Sod): class of enzymes that catalyze the dismutation of superoxide into oxygen and hydrogen peroxide

Glutathione peroxidase 1 (Gpx1): works in the detoxification of hydrogen peroxide and is one of the most important antioxidant enzymes in humans

Extracellular glutathione peroxidase (Gpx3): works in hydrogen peroxide detoxification in the extra-cellular compartment

Phospholipid hydroperoxidase (Gpx4): uses lipid-hydroperoxide as substrate; protects cells against membrane lipid peroxidation

Selenium binding protein (Sbp1): down-regulates GPx_s activity removing selenium

	Reference Lab (ISS)	Underground (LNGS)
Cat	-	↓
Sod	↑	↓
Gpx1	↑	-
Gpx2	-	-
Gpx3	-	↓
Gpx4	↑	-
Sbp1	↓	↑

Figure 2: Modulation of the expression of genes involved in the protection from oxidative damage after 1 month of continuous culture in RRE (ISS) or LRE (LNGS).

3 Experimental results on *in vitro* cell cultures

The hybridoma cell line (A11), kindly donated by Prof. Pamela Sykes, Flinders University, Adelaide, Australia, was used for experiments carried out up to 1 month of culture in different radiation environments. More specifically, 4 A11 cell cultures (A, B, C, D) were grown in parallel for up to 4 weeks at the ISS (RRE) and at the LNGS underground cell culture laboratory (LRE) in the presence of 5 cm Fe shield. Expression of genes involved in the protection from oxidative damage and protein expression of poly (ADP-ribose) polymerase-1 (PARP-1), a key protein in DNA repair as well as in physiological and pathological functions, from cell survival control to several forms of cell death [12-16], was evaluated. Fig.2 shows the differential modulation observed for the various oxidative stress response genes considered. After 1 month of continuous culture in RRE and LRE some of the selected genes are upregulated (↑) while others downregulated (↓).

With regard to PARP-1, after 1 month of continuous culture the concentration of activated form of the enzyme is drastically reduced in cells grown in LRE (Fig.3). It should be noted that A11 cells are subjected to passage twice a week and that reduction of activated PARP-1 occurs only after 4 days of culture and not after 3 days, probably because of starvation stress. Interestingly, when 4-day cultured A11 cells grown at LRE are brought to RRE laboratory and cultured for additional 2 weeks, PARP-1 cleavage increases and reaches normal levels, suggesting the cells can efficiently sense the variations of environment radiation and rapidly adapt their physiological responses.

In order to investigate the effect of the gamma dose increase, cleavage of PARP-1 has been studied in A11 cells grown for 4 weeks in three different environmental radiation conditions: RRE at the ISS; LRE at the LNGS in the presence or absence of Fe shield. The results, shown in Fig.4, did not show difference between the two LRE experimental conditions (i.e., with and without shielding).

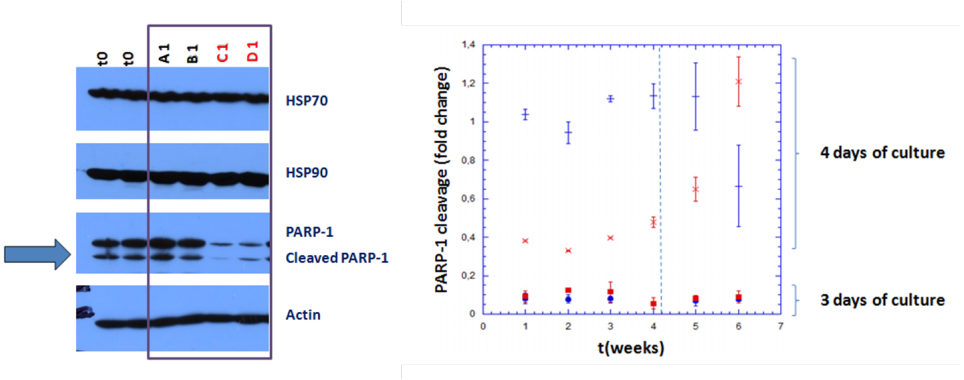

Figure 3: Activation of PARP-1 (as measured by the cleaved vs un-cleaved form of this enzyme) in A11 cells grown in RRE (•;+) or in LRE (■;x).

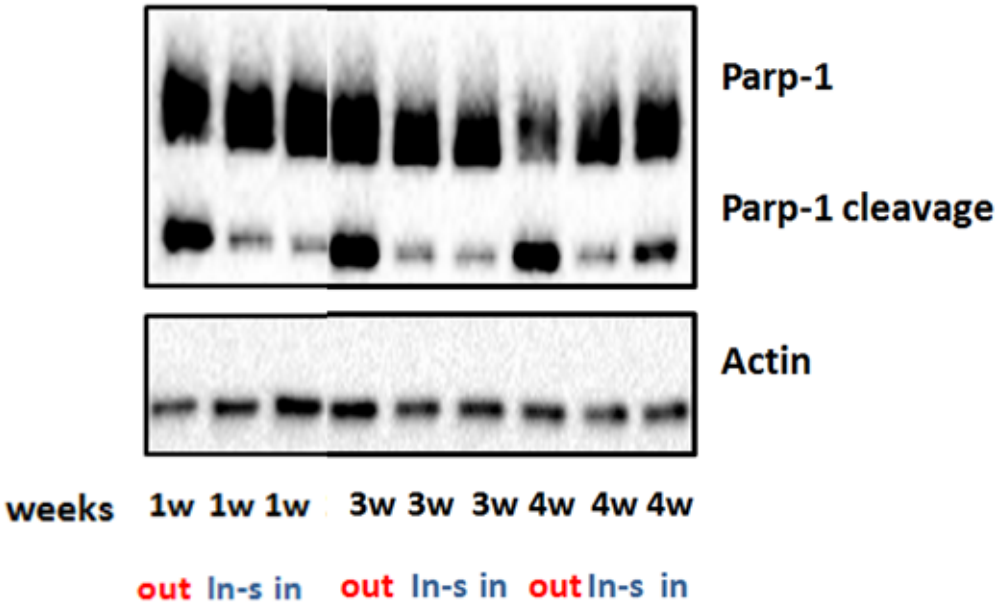

Figure 4: Expression level of PARP-1 protein in A11 cells grown for 4 weeks in three different environmental radiation conditions: at RRE, at the ISS (out), and at LRE: LNGS with 5 cm Fe shield (In-s) and LNGS without shield (in). Samples have been collected at the 1^{st}, 3^{rd} and 4^{th} week after 4 days of exponential culture.

In the attempt to expose the cells growing in LRE to known low doses of ionizing radiation experiments started in collaboration with J.B. Smith (Mexico State University) aimed at increasing the LRE background using KCl salt as radiation source (Fig.5). In this new set of experiments, V79 Chinese hamster cells have been used. Cells were cultured at LRE in different radiation environments, namely in the presence of shielding or in the presence of KCl salt. Cell growth and gene expression have been investigated. The results on cell growth do not show sig-

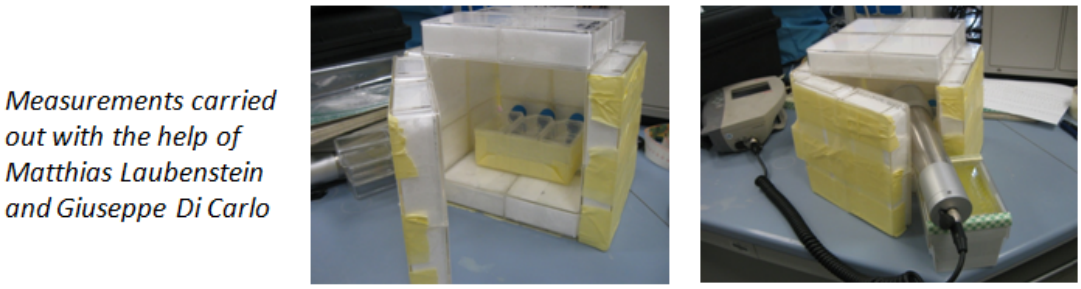

Figure 5: Set up of the KCl box that has been positioned inside the un-shielded incubator for culturing cell at the LNGS in the presence of an increased gamma dose.

nificant differences between the two conditions; gene expression data analysis is still in progress. The overall *in vitro* data obtained so far indicate a limited influence of the gamma component of the radiation spectrum and corroborate the hypothesis that other components of environmental radiation contribute to the development and maintenance of defence mechanisms in organisms living today Other results, consistent with our findings, have more recently been obtained using mammalian and bacterial cells grown under reduced radiation environmental conditions at the Waste Isolation Pilot Plant (WIPP), USA [17, 18].

4 The new facility for in vivo experiments

In addition to the *in vitro* experiments, that represent a fundamental approach to understand the biological effects of low-very low doses of ionizing radiation, for a more comprehensive knowledge *in vivo* studies are essential. It is well know that not all the damage has a local origin and that part of the biological response is due to non-cell-autonomous physiological mechanism that point to studies at organism level. To verify whether effects caused by extremely low-doses of environmental ionizing radiation, including cosmic radiation, exist *in vivo*, a facility for housing living organisms of different complexity in the phylogenetic tree has been designed to be set up underground at LNGS.
The animal housing facility will be constructed next to the PULEX cell culture laboratory. It will be provided with temperature, humidity and light control systems as well as with an independent ventilation system. This facility has been designed to host small animals and a 60 cages mice rack (Fig. 6).
Once it will be ready, the first planned experiments will be done with the fruit fly *Drosophila melanogaster*. Whether the lack of environmental radiations at the LRE affects metabolism will be analyzed in this well-established model organism.

To this aim, 2 different wild-type Drosophila strains and a transgenic line harboring the *lac Z* reporter gene will be grown at 23-25C at both the LNGS and the University of Rome laboratories. After 1, 3 and 6 months maintenance in standard medium, flies from all the three lines will be checked for life span, fertility, locomotor activity and genome integrity parameters. In addition, it will be determined somatic mutation frequency and tumor development by using somatic mutation and recombination test (SMART) and epithelial tumor detection tests, respectively. *lac Z* report gene-bearing flies will be exploited to carry out a molecular characterization of somatic mutations. It will finally be verified the sensitivity to known mutagens and chronic

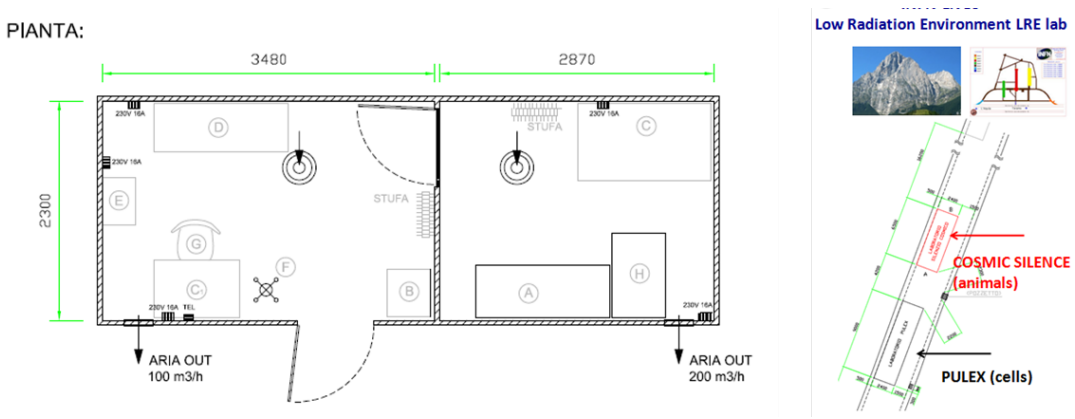

Figure 6: COSMIC SILENCE animal housing facility. It will be realized in the bypass, close to the PULEX cell cultures facility.

oxidative stress by performing the same set of analyses after exposing wild-type and *lac Z* carrying flies to X-rays, ethyl methanesulfonate (EMS) and paraquat, a well-known oxidative stress inducer.

5 Acknowledgements

We are indebted with Dr. M. Belli for the interesting discussions and suggestions and to Prof. P. Sykes, Flinders University, Australia, for sending us the pKZ1 cells and mice to be used in the framework of the Cosmic Silence collaboration.

6 List of Publications in 2015

1. Verní F., Cenci G (2015). The Drosophila histone variant H2A.V works in concert with HP1 to promote kinetochore-driven microtubule formation. *Cell Cycle* 14(4):577-88. doi: 10.4161/15384101.2014.991176.

2. Cenci G, Ciapponi L, Marzullo M, Raffa GD, Morciano P, Raimondo D, Burla R, Saggio I, Gatti G. (2015). The analysis of *pendolino (peo)* mutants reveals differences in the fusigenic potential among Drosophila telomeres. PLOS *Genetics* 11(6): e1005260

3. Fratini E., Carbone C., Capece D., Esposito G., Simone G., Tabocchini M.A., Tomasi M., Belli M., Satta L. (2015). *Low-radiation environment affects the development of protection mechanisms in V79 cells.* Radiat. Environ. Biophys. 54(2):183-94

4. Tabocchini M.A. *PULEX-COSMIC SILENCE: Extremely low radiation background facilities at the INFN-LNGS.* AIR2-Access to Infrastructures for Radiation protection Research, Issue 3, Dec.2015 (http://www.concert-h2020.eu/en/Concert−info/Access$_Infrastructures$)

5. G.B. Smith, H. Castillo and A. Tabocchini. Background Radiation Experiments (LBRE) on Biological Cells at the U.S. Waste Isolation Pilot Plant (WIPP) and the Italian Laboratori Nazionali di Gran Sasso. 15^{th} International Conference on the Chemistry and Migration Behaviour of Actinides and Fission Products in the Geosphere (MIGRATION 2015). September 13-18, 2015, Fanta Fe, NM, USA

6. F. Fischietti, A. Tessitore, P. Sykes, M. Chiti, A. Esposito, M. Balata, G. Cenci, G. Esposito, M.A. Tabocchini, L. Satta a nome della collaborazione "Silenzio Cosmico". *Il progetto silenzio cosmico: studio dellinfluenza della radiazione ambientale sul metabolismo e sulla risposta ad agenti genotossici di sistemi biologici di diversa complessit.* 101^0 Congresso Nazionale della Societ Italiana di Fisica (SIF), Roma, 21-25 settembre 2015. Book of Abstract p.196

7. F. Fischietti, A. Tessitore, P. Sykes, G. Cenci, M. Balata, M. Chiti, A. Esposito, G. Esposito, M. Belli, M.A. Tabocchini, L. Satta on behalf of the Cosmic Silence collaboration. *The underground biology at the Gran Sasso National Laboratory: from Pulex to Cosmic Silence.* Workshop on Deep Underground Laboratory Integrated Activity in biology (DULIA-bio), Canfranc, Spain, 13-14 October 2015

8. F. Fischietti, A. Tessitore, P. Sykes, G. Cenci; M. Balata, M. Chiti, A. Esposito, L. Satta, G. Esposito, M.A. Tabocchini on behalf of the Cosmic Silence collaboration. *The cosmic silence experiment: investigation of the molecular mechanisms involved in the biological response of living systems to environmental radiation.* 7th International MELODI Workshop. Munich, Germany, November 9-11, 2015

References

[1] The MACRO Collaboration (1990) Study of penetrating cosmic ray muons and search for large scale anisotropies at the Gran Sasso Laboratory. Phys Lett B 249:149 156

[2] Rindi A, Celani F, Lindozzi M, Miozzi S. *Underground neutron flux measurement.* Nucl Inst Meth A (1998)272:871-874

[3] Belli P., Bernabei R., DAngelo S., De Pascale M., Paoluzi L., Santonico R., Taborgna N.I.N., Villoresi G. *Deep underground neutron flux measurement with large BF3 counters.* Rivista del Nuovo Cimento A (1989) 101:959-966

[4] Satta L., Augusti-Tocco G., Ceccarelli R., Esposito A., Fiore M., Paggi P., Poggesi I., Ricordy R., Scarsella G., Cundari E. *Low environmental radiation background impairs biological defense of the yeast Saccharomyces cerevisiae to chemical radiomimetic agents.* Mutat Res (1995) 347(3-4):129-33

[5] Satta L., Antonelli F., Belli M., Sapora O., Simone G., Sorrentino E., Tabocchini M.A., Amicarelli F., Ara C., Cerú M.P., Colafarina S., Conti Devirgiliis L., De Marco A., Balata M., Falgiani A., Nisi S. *Influence of a low background radiation environment on biochemical and biological responses in V79 cells.* Radiat Environ Biophys (2002) 41 (3):217-24

[6] Carbone M.C., Pinto M., Antonelli F., Amicarelli F., Balata M., Belli M., Conti Devirgiliis. L., Ioannucci L., Nisi S., Sapora O., et al (2009) *The Cosmic Silence Experiment: on the putative adaptive role of environmental ionizing radiation.* Radiat. Environ. Biophys. 48:189-196

[7] Carbone M.C., Pinto M., Antonelli F., Amicarelli F., Balata M., Belli M., Conti Devirgiliis L., Sapora O., Simone G., Sorrentino E., Tabocchini M.A., Satta L. (2010) *Effects of deprivation of background environmental radiation on cultured human cells.* Il Nuovo Cimento 4:469-477

[8] Fratini E., Carbone C., Capece D., Esposito G., Simone G., Tabocchini M.A., Tomasi M., Belli M., Satta L. (2015) *Low-radiation environment affects the development of protection mechanisms in V79 cells.* Radiat. Environ. Biophys. 54(2):183-94, 2015

[9] Hooker A.M., Home R., Morley A., Sykes P.J. (2002) *Dose-dependent increase or decrease of somatic intrachromosomal recombination produced by etoposide.* Mut. Res. 500, 117-124.

[10] Day T.K., Zeng G., Hooker A.M., Bhat M., Scott B.R., Turner D.R. and Sykes P.J. (2006) *Extremely Low Priming Doses of X Radiation Induce an Adaptive Response for Chromosomal Inversions in pKZ1 Mouse Prostate.* Radiat Res. 166, 757766.

[11] Fiorini et al.,*Preliminary measurements of the gamma and neutron background in the Gran Sasso tunnel*, LNF-85/7(R)

[12] Livak K J and Schmittgen T D (2001) *Analysis of Relative Gene Expression Data Using Real-Time Quantitative PCR and the 2-[Delta][Delta]CT Method.* Methods, 25(4):402-408

[13] Grube K., Bürkle A. *Poly(ADP-ribose) polymerase activity in mononuclear leukocytes of 13 mammalian species correlates with species-specific life span.* Proc. Natl. Acad. Sci. U.S.A. (1992) 89 (24): 1175963. doi:10.1073/pnas.89.24.11759

[14] Muiras M.L., Mller M., Schächter F., Bürkle A. *Increased poly(ADP-ribose) polymerase activity in lymphoblastoid cell lines from centenarians.* J. Mol. Med. (1998) 76 (5): 34654. doi:10.1007/s001090050226

[15] Lebel M., Lavoie J., Gaudreault I., Bronsard M., Drouin R. *Genetic cooperation between the Werner syndrome protein and poly(ADP-ribose) polymerase-1 in preventing chromatid breaks, complex chromosomal rearrangements, and cancer in mice.* Am. J. Pathol. (2003) 162 (5): 155969. doi: 10.1016/S0002-9440(10)64290-3

[16] Bernstein H., Payne C.M., Bernstein C., Garewal H., Dvorak K.*Cancer and aging as consequences of un-repaired DNA damage.* (2008) Kimura H, Suzuki A, Ed. New York: Nova Science Publishers, Inc. pp.147

[17] Smith G.B., Grof Y., Navarrette A., Guilmette R.A. (2011) *Exploring biological effects of low level radiation from the other side of background.* Health Phys 100(3):263265

[18] Castillo H., Schoderbek D., Dulal S., Escobar G., Wood J., Nelson R. & Smith G. *Stress induction in the bacteria Shewanella oneidensis and Deinococcus radiodurans in response to below-background ionizing radiation.* (2015) Int. J. Radiat. Biol. 91(9):749-56 doi: 10.3109/09553002

ERMES
Low-level radium determination in groundwater by SF-ICP-MS

Lorenzo Copia[a,b], Stefano Nisi[b], Wolfango Plastino[a,b],
Marta Ciarletti[a,b], Pavel P. Povinec[d]

[a] Roma Tre University, Department of Physics, Italy
[b] National Institute of Nuclear Physics (INFN), Section of Roma Tre, Italy
[c] National Institute of Nuclear Physics (INFN), Gran Sasso National Laboratory, Italy
[d] Comenius University, Department of Nuclear Physics and Biophysics, Slovakia

Abstract

Inductively coupled plasma mass spectrometry (ICP-MS) techniques have been widely used for analysis of long-lived environmental radionuclides. It has been planned an optimization of the sector field (SF)-ICP-MS technique for the analysis of ^{226}Ra in groundwater samples using a method of pre-concentration of radium in water samples. The separation protocol and a sequential application of ion exchange and extraction chromatography have been optimized, and related polyatomic interferences and matrix effects affecting the ^{226}Ra signal were investigated. Analyzing 12 replicates (water spiking at 22 fg g^{-1} of ^{226}Ra), the ^{226}Ra recovery efficiency close to 100 % has been obtained. The instrumental ^{226}Ra detection limit of 0.09 fg g^{-1} (3 criterion) and the absolute detection limit of 0.05 fg in a 25-mL groundwater sample have been reached.

1 Introduction

Within the framework of the Environmental Radioactivity Monitoring for Earth Sciences (ERMES) project carried out at the Instituto Nazionale di Fisica Nucleare (INFN) Gran Sasso National Laboratory, 1-L groundwater samples have been collected weekly since 2008 at ten different sites located in the underground laboratory [1, 2, 3]. In order to analyze with high precision such large number of samples necessary for the development of ^{226}Ra time series, it has been proposed to develop a new analytical technology, which would be based on ICP-MS. Due to high-precision data requirements for the development of the ^{226}Ra groundwater time series, the original Lariviere et al. method [4] has been modified by adding a pre-concentration part, effects of which were thoroughly investigated. In order to determine ^{226}Ra in groundwater samples, a sector field (SF)-ICP-MS (Finnigan Element 2, Thermo Scientific), equipped with an Apex Q high-sensitivity introduction system (Element Scientific Inc.), was used. The Apex Q system was tested with three different micro-nebulizers: 64, 100, and 200 L/min, using a 100-ppt Thermo Tuning solution and monitoring of ^{238}U as a descriptive of heavy elements. The 100 L/min one showed the best performance. A spray chamber operational temperature of 100°C and a Peltier-cell condenser operational temperature of 2 °C, optimal for aqueous samples, were

chosen. The N2 flow pressure was not crucial for the gain of the system, in the sense that above a certain value, flux variations did not modify the counting rate in the uranium window. The instrument has been optimized daily with respect to the torch position and to the sample and the auxiliary gas flow, in order to reach a maximum counting rate and a stable signal. The acquisition parameters were chosen with an isotopic ratio measurement approach [5], with a narrow mass window in order to gain in sensitivity, and with a long acquisition time to improve counting statistics.

2 Results and discussion

Starting from the a priori assumption that ^{238}U decay chain is in secular equilibrium in the investigated groundwater samples, and having a ^{238}U concentration between 1 and 2 ng g^{-1}, a ^{226}Ra concentration around 0.3 - 0.7 fg g^{-1} was expected. At such a low concentration, radium was barely detectable by available instrumentation, so a preconcentration was needed. A pre-concentration factor of 50 was chosen because, on one side, it guarantees a measurable signal and a good counting statistics; on the other hand, a small sample amount of 25 mL of water is sufficient for the analysis. The ^{226}Ra ICP-MS measurements suffer of both spectral and nonspectral interferences; therefore, it is crucial to understand how these elements are separated in the procedure, how big are their levels in the final solution, and which are their effects on the measurement. Analyzing 12 replicates (water spiking at 22 fg g^{-1} of ^{226}Ra), the ^{226}Ra recovery efficiency close to 100 % has been obtained thanks to the optimization of the radium separation method and a pre-concentration of radium in groundwater samples. The same could be said with respect to the separation of the interfering elements, important for the quantitative ^{226}Ra analysis by SF-ICPMS. The improvements in the separation and preconcentration techniques also helped to improve the ^{226}Ra detection limit down to 0.05 fg/25 mL of groundwater sample. The absolute detection limit for a water sample equivalent of 1.95 10^{-18} g g^{-1} has been obtained [6].

3 Conclusion

The separation protocol and a sequential application of ion exchange and extraction chromatography have been optimized, and related polyatomic interferences and matrix effects affecting the ^{226}Ra signal were investigated. The ^{226}Ra recovery efficiency close to 100 % has been obtained thanks to the optimization of the radium separation method and a pre-concentration of radium in groundwater samples. The same could be said with respect to the separation of the interfering elements, important for the quantitative ^{226}Ra analysis by SF-ICP-MS. The improvements in the separation and preconcentration techniques helped to improve the 226Ra detection limit down to 0.05 fg/25 mL of groundwater sample. The absolute detection limit for a water sample is equivalent to 1.95 10^{-18} g g^{-1}.

References

[1] Plastino W, Povinec PP, De Luca G, Doglioni C, Nisi S, Ioannucci L, Balata M, Laubenstein M, Bella F, Coccia E, 2010. Uranium groundwater anomalies and L'Aquila earthquake, 6th April 2009 (Italy). J Environ Radioactiv 101:45-50.

[2] Plastino W, Panza GF, Doglioni C, Frezzotti ML, Peccerillo A, De Felice P, Bella F, Povinec PP, Nisi S, Ioannucci L, Aprili P, Balata M, Cozzella ML, Laubenstein M, 2011. Uranium groundwater anomalies and active normal faulting. J Radioanal Nucl Chem 288:101-107.

[3] Plastino W, Laubenstein M, Nisi S, Peresan A, Povinec PP, Balata M, Bella F, Cardarelli A, Ciarletti M, Copia L, De Deo M, Gallese B, Ioannucci L, 2013. Uranium, radium and tritium groundwater monitoring at INFN-Gran Sasso National Laboratory, Italy. J Radioanal Nucl Chem 295:585-592.

[4] Lariviere D, Epov VN, Reiber K, Cornett R, Evans R, 2005. Micro-extraction procedures for the determination of Ra-226 in well waters by SF-ICP-MS. Anal Chim Acta 528:175182.

[5] Hamester M, Wiederin D, Wills J, Kerl W, Douthitt CB, 1999. Strategies for isotope ratio measurements with a double focusing sector field ICP-MS. Fresen J Anal Chem 364:495-498.

[6] Copia L, Nisi S, Plastino W, Ciarletti M, Povinec PP, 2015. Low-level ^{226}Ra determination in groundwater by SF-ICP-MS: optimization of separation and pre-concentration methods. J Anal. Sci. Technol. 6:22.

THE VIP EXPERIMENT

S. Bartalucci[a], S. Bertolucci[b], M. Bragadireanu[a,c]
M. Cargnelli[d], A. Clozza[a], C. Curceanu[a],
S. Di Matteo[e], J-P. Egger[f], C. Guaraldo[a], M. Iliescu[a],
M. Laubenstein[g], J. Marton[d], E. Milotti[h], A. Pichler[d], D. Pietreanu[a,c],
K. Piscicchia[a], M. Poli Lener[a], T. Ponta[c], A. Romero Vidal[a],
A. Scordo[a], H. Shi[a], D.L. Sirghi[a,c], F. Sirghi[a,c], L. Sperandio[a],
O. Vazquez Doce[i], E. Widmann[d], J. Zmeskal[d]

[a] INFN, Laboratori Nazionali di Frascati, CP 13, Via E. Fermi 40, I-00044, Frascati (Roma)-Italy
[b] CERN, CH-1211, Geneva 23-Switzerland
[c] "Horia Hulubei" National Institute of Physics and Nuclear Engineering, Str. Atomistilor no. 407, P.O. Box MG-6, Bucharest - Magurele-Romania
[d] The Stefan Meyer Institute for Subatomic Physics, Boltzmanngasse 3, A-1090 Vienna-Austria
[e] Institut de Physique UMR CNRS-UR1 6251, Université de Rennes1, F-35042 Rennes-France
[f] Institut de Physique, Université de Neuchâtel, 1 rue A.-L. Breguet, CH-2000 Neuchâtel-Switzerland
[g] INFN, Laboratori Nazionali del Gran Sasso, S.S. 17/bis, I-67010 Assergi (AQ)-Italy
[h] Dipartimento di Fisica, Università di Trieste and INFN– Sezione di Trieste, Via Valerio, 2, I-34127 Trieste-Italy
[i] Excellence Cluster Universe, Technische Universität München, Garching, Germany

Abstract

The Pauli exclusion principle (PEP) and, more generally, the spin-statistics connection, stays at the very basis of our understanding of matter and the Universe. The PEP spurs, presently, a lively debate on its possible limits, deeply rooted in the very foundations of Quantum Mechanics and Quantum Field Theory. There are theories, starting from the quon-theory, and non-commutative geometries, which might allow for a tiny violation of PEP. Therefore, it is extremely important to experimentally test the limits of its validity. The VIP collaboration is testing the validity of PEP for electrons. We also consider the possibility to extend the scientific program towards the study of spontaneously emitted x-ray radiation, a phenomena experimentaly predicted in the framework of collapse models.

1 Introduction

The Pauli Exclusion Principle (PEP), which plays a fundamental role in our understanding of many physical and chemical phenomena, from the periodic table of elements, to the electric conductivity in metals and to the degeneracy pressure which makes white dwarfs and neutron

stars stable, is a direct consequence of the spin-statistics connection [1]. Although the principle has been spectacularly confirmed by the huge number and accuracy of its predictions, its foundation lies deep in the structure of quantum field theory and has defied all attempts to produce a simple proof [2]. Given its basic standing in quantum theory, it is not only appropriate, but as well necessary, to carry out precise tests of the PEP validity and, indeed, mainly in the last 20 years, several experiments have been performed to search for possible small violations [3, 4, 5, 6, 7, 8, 9, 10, 11, 12]. Many (if not all) of these experiments are using methods which are not obeying to the so-called Messiah-Greenberg superselection rule [13]. The indistinguishability and the symmetrization (or antisymmetrization) of the wave-function should be checked independently for each particle, and accurate tests were and are being done.

The VIP (VIolation of the Pauli Exclusion Principle) experiment has the goal to dramatically improve the limit on the probability of the violation of the PEP for electrons, ($P < 1.7 \text{ x } 10^{-26}$ established by E. Ramberg e G. A. Snow: *Experimental limit on a small violation of the Pauli principle*, Phys. Lett. **B 238** (1990) 438), exploring a region where new theories might allow for PEP violation.

The experimental method, originally described in [14], consists in the introduction of electrons into a copper strip, by circulating a current, and in the search for X rays resulting from the forbidden radiative transition that would occur if some of the "new" electrons are captured by copper atoms and cascade down to the 1s state already filled by two electrons with opposite spins. The energy of the $2p \rightarrow 1s$ transition would differ from the normal K_α transition by about 300 eV (7.729 keV instead of 8.040 keV) [15] providing an unambiguous signal of the PEP violation. The measurement alternates periods without current in the copper strip, in order to evaluate the X-ray background in conditions where no PEP violating transitions are expected to occur, with periods in which current flows in the conductor, thus providing "new" electrons, which might violate PEP.

The experiment is being performed at the LNGS underground Laboratories, where the X-ray background, generated by cosmic rays, is reduced.

Presently, the group is considering the extension of its scientific program to the study of the collapse models, by the measurements of the spontaneously emitted radiation (X rays), predicted by these models. Very encouraging preliminary results were obtained.

2 The VIP experimental setup

The first VIP setup was realized in 2005, using Charge Coupled Devices (CCD) as X-ray detectors [16, 17, 18, 19, 20], and consisted as main elements of a copper cylinder, were current was circulated, 4.5 cm in radius, 50 μm thick, 8.8 cm high, surrounded by 16 equally spaced CCDs of type 55.

The CCDs were placed at a distance of 2.3 cm from the copper cylinder, grouped in units of two chips vertically positioned. The setup was enclosed in a vacuum chamber, and the CCDs were cooled to about 165 K by the use of a cryogenic system. A schematic drawing of this setup is shown in Fig. 1. The setup was surrounded by layers of copper and lead (as seen in the picture) to shield it against the residual background present inside the LNGS laboratory, see Fig. 2.

The DAQ alternated periods in which a 40 A current was circulated inside the copper target with periods without current, referred as background.

This apparatus was installed at the LNGS Laboratory in Spring 2006 and was taking data in this configuration until Summer 2010.

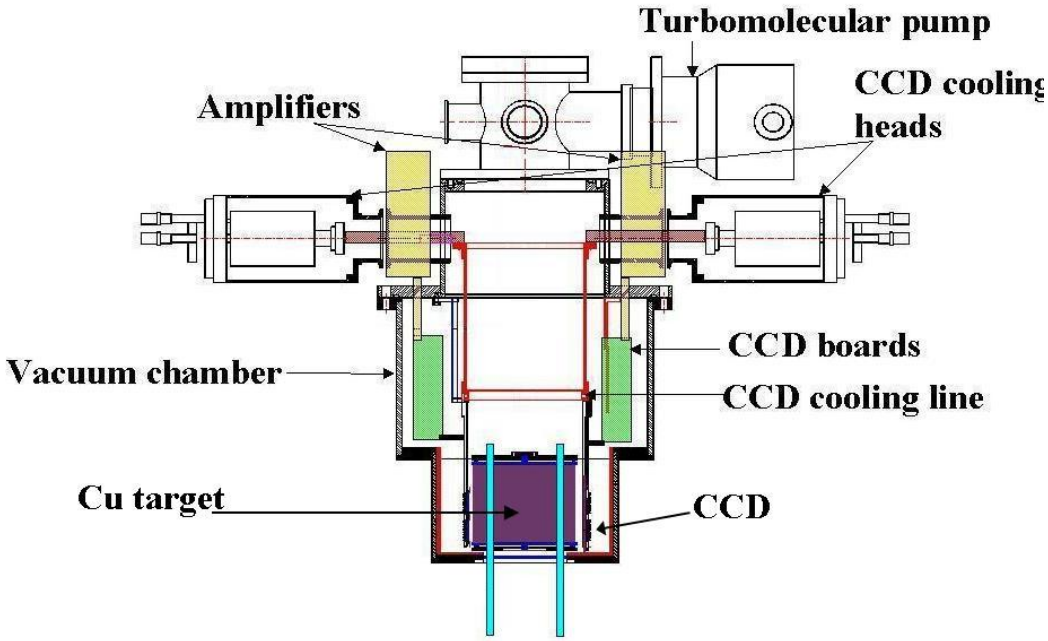

Figure 1: *The VIP setup. All elements af the setup are identified in the figure.*

In 2011 we started to prepare a new version of the setup, VIP2, installed in 2015 at the LNGS-INFN, with which we will gain a factor about 100 in the probability of PEP violation in the coming years.

3 The VIP results

3.1 VIP results on the probability of PEP violation

Until summer 2010 the VIP experiment was in data taking, alternating periods of "signal" (I=40 A) with periods without signal (I=0 A) at LNGS.

Data analyses were performed (energy calibration, sum of spectra, subtraction of background) and the probability of violation of PEP for electrons obtained in 2014 after a refined re-analysis of the data, involving charge transport correction for CCDs, is:

$$\frac{\beta^2}{2} < 3 \times 10^{-29} \tag{1}$$

3.2 Discussion of the results

We are attempting an interpretation of our results in the framework of quon-theory, which turned out to be a consistent theory of *small* violations of PEP. The basic idea of quon theory [21] is that (anti)commutators, are replaced by weighted sums

$$\frac{1-q}{2}\left[a_i, a_j^+\right]_+ + \frac{1+q}{2}\left[a_i, a_j^+\right]_- = a_i a_j^+ - q a_j^+ a_i = \delta_{i,j} \tag{2}$$

where $q = -1$ ($q = 1$) gives back the usual fermion (boson) commutators. The statistical mixture in equation (2) also shows that the PEP violation probability is just $(1+q)/2$ and thus

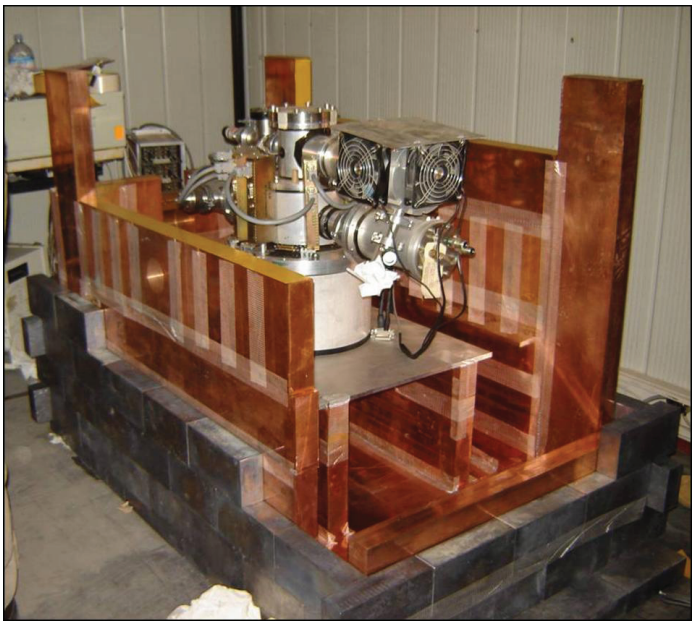

Figure 2: The VIP setup at the LNGS laboratory during the installation procedure.

our final experimental bound on q is

$$\frac{1+q}{2} < 3 \times 10^{-29} \tag{3}$$

We are in close contacts with theoreticians and philosophers, looking for implications of the possible small violation of the PEP in physics, cosmology and philosophy.

4 The VIP2 experiment

4.1 VIP2 - a new high sensitivity experiment

In order to achieve a signal/background increase which will allow a gain of two orders of magnitude for the probability of PEP violation for electrons, we built a new setup with a new target, a new cryogenic system and using new detectors with timing capability and an active veto system. As X-ray detectors we use Silicon Drift Detectors (SDDs) which were employed in the SIDDHARTA experiment measuring kaonic atoms at the DAΦNE electron-positron collider of Laboratori Nazionali di Frascati. SDDs have an even better energy resolution than CCDs and provide as well timing capability which allow to use anti-coincidence operation with scintillators and therefore an active shielding. The VIP2 system will provide:

1. signal increase with a more compact system with higher acceptance and higher current flow in the new copper strip target;

2. background reduction by decreasing the X-ray detector surface, more compact shielding (active veto system and passive), nitrogen filled box for radon radiation reduction.

In the table 1 the numerical values for the improvements in VIP2 are given which will lead to an expected overall improvement of a factor about 100.

Table 1: List of expected gain factors of VIP2 in comparison to VIP (given in the brackets).

Changes in VIP2	value VIP2(VIP)	expected gain
acceptance	12%	12
increase current	100A (50A)	2
reduced length	3 cm (8.8 cm)	1/3
total linear factor		8
energy resolution	170 eV(340 eV)	4
reduced active area	6 cm^2(114 cm^2)	20
better shielding and veto		5-10
higher SDD efficiency		1/2
background reduction		200-400
overall gain		**$\sim$120**

4.2 Status of VIP2 in 2015

From 2014 to 2015, we finished the production of 32 pieces of veto detectors made of plastic scintillators coupled to Silicon PhotoMmultipliers(SiPM). The preamplifiers for the SiPMs were fine tuned and with the veto detectors we took background data inside the laboratory. The six SDD elements with a total active area of 6 cm^2 were mounted inside the vacuum chamber and cooled down to 110 K, and we successfully took calibration data using an Fe-55 source. All the SDDs were performing according to expectation with an energy resolution of about 150 eV (FWHM) at 6 keV.

We define the trigger for data taking by either an event at any SDD or a coincidence between two layers of the veto detector. The trigger logic was implemented using the NIM standard modules and a VME-based data acquisition system was customized. From the cosmic ray events that produce coincidences between the veto scintillators and the SDDs, we confirmed the time correlation whose spread is characterized by the drift time of the SDD of less than 1 μs.

To make sure the heat from the Cu conductor when the electric current is applied does not affect the silicon detectors nearby, we monitored the temperatures of the setup while applying an electric current up to 80 Ampere. A water chiller with cooling capacity less than 900 W was confirmed to be sufficient to keep the Cu at the room temperature level.

The series of tests for the detectors, the trigger logic and the slow control/monitors have confirmed that the expected performances of the apparatus, as listed in Table 1, were reached. In November 2015, we transported the full setup from Vienna to the VIP-2 experiment site in Gran Sasso. We assembled the cryogenic system and the readout logic as shown in Fig. 4 and started the test run.

As an important step to confirm the operation of the SDDs after the transportation, we took calibration data by shining 22 keV X-rays on Zr and Ti foils placed near the SDDs. The spectra obtained are shown in Fig. 5, where all SDDs were in working condition and a preliminary analysis showed that the energy resolution is compatible to the one obtained in the tests in the SMI laboratory. We are presently in data taking at LNGS

Acknowledgements

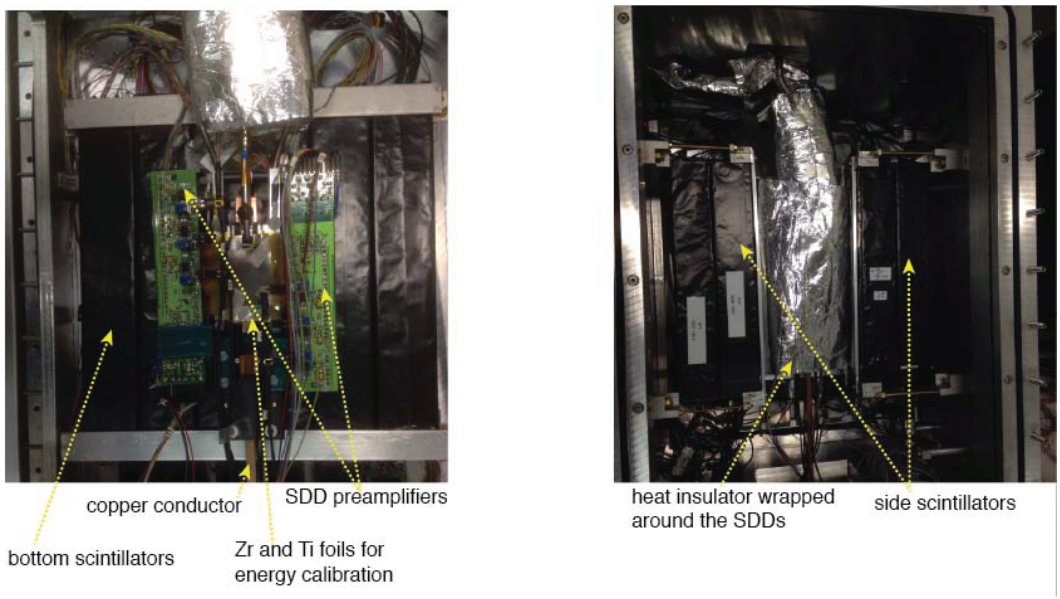

Figure 3: Pictures of the detectors inside the setup. Left : a top view of the setup after the SDDs and their preamplifier board were mounted close to the Cu conductor; the bottom layer of scintillators is also visible in the background; right : same angle of view after the heat insulator was wrapped around the SDDs, and the side layer of scintillators were mounted.

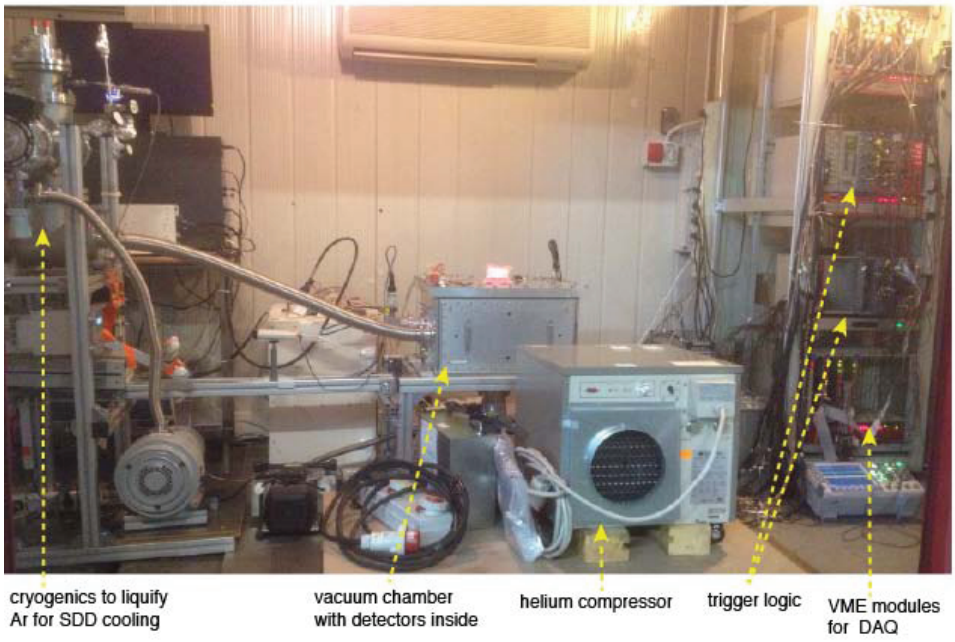

Figure 4: A picture of the VIP-2 setup in the barrack at LNGS as in November 2015.

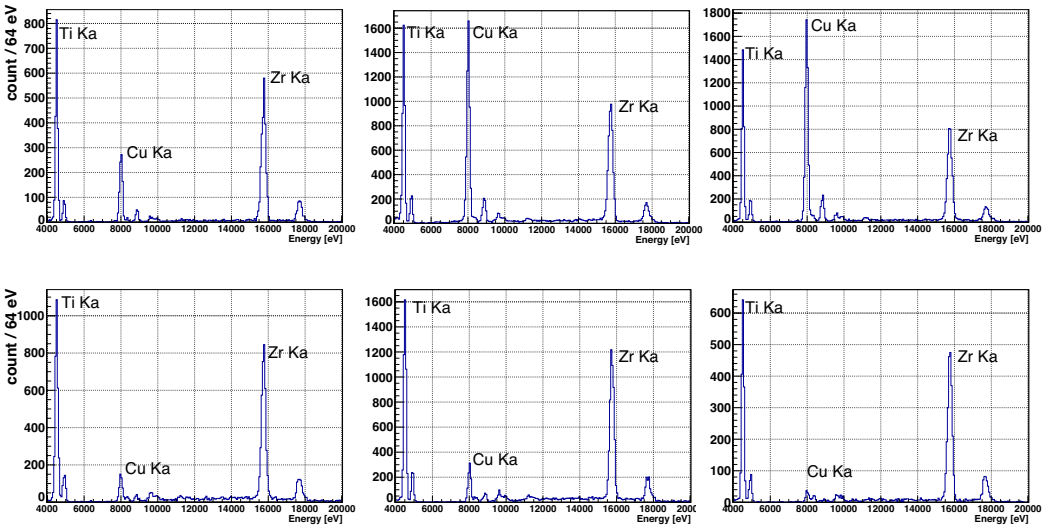

Figure 5: Energy spectra of SDDs from a calibration run in the VIP barrack at LNGS. The relative intensity of the Cu Ka varies due to geometrical reason.

The VIP2 Collaboration wishes to thank all the LNGS laboratory staff for the precious help and assistance during all phases of preparation, installation and data taking. The supports from Museo Storico della Fisica e Centro Studi e Ricerche Enrico Fermi, Roma, the HadronPhysics FP6, HadronPhysics2 and HadronPhysics3 FP7 and from the EU COST 1006 Action projects are acknowledged.

5 List of Publications

1. A. Pichler *et al.*, Application of photon detectors in the VIP2 experiment to test the Pauli Exclusion Principle, e-Print: arXiv:1602.00898 [physics.ins-det].

2. A. Pichler *et al.*, VIP 2: Experimental tests of the Pauli Exclusion Principle for electrons, e-Print: arXiv:1602.00867 [physics.ins-det].

3. C. Curceanu *et al.*, Spontaneously emitted X-rays: an experimental signature of the dynamical reduction models, Found. of Phys., 46 (2016) 263, DOI: 10.1007/D10701-015-9923-4.

4. H. Shi *et al.*, Searches for the Violation of Pauli Exclusion Principle at LNGS in VIP(-2) experiment, e-Print: arXiv:1601.05828 [physics.ins-det].

5. C. Curceanu *et al.*, X rays on quantum mechanics: Pauli Exclusion Principle and collapse models at test, J.Phys.Conf.Ser. 631 (2015) 1, 012068, DOI: 10.1088/1742-6596/631/1/012068.

6. C. Curceanu *et al.*, Experimental search for the impossible atoms Pauli Exclusion Principle violation and spontaneous collapse of the wave function at test, J.Phys.Conf.Ser. 626 (2015) 1, 012027, DOI: 10.1088/1742-6596/626/1/012027.

7. J. Remillieux *et al.*, High energy channelling and the experimental search for the internal clock predicted by Louis de Broglie, Nucl.Instrum.Meth. B355 (2015) 193-197, DOI: 10.1016/j.nimb.2015.02.005.

8. A. Pichler *et al.*, VIP 2: Experimental tests of the Pauli Exclusion Principle for electrons, Hyperfine Interact. 233 (2015) 1-3, 121-126, DOI: 10.1007/s10751-015-1180-6.

9. J. Marton *et al.*, High sensitivity tests of the Pauli Exclusion Principle with VIP2, J.Phys.Conf.Ser. 631 (2015) 1, 012070, DOI: 10.1088/1742-6596/631/1/012070.

10. C. Curceanu, B.C. Hiesmayr, K. Piscicchia, X-rays help to unfuzzy the concept of measurement, e-Print: arXiv:1502.05961 [quant-ph].

11. K. Piscicchia *et al.*, Beyond Quantum Mechanics? Hunting the 'Impossible' Atoms - Pauli Exclusion Principle Violation and Spontaneous Collapse of the Wave Function at Test, Acta Phys.Polon. B46 (2015) 1, 147-152, DOI: 10.5506/APhysPolB.46.147.

References

[1] W. Pauli, *Phys. Rev.* **58**, (1940), 716.

[2] R. P. Feynman, R. B. Leighton and M. Sands *The Feynman Lectures on Physics*, Addison-Wesley, Reading, MA (1963).

[3] R. Arnold, *et al.*, *Eur. Phys. J. A***6** (1999) 361.

[4] H.O. Back, *et al.*, *Eur. Phys. J. C***37** (2004) 421.

[5] A. Barabash, *Found. of Phys.* **40** (2010) 703.

[6] A.S. Barabash,*et al.*, *JETP Lett.* **68** (1998) 112.

[7] P. Belli, *et al.*, **460** (1999) 236.

[8] G. Bellini, *et al.*, *Phys. Rev. C* **81** (2010) 034.

[9] R. Bernabei, *et al.*, *Phys. Lett. B* **408** (1997) 439.

[10] R. Bernabei, *et al.*, *Eur. Phys. J. C* **62** (2009) 327.

[11] Y. Suzuki, *et al.*, *Phys. Lett. B* **311** (1993) 357.

[12] S. R. Elliott *et al.*, *Found. Phys.* **42** (2012) 1015.

[13] A.M.L. Messiah, O.W. Greenberg, *Phys. Rev.* **136** (1964) B248.

[14] E. Ramberg and G. A. Snow, *Phys. Lett. B* **238** (1990) 438.

[15] C. Curceanu *et al.* Evaluation of the X-ray transition energies for the Pauli-Principle-violating atomic transitions in several elements by using the Dirac-Fock method, LNF preprint, INFN-13-21/LNF, 21-11-2013.

[16] J. L. Culhane, *Nucl. Instrum. Methods A* **310** (1990) 1.

[17] J.-P. Egger, D. Chatellard and E. Jeannet, *Particle World* **3**, (1993) 139.

[18] G. Fiorucci, *et al. Nucl. Instrum. Methods A* **292** (1990) 141.

[19] D. Varidel, *et al.Nucl. Instrum. Methods A* **292** (1990) 147

[20] R. P. Kraft, *et al.Nucl. Instrum. Methods A* **372** (1995) 372.

[21] O. W. Greenberg *Phys. Rev. Lett.* **64** (1990) 705.

THE PIERRE AUGER OBSERVATORY

D. Boncioli[a], A. di Matteo[b], A.F. Grillo[a], S. Petrera[b,c], V. Rizi[b]
for the Pierre Auger Collaboration

[a] INFN Laboratori Nazionali del Gran Sasso, Assergi (Aq), Italy
[b] INFN and Department of Physical and Chemical Sciences,
University of L'Aquila, L'Aquila, Italy
[c] GSSI, Gran Sasso Science Institute, L'Aquila, Italy

Abstract

The Pierre Auger Project is an international Collaboration involving about 450 scientists from 16 countries, with the objective of studying the highest energy cosmic rays. Recent results from the Collaboration as well as further developments in the detector are presented in this report.

1 Introduction

Ultra-high energy cosmic rays are of intrinsic interest as their origin and nature are unknown. It is quite unclear where and how particles as energetic as $\approx 10^{20}$ eV are accelerated. Over 40 years ago it was pointed out that if the highest energy particles are protons then a fall in the flux above an energy of about 4×10^{19} eV is expected because of energy losses by the protons as they propagate from distant sources through the photon background radiation. At the highest energies the key process is photo-pion production in which the proton loses part of its energy in each creation of a Δ resonance. This is the Greisen–Zatsepin–Kuzmin (GZK) effect. It follows that at 10^{20} eV any proton observed must have come from within about 50 Mpc and on this distance scale the deflections by intervening magnetic fields in the galaxy and intergalactic space are expected to be so small that point sources should be observed. If nuclei are propagated from sources their photo-disintegration in the photon background field plays a role similar to the GZK effect in the depletion of the flux above 10^{20} eV and the limitation of the CR horizon, but the angular correlation with the sources is expected weaker because of the higher charges.

The main problem in examining whether or not the spectrum steepens is the low rate of events which, above 10^{20} eV, is less than 1 per km^2 per century so that the particles are only detectable through the giant air showers that they create.

These showers have particle footprints on the ground of ≈ 20 km^2 and suitably distributed detectors can be used to observe them. Also the showers excite molecules of atmospheric nitrogen and the resulting faint fluorescence radiation, which is emitted isotropically, can be detected from distances of several tens of kilometers.

The Pierre Auger Observatory has been developed by a team of about 500 scientists from 17 countries. The Observatory comprises about 1600 10 m^2 $\times$ 1.2 m water-Cherenkov detectors deployed over 3000 km^2 on a 1500 m hexagonal grid, plus a sub array, the Infill, with 71 water Cherenkov detectors on a denser grid of 750 m covering nearly 30 km^2. This part of the Observatory (the surface detector, SD) is over-looked by 24 fluorescence telescopes in 4 clusters located on four hills around the SD area which is extremely flat. The surface detectors contain 12 tonnes of clear water viewed by $3 \times 9''$ hemispherical photomultipliers. The fluorescence detectors (FD) are designed to record the faint ultra-violet light emitted as the shower traverses the atmosphere. Each telescope images a portion of the sky of 30° in azimuth and 1°–30° in elevation using a spherical mirror of 3 m^2 effective area to focus light on to a camera of 440×18 cm^2 hexagonal pixels, made of photomultipliers complemented with light collectors, each with a field of view of 1.5° diameter. 3 High Elevation Auger Telescopes (HEAT) located at one of the fluorescence sites are dedicated to the fluorescence observation of lower energy showers. The Observatory also comprises a sub array of 124 radio sensors (AERA, Auger Engineering Radio Array) working in the MHz range and covering 6 km^2, a sub Array of 61 radio sensors (EASIER, Extensive Air Shower Identification with Electron Radiometer) working in the GHz range and covering 100 km^2, and two GHz imaging radio telescopes AMBER and MIDAS with respectively $14° \times 14°$ and $10° \times 20°$ field of views.

An important feature of the design of the Observatory was the introduction of the hybrid technique as a new tool to study air showers. It is used here for the first time. The hybrid technique is the term chosen to describe the method of recording fluorescence data coincident with the timing information from at least one surface detector. Employing these two complementary observation methods provides the Auger Observatory with high quality information about angular reconstruction, determination of the core position of the shower and of the types of particles in the primary cosmic rays. Comparing results from the different types of detectors also helps scientists reconcile the two sets of data and produce the most accurate results about

the energy of primary cosmic rays.

2 Recent results from the Pierre Auger Observatory

The measurement of the energy spectrum of UHECRs, the inference on their mass composition and the analysis of their arrival directions bring different information, complementary and supplementary one to the other, with respect to their origin. In this section the main results presented by the Auger Collaboration on these topics at the 34th International Cosmic Ray Conference (ICRC 2015) are summarized [1].

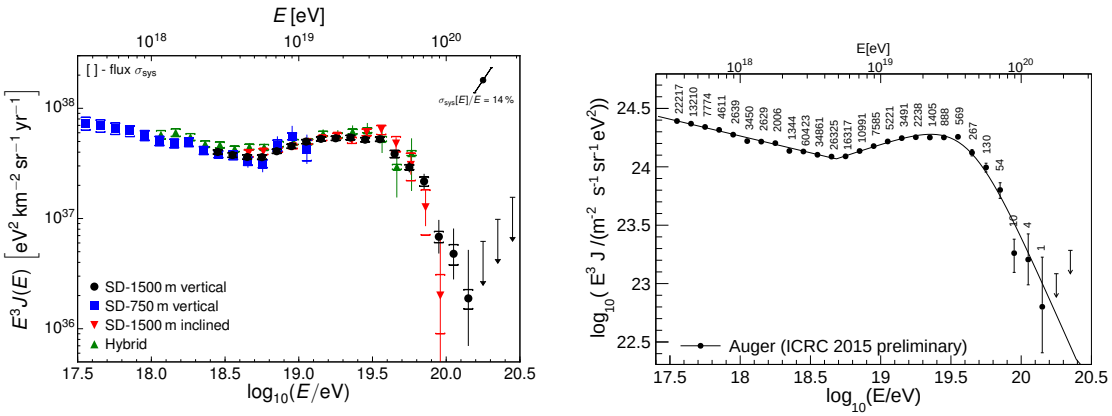

Figure 1: Left: The four energy spectra derived from SD and hybrid data. Right: The combined energy spectrum, fitted with a flux model (see text). As in the left panel, only statistical uncertainties are shown and the upper limits correspond to the 84% C.L.

The measurement of the flux of UHECRs has been one of the first outcomes of Auger data [2]. Two spectral features have been established beyond doubt [3, 4] : the hardening in the spectrum at about 5×10^{18} eV (the so-called ankle), and a strong suppression of the flux at the highest energies, starting at about 4×10^{19} eV. The all-particle flux of cosmic rays presented at ICRC 2015 [5] is an update of such measurement, being based on an exposure now larger than 50000 km^2 sr yr and on 190000 events. Combining four independent spectra (see Figure 1, left) from the two different SDs (and two data sets from the SD-1500 m, vertical and horizontal events) and from hybrid events, the measurement is emblematic of the power of using multiple detectors. Data from the SD-750 m allow for the determination of the energy spectrum down to 10^{17} eV. The SD-1500 m vertical data are crucial above the energy of full trigger efficiency of 3×10^{18} eV up to the highest energies, with horizontal events contributing above 4×10^{18} eV and providing an independent measurement in this energy range. Hybrid data bridge those from the two SDs, between 10^{18} eV and $10^{19.6}$ eV. The four spectra, in agreement within uncertainties, are combined into a unique one shown in Fig. 1, right panel, taking into account the systematics of the individual measurements. The evident features are quantified by fitting a model that describes the spectrum with two power-laws around the ankle, the second of which includes a smooth suppression at the highest energies. The ankle is found to be at $E_{\rm ankle} = (4.8\pm0.1\pm0.8)\times10^{18}$ eV. The spectral slope below the ankle is $\gamma_1 = 3.29\pm0.02\pm0.05$, and above the ankle is $\gamma_2 = 2.60\pm0.02\pm0.10$. The energy at which the differential flux falls to one-half of the value of the power-law extrapolation is $E_{\rm s} = (42.1\pm1.7\pm7.6)\times10^{18}$ eV.

The origin of the very precisely determined features in the all-particle spectrum has been in

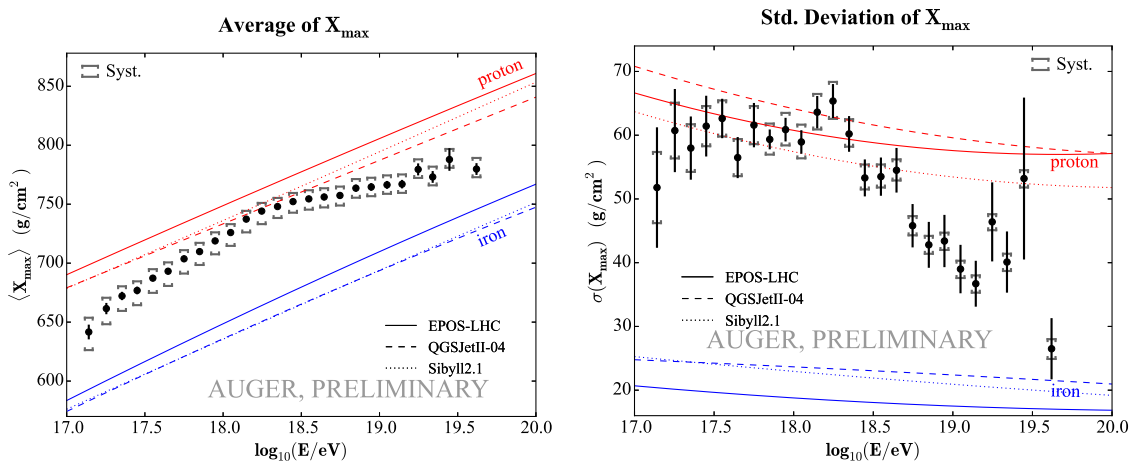

Figure 2: The mean (left) and the standard deviation (right) of the measured $X_{\max}$ distributions as a function of energy compared to air-shower simulations for proton and iron primaries.

parallel addressed by the Collaboration, likewise since many years [6], through the measurement of the depth of the shower maximum, $X_{\max}$, one of the most robust mass-sensitive EAS observables. The measurement, relying on hybrid data, has been recently updated in [7]. An extension of the measurement [8] has been presented at ICRC 2015, for the first time covering the whole energy range of the all-particle flux, down to 10^{17} eV. This has been possible for the inclusion of data from the HEAT telescopes. More than 18000 events collected by the standard FD telescopes (FD data) above $10^{17.8}$ eV, have been supplemented by about 5500 data collected with HEAT in coincidence with the closest FD, Coihueco (so-called HeCo data). By using for HeCo data the same selection and analysis strategy as for FD data [7], the first two moments of the $X_{\max}$ distributions, $\langle X_{\max}\rangle$ and $\sigma(X_{\max})$, are estimated from 10^{17} eV to $10^{18.3}$ eV. In agreement within uncertainties with those derived from FD data in the common energy range (from $10^{17.8}$ eV to $10^{18.3}$ eV), they are combined into the resulting $\langle X_{\max}\rangle$ and $\sigma(X_{\max})$ shown in Fig. 2, left and right, respectively, as a function of energy. Data are confronted to simulations, for proton and iron primaries, performed using three hadronic interaction models that were found to agree with recent LHC data. Between 10^{17} and $10^{18.3}$ eV, $\langle X_{\max}\rangle$ increases by around 85 g cm^{-2} per decade of energy; around $10^{18.3}$ eV, the rate of change of $\langle X_{\max}\rangle$ becomes significantly smaller ($\sim$ 26 g cm^{-2}/decade). These two values, consistent with those found with FD data alone [7], allow to extend the inferences on the evolution of the average mass composition down to 10^{17} eV. As the first value is larger than the one expected for a constant mass composition ($\sim$ 60 g cm^{-2}/decade), it indicates that the mean primary mass is getting lighter all the way from 10^{17} to $10^{18.3}$ eV. Above this energy, the trend inverts and the composition becomes heavier. The fluctuations of $X_{\max}$ start to decrease above the same energy $\sim 10^{18.3}$ eV, being rather constant below. The conversion of the first two moments of the $X_{\max}$ distributions to the mean value of $\ln A$ and its variance $\sigma^2(\ln A)$, presented too in the ICRC 2015 contribution [8], confirms, in a more quantitative way, such an evolution of the average composition, consistently for the considered models.

The last piece of study regarding UHECRs included in this report is that of the distribution of arrival directions on large scales [9]. This integrates other anisotropy searches, not only in terms of angular scale, but also of inferences, as large-scale anisotropies can be reflective either of a collective motion of cosmic rays (e.g., of their propagation), or of the global distribution

of their sources, or of both. As such studies are relevant at all energies, being complementary to spectrum and mass measurements, the large-scale analysis has been performed down to the lowest ones accessible by the Observatory, $\sim 10^{16}$ eV. The technique used is that of the harmonic analysis of the counting rate. The amplitudes of the first harmonic are obtained as upper limits to the equatorial component of the dipole as a function of energy, apart two energy bins where (between 1 and 2 EeV, and for the integral bin above 8 EeV, mean energy 14.5 EeV, respectively) amplitudes are determined. Both upper limits and measurements are at percent level. The evolution of the phases with energy shows a smooth transition of the first harmonic modulation in right ascension distribution from 270° to 100° around 1 EeV. Interestingly, the phase above 8 EeV is roughly the opposite than the one at energies below 1 EeV, which is in the general direction of the Galactic Centre. The percent limits to the amplitude of the anisotropy exclude the presence of a large fraction of Galactic protons at EeV energies [10]. Accounting for the inference from $X_{\rm max}$ data, that protons are in fact abundant at those energies, this might indicate that this component is extra-Galactic, gradually taking over a Galactic one. The low level of anisotropy would then be the sum of two vectors with opposite directions, naturally reducing the amplitudes. An intruiguing possibility, to be explored with additional data.

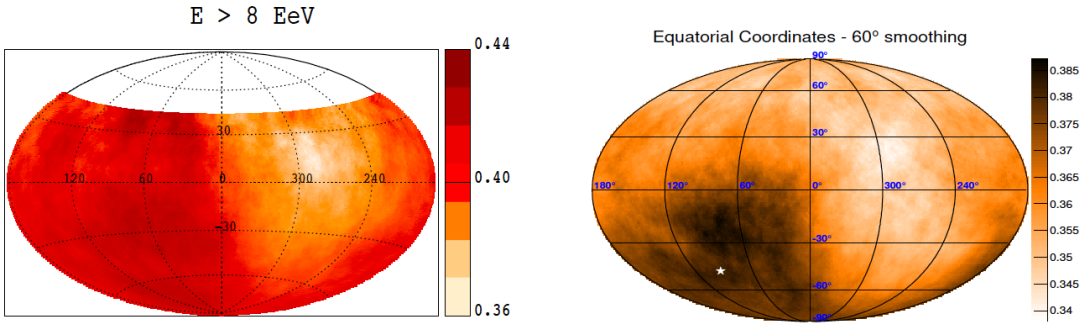

Figure 3: Sky maps in equatorial coordinates of flux, in $\mathrm{km}^{-2}\ \mathrm{yr}^{-1}\ \mathrm{sr}^{-1}$ units, smoothed in angular windows of 45° (60°) radius, for Auger (Auger and Telescope Array) events with E > 8 EeV (10 EeV), left (right) panel.

Similarly intruiguing is the indication of the departure from isotropy above 8 EeV, where the total amplitude of the dipole results to be 0.073±0.015 pointing to $(\alpha, \delta) = (95° \pm 13°, -39° \pm 13°)$. This finding is robust both assuming that the flux of cosmic rays is purely dipolar or purely dipolar and quadripolar [11]. Assumptions on the shape of the angular distribution can be avoided by analyzing it over the full sky. This has been done through a spherical harmonic analysis of Auger and Telescope Array data [12] and updated at ICRC 2015 [13]. No deviation from isotropy at discovery level is found at any multipoles. The largest deviation from isotropy, with a p-value of 5×10^{-3}, occurs for the dipolar moment. The amplitude, 0.065 ± 0.019, and the direction, $(\alpha, \delta) = 93° \pm 24°, 46° \pm 18°)$ are in agreement with that found with Auger-only data. The sky maps of the fluxes, in equatorial coordinates, in Fig. 3, offer a visualization of the dipolar patterns resulting from the two analyses.

3 Activity of the L'Aquila–Gran Sasso Group

The activity of the group has followed two main lines:

- Development of a Monte Carlo code (*SimProp*) for the propagation of UHECR nuclei in extragalactic space, and its use for the study of physical observables
- Development and operation of the Raman Lidar system for an enhanced atmospheric test beam within the Observatory.

The first activity is carried on within the Cosmic Ray Phenomenology task of the Pierre Auger Collaboration. Using outputs of *SimProp*, several physical analyses have been done primarily addressed to a combined fit of the energy spectrum and the mass composition of UHECRs detected in the Observatory [14, 15, 16]. This analysis has also been used as the basis of the scientific motivations for the upgrade of the Pierre Auger Observatory.
The study of predictions for the fluxes of cosmogenic neutrinos from GZK interactions has been also carried on [17, 18, 19].
Lorentz invariance violation has been also investigated, from the point of view of the effects on UHECR propagation and on interactions of particles in the Earth atmosphere [20].

The second activity concerns the atmospheric monitoring. The Raman lidar system has been fully operative at the Central Raman Laser Facility (CRLF). The measurements of the Vertical Aerosol Optical Depth (VAOD) are usually taken from boundary layer to free troposphere using Raman and Rayleigh backscatterings of atmospheric molecules. The Raman lidar applies the best available technique to determine the vertical profiles of the aerosol optical properties (aerosol backscatter and extinction coefficients). Since March 2015, automatic Raman lidar measurements are performed only during the FD measurement shifts, with three acquisition Raman lidar runs 12 minutes long: before, during and after the FD acquisition period. Given the importance of the aerosol measurement for a precise FD reconstruction, it is foreseen to schedule additional Raman lidar runs during the FD measurement shifts, and probably longer Raman lidar measurements for the nights in which the aerosol content is very low; this will also be useful for a better benchmarking of the side scattering tecnique used to estimate the aerosol contribution to the atmospheric optical depth. The latest studies concerning the Raman lidar system and technique used at Auger CRLF have shown that the typical indetermination on the estimated VAOD (with 210 m vertical resolution) is 0.006 due to to statistics and 0.011 due to systematics. The Raman lidar data (September 2013 - March 2016) are stored in LNGS and CSM/USA servers, and preliminary VAOD plots, as well as, of the aerosol backscatter coefficient and of the water vapour mixing ratio vertical profiles can be found at http://cetemps.aquila.infn.it/osservatorio/CLRF raman lidar/. The Raman LIDAR operations have been regular and smooth, and the Raman LIDAR analysis has shown to be robust; also the data quality check is quite positive [21]. The Raman lidar database is now ready for an extended comparison with side scattering technique, but also for atmospheric studies.

3.1 Talks

- A. di Matteo for the Pierre Auger Collaboration "Combined fit of spectrum and composition data as measured by the Pierre Auger Observatory", 34th International Cosmic Ray Conference 30 July 6 August, 2015 (ICRC 2015), The Hague, The Netherlands [arXiv:1509.03732[astro-ph.HE]].
- D. Boncioli, A. di Matteo, F. Salamida, R. Aloisio, P. Blasi, P.L. Ghia, A.F. Grillo, S. Petrera, T. Pierog, "Future prospects of testing Lorentz invariance with UHECRs", 34th International Cosmic Ray Conference 30 July 6 August, 2015 (ICRC 2015), The Hague, The Netherlands [arXiv:1509.01046 [astro-ph.HE]].

- A. di Matteo for the Pierre Auger Collaboration, Cosmic Rays International Seminar,"Surprises from extragalactic propagation of UHECRs," 14-16 Sep 2015. Gallipoli, Italy, arXiv:1512.02314 [astro-ph.HE].
- S. Petrera for the Pierre Auger Collaboration "Exploring the Ultra High Energy Cosmic Rays with the Pierre Auger Observatory", 28th Texas Symposium on Relativistic Astrophysics, December 13 to 18, 2015, Geneva, Switzerland.

References

[1] [Pierre Auger Observatory] Contributions to the 34th International Cosmic Ray Conference (ICRC 2015) [arXiv:1509.03732[astro-ph.HE]].
Piera Ghia for the Pierre Auger Observatory, Highlights from the Pierre Auger Observatory, ICRC 2015.

[2] J. Abraham *et al.* [Pierre Auger Collaboration], Phys. Rev. Lett. **101**, 061101 (2008) doi:10.1103/PhysRevLett.101.061101 [arXiv:0806.4302 [astro-ph]].

[3] J. Abraham *et al.* [Pierre Auger Collaboration], Phys. Lett. B **685**, 239 (2010) doi:10.1016/j.physletb.2010.02.013 [arXiv:1002.1975 [astro-ph.HE]].

[4] A. Aab *et al.* [Pierre Auger Collaboration], JCAP **1508**, 049 (2015) doi:10.1088/1475-7516/2015/08/049 [arXiv:1503.07786 [astro-ph.HE]].

[5] I. Valiño, for the Pierre Auger Collaboration, "The flux of ultra-high energy cosmic rays after ten years of operation of the Pierre Auger Observatory", ICRC 2015, [arXiv:1509.03732[astro-ph.HE]].

[6] J. Abraham *et al.* [Pierre Auger Collaboration], Phys. Rev. Lett. **104**, 091101 (2010) doi:10.1103/PhysRevLett.104.091101 [arXiv:1002.0699 [astro-ph.HE]].

[7] A. Aab *et al.* [Pierre Auger Collaboration], Phys. Rev. D **90**, no. 12, 122005 (2014) doi:10.1103/PhysRevD.90.122005 [arXiv:1409.4809 [astro-ph.HE]].

[8] A. Porcelli, for the Pierre Auger Collaboration, "Measurements of $X_{\rm max}$ above 10^{17} eV with the fluorescence detector of the Pierre Auger Observatory", ICRC 2015, [arXiv:1509.03732[astro-ph.HE]].

[9] I. Al Samarai for the Pierre Auger Collaboration, "Indications of anisotropy at large angular scales in the arrival directions of cosmic rays detected at the Pierre Auger Observatory", ICRC 2015, [arXiv:1509.03732[astro-ph.HE]].

[10] P. Abreu *et al.* [Pierre Auger Collaboration], Astrophys. J. Suppl. **203**, 34 (2012) doi:10.1088/0067-0049/203/2/34 [arXiv:1210.3736 [astro-ph.HE]].

[11] A. Aab *et al.* [Pierre Auger Collaboration], Astrophys. J. **802**, no. 2, 111 (2015) doi:10.1088/0004-637X/802/2/111 [arXiv:1411.6953 [astro-ph.HE]].

[12] A. Aab *et al.* [Telescope Array and Pierre Auger Collaborations], Astrophys. J. **794**, no. 2, 172 (2014) doi:10.1088/0004-637X/794/2/172 [arXiv:1409.3128 [astro-ph.HE]].

[13] O. Deligny for the Telescope Array and Pierre Auger Collaborations, "Large-Scale Distribution of Arrival Directions of Cosmic Rays Detected at the Pierre Auger Observatory and the Telescope Array above 10^{19} eV", ICRC 2015, [arXiv:1511.02103[astro-ph.HE]].

[14] D. Boncioli *et al.* [Pierre Auger Collaboration], arXiv:1512.02314 [astro-ph.HE].

[15] R. Alves Batista, D. Boncioli, A. di Matteo, A. van Vliet and D. Walz, JCAP **1510**, no. 10, 063 (2015) doi:10.1088/1475-7516/2015/10/063 [arXiv:1508.01824 [astro-ph.HE]].

[16] R. Aloisio, D. Boncioli, A. di Matteo, A. F. Grillo, S. Petrera and F. Salamida, arXiv:1505.01347 [astro-ph.HE].

[17] J. Heinze, D. Boncioli, M. Bustamante and W. Winter, arXiv:1512.05988 [astro-ph.HE].

[18] R. Aloisio, D. Boncioli, A. di Matteo, A. F. Grillo, S. Petrera and F. Salamida, JCAP **1510**, no. 10, 006 (2015) doi:10.1088/1475-7516/2015/10/006 [arXiv:1505.04020 [astro-ph.HE]].

[19] R. Aloisio, D. Boncioli, A. di Matteo, A. F. Grillo, S. Petrera and F. Salamida, Nucl. Part. Phys. Proc. **265-266**, 251 (2015) doi:10.1016/j.nuclphysbps.2015.06.065 [arXiv:1505.04742 [astro-ph.HE]].

[20] D. Boncioli *et al.*, arXiv:1509.01046 [astro-ph.HE].

[21] C. Medina-Hernandez, for the Pierre Auger Collaboration, "Studies in the atmospheric monitoring at the Pierre Auger Observatory using the upgraded Central Laser Facility", ICRC 2015, [arXiv:1509.03732[astro-ph.HE]].

4 List of Publications

1. J. Heinze, D. Boncioli, M. Bustamante and W. Winter, arXiv:1512.05988 [astro-ph.HE].
2. A. Aab *et al.* [Pierre Auger Collaboration], JINST **11**, no. 01, P01018 (2016) doi:10.1088/1748-0221/11/01/P01018 [arXiv:1512.02216 [physics.ins-det]].
3. D. Boncioli *et al.* [Pierre Auger Collaboration], arXiv:1512.02314 [astro-ph.HE].
4. M. G. Aartsen *et al.* [IceCube and Pierre Auger and Telescope Array Collaborations], JCAP **1601**, no. 01, 037 (2016) doi:10.1088/1475-7516/2016/01/037 [arXiv:1511.09408 [astro-ph.HE]].
5. M. G. Aartsen *et al.* [IceCube and Pierre Auger and Telescope Array Collaborations], arXiv:1511.02109 [astro-ph.HE].
6. R. U. Abbasi *et al.* [Telescope Array and Pierre Auger Collaborations], arXiv:1511.02103 [astro-ph.HE].
7. A. Aab *et al.* [Pierre Auger Collaboration], arXiv:1509.03732 [astro-ph.HE].
8. D. Boncioli *et al.*, arXiv:1509.01046 [astro-ph.HE].
9. A. Aab *et al.* [Pierre Auger Collaboration], [arXiv:1508.04267 [astro-ph.HE]].

10. R. Aloisio, D. Boncioli, A. di Matteo, A. F. Grillo, S. Petrera and F. Salamida, Nucl. Part. Phys. Proc. **265-266**, 251 (2015) doi:10.1016/j.nuclphysbps.2015.06.065 [arXiv:1505.04742 [astro-ph.HE]].

11. R. Alves Batista, D. Boncioli, A. di Matteo, A. van Vliet and D. Walz, JCAP **1510**, no. 10, 063 (2015) doi:10.1088/1475-7516/2015/10/063 [arXiv:1508.01824 [astro-ph.HE]].

12. R. Aloisio, D. Boncioli, A. di Matteo, A. F. Grillo, S. Petrera and F. Salamida, JCAP **1510**, no. 10, 006 (2015) doi:10.1088/1475-7516/2015/10/006 [arXiv:1505.04020 [astro-ph.HE]].

13. R. Aloisio, D. Boncioli, A. di Matteo, A. F. Grillo, S. Petrera and F. Salamida, arXiv:1505.01347 [astro-ph.HE].

14. A. Aab *et al.* [Pierre Auger Collaboration], Phys. Rev. D **91**, no. 9, 092008 (2015) doi:10.1103/PhysRevD.91.092008 [arXiv:1504.05397 [astro-ph.HE]].

15. A. Aab *et al.* [Pierre Auger Collaboration], JCAP **1508**, 049 (2015) doi:10.1088/1475-7516/2015/08/049 [arXiv:1503.07786 [astro-ph.HE]].

16. A. Aab *et al.* [Pierre Auger Collaboration], Nucl. Instrum. Meth. A **798**, 172 (2015) doi:10.1016/j.nima.2015.06.058 [arXiv:1502.01323 [astro-ph.IM]].

17. A. Aab *et al.* [Pierre Auger Collaboration], Astrophys. J. **802**, no. 2, 111 (2015) doi:10.1088/0004-637X/802/2/111 [arXiv:1411.6953 [astro-ph.HE]].

18. A. Aab *et al.* [Pierre Auger Collaboration], Astrophys. J. **804**, no. 1, 15 (2015) doi:10.1088/0004-637X/804/1/15 [arXiv:1411.6111 [astro-ph.HE]].

19. A. Aab *et al.* [Pierre Auger Collaboration], Eur. Phys. J. C **75**, no. 6, 269 (2015) doi:10.1140/epjc/s10052-015-3471-0 [arXiv:1410.0515 [astro-ph.HE]].

20. A. Aab *et al.* [Pierre Auger Collaboration], Phys. Rev. D **91**, no. 3, 032003 (2015) Erratum: [Phys. Rev. D **91**, no. 5, 059901 (2015)] doi:10.1103/PhysRevD.91.059901, 10.1103/PhysRevD.91.032003 [arXiv:1408.1421 [astro-ph.HE]].

21. A. Aab *et al.* [Pierre Auger Collaboration], Phys. Rev. D **90**, no. 1, 012012 (2014) Addendum: [Phys. Rev. D **90**, no. 3, 039904 (2014)] Erratum: [Phys. Rev. D **92**, no. 1, 019903 (2015)] doi:10.1103/PhysRevD.92.019903, 10.1103/PhysRevD.90.012012, 10.1103/PhysRevD.90.039904 [arXiv:1407.5919 [hep-ex]].

The Pierre Auger Collaboration

A. Aab[41], P. Abreu[72], M. Aglietta[51,50], E.J. Ahn[87], I. Al Samarai[31], I.F.M. Albuquerque[16], I. Allekotte[1], P. Allison[92], A. Almela[11,8], J. Alvarez Castillo[65], J. Alvarez-Muñiz[82], R. Alves Batista[40], M. Ambrosio[48], A. Aminaei[66], L. Anchordoqui[86], B. Andrada[8], S. Andringa[72], C. Aramo[48], F. Arqueros[79], N. Arsene[75], H. Asorey[1,25], P. Assis[72], J. Aublin[31], G. Avila[10], N. Awal[90], A.M. Badescu[76], C. Baus[36], J.J. Beatty[92], K.H. Becker[35], J.A. Bellido[12], C. Berat[32], M.E. Bertaina[52,50], X. Bertou[1], P.L. Biermann[b], P. Billoir[31], S.G. Blaess[12], A. Blanco[72], M. Blanco[31], J. Blazek[26], C. Bleve[54,46], H. Blümer[36,37], M. Boháčová[26], D. Boncioli[43,d], C. Bonifazi[23], N. Borodai[70], A.M. Botti[8], J. Brack[85], I. Brancus[73], T. Bretz[39], A. Bridgeman[37], F.L. Briechle[39], P. Buchholz[41], A. Bueno[81], S. Buitink[66], M. Buscemi[56,44], K.S. Caballero-Mora[63], B. Caccianiga[47], L. Caccianiga[31], M. Candusso[49], L. Caramete[74], R. Caruso[56,44], A. Castellina[51,50], G. Cataldi[46], L. Cazon[72],

R. Cester[52,50], A.G. Chavez[64], A. Chiavassa[52,50], J.A. Chinellato[17], J.C. Chirinos Diaz[89], J. Chudoba[26], R.W. Clay[12], R. Colalillo[58,48], A. Coleman[93], L. Collica[50], M.R. Coluccia[54,46], R. Conceição[72], F. Contreras[9], M.J. Cooper[12], A. Cordier[30], S. Coutu[93], C.E. Covault[83], J. Cronin[94], R. Dallier[34,33], S. D'Amico[53,46], B. Daniel[17], S. Dasso[5,3], K. Daumiller[37], B.R. Dawson[12], R.M. de Almeida[24], S.J. de Jong[66,68], G. De Mauro[66], J.R.T. de Mello Neto[23], I. De Mitri[54,46], J. de Oliveira[24], V. de Souza[15], J. Debatin[37], L. del Peral[80], O. Deligny[29], N. Dhital[89], C. Di Giulio[59,49], A. Di Matteo[55,45], M.L. Díaz Castro[17], F. Diogo[72], C. Dobrigkeit[17], W. Docters[67], J.C. D'Olivo[65], A. Dorofeev[85], R.C. dos Anjos[22], M.T. Dova[4], A. Dundovic[40], J. Ebr[26], R. Engel[37], M. Erdmann[39], M. Erfani[41], C.O. Escobar[87,17], J. Espadanal[72], A. Etchegoyen[8,11], H. Falcke[66,69,68], K. Fang[94], G. Farrar[90], A.C. Fauth[17], N. Fazzini[87], A.P. Ferguson[83], B. Fick[89], J.M. Figueira[8], A. Filevich[8], A. Filipčič[77,78], O. Fratu[76], M.M. Freire[6], T. Fujii[94], A. Fuster[8,11], F. Gallo[8,11], B. García[7], D. Garcia-Gamez[30], D. Garcia-Pinto[79], F. Gate[34], H. Gemmeke[38], A. Gherghel-Lascu[73], P.L. Ghia[31], U. Giaccari[23], M. Giammarchi[47], M. Giller[71], D. Głas[71], C. Glaser[39], H. Glass[87], G. Golup[1], M. Gómez Berisso[1], P.F. Gómez Vitale[10], N. González[8], B. Gookin[85], J. Gordon[92], A. Gorgi[51,50], P. Gorham[95], P. Gouffon[16], N. Griffith[92], A.F. Grillo[43], T.D. Grubb[12], F. Guarino[58,48], G.P. Guedes[18], M.R. Hampel[8], P. Hansen[4], D. Harari[1], T.A. Harrison[12], J.L. Harton[85], Q. Hasankiadeh[37], A. Haungs[37], T. Hebbeker[39], D. Heck[37], P. Heimann[41], A.E. Herve[36], G.C. Hill[12], C. Hojvat[87], N. Hollon[94], E. Holt[37], P. Homola[70], J.R. Hörandel[66,68], P. Horvath[27], M. Hrabovský[27], T. Huege[37], A. Insolia[56,44], P.G. Isar[74], I. Jandt[35], S. Jansen[66,68], C. Jarne[4], J.A. Johnsen[84], M. Josebachuili[8], A. Kääpä[35], O. Kambeitz[36], K.H. Kampert[35], P. Kasper[87], I. Katkov[36], B. Keilhauer[37], E. Kemp[17], R.M. Kieckhafer[89], H.O. Klages[37], M. Kleifges[38], J. Kleinfeller[9], R. Krause[39], N. Krohm[35], D. Kuempel[39], G. Kukec Mezek[78], N. Kunka[38], A. Kuotb Awad[37], D. LaHurd[83], L. Latronico[50], R. Lauer[97], M. Lauscher[39], P. Lautridou[34], P. Lebrun[87], M.A. Leigui de Oliveira[21], A. Letessier-Selvon[31], I. Lhenry-Yvon[29], K. Link[36], L. Lopes[72], R. López[60], A. López Casado[82], A. Lucero[8], M. Malacari[12], M. Mallamaci[57,47], D. Mandat[26], P. Mantsch[87], A.G. Mariazzi[4], V. Marin[34], I.C. Mariş[81], G. Marsella[54,46], D. Martello[54,46], H. Martinez[61], O. Martínez Bravo[60], J.J. Masías Meza[3], H.J. Mathes[37], S. Mathys[35], J. Matthews[88], J.A.J. Matthews[97], G. Matthiae[59,49], D. Maurizio[13], E. Mayotte[84], P.O. Mazur[87], C. Medina[84], G. Medina-Tanco[65], V.B.B. Mello[23], D. Melo[8], A. Menshikov[38], S. Messina[67], M.I. Micheletti[6], L. Middendorf[39], I.A. Minaya[79], L. Miramonti[57,47], B. Mitrica[73], L. Molina-Bueno[81], S. Mollerach[1], F. Montanet[32], C. Morello[51,50], M. Mostafá[93], C.A. Moura[21], G. Müller[39], M.A. Muller[17,20], S. Müller[37], S. Navas[81], P. Necesal[26], L. Nellen[65], A. Nelles[66,68], J. Neuser[35], P.H. Nguyen[12], M. Niculescu-Oglinzanu[73], M. Niechciol[41], L. Niemietz[35], T. Niggemann[39], D. Nitz[89], D. Nosek[28], V. Novotny[28], H. Nožka[27], L.A. Núñez[25], L. Ochilo[41], F. Oikonomou[93], A. Olinto[94], N. Pacheco[80], D. Pakk Selmi-Dei[17], M. Palatka[26], J. Pallotta[2], P. Papenbreer[35], G. Parente[82], A. Parra[60], T. Paul[91,86], M. Pech[26], J. Pękala[70], R. Pelayo[62], J. Peña-Rodriguez[25], I.M. Pepe[19], L. Perrone[54,46], E. Petermann[96], C. Peters[39], S. Petrera[55,45], J. Phuntsok[93], R. Piegaia[3], T. Pierog[37], P. Pieroni[3], M. Pimenta[72], V. Pirronello[56,44], M. Platino[8], M. Plum[39], C. Porowski[70], R.R. Prado[15], P. Privitera[94], M. Prouza[26], E.J. Quel[2], S. Querchfeld[35], S. Quinn[83], J. Rautenberg[35], O. Ravel[34], D. Ravignani[8], D. Reinert[39], B. Revenu[34], J. Ridky[26], M. Risse[41], P. Ristori[2], V. Rizi[55,45], W. Rodrigues de Carvalho[82], J. Rodriguez Rojo[9], M.D. Rodríguez-Frías[80], D. Rogozin[37], J. Rosado[79], M. Roth[37], E. Roulet[1], A.C. Rovero[5], S.J. Saffi[12], A. Saftoiu[73], H. Salazar[60], A. Saleh[78], F. Salesa Greus[93], G. Salina[49], J.D. Sanabria Gomez[25], F. Sánchez[8], P. Sanchez-Lucas[81], E.M. Santos[16], E. Santos[17], F. Sarazin[84], B. Sarkar[35], R. Sarmento[72], C. Sarmiento-Cano[25], R. Sato[9], C. Scarso[9], M. Schauer[35], V. Scherini[54,46], H. Schieler[37], D. Schmidt[37], O. Scholten[67,c], H. Schoorlemmer[95], P. Schovánek[26], F.G. Schröder[37], A. Schulz[37], J. Schulz[66], J. Schumacher[39], S.J. Sciutto[4], A. Segreto[42,44], M. Settimo[31], A. Shadkam[88], R.C. Shellard[13], G. Sigl[40], O. Sima[75], A. Śmiałkowski[71], R. Šmída[37], G.R. Snow[96], P. Sommers[93], S. Sonntag[41], J. Sorokin[12], R. Squartini[9], D. Stanca[73], S. Stanič[78], J. Stapleton[92], J. Stasielak[70], M. Stephan[39],

F. Strafella[54,46], A. Stutz[32], F. Suarez[8,11], M. Suarez Durán[25], T. Suomijärvi[29], A.D. Supanitsky[5], M.S. Sutherland[92], J. Swain[91], Z. Szadkowski[71], O.A. Taborda[1], A. Tapia[8], A. Tepe[41], V.M. Theodoro[17], C. Timmermans[68,66], C.J. Todero Peixoto[14], G. Toma[73], L. Tomankova[37], B. Tomé[72], A. Tonachini[52,50], G. Torralba Elipe[82], D. Torres Machado[23], P. Travnicek[26], M. Trini[78], R. Ulrich[37], M. Unger[90,37], M. Urban[39], J.F. Valdés Galicia[65], I. Valiño[82], L. Valore[58,48], G. van Aar[66], P. van Bodegom[12], A.M. van den Berg[67], A. van Vliet[66], E. Varela[60], B. Vargas Cárdenas[65], G. Varner[95], R. Vasquez[23], J.R. Vázquez[79], R.A. Vázquez[82], D. Veberič[37], V. Verzi[49], J. Vicha[26], M. Videla[8], L. Villaseñor[64], S. Vorobiov[78], H. Wahlberg[4], O. Wainberg[8,11], D. Walz[39], A.A. Watson[a], M. Weber[38], K. Weidenhaupt[39], A. Weindl[37], L. Wiencke[84], H. Wilczyński[70], T. Winchen[35], D. Wittkowski[35], B. Wundheiler[8], S. Wykes[66], L. Yang[78], T. Yapici[89], A. Yushkov[41], E. Zas[82], D. Zavrtanik[78,77], M. Zavrtanik[77,78], A. Zepeda[61], B. Zimmermann[38], M. Ziolkowski[41], Z. Zong[29], F. Zuccarello[56,44]

[1] Centro Atómico Bariloche and Instituto Balseiro (CNEA-UNCuyo-CONICET), Argentina

[2] Centro de Investigaciones en Láseres y Aplicaciones, CITEDEF and CONICET, Argentina

[3] Departamento de Física, FCEyN, Universidad de Buenos Aires, Argentina

[4] IFLP, Universidad Nacional de La Plata and CONICET, Argentina

[5] Instituto de Astronomía y Física del Espacio (IAFE, CONICET-UBA), Argentina

[6] Instituto de Física de Rosario (IFIR) – CONICET/U.N.R. and Facultad de Ciencias Bioquímicas y Farmacéuticas U.N.R., Argentina

[7] Instituto de Tecnologías en Detección y Astropartículas (CNEA, CONICET, UNSAM) and Universidad Tecnológica Nacional – Facultad Regional Mendoza (CONICET/CNEA), Argentina

[8] Instituto de Tecnologías en Detección y Astropartículas (CNEA, CONICET, UNSAM), Centro Atómico Constituyentes, Comisión Nacional de Energía Atómica, Argentina

[9] Observatorio Pierre Auger, Argentina

[10] Observatorio Pierre Auger and Comisión Nacional de Energía Atómica, Argentina

[11] Universidad Tecnológica Nacional – Facultad Regional Buenos Aires, Argentina

[12] University of Adelaide, Australia

[13] Centro Brasileiro de Pesquisas Fisicas (CBPF), Brazil

[14] Universidade de São Paulo, Escola de Engenharia de Lorena, Brazil

[15] Universidade de São Paulo, Inst. de Física de São Carlos, São Carlos, Brazil

[16] Universidade de São Paulo, Inst. de Física, São Paulo, Brazil

[17] Universidade Estadual de Campinas (UNICAMP), Brazil

[18] Universidade Estadual de Feira de Santana (UEFS), Brazil

[19] Universidade Federal da Bahia, Brazil

[20] Universidade Federal de Pelotas, Brazil

[21] Universidade Federal do ABC (UFABC), Brazil

[22] Universidade Federal do Paraná, Setor Palotina, Brazil

[23] Universidade Federal do Rio de Janeiro (UFRJ), Instituto de Física, Brazil

[24] Universidade Federal Fluminense, Brazil

[25] Universidad Industrial de Santander, Colombia

[26] Institute of Physics (FZU) of the Academy of Sciences of the Czech Republic, Czech Republic

[27] Palacky University, RCPTM, Czech Republic

[28] University Prague, Institute of Particle and Nuclear Physics, Czech Republic

[29] Institut de Physique Nucléaire d'Orsay (IPNO), Université Paris 11, CNRS-IN2P3, France

[30] Laboratoire de l'Accélérateur Linéaire (LAL), Université Paris 11, CNRS-IN2P3, France

[31] Laboratoire de Physique Nucléaire et de Hautes Energies (LPNHE), Universités Paris 6 et Paris 7, CNRS-IN2P3, France

[32] Laboratoire de Physique Subatomique et de Cosmologie (LPSC), Université Grenoble-Alpes, CNRS/IN2P3, France

[33] Station de Radioastronomie de Nançay, France

[34] SUBATECH, École des Mines de Nantes, CNRS-IN2P3, Université de Nantes, France

[35] Bergische Universität Wuppertal, Fachbereich C – Physik, Germany

[36] Karlsruhe Institute of Technology, Institut für Experimentelle Kernphysik (IEKP), Germany

[37] Karlsruhe Institute of Technology, Institut für Kernphysik (IKP), Germany

[38] Karlsruhe Institute of Technology, Institut für Prozessdatenverarbeitung und Elektronik (IPE), Germany

[39] RWTH Aachen University, III. Physikalisches Institut A, Germany

[40] Universität Hamburg, II. Institut für Theoretische Physik, Germany

[41] Universität Siegen, Fachbereich 7 Physik – Experimentelle Teilchenphysik, Germany

[42] INAF – Istituto di Astrofisica Spaziale e Fisica Cosmica di Palermo, Italy

[43] INFN Laboratori del Gran Sasso, Italy

[44] INFN, Sezione di Catania, Italy

[45] INFN, Sezione di L'Aquila, Italy

[46] INFN, Sezione di Lecce, Italy

[47] INFN, Sezione di Milano, Italy

[48] INFN, Sezione di Napoli, Italy

[49] INFN, Sezione di Roma "Tor Vergata", Italy

[50] INFN, Sezione di Torino, Italy

[51] Osservatorio Astrofisico di Torino (INAF), Torino, Italy

[52] Università Torino, Dipartimento di Fisica, Italy

[53] Università del Salento, Dipartimento di Ingegneria, Italy

[54] Università del Salento, Dipartimento di Matematica e Fisica "E. De Giorgi", Italy

[55] Università dell'Aquila, Dipartimento di Chimica e Fisica, Italy

[56] Università di Catania, Dipartimento di Fisica e Astronomia, Italy

[57] Università di Milano, Dipartimento di Fisica, Italy

[58] Università di Napoli "Federico II", Dipartimento di Fisica, Italy

[59] Università di Roma "Tor Vergata", Dipartimento di Fisica, Italy

[60] Benemérita Universidad Autónoma de Puebla (BUAP), México

[61] Centro de Investigación y de Estudios Avanzados del IPN (CINVESTAV), México

[62] Unidad Profesional Interdisciplinaria en Ingeniería y Tecnologías Avanzadas del Instituto Politécnico Nacional (UPIITA-IPN), México

[63] Universidad Autónoma de Chiapas, México

[64] Universidad Michoacana de San Nicolás de Hidalgo, México

[65] Universidad Nacional Autónoma de México, México

[66] Institute for Mathematics, Astrophysics and Particle Physics (IMAPP), Radboud Universiteit, Nijmegen, Netherlands

[67] KVI – Center for Advanced Radiation Technology, University of Groningen, Netherlands

[68] Nationaal Instituut voor Kernfysica en Hoge Energie Fysica (NIKHEF), Netherlands

[69] Stichting Astronomisch Onderzoek in Nederland (ASTRON), Dwingeloo, Netherlands

[70] Institute of Nuclear Physics PAN, Poland

[71] University of Łódź, Poland

[72] Laboratório de Instrumentação e Física Experimental de Partículas – LIP and Instituto Superior Técnico – IST, Universidade de Lisboa – UL, Portugal

[73] "Horia Hulubei" National Institute for Physics and Nuclear Engineering, Romania

[74] Institute of Space Science, Romania

[75] University of Bucharest, Physics Department, Romania

[76] University Politehnica of Bucharest, Romania

[77] Experimental Particle Physics Department, J. Stefan Institute, Slovenia

[78] Laboratory for Astroparticle Physics, University of Nova Gorica, Slovenia

[79] Universidad Complutense de Madrid, Spain

[80] Universidad de Alcalá de Henares, Spain

[81] Universidad de Granada and C.A.F.P.E., Spain

[82] Universidad de Santiago de Compostela, Spain

[83] Case Western Reserve University, USA

[84] Colorado School of Mines, USA

[85] Colorado State University, USA

[86] Department of Physics and Astronomy, Lehman College, City University of New York, USA

[87] Fermi National Accelerator Laboratory, USA

[88] Louisiana State University, USA

[89] Michigan Technological University, USA

[90] New York University, USA

[91] Northeastern University, USA

[92] Ohio State University, USA

[93] Pennsylvania State University, USA

[94] University of Chicago, USA

[95] University of Hawaii, USA

[96] University of Nebraska, USA

[97] University of New Mexico, USA

[a] School of Physics and Astronomy, University of Leeds, Leeds, United Kingdom

[b] Max-Planck-Institut für Radioastronomie, Bonn, Germany

[c] also at Vrije Universiteit Brussels, Brussels, Belgium

[d] also at Deutsches Elektronen-Synchrotron (DESY), Zeuthen, Germany